

# PLASMA PHYSICS AND TECHNOLOGY

2015



CZECH  
TECHNICAL  
UNIVERSITY  
IN  
PRAGUE



VOLUME 2  
NUMBER 3

ISSN: 2336-2626  
MK ČR E 21495

## Contents

The Problem of Chemically Active Plasma Nonequilibrium. Review.....	226
<i>Chernyak V., Nedybaliuk O., Martysh E., Solomenko O., Fedirchik I., Iukhymenko V., Prysiazhnevych I., Veremii Iu.</i>	
Why the Arc, and its Interactions with the Electrodes, Are Important in Predictive Modelling of Arc Welding .....	233
<i>Murphy A. B.</i>	
Development of Long Flashover and Multi-Chamber Arresters and Insulator-Arresters for Lightning Protection of Overhead Distribution and Transmission Lines.....	241
<i>Podporkin G. V.</i>	
Pulsed Plasma Spraying of Liquid Feedstock for Coating Elaboration .....	251
<i>Rat V., Mavier F., Bienia M., Lejeune M, Coudert J.F.</i>	
Arc Modeling Challenges.....	261
<i>Rümppler Ch., Narayanan V.R.T.</i>	
Future Perspectives on High Voltage Circuit Breaker Research.....	271
<i>Seeger M.</i>	
Extended Methods of Emission Spectroscopy for the Analysis of Arc Dynamics and Arc Interaction with Walls.....	280
<i>Uhrlandt D., Methling R., Franke St., Gorchakov S., Baeva M., Khakpour A., Brüser V.</i>	
Modelling of Turbulent SF <sub>6</sub> Switching Arcs.....	290
<i>Zhang Q., Yan J. D., Yan G.</i>	
Modelling Radiative Properties of SF <sub>6</sub> Arc Plasma .....	300
<i>Bartlova M., Bogatyreva N., Aubrecht V.</i>	
Diffuse Coplanar Surface Barrier Discharge: Influence of Gas Humidity on Plasma Parameters .....	304
<i>Čech J., Šťáhel P., Dvořáková H., Černák M.</i>	
Microdischarge in the Vortex Gas Flow .....	308
<i>Chernyak V., Solomenko Ok., Solomenko Ol., Lendiel V., Kalustova D., Prysiazhnevych I.</i>	
Change of the Thermal Profile in the Modern MCCB by the Different Electrical Contact Resistance.....	312
<i>Dostál L., Dohnal P., Valenta J.</i>	
Preliminary Study of Mixing of Plasma Species in a Hybrid-Stabilized Argon-Water Electric Arc .....	316
<i>Jeništa J., Takana H., Uehara S., Nishiyama H., Murphy A. B., Bartlová M., Aubrecht V.</i>	
Nisin Immobilization on Plasma Treated Polyvinyl Alcohol Films .....	320
<i>Kolarova Raskova Z., Šťáhel P., Hrabalíková M., Sedlarik V.</i>	
Investigation of Plasma Properties in a Narrow Gap for Short Time Current .....	324
<i>Runge T., Kopp T., Kurrat M.</i>	
Diagnostics of Extinguishing Process in Low Voltage Devices by Pressure Field Measurement .....	328
<i>Valenta J., Dohnal P., Dostál L.</i>	

## The Problem of Chemically Active Plasma Nonequilibrium. Review

Chernyak V., Nedybaliuk O., Martysh E., Solomenko O., Fedirchik I., Iukhymenko V.,  
Prisiazhnevych I., Veremii Iu.

<sup>1</sup> Taras Shevchenko National University of Kyiv, Faculty of Radio Physics, Electronics and Computer Systems, Kyiv, Ukraine, [chernyak\\_v@ukr.net](mailto:chernyak_v@ukr.net)

<sup>2</sup> A.J. Drexel Plasma Institute Drexel University 3141 Chestnut Street Philadelphia, PA 19104, USA

Data on the negative impact of exothermic chemical reactions on the level of non-isothermal plasma are presented. Therefore the transition from the plasma activation of the fuel mixture (fuel/oxidant) to only plasma activation of oxidant leads to a substantial increase in the coefficient of electric energy transformation into chemical energy ( $\alpha$ ) of produced synthesis gas in hybrid plasma-catalysis system of hydrocarbons reforming ( $\alpha \leq 400$ ).

**Keywords:** non-isothermal plasma, plasma-catalysis system, hydrocarbons reforming

### 1 INTRODUCTION

Previous studies have shown that in regards to fundamental and applied plasma physics, nonequilibrium plasma-chemical systems, which make the chemical transformations selectively with high energy efficiency are the most interesting. Therefore review is focused on plasma devices, in which not only the electrons temperature but also the vibrational temperature significantly exceed the rotational and gas temperature as a whole. High vibrational temperature in these devices significantly accelerates the direct processes of obtaining useful product, and low translational temperature slows down reverse reactions and provides stability of the products formed in the non-equilibrium plasma. Special emphasis has been made on hybrid plasma-catalysis systems of hydrocarbons reforming. The reduction of energy consumption for the destination product is interconnected with the selective plasma chemical transformation. It is known that achievement of chemical reactions high selectivity and their products purity at plasma chemical systems outlet is possible with usage of non-equilibrium "cold" plasma. Its specific characteristics are: high level of electron energy and concentrations of excited and charged particles at the low gas temperature [1].

High rates of plasma-chemical reactions as a rule are caused by high concentration of excited atoms and molecules in electric discharges. At the same time, the physical and chemical processes in quasi-equilibrium and non-equilibrium plasmas are multi-channel. It is

connected with fact that they passed through a large number of vibrational or electron-vibrational levels and there is formation of excited states and excited intermediate products in different quantum states. The presence of deviations from thermodynamic equilibrium of chemically active plasma leads to the fact that the direct and inverse processes are often passed through different quantum states.

So remains the question: how to change the non-equilibrium state level in plasma systems when reactive components are injected to them. We think that it should have the special importance in the case of exothermic processes. Some aspects of this problem are investigated in this paper.

### 2 THE ENERGY CHANGE OF THE PARTICLES IN CHEMICAL REACTIONS

Traditionally [2] introduced the concept of the reaction path when considering the energy of chemical reactions. So the way reaction of exchange ( $A + BC \rightarrow AB + C$ ) there is a line in the configuration space leading from the initial to the final particles corresponding to the minimum energy of the interaction of atoms and molecules. Cross-section of the potential energy surface along the reaction path is called a profile reaction path. The differences between the potential energies of  $Q_0$  for the initial and final states are characterized by the energy change for the reaction. In particular, the heat of reaction  $Q$  is defined as the total change in potential energy  $Q_0$  and change the zero oscillation energy

$$Q = Q_0 + \Delta E_z \quad (1)$$

where  $\Delta E_z$  is the difference of zero-point energies oscillation source and target molecules  $\Delta E_z = E_z - E'_z$ . The most chemical reactions have the potential barrier on reaction path.

The occurrence of the energy barrier is required to restructure the electronic structure of molecules involved in the reaction which is reduced to the destruction of the chemical bond BC and the formation of a new bond AB [2]. This energy barrier is named as the activation energy of a chemical reaction.

The using of approach similar to the Fridman-Macheret  $\alpha$ -model [3-5] for qualitative analysis of the influence of chemical processes to increase the internal energy of the products indicating an increase in the activation energy of a chemical reaction for exothermic and endothermic processes [6]. Although mentioned earlier the activation energy increasing is much smaller in the case of exothermic processes (Fig.1).

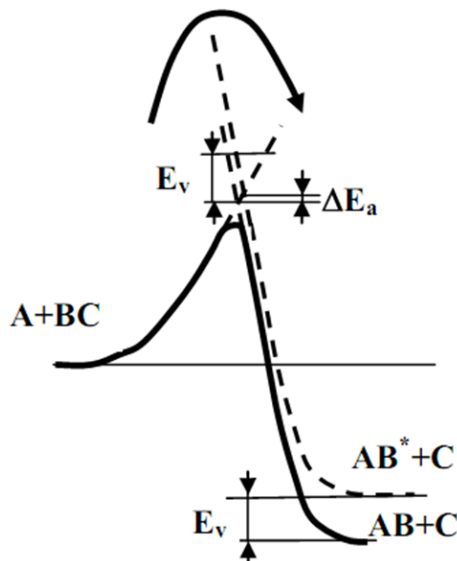


Fig.1: Growth of the activation energy of the exothermic reaction with the excited products in exchange reaction  $A + BC \rightarrow AB + C$ . Solid curve – reaction profile; dashed line represents a oscillatory term, corresponding to an atom C interaction with a vibrationally excited molecule  $AB^*(E_v)$

According to Arrhenius law it indicates a lower reaction rate with the internal states of the reaction product pumping compared to the reaction without it.

A large number of data on excitation of the

products of elementary chemical processes vibrational levels was obtained in the study of atomic reactions. This research was initiated by Boudart and his colleagues [7]. Theoretical analysis of the energy distribution in reaction products was first implemented by M. Evans and M. Polanyi in 1939 – and based on H. Eyring and M. Polanyi conception of the chemical reaction  $A + BC \rightarrow AB + C$  as three particles A, B and C classical motion as a potential surfaces in one dimension (all three particles are on the same line). M. Evans and M. Polanyi revealed that in the case when the exothermic reaction energy is distinguished at the moment of atom A approaching to molecule BC, basic part of energy is converted into vibrational energy of the reaction product AB. But if this energy is evolved in the process last phase, i.e. when AB and C are divorced, the molecule AB vibrational energy is small and the main part of the released energy takes the form of the reaction products translational energy. The case, realized in practice is determined by the shape of the potential surface i.e. character of the dependence of the potential energy on the distance between the particles [2].

Also the data on chemical lasers [8] analysis indicates that near half of released in the exothermic chemical reactions energy goes into increasing the translational temperature.

When temperature increases there is growth of VT relaxation rate [3] and it also leads to a substantial increase the translational temperature during the exothermic chemical processes.

There are additional factors which increase the translational temperature of heavy component chemically active plasma due to chemical processes [6]:

- the chemical processes in most cases are multi-stage [9],
- direct and inverse processes are took place in statistical systems,
- the low-temperature plasma ability to stimulate chemical processes that do not occur in standard chemical systems. Researches on plasma burning support (S. Starikovskaya and A. Starikovskii 2004, 2006) are shown that non-equilibrium plasma is able to stimulate

the low-temperature fuel oxidation even without the combustible mixture ignition [10]. Kinetics investigations of the hydrocarbons partially-oxidative reforming supported by plasma there revealed simultaneous occurrence of hydrocarbons complete oxidation [11].

- a very high level of energy which is evolved during the exothermic chemical reactions ( $\geq 1$  eV/molecule, f.e. at ethanol full oxidation -13.26 eV/molecule).

All above mentioned indicates that chemical reactions effect on the level of plasma non-isothermality may be extremely high and aimed at reducing the separation among translational temperature and internal states population temperature. It is occurred because the increasing of translational temperature heavy component has its priority in exothermic chemical reactions.

### 3 EXPERIMENTAL STUDY OF THE INFLUENCE OF CHEMICAL REACTIONS ON THE NON-ISOTHERMAL LEVEL OF PLASMA

Earlier results of studies of the exothermic chemical reactions effect on the level of non-equilibrium plasma of transverse discharge – TD (Fig.2) and the discharge in the gas channel with liquid wall – DGCLW (Fig.3) were presented at [6, 12].

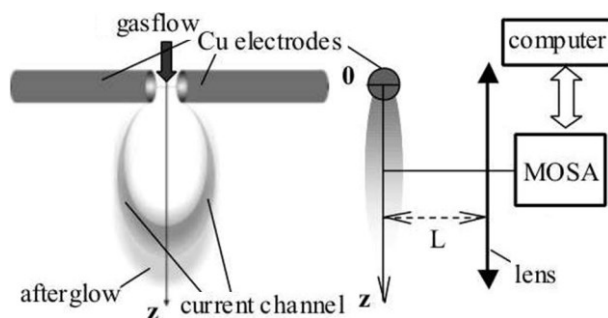


Fig.2: Electric discharge in transversal gas flow

The comparative analysis of plasma parameters of transverse arc and discharge in the gas channel with liquid wall was made for different working gas and liquids (air, distilled water and its mixtures with ethanol). Electron temperature  $T_e^*$  of atom excitations, molecule vibration  $T_v^*$  and rotation  $T_r^*$  temperatures of

the generated plasma were determined by optical emission spectroscopy. Discharge realized in air or a lean fuel mixture (Air/C<sub>2</sub>H<sub>5</sub>OH) in the case of TD, and if DGCLW discharge were implemented in the air channel surrounded by the liquid distilled water and in the air channel surrounded by liquid ethyl alcohol (rich fuel mixture).

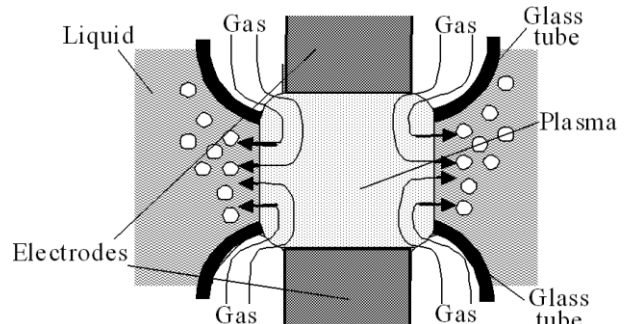


Fig.3: Electric discharge in the gas channel with liquid wall

The main conclusions [6, 12] are:

- TD and DGCLW generate non-equilibrium plasma in the case when working gas is air and working liquid – distilled water. Here the working gas was inactive chemical mixture (dry or moist air).
- Adding fuel to the working gas of plasma system with air leads to a predominant increase of the rotational temperatures and slight increase of the vibrational temperature of the molecules. These temperatures become equal to each other within experimental error. This may indicate that the exothermic reactions reduce the level of the generated plasma non-thermality as a result of additional energy supply for heavy components in the process of complete hydrocarbons combustion.

Adding the final reaction products to the initial reactants can substantially reduce the chemical reactions rates (e.g. extinguishing of the hydrocarbons combustion in the air by adding H<sub>2</sub>O or CO<sub>2</sub>).

Thus impact on the non-equilibrium plasma by adding CO<sub>2</sub> to plasma-chemical system with a hydrocarbon fuel mixture is in particular interest. These experimental studies have been conducted using the plasma chemical system with an electric discharge with liquid electrode in the TORNADO type gas reverse vortex flow (Fig.4). Detailed description of this setup is shown in [13].

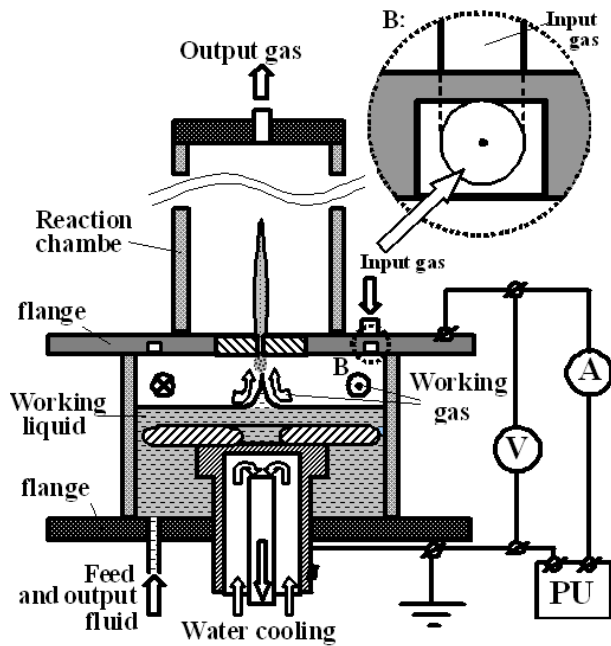
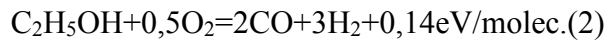


Fig.4: Electric discharge in the reverse vortex gas flow TORNADO type with liquid electrode

The Fig.5 shows the typical dependences of the temperatures of excited electronic ( $T_e^*$ ), vibrational ( $T_v^*$ ) and rotational ( $T_r^*$ ) levels of plasma components from  $C_2H_5OH$  concentration in plasma at the constant air flow ( $55 \text{ cm}^3/\text{s}$ ) current is 320 mA. The stoichiometry of reaction (2) has been performed at ethanol concentration of 4.4 mol/L:



Reaction (2) is endothermic and accompanied by heat absorption. The extra oxygen is formed at its lower values which can stimulate ethanol full oxidation.

On Fig.6 and Fig.7 shows the filling temperatures of excited electronic, vibrational and rotational levels of plasma components for cases when the working fluid is distilled water (Fig.6) and solution of ethanol in water is 1/4 (Fig.7).

In case of using distilled water as the working fluid only a slight tendency to filling temperature of excited hydrogen electronic levels ( $T_e^*(H)$ ) decrease has been noticed from  $CO_2$  percentage increasing in the working gas. Such changes are insignificant given the fact that temperature bias is  $\pm 500 \text{ K}$ .

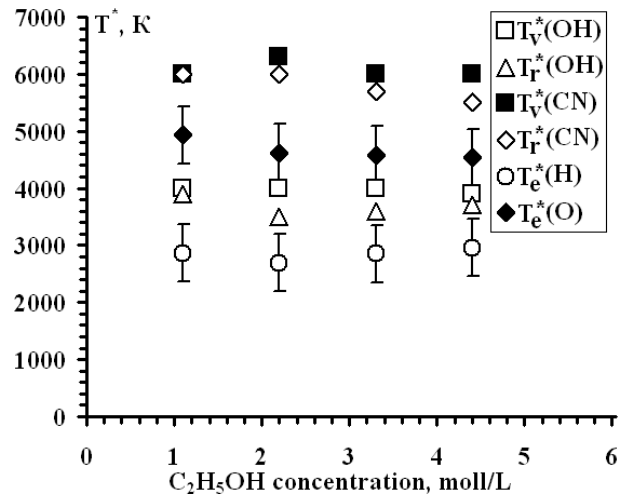


Fig.5: Dependence of  $T_e^*$ ,  $T_v^*$  and  $T_r^*$  from  $C_2H_5OH$  concentration

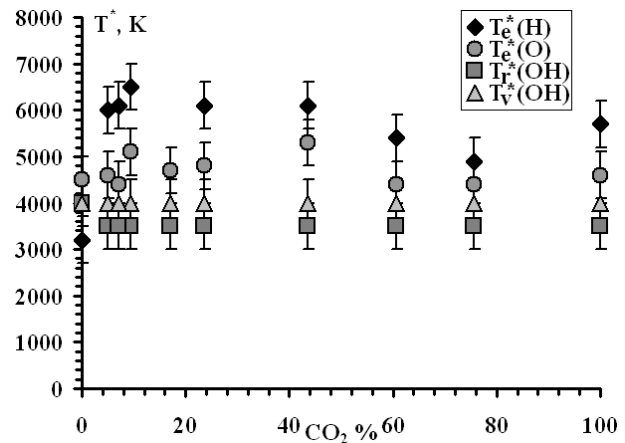


Fig.6: Dependence of  $T_e^*$ ,  $T_v^*$  and  $T_r^*$  of interelectrode gap plasma components from  $CO_2$  percentage in the working gas (air/ $CO_2$ ). The working fluid – distilled water

In case of using the mixture of  $H_2O/C_2H_5OH$  as the working fluid adding  $CO_2$  in the studied  $CO_2/\text{air}$  ration range ( $I = 300 \text{ mA}$ ,  $U = 2-2.2 \text{ kV}$ , air flow – 55 and  $82.5 \text{ cm}^3/\text{s}$ , the flow of  $CO_2$  – 4.25, 8.5 and  $17 \text{ cm}^3/\text{s}$ ) slightly affects the  $T_e^*(H)$  and filling temperatures of excited vibrational molecules levels. The  $CO_2$  concentration increase in the working gas leads to the differences in temperatures of components (reduction of the filling temperature of excited molecules rotational levels).

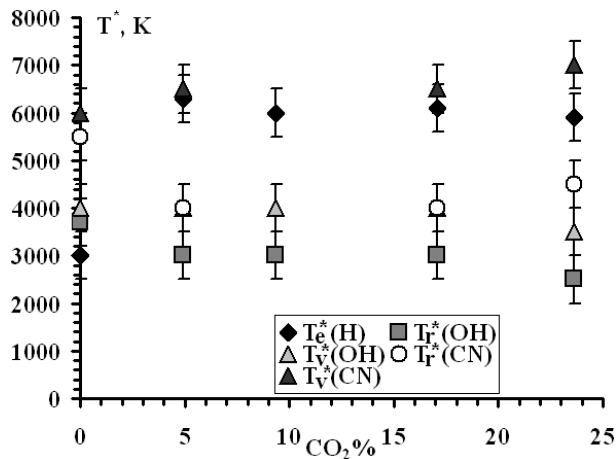


Fig.6: Dependence of  $T_e^*$ ,  $T_v^*$  and  $T_r^*$  of interelectrode gap plasma components from  $\text{CO}_2$  percentage in the working gas (air/ $\text{CO}_2$ ). The working fluid – bioethanol

#### 4 ENERGY EFFICIENCY OF HYDROCARBONS REFORMING IN PLASMA AND PLASMA-CATALYSIS SYSTEMS

The plasma is a source of chemically active species (radicals, ions, excited atoms and molecules) and particles (electrons, photons) for chemical processes activating. This fact is enabled its use in a variety of technologies. Chemical technologies with plasma are usually constructed exclusively as plasma-chemical systems and hybrid systems. At the last case the plasma devices are fitted into standard chemical system. The first has the feature when plasma is generated either in gaseous medium which is a mixture of starting reactants and some buffer gas (e.g., Ar,  $\text{N}_2$ ) or the starting reactants leading in the pre-ionized buffer gas stream. In the first case as plasma generators usually the various gas discharges are used creating non-equilibrium plasma. The isothermal plasma acts as a heat-transfer medium in the second case. It has the  $10^4$  K temperature and products rapid quenching is required at the outlet of the reaction zone.

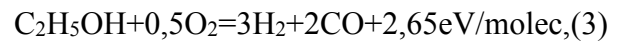
The main features of the hybrid system are the following:

- the reactive species are generated in the plasma and are injected into the reactor where they stimulate chemical processes;
- the cost of electricity on the plasma generation are a few percent of the total process. This effect is called “plasma catalysis” [3]. Combined plasma-catalysis systems are construct-

ed in a variety of configurations this is led to plasma and catalysis synergy. One of such configurations is called plasma pre-treatment, when plasma is treated before entering in catalytic reactor. Another configuration, which is called plasma post-processing involves gas processing after exiting catalytic reactor.

Today it can be argued that the problems of hydrocarbons plasma-chemical conversion into synthesis-gas ( $\text{CO} + \text{H}_2$ ) and other hydrogen-rich mixtures were solved using all known named above plasma-chemical systems and performed for a large number of hydrocarbons. Therefore the particular interest prefers a comparative analysis which is given for the various schemes effectiveness of just this chemical process.

The partially-oxidative and steam reforming and their combinations are most completely investigated. There are following reactions in the case of ethyl alcohol reforming:



Results of the different methods comparison are given in [14] for plasma ethanol reformer efficiency  $\eta$  by different methods of hydrocarbons conversion into syngas.

$$\eta = \frac{\text{H}_2 \times \text{LHV}(\text{H}_2) + \text{CO} \times \text{LHV}(\text{CO})}{\text{IPE} + \text{fuel injected} \times \text{LHV}(\text{fuel})} \quad (5)$$

where LHV is defined as the lower heating values of each component. IPE is the input plasma energy.

This comparison indicates that selection of plasma reforming method has slight effect on  $\eta$ . But comparison of these methods gives more significant differences between rates of electrical energy transformation into chemical energy ( $\alpha$ ) by plasma-chemical method and the hybrid one.

$$\alpha = \frac{\text{H}_2 \times \text{LHV}(\text{H}_2) + \text{CO} \times \text{LHV}(\text{CO})}{\text{IPE}} \quad (6)$$

It follows from the data given in [12, 15], that  $\alpha < 3$  for ethanol reforming by plasma-chemical method and  $\alpha > 30$  for hybrid plasma-catalysis one [5].

However it should be noted that both components of the fuel mixture (air + fuel) are in-

jected typically to plasma under partially-oxidation reforming by hybrid plasma-catalysis method. Conforming to the data presented in the previous sections it should lead to a decrease in the level of non-equilibrium plasma. That is why the data which are obtained by A. Czernichowski in researches on reforming of glycerol in the hybrid plasma-catalysis system with the low-power (50 W) gliding arc [16]:

- when both components of the fuel mixture are injected to plasma simultaneously the maximum is  $\alpha \approx 60$ ,
- when only oxidant activating by the plasma  $\alpha > 250$ .

Series of experiments studying the plasma-catalytic reforming of different liquid hydrocarbons was carried out in [17, 18]. The hybrid system based on low power rotating gliding arc with solid electrodes, was used for investigation of the liquid hydrocarbons reforming process. Conversion was realized by partial oxidation. Part of the oxidant flow was activated by discharge. Synthesis-gas composition was analyzed by mass-spectrometry and gas-chromatography. A standard boiler, which operates on natural gas and liquid propane, was used for synthesis-gas burning and calorimetry of its combustion correspondingly.

It was showed that the electric energy transformation coefficient by using this scheme of plasma-catalytic reforming of liquid hydrocarbons into synthesis-gas to several tens times higher ( $\alpha \approx 90\div 400$ ) than in plasma reforming ( $\alpha < 3$  [6]) and higher than well-known analogues ( $\alpha \approx 30 \div 40$  [5]); reactor temperature substantially less (about 50 %) as compared with a conventional pyrolysis (450°C°); synthesis-gas component composition varies little and C<sub>2</sub>H<sub>5</sub>OH conversion efficiency (65÷90 %) in the tested power range. The synthesis gas is efficiently burned in the NAVIEN boiler that runs on natural gas and LPG.

The Fig. 8 shows the coefficient of transformation of electrical energy into chemical energy of produced synthesis-gas ( $\alpha$ ) and plasma ethanol reformer efficiency ( $\eta$ ) as function of the input plasma energy (discharge power) at different LHV<sub>C<sub>2</sub>H<sub>5</sub>OH</sub>.

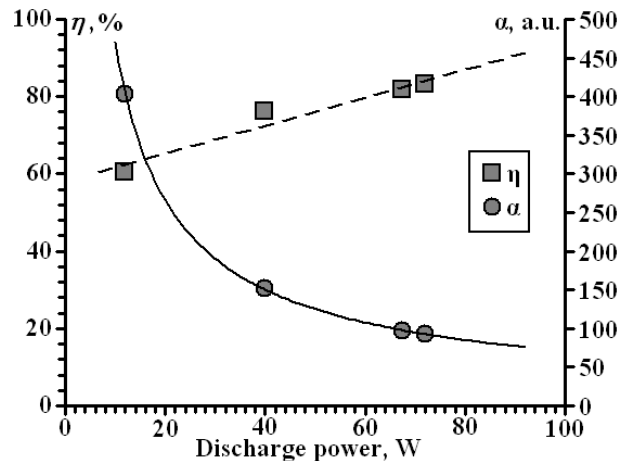


Fig. 8: The  $\alpha$  and  $\eta$  as function of the input plasma energy (discharge power) at different flow of ethanol (LHV<sub>C<sub>2</sub>H<sub>5</sub>OH</sub> = 8 kW)

## 5 CONCLUSION

- The effect of chemical reactions on the level of non-isothermal plasma itself can be extremely high and aimed at reducing the separation of the translational temperature from the temperature of energy level.
- Our experimental researches demonstrate that small addition of ethanol into non-equilibrium air plasma leads to full disappearing of difference between population temperature of vibration and rotation states. This difference has initial value in some thousands degrees.
- Introduction of exothermic chemical inhibitor process to the working gas can effectively influence the separation of the rotational temperature from the vibrational one.
- The full oxidation with plasma activation takes place under plasma formation in mixtures with very low fuel consistence.
- The separation of  $T_v$  from  $T_{tr}$  is increased due to translational temperature significant reduction. It is occurred when an inhibitor of the exothermic process is injected to the plasma-forming gas.
- The transformation ratio of electrical energy into chemical energy is significantly higher at hydrocarbons reforming with plasma-catalysis technologies than with plasma-chemical technologies.
- The transformation of electrical energy into chemical energy under syngas production has strong functional dependence from input plasma energy, especially power area  $\sim$  tens

Watts. When this power has change from 20 to 40 Wt, corresponding coefficient of transformation is dropping at five times.

- The transition from the plasma activation of the fuel mixture (fuel/oxidant) to only plasma activation of oxidant leads to substantial increase in the coefficient of transformation of electric energy into chemical energy of produced synthesis-gas in hybrid plasma-catalysis system of hydrocarbons reforming.

#### Acknowledgements

This work was partially supported by the State Fund for Fundamental Researches, Ministry of Education and Science of Ukraine, National Academy of Science of Ukraine.

#### REFERENCES

- [1] Slovetskij D, Mechanisms of chemical reactions in non-equilibrium plasma, Nauka, Moscow 1980. (In Russian).
- [2] Kondratyev V, Nikitin E, Kinetics and mechanism of gas-phase reactions, Science, 1974. (In Russian).
- [3] Fridman A, Plasma chemistry, Cambridge University Press 2008.
- [4] Levitsky A, Macheret S., Polak L., Fridman A.. Sov. Phys., High Energy Chem. 17 (1983) 625.
- [5] Rusanov V., Fridman A, Physics of Chemically Active Plasma, Nauka (Science), Moscow 1984. (In Russian).
- [6] Chernyak V, Nedybaliuk O, Martysh E, et al., Problems of Atomic Science and Technology. Series: Plasma Physics 94 (2014) 124-129.
- [7] Mc Kinley J, Garvin D, Boudart M J, Chem. Phys. 23 (1955) 784.
- [8] Oraevsky A N, Chemical lasers. Handbook on lasers. Sovetskoe radio, Moscow 1978. (In Russian).
- [9] <http://www.chem.msu.su/rus/teaching/general.html> (on-line on 5.5.2015). (In Russian).
- [10] Starikovskaia S, Kukaev E, Kuksin A.Yu, Nudnova M N, Starikovskii A Yu, Combustion & Flame 139 (2004) 177.
- [11] Levko D, Shchedrin A, Chernyak V, Olaszewski S, Nedybaliuk O, J. Phys. D: Appl. Phys. 44 (2011) 145206.
- [12] Chernyak V, Iukhymenko V, Prysiazhnevych I, Martysh Eu, Problems of Atomic Science and Technology. Series: Plasma Electronics and New Methods of Acceleration 86 (2013) 200-203.
- [13] Chernyak V, Nedybaliuk O, Martysh E, Olaszewski S, Solomenko O, Shchedrin A, Levko D, Demchina V, Kudryavzev V, Nukleonika 57 (2012) 301-305.
- [14] Petitpas G, Rollier J-D, Darmon A, Gonzales-Aguilar J, Metkemeijer R, Fulcheri L, Int. J. Hydrogen Energy 32 (2007) 2848-2867.
- [15] Chernyak V, Nedybalyuk O, Yukhimenko V, Colgan V, Solomenko E, Martysh E, Solomenko O, Demchina V, et al., In: Contr. Physics of Low-temperature Plasma (PLTP 2014), May 20-23, 2014, Kazan, Russia. 2, 2014, 130-134. (In Russian).
- [16] Changming Du, Hongxia Li, et al., International Journal of Hydrogen Energy 37 (2012) 8318-8329.
- [17] Czernichowski A, In: 19th Int. Symp. on Plasma Chem. (ISPC-19), Bochum, Germany, 2009.
- [18] Nedybaliuk O, Solomenko OI, Martysh E, Fedirchuk I, Problems of Atomic Science and Technology. Series: Plasma Physics 94 (2014) 191-194.

# Why the Arc, and its Interactions with the Electrodes, Are Important in Predictive Modelling of Arc Welding

Murphy A. B.<sup>1</sup>

<sup>1</sup>CSIRO Manufacturing, PO Box 218, Lindfield NSW 2070, Australia, tony.murphy@csiro.au

The importance of two-way interactions between the arc and electrodes in welding is demonstrated by three examples: the influence of weld pool surface deformation on heat transfer, the momentum and energy transferred by droplets, and the effects of metal vapour on the arc and weld pool. It is concluded that a predictive model of arc welding requires the arc to be included in the computational domain. This will also facilitate calculation of properties such as microstructure and residual stress.

**Keywords:** arc welding, computational modelling, metal vapour, droplets, thermal plasma

## 1 INTRODUCTION

Arc welding is the most widely-used industrial thermal plasma process. An arc is struck in a shielding gas between two electrodes, one of which is the workpiece, i.e., the metal components that are joined by the welding process. The workpiece partially melts, forming a weld pool; when this solidifies, the components are bonded.

There are many types of arc welding. The most widely used in manufacturing is metal inert-gas (MIG) welding, in which the upper electrode is a metal wire, and the lower electrode is the workpiece. Usually the wire is the anode and the workpiece is the cathode. The tip of the wire melts to form droplets that pass through the arc into the weld pool.

Metal inert-gas welding is known as metal active-gas (MAG) welding when the shielding gas contains oxygen or carbon dioxide. Typical shielding gases are argon or helium in MIG welding, and argon-oxygen, argon-carbon dioxide or pure carbon dioxide in MAG welding. MIG/MAG welding is also known as gas metal arc welding (GMAW).

### 1.1 APPROACHES TO MODELLING OF ARC WELDING

The most important factor in arc welding is the properties of the welded joint. For this reason, the focus of arc welding models is the workpiece. Sophisticated models have been developed that predict properties including the weld depth and shape, the changes to microstructure resulting from the heating and cooling of the metal, and the residual stresses that develop in the workpiece.

Because of the focus on the workpiece proper-

ties, the great majority of computational models of arc welding do not include the arc or the wire electrode in the computational domain. The arc is taken into account only through boundary conditions at the surface of the workpiece and weld pool. This is a very significant simplification. However, determination of the boundary conditions representing the arc creates significant difficulties.

A typical example is provided by the approach of Zhang et al. [1], who assumed Gaussian distributions of the heat flux  $Q_a$ , electric current  $J_a$  and pressure  $P_a$  at the weld pool surface:

$$\begin{aligned} Q_a &= \frac{\alpha IV}{2\pi R_q^2} \exp\left(-\frac{r^2}{2R_q^2}\right) - h_c(T_w - T_a), \\ P_a &= \frac{F}{2\pi R_p^2} \exp\left(-\frac{r^2}{2R_p^2}\right), \\ J_a &= \frac{I}{2\pi R_q^2} \exp\left(-\frac{r^2}{2R_q^2}\right), \end{aligned} \quad (1)$$

where  $I$  is the arc current,  $V$  is the arc voltage,  $r$  is the radial coordinate and  $T_w$  is the temperature of the workpiece surface. Six parameters have to be determined empirically or otherwise estimated: the efficiency of energy transfer  $\alpha$ , a convective heat transfer coefficient  $h_c$ , the arc force  $F$ , the arc temperature adjacent to the workpiece  $T_a$ , and effective radii for heat transfer and pressure,  $R_q$  and  $R_p$  respectively. These parameters are typically estimated by comparing predictions of

the model against measurements, for example of weld depth and shape.

A less common approach to modelling of arc welding is to include the arc in the computational domain. This has the disadvantage that the model becomes much more complex, since the properties of the arc, and its interactions with the wire and workpiece, have to be calculated. However, if the arc is included self-consistently, then the boundary conditions between the arc and weld pool are determined by the model, and so do not have to be estimated.

## 1.2 OUTLINE OF PAPER

In this paper, I first describe the methods used in developing a computational model of MIG welding that includes the wire electrode and arc in the computational domain. I then present results that demonstrate the value of this approach. In particular, I show that the deformation of the weld pool surface, the transfer of energy and momentum by the droplets, and the production of metal vapour (a) are of great importance in determining the properties of the weld, and (b) can only be predicted accurately by including the arc and the wire electrode in the computational domain.

Finally, I consider the value of the second approach in predicting the microstructure of the heat-affected zone, and the residual stress in the workpiece, which are critical factors in determining the reliability of the weld.

## 2 THE COMPUTATIONAL MODEL

The computational model solves the equations of incompressible viscous flow, modified to include plasma effects and the conduction of electric current, in a computational domain that includes the wire electrode, the arc plasma, and the workpiece. The equations have been presented previously [1,2]; here a brief summary is provided.

The equations describe conservation of mass, momentum, energy and electric charge, with an additional equation to allow the magnetic potential to be determined from the current density. While the model can operate in either time-dependent or steady-state mode, only steady-state calculations are considered here.

The momentum and energy equations are transformed into the frame of reference of the

wire electrode, which moves with respect to the fixed workpiece, using the approach of Mundra et al. [3].

The rate of vaporization of the electrode and weld pool is calculated self-consistently using the Hertz–Langmuir equation and depends on the local temperature of the wire electrode or weld pool surface and the mass fraction of the vapour in the adjacent plasma [2]. Modelling of the diffusion of the metal vapour required an additional conservation equation, for the mass fraction  $Y_M$  of metal species (atoms, ions and the electrons derived from metal atoms):

$$\nabla \cdot (\rho \mathbf{v} Y_M) = -\nabla \cdot \mathbf{J}_M = S_M, \quad (2)$$

where  $\rho$  is the mass density,  $\mathbf{v}$  is the flow velocity,  $S_M$  is the metal vapour source term (proportional to the rate of vaporization), and  $\mathbf{J}_M$  is the diffusion mass flux, calculated using the combined diffusion coefficient approach, which is equivalent to the full multi-component approach [4].

The equations are solved in three-dimensional Cartesian geometry, using the finite volume method of Patankar [5], incorporating the SIMPLEC algorithm of van Doormaal and Raithby [6].

### 2.1 TREATMENT OF DROPLETS

Droplets are formed at the molten tip of the wire electrode. They detach and pass through the arc, transferring mass, momentum and energy to the weld pool. A full treatment of the droplet formation and transport requires a surface-tracking approach such as the volume-of-fluids method [7]; this is, however, highly computationally-intensive and is only applicable to time-dependent calculations.

An alternative time-averaged treatment of the influence of the droplets was developed [8]; this treatment is computationally much faster than the volume-of-fluids method, but still allows the influence of the droplets on the arc plasma and the weld pool to be determined. The temperature, velocity and diameter of the droplets are tracked from their detachment from the wire to their impact with the weld pool, with the heat, momentum and mass transfer determined using the PSI-CELL ap-

proach of Crowe et al. [9]. The effects of the droplets on the plasma and weld pool are taken into account using source terms averaged over the spatial extent of the droplets' path and over time. The main drawback of the approach is that changes in the shape of the tip of the wire as droplets form and detach are not considered.

## 2.2 INTERNAL BOUNDARIES

The internal boundaries between the electrodes and plasma, and between molten and solid metal, have to be treated carefully.

The latent heat of melting is taken into account at the liquid–solid interfaces using the method of Voller et al. [10]; this approach ensures numerical stability.

The shape of the free surface between the weld pool and the arc plasma is calculated by minimizing the total surface energy of the liquid metal, using the approach presented by Kim and Na [11]. This method takes into account the surface tension and surface curvature, the arc and droplet pressure, buoyancy in the weld pool, and the volume of metal transferred to the weld pool by droplets.

Four physical factors are important in determining the influence of the arc plasma on the weld pool: the heat flux, the current density, the arc pressure, and the shear stress applied by the plasma flow, all at the weld pool surface. Note that the first three of these parameters are typically defined as boundary conditions in models that do not include the arc in the computational domain, as per the example given in Eq. (1). In the model presented here, however, the parameters are determined self-consistently.

The workpiece is a non-thermionic cathode, for which the electron emission mechanism is not well understood. A simple expression is used for the heat flux [12] :

$$S = j(V_i - \varphi_w) - k \partial T / \partial x_{\perp}. \quad (3)$$

The first term describes heating due to electron flux, and is the difference between sheath heating and the energy required to remove electrons from the metal;  $j$  is the current density,  $V_i$  is the sheath voltage, and  $\varphi_w$  is the work function of the metal. The second term is thermal conduction;  $k$  is the thermal conduc-

tivity,  $T$  is the temperature, and  $x_{\perp}$  is position perpendicular to the workpiece surface.

The boundary conditions for momentum transfer across the arc–weld-pool interface parallel and perpendicular to the weld pool surface are respectively

$$\begin{aligned} \tau_a - \tau_w + (d\gamma/dT)(dT/dx_{\parallel}) &= 0, \\ P_a - P_w + \gamma\kappa &= 0. \end{aligned} \quad (4)$$

The parallel boundary condition states that the difference between the shear stresses in the arc  $\tau_a$  and in the weld pool  $\tau_w$  is determined by the Marangoni term  $d\gamma/dx_{\parallel}$ , which describes the variation of the surface tension  $\gamma$  due to the gradients of temperature parallel to the weld pool surface. The perpendicular boundary condition states that the difference between the arc pressure  $P_a$  and weld pool pressure  $P_w$  is determined by the product of the surface tension and the surface curvature  $\kappa$ .

The heat flux to the wire anode is given by

$$S = j\varphi_w - k \partial T / \partial x_{\perp}, \quad (5)$$

where the first term again describes heating due to electron flux (in this case electron condensation), and the second due to thermal conduction from the arc plasma.

## 2.3 THERMOPHYSICAL PROPERTIES

The thermophysical properties of the shielding gases, such as thermal conductivity and electrical conductivity, were taken from Murphy and Arundell [13] for argon, with properties for mixtures of argon and aluminium vapour calculated as described by Murphy [14].

Net radiative emission coefficients for argon were taken from Cram [15] and for aluminium from Essoltani et al. [16], with data for mixtures calculated based on mole fractions as recommended by Gleizes et al. [17].

## 3 RESULTS AND DISCUSSION

The computational model was run for bead-on-plate weld geometry, in which the workpiece is a flat plate, and the wire electrode is oriented vertically. Results obtained neglecting and including the influence of metal vapour are presented. The parameters used for the calculations are given in Table 1.

Table 1: Parameters used for calculations

Parameter	Value
Average arc current	95 A
Welding speed	15 mm s <sup>-1</sup> (in -y direction)
Wire diameter	1.2 mm
Wire feed rate	72 mm s <sup>-1</sup>
Droplet frequency	93 s <sup>-1</sup> (one-drop per pulse)
Arc length	5 mm (for flat workpiece)
Workpiece thickness	3 mm
Wire and workpiece alloy	AA5754 (Al + 3.1wt% Mg)
Shielding gas	Argon

### 3.1 DEFORMATION OF THE WELD POOL SURFACE

Droplets transfer molten metal from the wire to the weld pool, leading to an increase in the weld pool surface height. The arc tends to attach to the highest region of the weld pool, since this is typically the configuration that minimizes the arc voltage.

Fig.1 shows a comparison of the current density distributions predicted under the assumption that the weld pool surface remains flat, and by a calculation that includes the deformation of the surface due to the transfer of metal by droplets. In the former case, the current density distribution is approximately Gaussian, as per Eq. (1). In the latter case, the current density distribution is strongly asymmetric.

The current density distribution is critical in determining the heat flux to the weld pool, since the most important contribution to the heat transfer is the electron flux, which is proportional to the current density (see Eq. (3)).

This is an example of the importance of two-way interactions between the arc and the electrodes. The arc melts the wire and the workpiece, leading to droplet formation and a deformed weld pool. This in turn affects the location of the arc attachment, and thereby the transfer of energy from the arc to the weld pool.

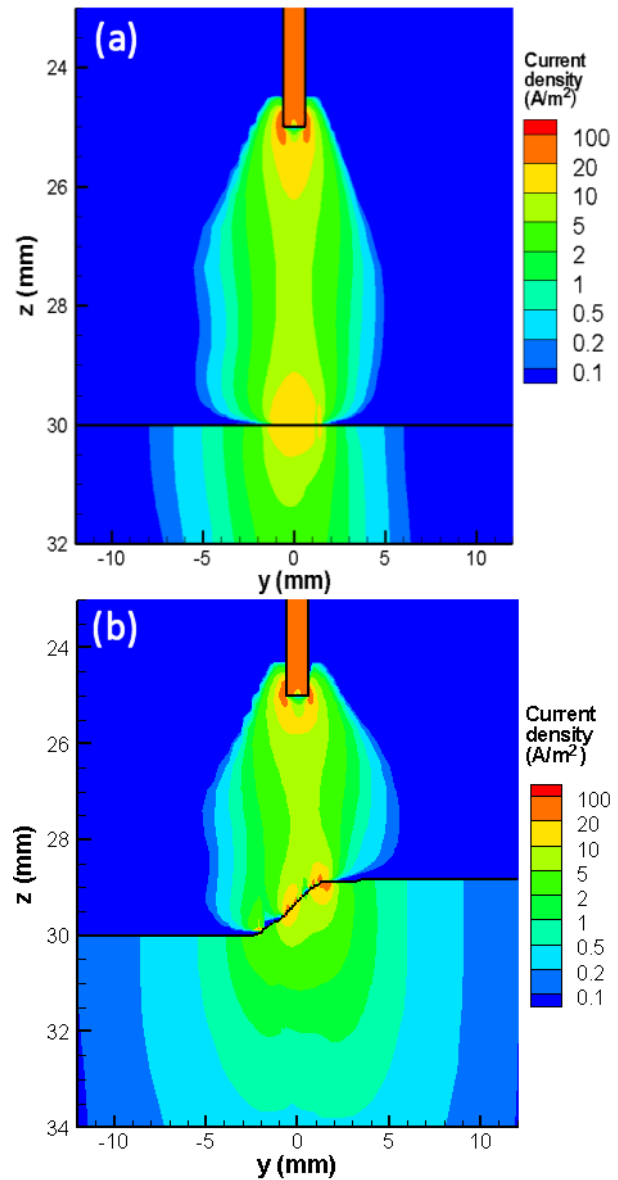


Fig.1: Current density distribution in a vertical cross-section through the wire, arc and workpiece: (a) assuming a flat weld pool surface, (b) including the deformation of the weld pool surface due to the transfer of metal by droplets; in both cases, metal vapour is neglected and the welding direction is to the left; from [1], © IOP Publishing; reproduced with permission; all rights reserved

### 3.2 DROPLETS

The momentum and heat energy transferred to the weld pool by the droplets have a large influence on the weld pool properties.

The initial temperature of the droplet is determined by the temperature of the tip of the wire when the droplet detaches. The initial velocity of the droplet is largely determined by the current density at the tip. Subsequently, heat and momentum are transferred to the droplet from the arc, since the temperature of the arc is

much higher than that of the droplet, and the plasma velocity is much higher than the droplet velocity [8].

Fig.2 shows the calculated radius, temperature and velocity of a droplet as it moves through the arc.

The influence of the droplet on the weld pool can be assessed by calculating the weld pool properties including and neglecting the transfer of momentum and energy by the droplet. The results are shown in Fig.3.

When all effects are taken into account, there is a strong downwards flow in the weld pool, starting at the position of droplet impact. However, when the droplet momentum is neglected, the flow is much weaker. When the droplet energy is neglected, the weld pool is significantly shallower.

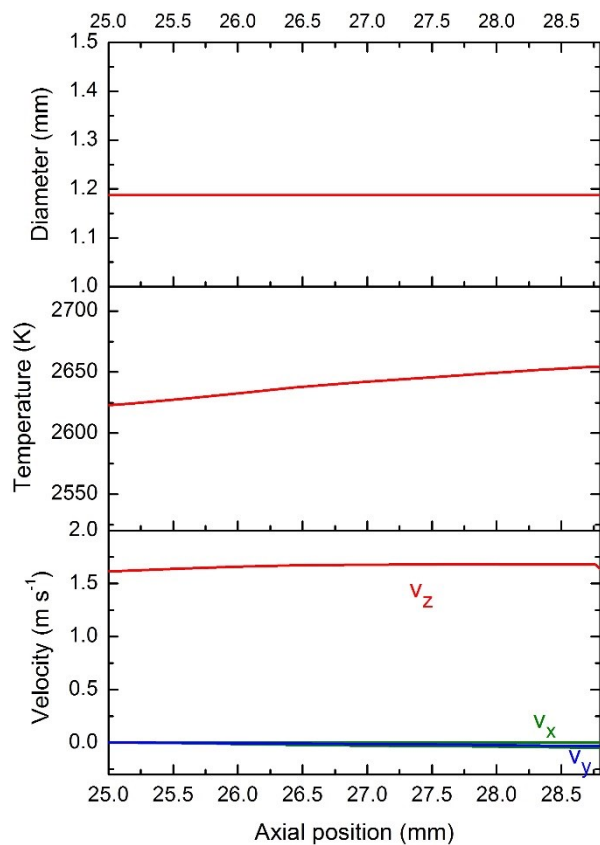


Fig.2: Diameter, temperature and components of the velocity of droplets as they pass through the arc from wire tip (at 25.0 mm) to the weld pool (at 28.75 mm); republished with permission of Maney Publishing from [8]; permission conveyed through Copyright Clearance Center, Inc.

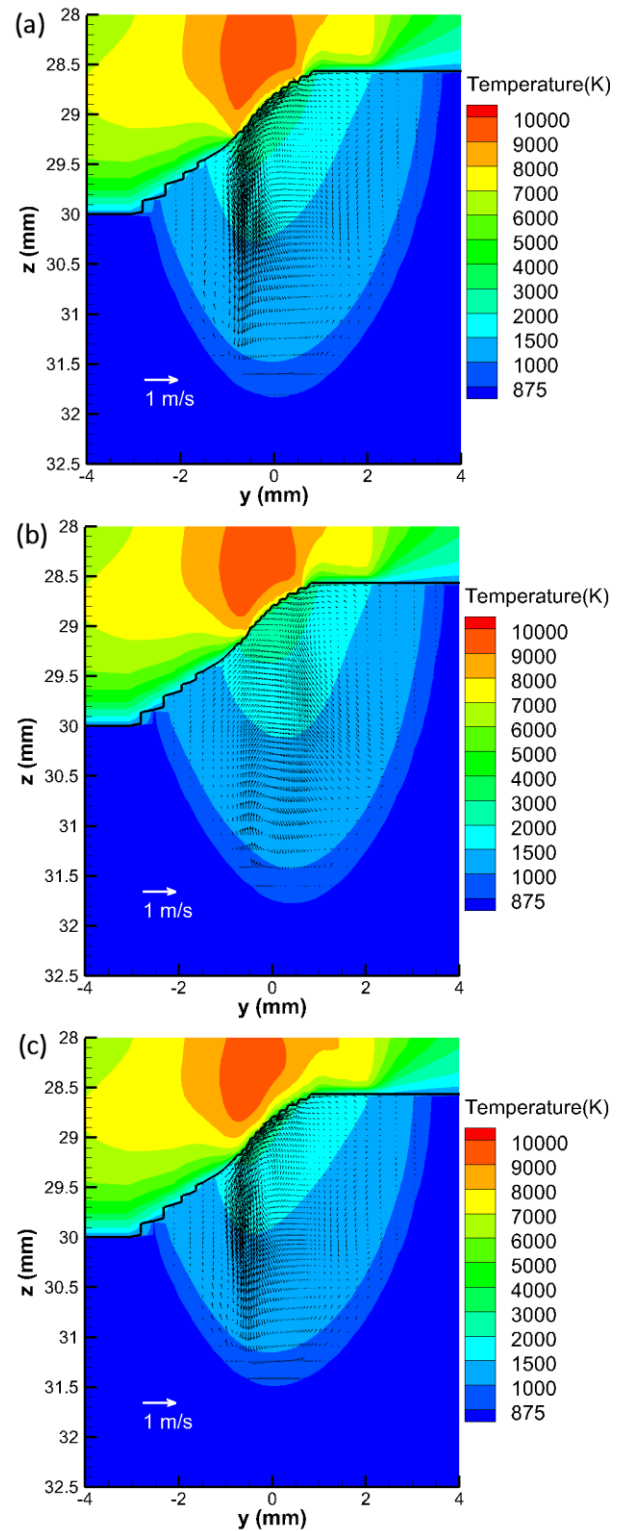


Fig.3: Vertical cross-section of weld pool, showing temperature distribution and velocity vectors, for (a) standard case, and cases in which (b) momentum, and (c) enthalpy, transferred by droplets is neglected; the welding direction is to the left; republished with permission of Maney Publishing from [8]; permission conveyed through Copyright Clearance Center, Inc.

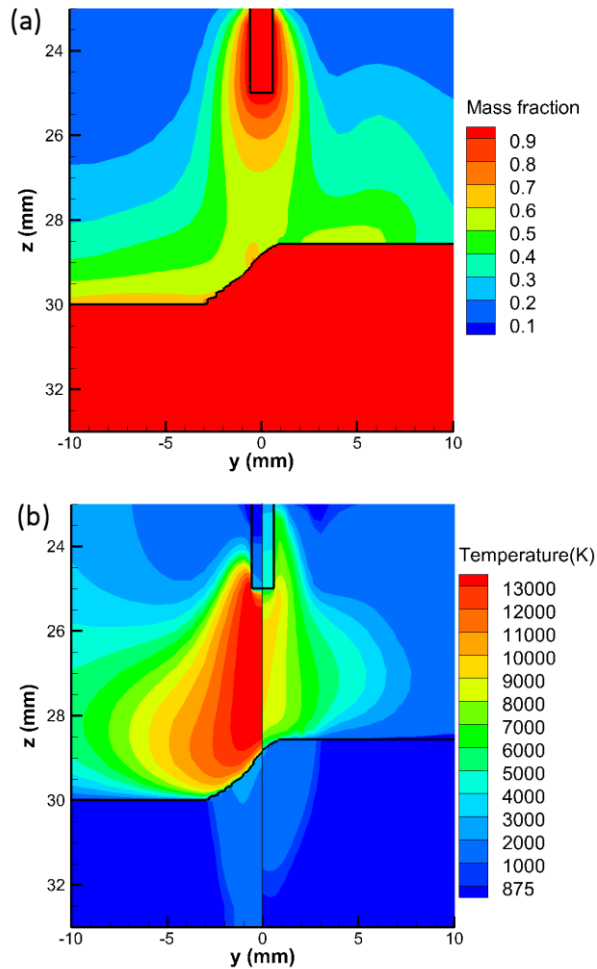


Fig.4: Distributions of (a) mass fraction of aluminium vapour, (b) temperature, in a vertical cross-section through the wire, arc and workpiece; in (b), the left-hand side shows temperature neglecting the influence of metal vapour, and the right-hand side shows temperature including the effects of metal vapour; the welding direction is to the left; from [2]; © IOP Publishing; reproduced with permission; all rights reserved

It is thus apparent that both the momentum and the energy transferred by the droplets make a significant contribution to the weld pool properties.

Droplets therefore provide a second example of the importance of two-way interactions between the arc and electrodes. The droplet momentum and energy are largely determined by the arc parameters, through the interaction of the arc with both the wire electrode and the droplets, and in turn the droplet momentum and energy influence the properties of the weld pool and therefore the weld.

### 3.3 METAL VAPOUR

Metal vapour, produced from the tip of the wire, the droplet and the weld pool, has a very significant influence on the arc temperature. Emission spectroscopy measurements performed in MIG welding arcs with steel electrodes have shown the existence of a local temperature minimum in the centre of the arc [18]. Modelling has demonstrated that this is mainly due to the strong radiative emission from iron vapour, which is concentrated around the arc axis [19].

In Fig.4, the predicted distribution of metal vapour in the arc, and the influence of the metal vapour on arc and weld pool temperature, are shown. The aluminium vapour is produced mainly from the wire tip, and is convected downwards by the strong flow in the arc; the flow velocity is over  $100 \text{ m s}^{-1}$  near the wire tip. The mass fraction of aluminium vapour is over 50% near the arc axis. The arc temperature is reduced due to the strong radiation from the aluminium vapour, and also because the temperature of the inflowing vapour is lower than that of the argon arc [2]. There is, however, no local temperature minimum, since aluminium vapour does not radiate as strongly as iron vapour, so the cooling is not as strong [2]. Recent laser-scattering measurements have confirmed the absence of a local temperature minimum in a MIG welding arc with aluminium electrodes [20].

Fig.5 shows a comparison of a measured weld cross-section with cross-sections predicted by the model both including and neglecting the influence of metal vapour. The presence of metal vapour significantly decreases the depth of the weld. This is partly due to the reduction in thermal conduction to the workpiece associated with the lower arc temperature, and partly to the decreased current density at the workpiece. The latter effect a consequence of the increased electrical conductivity of the plasma at low temperatures, which spreads out the arc attachment region. The increased conductivity at low temperatures is a consequence of the lower ionization enthalpy of aluminum atoms [14]. Eq. (3) shows both that both effects decrease the heat flux to the workpiece.

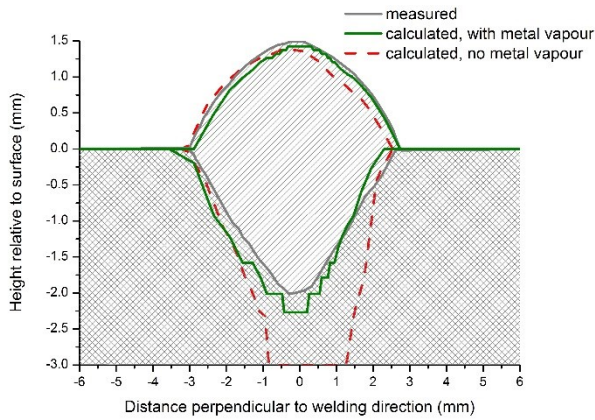


Fig.5: Comparison of measured weld cross-section (light-grey shaded region) with weld cross-sections calculated including (green solid line) and neglecting (red broken line) the effects of metal vapour; from [2]; © IOP Publishing; reproduced with permission; all rights reserved

Metal vapour provides a third example of the importance of two-way interactions between the arc and electrodes. The arc heats the wire and weld pool, leading to melting and vaporization of the metal; the metal vapour in turn affects the arc and the weld pool properties.

### 3.4 MICROSTRUCTURE AND RESIDUAL STRESS

While the weld depth and shape are of fundamental importance in welding, there are several other important factors, such as the residual stress in, and consequent deformation of, the welded metal, and the microstructure of the metal in the heat-affected zone. These factors are critical in determining the in-service reliability of the weld.

Modelling of residual stress and microstructure require thermal histories (the dependence of temperature on time) at every point in the workpiece. In standard approaches, which generally use finite-element models, the thermal history is calculated using a two-dimensional or three-dimensional heat source. An example of a two-dimensional heat source is given by the heat flux equation in Eq. (1). Three-dimensional heat sources are typically expressed as an ellipsoid, such as:

$$Q = \alpha VI \exp \left\{ - \left[ \left( \frac{x}{r_1} \right)^2 + \left( \frac{y}{r_2} \right)^2 + \left( \frac{z}{r_3} \right)^2 \right] \right\} \quad (6)$$

where the  $r_i$  are the radii of the ellipsoid in the

$x$ ,  $y$  and  $z$  directions. The free parameters  $\alpha$  and  $r_i$  are usually determined by measuring thermal histories at several position in the workpiece with thermocouples, and fitting the measured values to those predicted by the model [21].

The MIG welding model presented in this paper allows accurate prediction of the thermal history at every point in the workpiece. An example is shown in Fig.6. Coupling the MIG welding model with residual stress and microstructure models would therefore allow prediction of these properties over a wide range of welding parameters, without the need for measurements of the thermal history in each case.

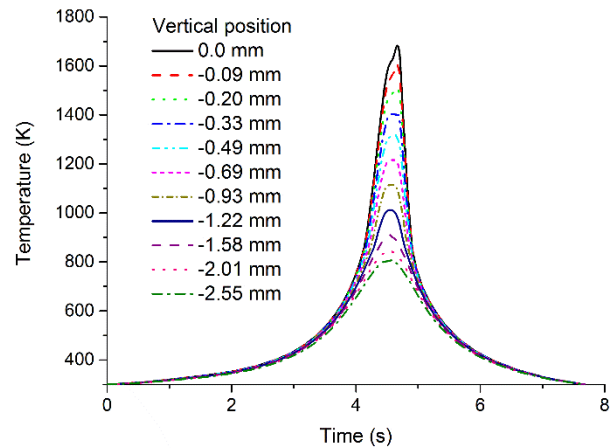


Fig.6 Thermal histories at different vertical positions in the workpiece on the arc axis; the vertical positions are measured from the top of the original workpiece surface, and correspond to those in Fig.5

## 4 CONCLUSIONS

I have presented three examples of two-way interactions between the arc and the electrodes in MIG welding: (1) the influence of deformation of the weld pool surface on transfer of energy from the arc to the weld pool; (2) the influence of the arc on droplet properties, which in turn affect the weld pool; and (3) the vaporization of the electrodes by the arc, and the consequent decrease in weld pool depth. In all three cases, it is only possible to predict the effects on the weld pool by including the arc in the computational domain. If the arc is instead represented by boundary conditions on the weld pool surface, the free parameters inherent in representation have to be re-

determined for every significant change in welding parameters.

A further advantage of including the arc in the computational domain is that reliable calculations of the thermal history of the workpiece can be performed. This data could be coupled to models that predict microstructure and residual stress in the workpiece, dispensing with the need for the use of heat sources that require calibration against measurements of temperature in the workpiece.

By including the arc and the wire electrode self-consistently within the computational domain, it should therefore be possible to develop a truly predictive model of arc welding, i.e., one in which repeated calibration against measurements is not required.

#### Acknowledgements

The support provided for the work reported here by General Motors, General Motors Holden, and the Commonwealth of Australia, through the AutoCRC, is gratefully acknowledged, as are useful discussions with Drs John Lowke, Eugene Tam, Vu Nguyen, Yuqing Feng and Dayalan Gunasegaram of CSIRO, and Dr Hui-Ping Wang of General Motors.

#### REFERENCES

- [1] Murphy A B, J Phys D: Appl Phys 44 (2011) 194009.
- [2] Murphy A B, J Phys D: Appl Phys 46 (2013) 224004.
- [3] Mundra K, DebRoy T, Kelkar K M, Numer Heat Transfer A 29 (1996) 115-129.
- [4] Murphy A B, Phys Rev E 48 (1993) 3594-3603.
- [5] Patankar S V, Numerical Heat Transfer and Fluid Flow, Hemisphere, Washington DC 1980.
- [6] van Doormaal J P, Raithby G D, Numer Heat Transfer 7 (1984) 147-163.
- [7] Hirt C W, Nichols B D, J Comput Phys 39 (1981) 201-225.
- [8] Murphy A B, Sci Technol Weld Join 18 (2013) 32-37.
- [9] Crowe C T, Sharma M P, Stock D E, J Fluid Eng 99 (1977) 325-332.
- [10] Voller V R, Prakash C, Int J Heat Mass Transfer 30 (1987) 1709-1719.
- [11] Kim J-W, Na S-J, Weld J 74 (1995) 141s-152s.
- [12] Lowke J J, Tanaka M, In: Proc. 17th International Conference on Gas Discharges and their Applications, Cardiff, UK, 7-12 September 2008. (Ed. Jones JE). 2008, 137-140.
- [13] Murphy A B, Arundell C J, Plasma Chem Plasma Process 14 (1994) 451-490.
- [14] Murphy A B, J Phys D: Appl Phys 43 (2010) 434001.
- [15] Cram L E, J Phys D: Appl Phys 18 (1985) 401-411.
- [16] Essoltani A, Proulx P, Boulos M I, Gleizes A, Plasma Chem Plasma Process 14 (1994) 437-450.
- [17] Gleizes A, Cressault Y, Teulet P, Plasma Sources Sci Technol 19 (2010) 055013.
- [18] Zielinska S, Musiol K, Dzierzega K, Pellerin S, Valensi F, de Izarra C, Briand F, Plasma Sources Sci Technol 16 (2007) 832-838.
- [19] Schnick M, Fuessel U, Hertel M, Haessler M, Spille-Kohoff A, Murphy A B, J Phys D: Appl Phys 43 (2010) 434008.
- [20] Kühn-Kauffeldt M, Marqués J-L, Schein J, J Phys D: Appl Phys 48 (2015) 012001.
- [21] Muránsky O, Smith M C, Bendeich P J, Holden T M, Luzin V, Martins R V, Edwards L, Int J Sol Struct 49 (2012) 1045-1062.

# Development of Long Flashover and Multi-Chamber Arresters and Insulator-Arresters for Lightning Protection of Overhead Distribution and Transmission Lines

Podporkin G. V.

*Streamer Electric Company, 195220 Saint-Petersburg, Russia, [georgij.podporkin@streamer.ru](mailto:georgij.podporkin@streamer.ru)*

Long Flashover Arresters (LFAs) were suggested and developed for lightning protection of Medium voltage lines 3-35 kV against induced overvoltages and direct lightning strokes. Main feature of LFAs is increased length of lightning flashover path. The LFA's length may be several times greater than that of an insulator (string, etc.). Due to a special inner structure the LFA impulse flashover voltage is lower than that of the insulator and when subjected to lightning overvoltage the LFA flashovers before the insulator. Increased length of flashover insures quenching of power arc follow when current crosses zero. This phenomena can be called "zero quenching". Main advantage of LFAs is that current and energy pass outside the arresters. Reported also are results of research and development of multi-chamber arresters (MCA) and insulators (MCIA) that combine characteristics of insulators and arresters. The base of multi-chamber arresters (MCA), including MCIA, is the multi – chamber system MCS. MCS of first generation comprises a large number of electrodes mounted in a silicon rubber length. Holes drilled between the electrodes and going through the length act as miniature gas discharge chambers. MCS of this type insures power arc quenching when follow current crosses zero ("zero quenching"). MCS of second generation has more complicated chamber design but it quenches impulse arcs without a follow power arc ("impulse quenching"). The devices permit protection of overhead power lines rated at 10 to 220 kV and above against induced overvoltages and direct lightning strokes without using a shield wire.

**Keywords:** lightning protection, overhead lines, flashover, arc, quenching, multi chamber arresters

## 1 INTRODUCTION

Overhead power transmission lines (OHL) are tall and rather extended objects. For instance, total length of 6-10kV OHLs in Russia is approximately 2 million km and in China – 10 mln. km. That is why overhead lines are exposed to frequent lightning strikes that are able to cause the line short circuits, cut-offs and, in some cases, insulators breakdown, cable burnouts, wood poles splitting and similar faults. So, OHLs should be protected from lightning surges.

OHLs of 110kV and higher are traditionally protected by means of a shielding wire. However, in case of high soil resistivity (rocks, sand, permafrost), the required low tower footing resistance is failed to be ensured. At high values of tower footing resistance the shielding wire will not protect OHL from direct lightning strike (DLS) to the line, since so called back flashover occurs.

In regions with strong ice-forming the use of a shielding wire is very inconvenient either, since the ice formed on the wire will cause a large slack of the wire and frequently – its breakage and fall down the OHL cables, i.e. a

serious accident. Melting of ice is an expensive and labor-consuming procedure. Attempts to discard the use of shielding wire have led to very frequent lightning outages.

In principle, in order to ensure the required lightning-surge proofness, the use of metal – oxide surge arresters (MOA) is possible, but the cost of such technical solution is rather high.

For 6-35kV OHLs shielding wires are not used, as a rule, since there occurs a back flashover upon lightning strike to the wire. In fact, up to the late 1990-s OHLs of 6-35kV in Russia were constructed with no lightning protection at all.

During 1995-2003, 'Streamer Electric Company' developed a lightning protection system for 10kV OHLs by means of long flashover arresters (LFA) [1,2]. The LFA operating principle is that a rather long flashover path on the LFA surface is ensured with the use of creeping discharge effect. Due to this long flashover path, a transfer of surge discharge to power arc follow (PAF) of commercial frequency is ruled out. A distinctive feature of LFAs is that the discharge occurs outside the

device and is not of serious hazard thereto. Since 1999, LFAs have been applied at a series of 12 kV OHLs. As of 2015, there is over a million LFAs successfully operating in various utilities.

Since 2004 and up to present time, 'Streamer', has carried out intensive research work on arresters with multi-chamber system (MCS), as a result of which arresters for voltage classes 6 to 35kV have been successfully developed [3]. Then a new type MCS ensuring lightning overvoltage arc blowout with no PAF has been created [4,5]. Arresters on the base of such MCS may be used in networks with high short-circuit currents (around 30kA and higher). Also, offered was a principally new device: multi-chamber insulator arrester (MCIA) combining properties of insulator and arrester at the same time. When using MCIA, it is possible to provide protection for OHLs of any voltage class, i.e. the higher the voltage class, the higher the number of insulators in the string and, accordingly, the higher the rated voltage and the arc blowout capacity of the MCIA string.

There are different designs of insulators with arrester characteristics possible. MCIA's are based on standard commercially manufactured insulators (glass, porcelain or polymer ones) with MCS installed in a special way. At that, installation of MCS will not cause deterioration of insulating properties of the insulator, but will add properties of arrester thereto. That is why, in case of MCIA use on the OHL, it is possible to discontinue applying a shielding wire. This will help to lower the height, weight and cost of towers, as well as cost of the whole OHL system, and ensure a reliable lightning protection of the lines, i.e. curtail drastically a number of the line cut-offs and decrease losses from undersupply of energy and operating expenses.

LFA and MCA are Russian products and according to their design parameters, technical specifications and functional capabilities represent a special class of lightning protection devices that have no world analogues. LFA and MCA are patented, apart from Russia, in USA, EC and other countries.

## 2 LONG FLASHOVER ARRESTERS

### 2.1 LFA OF LOOP TYPE

Fig. 1 presents an LFA of Loop type (LFA-L) installed on a metal structure which models distribution line pole [1]. A piece of cable with steel cord is bent in a loop and connected to the pole with a clamp. A metal tube is placed over the insulated loop in its middle part forming, together with the line conductor, a sparkover air gap  $S$ . At one arm of the loop, intermediate ring electrodes are installed. The loop is at the same potential as the structure.

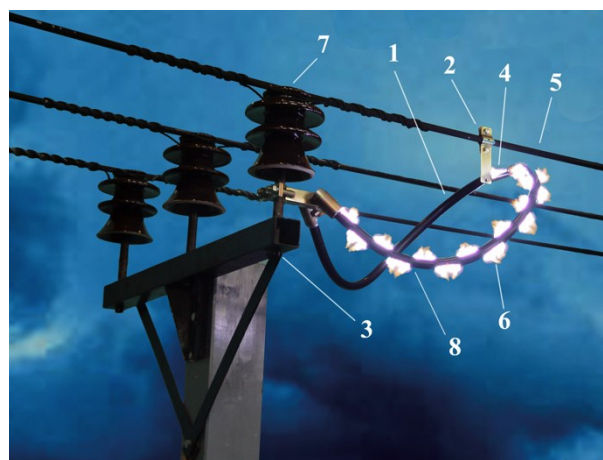


Fig.1: Loop-shaped LFA

1 – cable loop; 2 – clamp; 3- steel structure; 4 – metal tube; 5 – power line conductor; 6 – flashover channel; 7 – insulator; 8 - intermediate ring electrodes

Due to a relatively big capacitance between the metal tube and the steel cord inside the cable, the tube is practically at the same potential as the pole. Therefore an overvoltage taking rise between the line conductor and the pole will be also applied between the metal tube and the line conductor. If the overvoltage is large enough, the sparkover gap  $S$  will break down and the overvoltage will be applied between the metal tube and the steel cord inside the cable to its insulation. Due to the overvoltage, a creeping flashover develops from the metal tube to a clamp of the insulated loop passing intermediate ring electrodes and next to the structure, thus completing the discharge circuit. The intermediate electrodes have protrusions at opposite sides.



### 3 MULTI-CHAMBER SYSTEMS, MCS, “ZERO QUENCHING”

The base of multi-chamber arresters (MCA), including MCIA, is the MCS shown in Fig. 5. It comprises a large number of electrodes mounted in a length of silicon rubber. Holes drilled between the electrodes and going through the length act as miniature gas discharge chambers. When a lightning overvoltage impulse is applied to the arrester, it breaks down gaps between electrodes. Discharges between electrodes take place inside chambers of a very small volume; the resulting high pressure drives spark discharge channels between electrodes to the surface of the insulating body and hence outside, into the air around the arrester. A blow-out action and an elongation of inter-electrode channels lead to an increase of total resistance of all channels, i. e. that of the arrester, which limits the current.

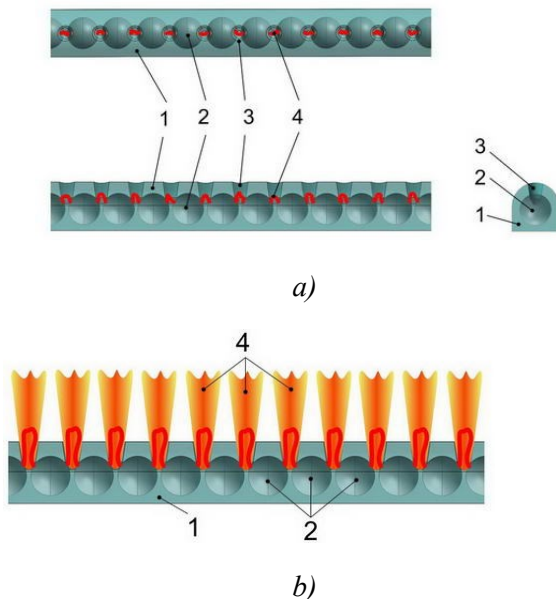


Fig. 5: Multi-chamber system (MCS)  
 a) diagram showing the discharge onset instant;  
 b) diagram showing the discharge end instant;  
 1 – silicon rubber length; 2 – electrodes; 3 – arc quenching chamber; 4 – discharge channel

#### Multi-Chamber Arresters 24 kV

The principal components of a 24 kV MCA (see Fig. 6) are an MCS, a fiberglass bearing rod and an assembly for securing arresters to insulator pins. Arresters are mounted on insulator pins with air gaps of 3 to 6 cm between top ends of arresters and the

conductor. A lightning overvoltage first breaks down the air spark gap and next the arrester’s MCS, which assures extinction of follow current.

Shown in Fig. 6 is an arrester with 40 gas discharge chambers intended for protection of 24 kV overhead lines against induced overvoltages. One piece of this model is installed on each phase-interlacing pole as for LFA (see Fig. 3). In this case, the path of AC follow currents that are associated with lightning overvoltage-induced multi-phase includes the tower-grounding resistance circuits. Thanks to an extra resistance of the pole grounding circuit, follow currents are made lower, which raises the quenching efficiency of the arrester.



Fig. 6: 24 kV multi-chamber arrester MCA-24 for protection against induced overvoltages

### 4 MULTI-CHAMBER SYSTEMS, MCS, “IMPULSE QUENCHING”

To increase the follow current quenching efficiency of an MCS, it is offered to have a four- to twenty-fold longer elementary gap of a discharge chamber, compared to the MCS described in section 3 [4,5]. A low discharge voltage of such an advanced MCS can be attained through use of creeping discharge and cascading operation of MCS circuit chambers (see Fig. 7).

Creeping discharge flashover voltage is known to depend little on the electrode spacing, i. e. a fairly large gap can be flashed over even at a relatively low voltage (see, for

instance, [1]).

Cascading is caused by effect of an additional electrode set up along the entire MCS (Fig. 7). It is connected to the last electrode of the last chamber and isolated from all the other electrodes.

The additional electrode is connected to the ground and thus has a zero potential. As the MCS gets actuated the high potential  $U$  is applied to the first electrode. The voltage gets distributed among chambers' spark gaps most unevenly. The cascade operation of discharge gaps assures needed low flashover voltages for actuation of an MCS as a whole.

Shown in Fig. 7 is an MCS design with electrodes as pieces of stainless steel tube and additional electrode passing through these electrodes. Length of breakdown gaps is additionally increased by using diagonal discharge slots. Due to such design MCS becomes more compact. Besides capacitance between tube electrodes and additional electrode of a discharge chamber  $C_0$  is much higher than between adjacent electrodes of the chamber  $C_1$ . This insures very non uniform distribution of voltage among discharge chambers and consequently decreases discharge voltage.

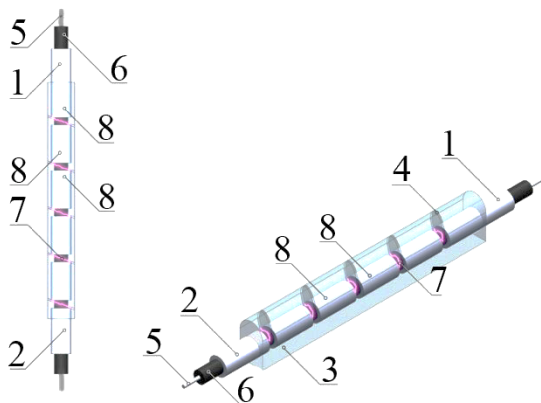


Fig. 7: MCS with additional electrode passing via metallic tube electrodes

1 - main high potential electrode; 2- main low potential electrode; 3- silicone rubber; 4 - discharge slot; 5- additional electrode (cable conductor); 6 - cable insulation; 7 - discharge channel; 8 - intermediate electrodes

Shown in Fig. 8 is a sketch of a gas discharge chamber intended for use in arresters protecting overhead lines against direct

lightning strokes. The discharge chamber is strengthened mechanically by a glass- fiber plastic sleeve.

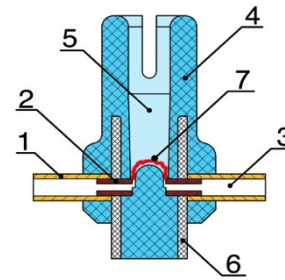


Fig.8: Cross-section of discharge chamber of multi-chamber arrester

1- outer tube; 2 - inner tube; 3 - cavity; 4 - silicone rubber; 5 - discharge slot; 6- fiber-glass plastic sleeve; 7 - discharge channel

### Multi-Chamber Arresters and Insulator-Arresters

Fig. 9 presents MCA for protection 12 kV line against induced overvoltages (MCA12-I). MCS of the arrester consists of 10 chambers made in accordance with Fig. 7. For avoiding of connection between plasma clouds outgoing from discharge chambers at their operation the chambers alternately directed in opposite sides: five odd chambers directed in one side and 5 even - in opposite side.

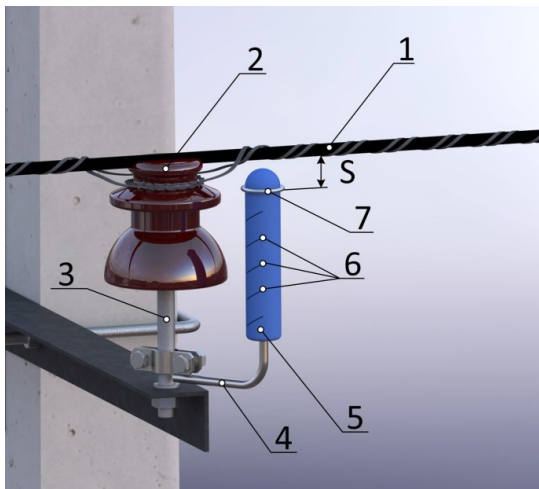
MCA12-I should be installed at overhead lines in the same manner as Long Flashover Arresters of Loop type (LFA-L), i. e. one arrester per pole with phase interlacing (see Fig. 3).

MCA12-I quenches discharge impulse arc of induced overvoltages without power follow current. Conductor erosion caused by impulse current with amplitude of about 1 kA and duration 5 mcs is insignificant. This enables to use the arrester without additional clamps on conductors (bared and covered as well).

At Fig. 10 a prototype of MCA for protection 12 kV lines against direct lightning strikes (MCA12-D) is presented. MCS of the arrester consists of 10 chambers made in accordance with Fig. 8. Due to lightning overvoltage at the line conductor sparkover gap  $S$  between the conductor and arrester electrode breaks down and the MCS operates.

For protection against direct lightning strikes

the arresters should be installed at all three phases at a pole (as at Fig. 4).



a)



b)

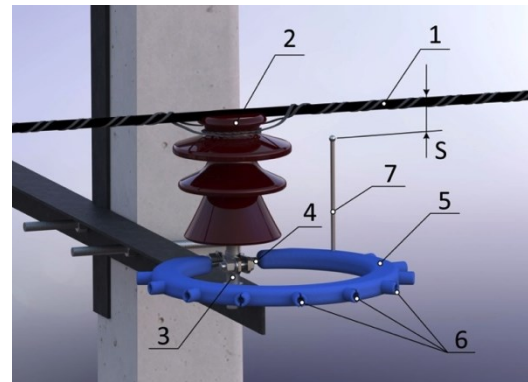
Fig. 9: MCA for protection 10 kV line against induced overvoltages (MCA10-I)

a) general view; b) test photo

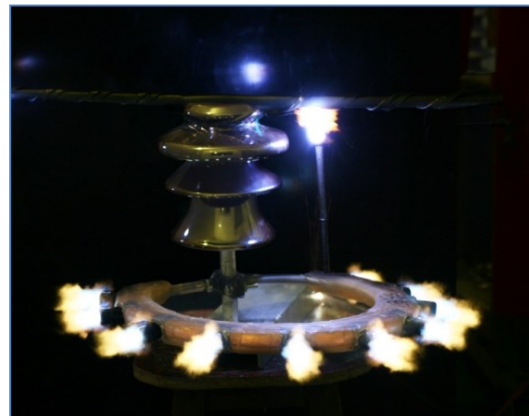
1 – conductor; 2 – insulator; 3 – rod; 4 – clamp;  
5 – silicon rubber body; 6 – discharge splits;  
7 – electrode; S – sparkover gap

Fig. 11 shows a string of two MCIAs based on a U120AD insulator. Strings of multi-chamber insulators-arresters (MCIAS) are intended for protecting 35 to 220 kV and above overhead lines against direct lightning strokes.

The MCS of an insulator-arrester comprises 14 chambers made in accordance with Fig. 8.



a)



b)

Fig. 10: MCA for protection 10 kV line against direct lightning strikes (MCA10-D)

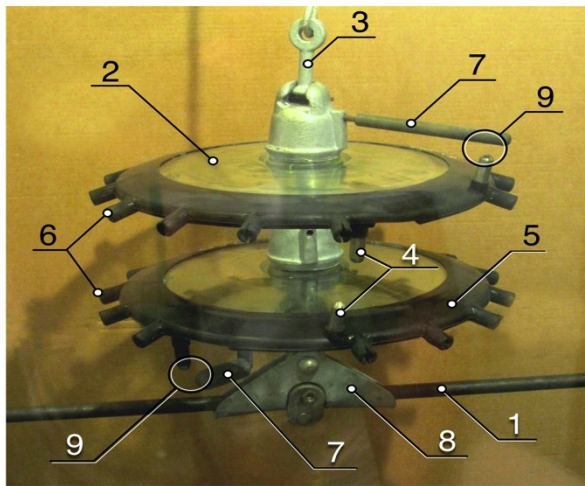
a) general view; b) test photo

1 – conductor; 2 – insulator; 3 – rod; 4 – ring of steel rod; 5 – silicon rubber body; 6 – discharge splits; 7 – electrode; S – sparkover gap

As a line conductor gets exposed to lightning overvoltage air gaps between electrodes and respective taps, as well as gaps between taps of adjacent insulators, are sparked over actuating the MCS as a whole.

Discharges between electrodes take place inside chambers of a very small volume; the resulting high pressure drives spark discharge channels between electrodes to the surface of the insulating body and hence outside, into the air around the MCS.

A blow-out action and an elongation of inter-electrode channels lead to an increase of total resistance of all channels, i. e. that of the MCS, which limits the lightning overvoltage impulse current and quenches impulse arc.



a)



b)

Fig. 11: String of two MCIA prototypes based on UI20AD insulator:

a) general view; b) during tests:

1 – conductor; 2 – UI20AD insulator; 3 – ball eye; 4 – taps; 5 – arrester's body; 6 – discharge chambers; 7 – electrodes; 8 – suspension clamp; 9 – upper and lower coordination spark gaps

## 5 ARC QUENCHING TESTS

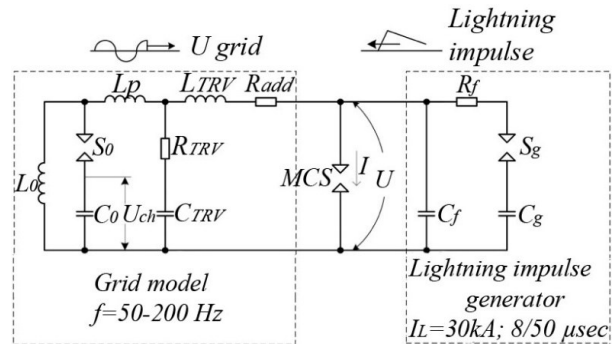
### Test procedure

The circuit diagram of the tests is shown in Fig. 12. Follow current quenching tests were carried out according to the procedure described in [4] for three modes:

**1. Induced overvoltages** (surge capacitance of voltage and current impulse generator

$C_g = 0,02 \mu\text{F}$ ; impulse current  $I_{\text{max}} \approx 2,5 \text{ kA}$ ;  $1/4 \mu\text{s}$ );

**2. Back flashover overvoltages** ( $C_g = 0,5 \mu\text{F}$ ;  $I_{\text{max}} \approx 2,5 \text{ kA}$ ;  $1,2/50 \mu\text{s}$ );



**Grid simulator:**

$C_o = 350 \mu\text{F}$  – capacitance of oscillatory circuit;  
 $L_o = 22 \text{ mH}$  – inductance of oscillatory circuit;  
 $L_p = 11 \text{ mH}$  – inductance,  
 $L_{TRV} = 1 \text{ mH}$  – Transient Return Voltage (TRV)-governing inductance;  
 $R_{TRV} = 50 \text{ Ohm}$  – TRV-governing resistance;  
 $C_{TRV} = 0,125 - 3,375 \mu\text{F}$  – TRV-governing capacitance;  
 $R_{add} = 0 - 10 \text{ Ohm}$  – additional resistance;  
 $S_o$  – spark discharge gap of grid simulator;

**Lightning voltage and current impulse generator:**

$C_g = 0,02 - 6,5 \mu\text{F}$  – capacitance of impulse generator;  
 $R_f = 5 - 100 \text{ Ohm}$  – front resistance;  
 $C_f = 4500 \text{ pF}$  – front capacitance;  
 $S_g$  – total spark discharge gap of impulse generator;  
MCS – test MCS;

Fig. 12: Circuit diagram of test setup

**3. Direct lightning stroke overvoltages** ( $C_g = 6,5 \mu\text{F}$ ;  $I_{\text{max}} \approx 30 \text{ kA}$ ;  $8/50 \mu\text{s}$ ).

Negative polarity lightnings account for some 90% of the total number. For this reason impulses simulating the lightning overvoltage impulse were taken to be negative. A lightning can strike at any instantaneous value of the grid voltage.

The worst possible case is a negative direct lightning stroke on a line conductor at negative instantaneous grid voltage. Here the total current across the arrester, made up by the overvoltage impulse current and the follow current of the grid, tends to reach the fault current level of the grid without crossing zero. That is why most of the tests concentrated on this particular ratio of overvoltage impulse and grid polarities (-/-). However in some cases (-/+) ratio was used.

The test procedure was as follows: first, the

capacitor bank  $C_o$  and the impulse generator were charged; operation of the impulse generator led to breakdown of the test MCS and the auxiliary arrester  $S_o$ . Thus both a lightning overvoltage impulse and the AC voltage were applied to the test MCS simultaneously. As the lightning overvoltage impulse ends, only power frequency voltage remains applied to the arrester.

Voltage and current oscillograms were recorded during the tests (see Fig. 13). Fig. 13,b also presents additional computer oscilloscope patterns of arc dynamic resistance  $R_{dyn}$  obtained by dividing the digital oscilloscope pattern of voltage  $U$  by the oscilloscope pattern of current  $I$ .

Studies have shown that spark discharge quenching can take place in two instances: 1) when the instantaneous value of lightning overvoltage impulse drops to a level equal to or larger than the instantaneous value of power frequency voltage, i. e. lightning overvoltage current gets extinguished with no follow current in the grid (this type of discharge quenching is further referred to as impulse quenching, see Fig. 13 a); 2) when 50 Hz follow current crosses zero (this type of discharge quenching is further referred to as zero quenching, see Fig. 13 b).

### Principal test results

#### LFA and LFA-M (see section 2)

LFA and LFA-M arresters quench the follow current arc upon its zero crossing, i. e. zero quenching (see Fig. 13 b).

Of the practical interest here is so-called critical gradient, i.e. operating voltage gradient of the flash over path at which the impulse sparkover transition to arc does not occur:  $E_{cr} = U/l$  (where  $U$  – current value of applied voltage;  $l$  – lightning sparkover length).

Principal results of completed experimental research, as well as the most representative data of other authors are shown in Fig. 14. Generally, the research was carried out with active pattern of the follow current within the range of current variation from 20A to 10kA.

As it is seen on Fig. 14, the critical gradient is highly dependable on the line short-circuit current.

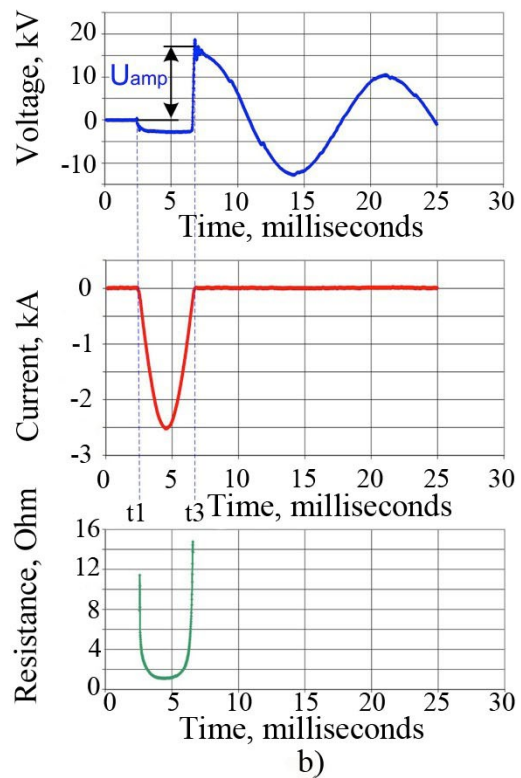
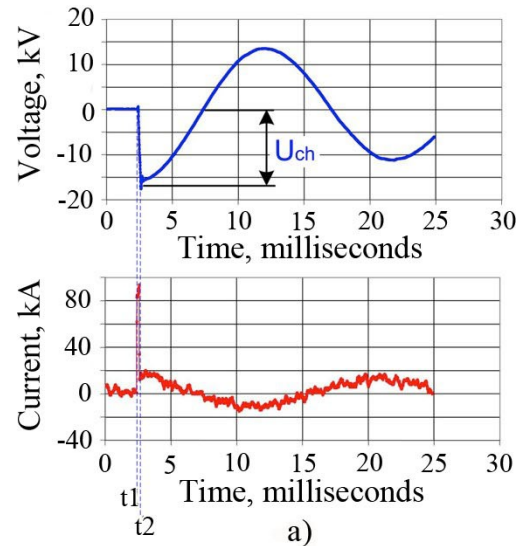


Fig. 13: Typical voltage, current and resistance oscillograms in power follow current quenching tests

- a) impulse quenching; b) zero quenching;
- $t_1$ -application of AC and lightning impulse;
- $t_2$ - quenching of lightning impulse;
- $t_3$ - quenching of power follow current

The higher the short circuit current within the range from 20A to 300A, the lower the critical gradient.

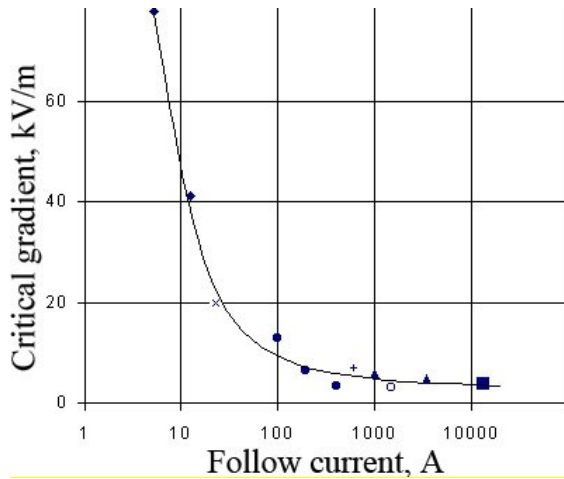


Fig. 14: Relationship between critical gradient of impulse sparkover transition to arc and effective value of follow current x – lab. [6]; • - lab.[1,2]; ○ - OHL [7]; + - OHL [8]; ▲ - OHL [9]; ■ - OHL [10]; ◆-lab. [7], capacitive current

In order to exclude the impulse sparkover transition to power arc, the sparkover length  $L$  of LFA can be determined as  $L = U / E_{cr}$ .

**MCA zero quenching** (see section 3)

It was shown by the tests that quenching occurs ‘in impulse’ at low values of  $U_{ch}$  but ‘in zero’ as  $U_{ch}$  increases.

Of interest is the fact that both at impulse quenching (Fig. 13 a) and at zero quenching (Fig. 13 b), voltage does not get chopped to zero, as it happens in standard rod-plane and rod-rod gaps, and a considerable residual voltage exists.

Shown in Fig. 15 are oscilloscope patterns obtained for various numbers of MCA chambers. Fig. 16 shows experimental values of grid voltage at which follow current is quenched versus the number of MCS chambers.

The data of Fig. 6 make it possible to estimate the needed number of MCS chambers for arresters of different voltage classes.

**MCA impulse quenching** (see section 4)

Given below are some test results (see Table 1). The grid simulator had to imitate the operating environment of e crest value of fault current is  $I_f^* = 30 \cdot \sqrt{2} = 42.4$  kA (ampl.). Earlier studies demonstrated that the issue of impulse or zero follow current quenching pattern is settled close to the instant  $t = 100 \mu s$ . With a sine form of 50 Hz current, its instantaneous value at this moment equals  $i = I_f^* \sin(\omega t) = 42.4 \sin(314 \cdot 100 \cdot 10^{-6}) \approx 1.3$  kA. That was why

the grid simulation was set up so as to assure a near-linear build-up of current from zero to 1.3 kA in 100  $\mu s$ .

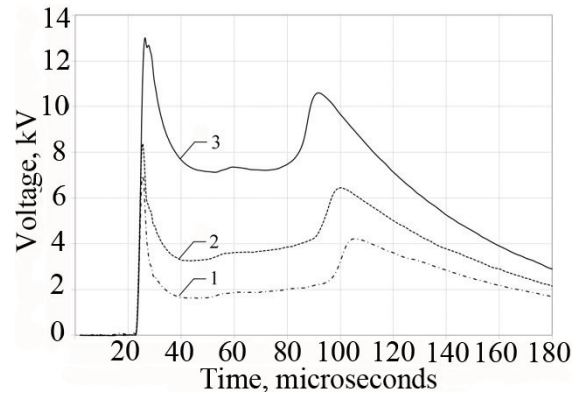


Fig. 15: Oscilloscope patterns for MCS with different chamber numbers m 1 – 50; 2 – 100; 3 – 200

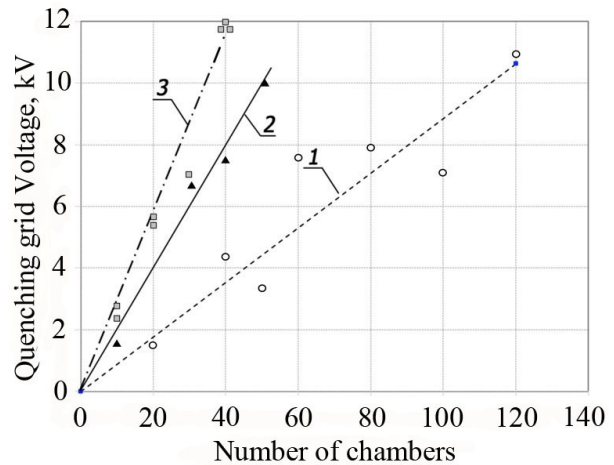


Fig. 16: Follow current-quenching grid voltage vs. number of MCS chambers

1 - impulse quenching (instantaneous value) ○; 2 - zero quenching at  $R_g = 0$  (effective value) ▲; 3 - zero quenching at  $R_g = 10$  Ohm (effective value) □

This condition is met with frequency of the grid’s oscillatory circuit being  $f = 200$  Hz.

Table 1 shows principal test findings for MCIAS comprising two insulators-arresters (see Fig. 11). The crest voltage capacity of the grid simulator is within  $U_{ch} = 30$  kV. This determined the number of MCIAS in a string during the tests.

The maximum permissible phase voltage  $U_{max}$  of a 220 kV line is 146 kV. As seen from Table 1, a two-insulator MCIAS assures arc quenching at  $U_{2 MCIAS}$  of 21 kV. At 14 units

per string an MCIAS can be believed to assure quenching at  $U_{14MCI A}$  of  $7 \cdot 21 = 147$  kV. Thus a fourteen-unit insulator MCIAS can assure

quenching of lightning overvoltage impulse arc without generating follow current.

Table 1.

Test object Fig. No.	Current impulse		Over-voltage	$\frac{U_{ch}}{U_{quench}}$ , kV
	$I_{max}$ , kA	Time, $\mu s$		
<u>MCA12-I</u> 9	2,5	1/4	in-duced	$\frac{12}{8,5}$
<u>MCA12-D</u> 10	30	8/50	direct strike	$\frac{12}{8,5}$
<u>2x MCI A</u> 11	30	8/50	direct strike	$\frac{30}{21}$

*Note:*  $U_{ch}$  – charging voltage of grid unit capacitors;  $U_{quench} = U_{ch}/\sqrt{2}$  – respective effective phase voltage of grid

## 6 CONCLUSIONS

1. Effective method for lightning protection of overhead distribution lines by Long Flashover Arresters (LFA) is presented. The LFA, which is based on the principle of surface discharge along a piece of insulated conductor, increases the lightning flashover length significantly and by this manner eliminates Power Arc Follow.
2. Multi-chamber systems have been designed that assure quenching of lightning overvoltage impulse arc without follow current in the grid, which permits application of MCS-based insulators-arresters in grids with fault currents as heavy as 30 kA.
3. New type arresters for protection 12 kV lines against induced overvoltages and direct lightning strikes are suggested.
4. A novel insulator-arrester design has been developed, based on a cap-and-pin insulator.
5. Strings of 14 insulators-arresters are capable of assuring lightning protection of 220 kV overhead power lines with no shielding wire.
6. New type arresters and insulators-arresters can be relatively easily adapted for application on power lines of other voltage classes.

## REFERENCES

[1] Podporkin G V, Sivaev A D, IEEE Transactions on Power Delivery 13 (1998) 814-823.

[2] Podporkin G V, Pilshikov V E, Sivaev A D, IEEE Transactions on Power Delivery 18 (2003) 781-787.

[3] Podporkin G V, Enkin E Yu, Kalakutsky E S, Pilshikov V E, Sivaev A D, IEEE Transactions on Power Delivery 26 (2011) 214-221.

[4] Podporkin G V, Enkin E Yu, Pilshikov V E, Lightning Protection of Overhead Distribution and Transmission Lines by multi-chamber insulators-arresters of a novel design, CIGRE SC C4 2012 HAKODATE Colloquium, Japan.

[5] Podporkin G V, Enkin E Yu, Pilshikov V E, Zhitenev V V, Lightning Protection of Overhead Distribution and Transmission Lines by Multi-Chamber Arresters and Insulators – Arresters of a Novel Design, CIGRE SC C4 2014, 10-14 May, Lyon, France.

[6] Bellaschi P L, Lightning and 60-Cycle Power Tests on Wood Pole Line Insulation, A.I.E.E. Trans. 66 (1947) 838-50.

[7] Podporkin G V, Lightning protection of 6-10 kV overhead power lines by long flashover arresters, S. Petersburg University 2001 (in Russian).

[8] Burgsdorf V V, Lightning Protection of Overhead Transmission Lines and Operating Experience in the U.S.S.R., CIGRE Paper, No. 326, Paris, 29pp., 1958.

[9] Armstrong H R, Stoelting H O, Veverka E F, IEEE Trans. on PAS, PAS-86 (1967) 206 - 214.

[10] Morooka Y et al., Insulation Cover Thickness Required For Line Breakage Prevention Capitalizing on Creeping Discharge Characteristics of Insulated Wires, In: Proc. 24<sup>th</sup> ICLP, 984-988.

# Pulsed Plasma Spraying of Liquid Feedstock for Coating Elaboration

Rat V., Mavier F., Bienia M., Lejeune M., Coudert J.F.

CNRS, University of Limoges, ENSCI, SPCTS UMR7315, European Ceramic Centre  
12 rue Atlantis 87068 Limoges cedex, France, vincent.rat@unilim.fr

Self-sustained nitrogen pulsed plasma is studied by electrical and optical diagnostics. It is used to deposit coatings when the injection of suspensions of nanoparticles is synchronized with the arc voltage.

**Keywords:** pulsed plasma torch, plasma spraying, diagnostics, model

## 1 INTRODUCTION

Growing needs in energy demand from industrialized and emerging nations compel many researches to improve the efficiency of energy management by focusing on the development of renewable energy sources and by tackling ecological concerns. For example, fuel cells, thermal barrier coatings in gas turbine industry or photo-catalytic coatings require advanced elaboration processes capable to manufacture nanostructured ceramic coatings. These materials must have specific service properties, like finely structured architectures and graded properties (porosity/chemical composition). Such refractory materials are deposited by cost-effective plasma spraying techniques possessing the advantage to treat materials with high rates ( $> \text{kg/h}$ ) in high enthalpy medium ( $> 10 \text{ MJ/kg}$ ). Ceramic nanostructured coatings can now be achieved whether nanopowders are injected or formed into arc plasma jet. Two emerging plasma spraying processes are currently under study, namely Suspension Plasma Spraying (SPS) and Solution Precursor Plasma Spraying (SPPS) [1]. In the former process, nanopowders are dispersed in a liquid with chemical additives avoiding particles agglomeration and are injected into plasma. In SPPS process, fully liquid chemical solutions containing the dissolved elements to deposit are injected in the plasma jet. Owing to plasma treatment, solid materials are in-flight synthesized and simultaneously sprayed onto a prepared substrate. The suspensions and solutions are usually injected either as a liquid jet (about  $200 \mu\text{m}$  diameter) or as atomized droplet spray ( $5\text{-}80 \mu\text{m}$  droplet diameters).

Depending on heat and momentum transfers, droplets can be fragmented and vaporized, and

nanoparticles are subsequently plasma treated [2]. Controlling electric arc instabilities confined in non-transferred arc plasma torch is therefore a key issue to get reproducible coating properties. All studies are currently devoted to stabilize the arc by means of multi-electrodes plasma torches. Alternatively, it is proposed to study self-sustained pulsed arc plasma jet associated with a synchronous injection of droplets containing nanopowders [3-4]. By adjusting the injection timing relatively to time-dependent enthalpy variations, heat and momentum transfers from plasma to materials are expected to be efficiently controlled. The electrical features of such a pulsed arc are presented and the enthalpy modulation is studied by means of optical emission spectroscopy. Temperature measurements are interpreted with a simplified time-dependent model of heat transfers inside the torch. The plasma treatment of droplets is also shown to be dependent on the injection timing. Coatings are also analyzed. At last, conclusion is given.

## 2 EXPERIMENTAL DESCRIPTIONS

### 2.1 EXPERIMENTAL DEVICES

A home-made plasma torch operates at atmospheric pressure in ambient air and is power supplied by a current regulated source. As shown in figure 1, the arc is ignited between the thoriated tungsten cathode tip and a water-cooled copper nozzle. The mean gas flow rate is maintained constant during experiments and is controlled by a mass flowmeter upstream the gas feeding line. The nitrogen gas is delivered to the cathode cavity with flow rates ranging between 2 and 4 standard litres per minute (slm). The internal diameter of the nozzle channel,  $D$ , can be changed between 3 and 4 mm. The arc current

$I$ , the mean arc voltage  $\bar{V}$ , and the heat losses to the electrodes  $Q_{\text{loss}}$  are measured, over a period of a few minutes. These values are used to determine the effective specific enthalpy,  $\bar{h}_L$ , available at the exit of the nozzle,  $L$  in length, such as  $\bar{h}_L = (\bar{V}I - Q_{\text{loss}})/\dot{q}_m$  where  $\dot{q}_m$  is the gas mass flow rate. The specific enthalpy  $\bar{h}_L$  represents a quantity which is averaged in time and also in the cross section of the plasma jet at the torch exit. The heat losses to electrodes are evaluated by means of calorimetric measurements of torch cooling water.

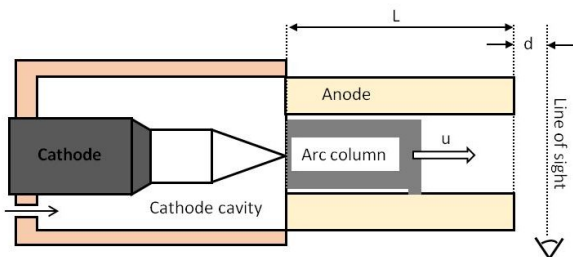


Fig.1: Simplified scheme of dc plasma torch

This set of measurements is also used to check the reproducibility of results. The instantaneous arc voltage,  $V(t)$  where  $t$  is time, is measured by using a data acquisition computer card piloted by Labview software at a sampling rate of 320 kS/s rate during 0.2 s, giving a maximum frequency of 160 kHz and a frequency resolution of 5 Hz in calculated power spectra.

Figure 2 presents the experimental set-up including the dc plasma torch, a fast-shutter camera, a pulsed laser diode, a spectrometer, a synchronization unit and an injector of droplets. Time-resolved imaging of plasma jet is performed by means of a fast-shutter camera (PCO, Kelheim, Germany) with 1392 x 1040 pixels resolution and which can be externally triggered. The imaging is associated with a 50 W laser diode designed for illumination applications (HiWatch, Oseir, Tampere, Finland) and permit to observe injected materials inside the plasma at the emission wavelength of 801 nm. The pulse duration is 1  $\mu$ s.

Optical Emission Spectroscopy (OES) is carried out by using the IsoPlane spectrograph (Princeton Instruments, Trenton, USA). The focal length is 320 mm and the focal plane size is 27 mm wide x 14 mm high. The arrangement of optical components reduces optical aberrations. The spectrograph is equipped with a triple grating turret (68 mm x 68 mm grating size). It is associated with an Intensified CCD camera (PIMAX4 1024i, Princeton Instruments, Trenton, USA) with 1024 x 1024 pixels resolution (12.6  $\mu$ m pixel size) including a fast gate intensifier (down to 3 ns). A UV objective (105 mm focal length, f/4 aperture ratio) is mounted on the spectrograph to image the plasma, providing a -0.3 magnification.

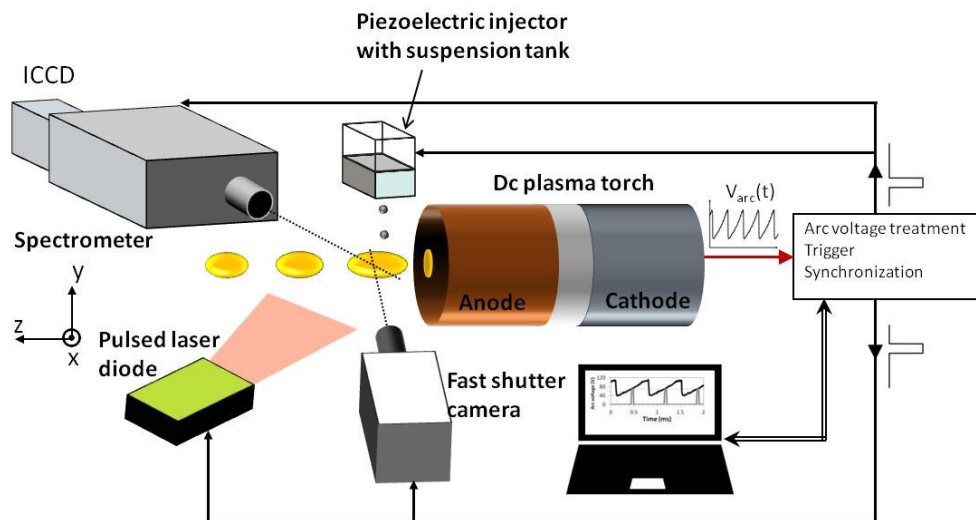


Fig. 2: Experimental setup

Lightfield software (64 bits, Princeton Instruments, Trenton, USA) is used to control spectroscopic devices and record the spectra. The spectrometer is calibrated thanks to a tungsten ribbon lamp used as a standard source which is power supplied by a current regulated source.

A pyrometer is used to measure the tungsten ribbon temperature at given lamp current. The spectral radiance of the tungsten ribbon lamp is calculated for a given temperature by using the Planck's law and the spectral emissivity of tungsten. The spectrometer response to the tungsten ribbon lamp is known for given set of spectrometer parameters what enables to deduce the spectral radiance of the plasma.

The injection technology is based on drop-on-demand (DOD) method commonly used in the inkjet printing (Ceradrop, Limoges, France). The printing head contains 128 independent nozzles spaced by 0.5 mm and is controlled by LabView software. The liquid is ejected out of small orifices (diameter equal to 50  $\mu\text{m}$ ) due to the pressure generated by a voltage pulse driven piezoelectric actuator. The drops have a diameter of 50  $\mu\text{m}$  and the velocities in the range of 2 to 10  $\text{ms}^{-1}$ . The ejection frequency can be adjusted up to 20 kHz. The suspension used in the experiment is composed of titanium dioxide (90%  $\text{TiO}_2$  rutile phase) powder and it consists of 42 wt.% of powder and 58 wt.% of water. The particle size distribution is mainly bimodal, i.e. 70 and 350 nm.

## 2.2 ARC VOLTAGE FEATURES

Undesired arc instabilities usually occur in dc arc torches for plasma spraying applications and have been studied for several decades [5]. Recent works are shown that they originate in complex coupling of different fluctuation modes. The well known retriage mode corresponds to random rearing phenomena which are controlled by physical properties of the cold boundary layer (CBL) between the arc column and the anode wall in the arc channel. Local overheating of CBL leads to a dramatic increase of the electrical conductivity resulting in shunting the existing arc root and creating a new one at a different location [6].

The arc length is abruptly reduced and just after rearing it increases again due to the plasma flow. This process is more or less randomly repeated with characteristic times of a few tens of  $\mu\text{s}$  so that the arc voltage waveform is roughly saw-tooth shaped.

The second important fluctuation mode, called Helmholtz mode, refers to as oscillation imposed by gas compressibility effects inside the cathode cavity. This mode is characterized by a strong oscillation with frequencies ranges between 3 and 5 kHz depending on operating conditions in common plasma torches ( $\sim 20\text{-}50\text{kW}$ ) used in plasma spraying. Pure acoustic oscillation modes can also be observed at higher frequencies but weakly affects the arc voltage. Unlike common torches where these modes are decoupled, the presented torch works in operating conditions allowing the coupling of Helmholtz and retriage modes.

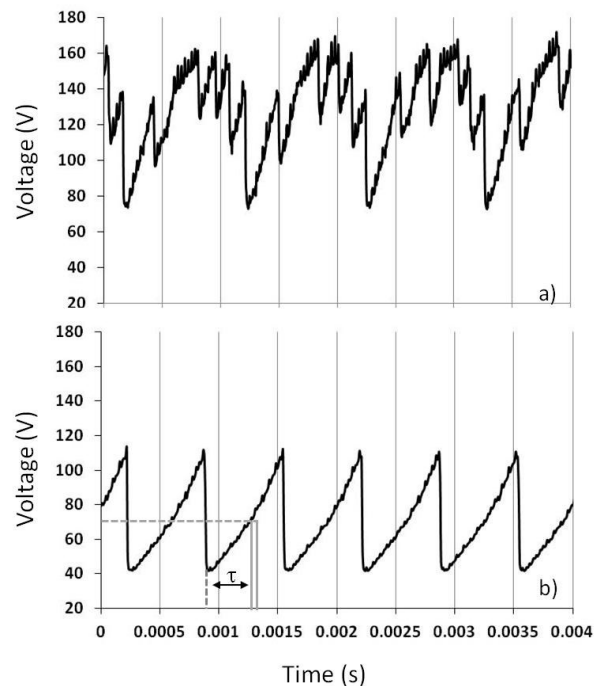


Fig.3: Arc voltage signals: a) internal nozzle diameter  $d = 3.5 \text{ mm}$ ,  $I = 25 \text{ A}$ ,  $2.7 \text{ slm } \text{N}_2$ ,  $\bar{V} = 129 \text{ V}$ ,  $f = 970 \text{ Hz}$ ; b) Mosquito mode:  $d = 4 \text{ mm}$ ,  $I = 15 \text{ A}$ ,  $2 \text{ slm } \text{N}_2$ ,  $\bar{V} = 73.7 \text{ V}$ ,  $f = 1410 \text{ Hz}$  (Time  $\tau$ , trigger signal)

Figure 3 depicts two arc voltage signals obtained for different operating conditions. In Fig. 3a, rearing events (retriage) are superimposed to the lower frequency

Helmholtz oscillation. In fig.3b where both modes are coupled following appropriate operating conditions, very repeatable saw-tooth shape voltage signal is obtained. The arc length oscillates between positions in the nozzle corresponding to voltages changing between  $V_{\min} = 40\text{V}$  and  $V_{\max} = 110\text{V}$ .

The calculated power spectrum of the arc voltage displayed in Figure 4 exhibits a strong fundamental frequency of  $f_H=1410\text{ Hz}$  with high quality factor ( $Q=\Delta f/f_H=235$ ) and higher frequency harmonics.

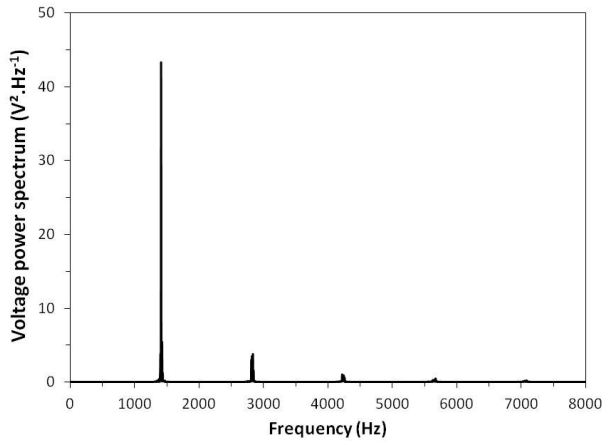


Fig.4: Power spectrum of mosquito mode (Fig3.b)

This frequency can also be evaluated with the Helmholtz frequency, i.e.:

$$f_H = K_H \cdot \sqrt{(\gamma_g P / \rho_p)} \quad (1)$$

where  $\gamma_g$ ,  $P$ , and  $\rho_p$  are respectively the isentropic coefficient of plasma forming gas, the pressure inside the cathode cavity, the mass density of plasma.

The constant  $K_H$  accounts for the torch geometry, namely the cross section area of the arc channel, the channel length and the volume of the cathode cavity [4].

In the so-called mosquito mode obtained with pure nitrogen ( $4.510^{-5}\text{ kg}\cdot\text{s}^{-1}$  mass flow rate) in Fig.3b, the mean arc voltage is  $\bar{V}=73.7\text{ V}$ , the arc current  $I=15\text{ A}$  and the mean specific enthalpy  $\bar{h}_L=13.4\text{ MJ}\cdot\text{kg}^{-1}$ .

The steep falling fronts of the voltage signal represent accurate events which are used to define rectangular pulses (see Figure 3b), delayed by an adjustable amount of time,  $\tau$ , ranging between 0 and  $710\text{ }\mu\text{s}$ , which also

corresponds to a voltage threshold (see Fig.3b). Thanks to a synchronization device, these pulses are used to trigger the fast-shutter PCO camera, the laser diode and the ICCD detector, so that the plasma pictures and the spectrum are simultaneously recorded, for a given instantaneous voltage. The exposure time of the camera is  $\tau_{\text{exp}} = 30\text{ }\mu\text{s}$ . For the ICCD the exposure time,  $\tau_{\text{gate}}$ , is between 15 and  $30\text{ }\mu\text{s}$  for each received trigger. It is possible to accumulate  $N_{\text{acc}}$  signals at a rate corresponding to the pulsed mode frequency that is  $1410\text{ Hz}$ , so that the total exposure time is  $N_{\text{acc}} \cdot \tau_{\text{gate}}$ . The number  $N_{\text{acc}}$  is between 10 and 500 depending on operating conditions.

The same trigger voltage with appropriate  $\tau$  delay is used to eject droplets from the piezoelectric head. The laser diode can also be triggered.

### 3 RESULTS AND DISCUSSION

#### 3.1 TIME-RESOLVED OPTICAL EMISSION SPECTROSCOPY OF PLASMA

At nozzle exit, the identification of emitting systems of nitrogen plasma mainly highlights the first negative system of the molecular ion  $\text{N}_2^+$ , referenced to as  $\text{N}_2^+(1-)$  in the following. The second positive system of  $\text{N}_2$  molecule and the violet system of  $\text{CN}$  molecule dominate downstream the nozzle exit where the plasma is cooled down by mixing with the ambient atmosphere and is recombining. Rotational temperatures are measured at nozzle exit from the simulation of the sequence  $\Delta v=v'-v''=0$ , where  $v$  is the vibrational quantum number and the single prime corresponds to an upper vibrational level and the double prime to a lower level. Spectra are fitted to experimental ones to deduce the rotational temperatures. Specair software [7] is used to simulate and fit the experimental spectra after the determination of the slit function.

The best-fit spectra allow estimating the measurements precision of  $\pm 150\text{ K}$  for a measured value of  $7500\text{ K}$ . Figure 5 depicts the spectra obtained at  $1\text{ mm}$  from the nozzle for different time delays  $\tau$ , corresponding to different arc voltage levels, namely 105, 85,

75 and 62 V.

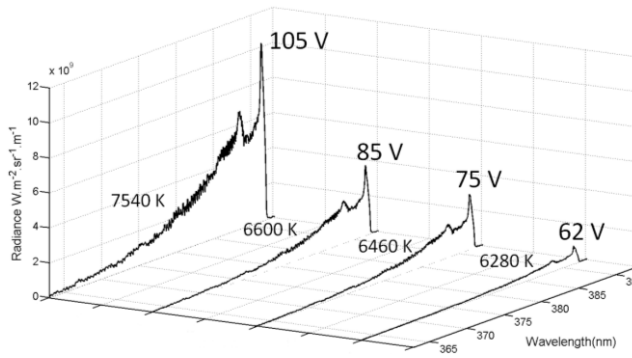


Fig. 5: Emission spectra at 1 mm from nozzle exit for different values of arc voltage. Rotational temperatures obtained are reported

Rotational temperatures vary between 6280 and 7540 K for arc voltages changing between 62 V and its maximum value around 105 V.

### 3.2 INTERPRETATION OF MEASURED TEMPERATURES

Temperatures need to be interpreted in terms of specific enthalpy which is the quantity useful to quantify for example the heat transfers between plasma and materials. It can be shown that the heat conduction potential, defined as  $\phi(T) = \int K(T')dT'$  where K and T are respectively the thermal conductivity and temperature, is related to the specific enthalpy. The use of thermodynamic data permits to establish the link between temperature and enthalpy. Figure 6 shows this dependence (full line). It results that enthalpy changes between 14.35 and 38.20 MJ.kg<sup>-1</sup>, i.e. a modulation ratio of 2.66. However, for a mean value of  $\bar{V} = 73.7$  V, the mean specific enthalpy obtained with calorimetric measurement gives  $\bar{h}_L = 13.4$  MJ.kg<sup>-1</sup>.

Consequently, the interpretation of temperature measurements should consider an enthalpy profile effect to resolve this inconsistency. The molecular spectra results from measurements averaged in a cross section at the nozzle exit (xy plane in Fig.2). The Abel inversion is not performed because it requires several hundreds of inversions for a single spectrum that provokes noise amplification and increases significantly the

residual obtained at the end of the fitting procedure. Actually, the measured temperature results from a measurement weighted by the local emission coefficient.

It is supposed that the specific enthalpy follows a parabolic profile,  $h(r)$  where r is the radial coordinate, compatible with measurements of  $(\bar{h}_L, Q_{loss})$ . This assumption is backed by the laminar feature of plasma flow [3-4]. A corresponding temperature profile  $T(r)$  is obtained from thermodynamic data of nitrogen plasma. Assuming the local thermodynamic equilibrium, the radial distribution of the emission coefficient  $\epsilon_{00}(r)$  of (0-0) band of N<sub>2</sub><sup>+(1-)</sup> is calculated.

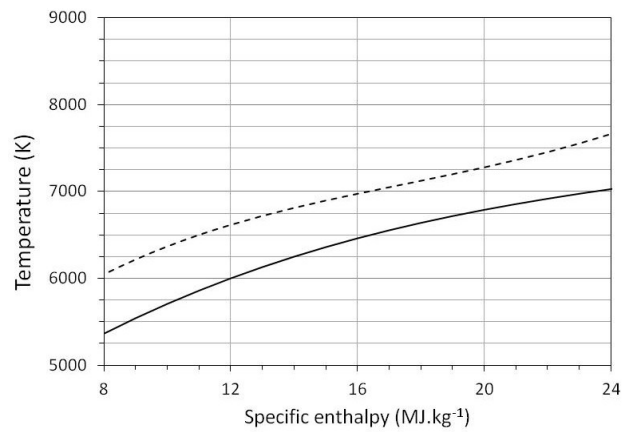


Fig.6: Dependence of temperature on enthalpy. Full line: thermodynamic data, dashed line: temperature weighted by emission coefficient

According to this procedure, the measured temperature  $T_{spectro}$  is assimilated to the mean value given by:

$$T_{spectro} = \frac{\int_0^R T(r)\epsilon_{00}(r)rdr}{\int_0^R \epsilon_{00}(r)rdr} \quad (2)$$

where R is the radius of the plasma.

In Figure 6 is the reported this temperature weighted by the emission coefficient (dashed line). It can be seen that, for the measured temperatures 6280 and 7540 K, we respectively obtain 10 and 23 MJ.kg<sup>-1</sup>. The enthalpy modulation ratio is close the previous one, but enthalpies are shifted to lower values by considering the profile effect.

### 3.3 MODEL OF ENTHALPY MODULATION

The interpretation of previous measurements can be carried out by means of a simplified model which establishes the relationship of the amplitudes and phase shift between the arc voltage and the specific enthalpy. It is also important because the material injection inside the plasma is triggered with the arc voltage whereas the local enthalpy is responsible for material treatment.

The available energy obviously depends on heat losses inside the arc channel. Thermal losses ( $Q_{loss}$ ) are due to electrode phenomena and convective/radiative heat transfers between the arc column and the wall. We suppose that the latter is proportional to the nozzle length  $L$  and the mean specific enthalpy at nozzle exit:

$$Q_{loss} = V_{elec} I + \alpha_{th} L h_L \quad (3)$$

where  $V_{elec}$  and  $\alpha_{th}$  are respectively an equivalent arc voltage accounting for electrode phenomena and a heat transfer coefficient.

Calorimetric measurements with  $L$  changes permits to estimate  $V_{elec}=17\pm 4V$  and  $\alpha_{th}=1.1\pm 0.310^{-3} \text{ kg}\cdot\text{m}^{-1}\cdot\text{s}^{-1}$ .

In the following heat losses due to electrode phenomena are supposed constant during voltage fluctuations and to be decoupled from convection and radiative heat transfers. We only consider heat exchanges with the walls in the arc channel and plasma convection.

By using quantities averaged over the channel cross section,  $S = \pi R^2$ , the energy conservation is written as:

$$\rho \frac{\partial h}{\partial t} + \rho u \frac{\partial h}{\partial z} = -p_{th} \quad (3)$$

$z$  is the axial coordinate, with  $0 < z < L$ ,  $\rho$  and  $u$  are respectively the mass density and plasma velocity,  $p_{th}$  is the power per unit volume lost by heat transfer to the anode, so that  $p_{th} S L = \alpha_{th} L h_L$ .

The enthalpy averaged over a cross section is supposed to be  $h_L = \bar{h}_L + h'$  where  $h'$  is the fluctuating component of enthalpy.

The energy equation permits to obtain a simple first-order differential equation between  $h'$  and the fluctuating component of the arc voltage  $v'_{arc}$ :

$$\frac{dh'}{dt} + \frac{h'}{\tau_{th}} = \frac{v'_{arc}}{(q_m + \alpha_{th} L) \tau_{th}} I \quad (4)$$

where  $t$  is time,  $q_m$  the mass flow rate, and  $\tau_{th}$  a characteristic time of heat transfer given by:

$$\frac{1}{\tau_{th}} = \frac{q_m + \alpha_{th} L}{m_p} \quad (5)$$

where  $m_p$  is the plasma mass contained in the anode nozzle evaluated from the plasma mass density.

In the present operating conditions,  $\tau_{th}$  is about  $130\mu\text{s}$ .

By using equation 5, the following transfer equation can be written:

$$\frac{H(\omega)}{V(\omega)} = \left( \frac{I}{q_m + \alpha_{th} L} \right) \frac{1}{1 + j\omega\tau_{th}} \quad (6)$$

where  $H(\omega)$  and  $V(\omega)$  are the Fourier component of  $h'(t)$  and  $v'(t)$  respectively.

The periodic arc voltage of fig.3 b,  $T_0$  in period and  $\bar{A}$  in amplitude, is expanded in a Fourier series that is used, thanks to eq. 6 to define the time dependent enthalpy function, following:

$$h_L(t) = \bar{h}_L + \sum_{n=1}^{\infty} H_n \sin(\omega_n(t - \theta_n)) \quad (7)$$

$$\text{with } H_n = \frac{(-1)^{n+1}}{n\pi(q_m + \alpha_{th} L)} \frac{\bar{A}I}{\sqrt{1 + (\omega_n \tau_{th})^2}}$$

$$\text{and } \theta_n = \frac{T_0}{2\pi n} \arctan(\omega_n \tau_{th})$$

where  $T_0=1/f_H=710 \mu\text{s}$  is the period of periodic arc voltage signal and  $\bar{A} = V_{max} - V_{min} = 70V$  the amplitude of arc voltage.

Figure 7 displays the simulated arc voltage and the calculated specific enthalpy (equation 7). An equivalent "thermal" voltage is defined as  $V_{th}=Q_{loss}/I$ , i.e.:

$$V_{th}(t) = V_{elec} + \alpha_{th} L h_L(t) / I \quad (8)$$

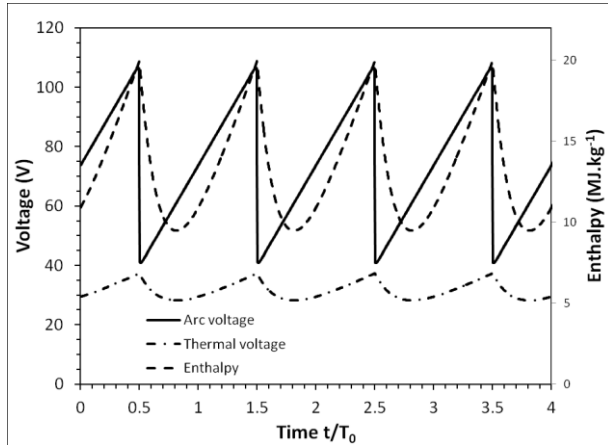


Fig.7: Fluctuations of arc voltage, enthalpy and thermal voltage calculated from the model

We can note that the modulation ratio is about 2 with  $h_{max}=20$  and  $h_{min}=10$  MJ.kg<sup>-1</sup>. These values are close to those obtained by OES measurements when considering the profile effect. The enthalpy maxima are almost synchronous with the voltage maxima, the minimum values are delayed by about one third of period. The particular voltage of 62 V is almost synchronous with the minimum of enthalpy (therefore with the minimum of temperature). It seems that the minimum temperature remains above 6000 K even though the trigger voltage is not the minimum. Consideration of characteristic times of heat transfer ( $m_p/\alpha_{th}L$ ) and of residence time ( $m_p/q_m$ ) has a low-pass filter effect on enthalpy smoothing fast variations.

The decreasing branches of enthalpy corresponds to a plasma generated during the preceding period whereas the growing branches of enthalpy follow the arc voltage with a delay decreasing with time up to the maximum.

The mean value of thermal voltage is 36 V and fluctuates between 30 and 40 V.

### 3.4 INJECTION OF SUSPENSIONS IN PULSED ARC JET

The previous section shows that enthalpy is modulated with a ratio of approximately 2 at nozzle exit. This is confirmed when observing

the arc jet for two different delays as shown in Figure 8.

In figure 8a where imaging is triggered at high voltage, the arc column is fully developed. In figure 8b, imaging is triggered at low voltage (around 55 V) which should be very close to the minimum of enthalpy as shown in Figure 7. At nozzle exit, in this case, a minimum of radiative emission can indeed be noted.

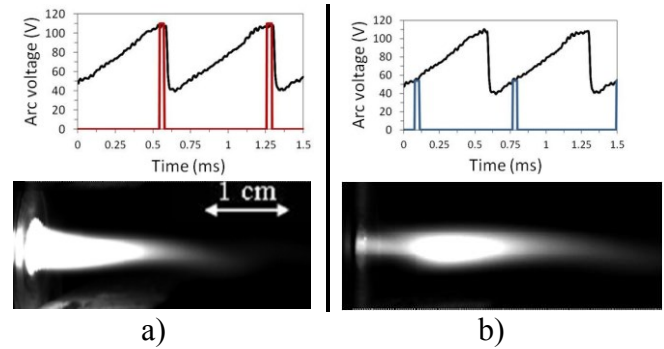


Fig.8: Time-resolved imaging of pulsed jet. a) imaging triggered at high voltage, b) imaging triggered at lower voltage

The interest to use such a pulsed plasma jet is twofold. First, if a pulsed injection of materials is associated with the plasma, it is expected to obtain reproducible heat and momentum transfers between materials and plasma and therefore to reach repeatable coating properties. Second, the modulation of enthalpy at nozzle exit is expected to influence the trajectories of materials in plasma plume and hence modulate heat transfers. This can be an additional experimental parameter, non-existing in conventional plasma spraying of liquid feedstock, to treat materials more or less sensitive to heat transfers.

In the following, suspensions of TiO<sub>2</sub> nanopowders are synchronously injected with the arc voltage by using the piezo-electric injection head as explained above.

The suspension flow rate injected is 5.10<sup>-3</sup> mL.min<sup>-1</sup> and the mass flow rate is 2.810<sup>-3</sup> g.min<sup>-1</sup>.

Figure 9 displays a picture of the plasma with synchronized injection of TiO<sub>2</sub> suspensions (aperture time 125 μs). At about 30 mm, a substrate can intercept the plasma either to collect particles or to deposit a coating.



Fig. 9: Picture of pulsed arc jet with synchronous injection of  $TiO_2$  suspensions (exposure time 125  $\mu s$ )

At nozzle exit, the nitrogen plasma alone is observed with pink emissions of nitrogen. Suspensions droplets are perpendicularly injected with respect to the nozzle axis at about 4 mm from the nozzle exit. Upon the penetration of 50  $\mu m$  droplets into plasma, they can undergo liquid fragmentation and vaporization. The breakup of a droplet is governed by the dynamic pressure applied by the plasma flow on droplet, surface tension effects and viscous forces. In conventional suspension plasma spraying in higher power plasma torches, the characteristic time of fragmentation is by far much higher than that of vaporization ( $\sim \mu s$  and 0.1 ms respectively) [2]. In the present alternative process, the primary liquid fragmentation is absent because of low plasma velocity ( $\sim 50-100 m.s^{-1}$ ). This can be shown when evaluating the Weber number which compares the aerodynamic forces to the surface tension forces, i.e.

$We = \rho_p v_r^2 d_\ell / \sigma_\ell$  where  $\rho_p$ ,  $v_r$ ,  $d_\ell$ , and  $\sigma_\ell$  are respectively the plasma mass density (depending on enthalpy), the relative velocity between the plasma and the droplet, the diameter of droplet and surface tension of droplet. The Weber number is always weak, below 0.5. However, it has been observed a “thermal fragmentation” as shown in Figure 10. It depicts the injection of droplets, first, through a slit behind which the piezo-electric head is mounted, and second the interaction with plasma. The latter is not shown because the pulsed laser diode is used with an interferential filter centered at 801 nm. It can be seen that a droplet is isotropically fragmented, even in the reverse direction of plasma flow, what could not be possible in the case of pure momentum transfer.

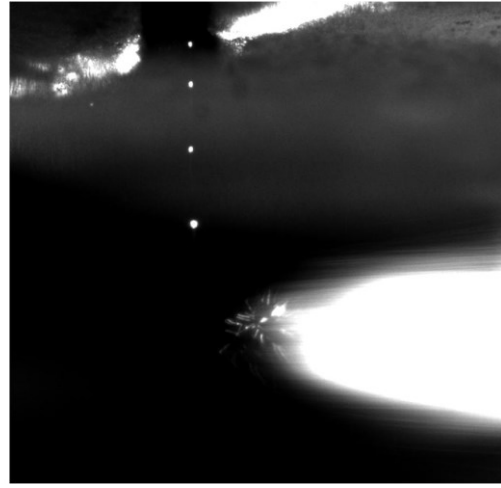


Fig.10: Fragmentation of suspension droplet due to the plasma (exposure time 270  $\mu s$ )

The highly luminous region at the right hand side of the on-going droplet fragmentation corresponds to the plasma treatment of the previous droplet.

An estimation of the vaporization time can be given by using the property of linearity between the heat conduction potential and plasma enthalpy:  $\varphi(T) = a_\varphi h(T)$ . It follows:

$$\tau_{vap} = \frac{\rho_\ell L_v}{4N_u a_\varphi} \left[ 1 - \left( 1 + \frac{1 - x_m \rho_s}{x_m \rho_\ell} \right)^{-2/3} \right] \frac{d_\ell^2}{h_p} \quad (9)$$

where  $\rho_\ell$ ,  $\rho_s$ ,  $L_v$ ,  $x_m$ , and  $h_p$  are respectively the mass density of liquid (water) and of solid phase, the latent heat of vaporization of water, the mass fraction powder in water, and plasma enthalpy. The constant  $N_u$  and  $a_\varphi$  are respectively the Nusselt number and a proportionality constant between enthalpy and heat potential.

Equation (9) highlights its dependence on the plasma enthalpy; the order of magnitude of the vaporization time is about 100  $\mu s$ .

After vaporization of water, nanopowder are heated by the plasma what produces intense radiative emission of lines of titanium atoms (Ti I) and titanium ions (Ti<sup>+</sup>I). These metallic vapors appear in near UV domain (300-400 nm) and visible domain as seen in figure 9 (blue color).

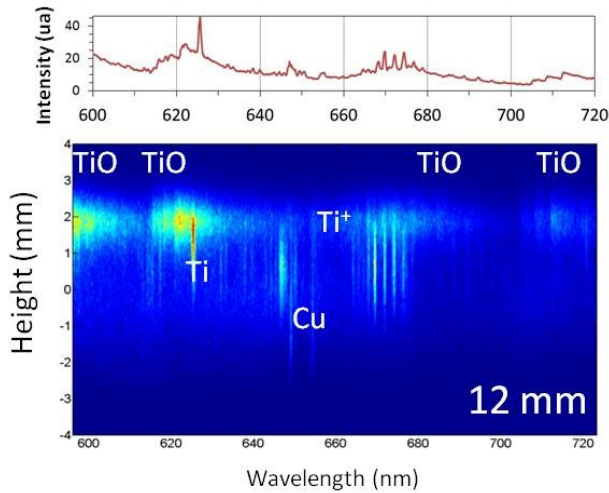


Fig.11: Synchronized spectral image of droplet/plasma interaction at 12 mm from nozzle exit. Height is the y direction given by Fig.2. ( $y=0$  corresponds to the torch axis)

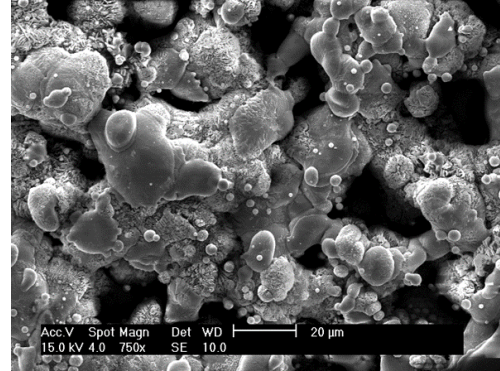
At higher distances, red/orange emissions are seen in Figure 9 which corresponds to red and orange-red systems of the TiO molecule [8]. The image is synchronized at high voltage (105 V) at 12 mm from the nozzle exit. For lower voltage (55 V), it is observed that molecular emissions of TiO occur farther downstream, i.e. at 20 mm, mainly in the fringes of the plasma jet ( $y=2\text{mm}$ ). Consequently, it can be supposed that, first, the molecule formation starts in the fringes of the plasma plume with the atomic oxygen of air ( $\text{Ti}+\text{O}\rightarrow\text{TiO}$ ). Second, the modulation of enthalpy affects the heat treatment of nanopowders what delays the formation of TiO molecule.

### 3.5 COATING DEPOSITION

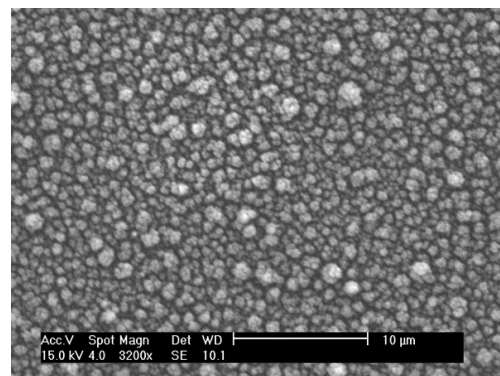
First attempts to deposit  $\text{TiO}_2$  coatings are made onto stainless steel substrates by performing synchronous injection with arc voltage. The surface of coatings obtained with and without synchronization is analyzed by scanning electron microscopy (SEM).

If no synchronization is performed, a very non-homogeneous coating is obtained with large porosities, coarse melted zones which the characteristic size is much larger than the initial nanoparticle sizes (70-350 nm), but also very fine structures. With synchronization, a much more homogeneous surface coating is

observed which has typical features of vapor condensation. This is consistent with spectroscopy studies where metallic and TiO vapors are seen. It is then supposed that the coating results from the association of condensed vapors and large melted zones which the proportion should depend on synchronization.



a)



b)

Fig. 12: SEM images of  $\text{TiO}_2$  coating surfaces for a) without synchronization, b) with synchronization

### 4 CONCLUSION

Plasma spraying of liquid feedstock allows depositing finely structured ceramic coatings for many applications, such as for instance photo-catalytic coatings, fuel cells, thermal barrier coatings. The liquid phase is used as a carrier medium either to inject nanosized particles in the plasma core or to directly synthesize them in plasma. Reproducible plasma treatment is therefore of great importance to achieve desired coatings properties. That is why controlling arc instabilities must be performed. In this paper, we have proposed to

generate a pulsed arc jet associated with a synchronous injection of droplets. Adjusting the timing injection should permit to reproduce and control the heat and momentum transfers, and coating properties.

A self-sustained pulsed nitrogen plasma jet is obtained by coupling two modes of arc instabilities. By means of time-resolved emission spectroscopy, the specific enthalpy at nozzle exit was shown to oscillate between 10 and 20 MJ.kg<sup>-1</sup>.

A time-dependent simplified model of heat transfers inside the torch has confirmed this modulation and has highlighted a phase shift between voltage and enthalpy fluctuations due to the characteristic time of heat transfer and of residence time of plasma inside the nozzle. This should be considered when triggering the injection of droplets for synchronization.

During the interaction between droplets containing nanosized particles of TiO<sub>2</sub>, metallic vapours are observed and TiO vapours as well. The comparison of SEM surfaces of coatings have shown more homogeneous microstructure when the synchronisation of injection is performed.

### **Acknowledgements**

The French National Research Agency is acknowledged for financial support in the frame of PLASMAT program (ANR-12-JCJC-JS09-0006-01).

### **REFERENCES**

- [1] Killinger A, Gadow R, Mauer G, Guignard A, Vaßen R, Stöver D, J. Thermal Spray Technol. 20 (2011) 677-695.
- [2] Fazilleau J, Delbos C, Rat V, Coudert J F, Fauchais P, Pateyron B, Plasma Chem. Plasma Process. 26 (2006) 371-391.
- [3] Krowka J, Rat V, Coudert J F, J. Phys. D: Appl. Phys. 46 (2013) 224018.
- [4] Krowka J, Rat V, Coudert J F, J. Phys. D: Appl. Phys. 46 (2013) 505206.
- [5] Wutzke SA, Pfender E, Eckert ERG, AIAA. J. 5 (1967) 707-714.
- [6] Nemchinsky V, IEEE Trans. Plasma Sci. 42 (2014) 4026-4030.
- [7] Laux C O, Radiation and nonequilibrium collisional-radiative models (von Karman Institute Special Course on Physico-chemical Modeling of High Enthalpy and Plasma Flows, Rhode-Saint-Genèse, Belgium 4-7 June 2002).
- [8] Pearse R W B, Gaydon A G, The identification of molecular spectra, John Wiley & Sons Inc., New York 1976.

## Arc Modeling Challenges

Rümppler Ch.<sup>1</sup>, Narayanan V.R.T.<sup>2</sup>

<sup>1</sup>Eaton, 1000 Cherrington Pkwy, Moon Township, PA 15108, USA

<sup>2</sup>Eaton, Bořivojova 2380, 252 63 Roztoky, Czech Republic

ChristianRuempler@Eaton.com

Modeling of arcing phenomena has evolved towards becoming a state-of-the-art tool, supporting the design process of power distribution equipment in low-, medium-, and high-voltage applications. Modeling provides a better understanding of the physical processes within the devices which is needed in order to enhance product performance and mitigate risks in the development cycle. In this contribution, modeling challenges related to some of these applications are discussed: a) the calculation of thermodynamic and transport properties, b) the modeling approach for contact arm motion during arc interruption in low-voltage molded case circuit breakers (MCCB's), c) the model approach for arc flash events in medium-voltage (MV) switchgear.

**Keywords:** arc simulation, plasma transport properties, circuit breaker, switchgear

### 1 INTRODUCTION

Arcing phenomena are crucial in various applications in the power distribution system. Arcs are used either as a switching element, e.g. in circuit breakers with electromechanical contact systems or arcs occur as a fault event, e.g. as arc flash in low-voltage or medium-voltage switchgear. Due to the complex nonlinear processes associated with arcing phenomena, modeling has several useful aspects. A major factor for increased modeling activities in this field is the drive for miniaturization and cost reduction, which leads to increased power density and performance requirements. Here the model driven approach can help to optimize the design towards increased performance. Another aspect is the expensive testing done during development and certification. Having better confidence about the design helps to reduce expensive design-test cycles. In this paper we discuss some of the challenging aspects related to the modeling of arc interruption and arc flash phenomena. Basis for any modeling approach are the necessary input data. In our MHD (magneto-hydrodynamics, [1]) based approach which is introduced in section 2, the thermodynamic and transport properties of the plasma are crucial input data. The calculation method and some results are discussed in the 3<sup>rd</sup> section. Furthermore, two application specific problems will be discussed, the contact arm motion modeling approach for low-voltage molded case circuit breakers (MCCB's) in section 4 and the mod-

eling approach for arc flash in medium-voltage switchgear in section 5.

### 2 SIMULATION APPROACH

A modeling approach has been developed that covers the highly nonlinear physical processes during high-current arcing [2].

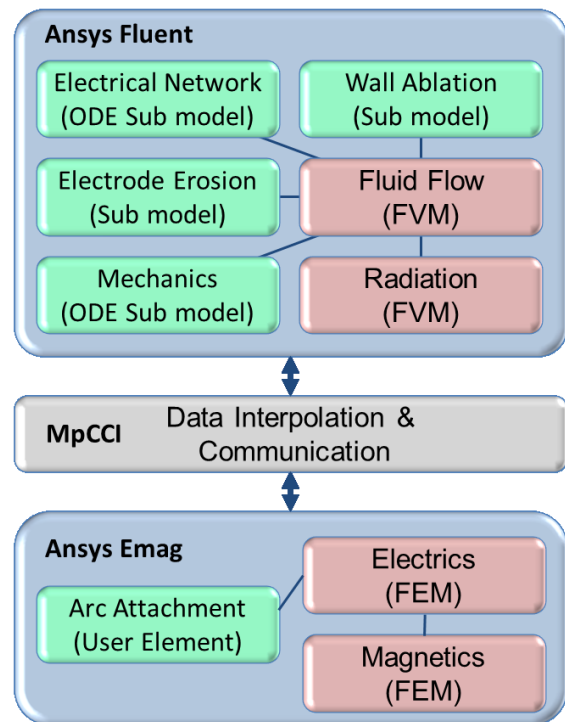


Fig. 1: Simulation system

The set of partial differential equations (PDEs) that describes the fluid flow, electromagnetic field, and radiation transport, respectively, are solved in a code coupling approach which is based on customized commercial solvers.

Splitting the calculation problem into separate tasks for fluid flow and electromagnetics enables a high performance solution. The basic setup of our simulation system is shown in fig. 1.

The mass, momentum, and energy balance equations as well as radiation equations are solved using a finite volume approach (FVM) by means of the ANSYS/Fluent solver [3]. Several sub models have been implemented as enhancements of the fluid flow (CFD) code, using the user programming interface the solver offers:

- An ordinary differential equation (ODE) can be solved in order to describe the interaction with the electric network that is connected to the modeled device.
- A model for the erosion of electrode material is used to calculate the mass of metal vapor that is ejected into the fluid region.
- Another sub model predicts the ablation of plastic materials [4].
- In case of MCCB modeling an ODE can be solved that predicts the rotational or translational motion of the contact arm, driven by magnetic forces.

To describe the electro-magnetic processes, the finite element approach (FEM) is used. Therefore the ANSYS/Emag [3] solver is customized, dividing the solution process into two steps, the solution of the electric and the magnetic equations. For the description of the arc attachment, a user defined element has been implemented that is able to represent the plasma sheath voltage drop [2].

The necessary data exchange and interpolation between the two mesh based codes is provided by the coupling server MpCCI [5].

### 3 PLASMA TRANSPORT PROPERTIES

In order to numerically model the arc dynamics within complex circuit breaker and switch-gear geometries, accurate thermodynamic, transport and radiation properties of relevant gas mixtures are required as input. In this work, we primarily focus on calculating the thermodynamic and transport properties of air-metal vapor mixtures. The results will be provided for air-copper and air-tungsten mixtures, since copper-tungsten (Cu-W) is a commonly

used alloy for metallic electrodes. The LTE-based transport properties are calculated following the works of Devoto [6, 7], in which the Chapman-Enskog formulation [8] for pure gases was extended to consider partially ionized and fully ionized gases. In this formulation, all the transport properties of interest can be obtained as a ratio of determinants of two matrices and the size of the matrices depends on the desired degree of accuracy ( $\zeta$ ) of the properties.

Calculation of collision integrals  $\Omega_{ij}^{(l,s)}$  is an integral part of the Chapman-Enskog method, which requires the solution of equations (1)-(3).

$$\Omega_{ij}^{(l,s)} = \left( \frac{kT_{ij}^*}{2\pi\mu_{ij}} \right) \int_0^\infty e^{-\gamma_{ij}^2} \gamma_{ij}^{2s+3} Q_{ij}^{(l)} d\gamma_{ij} \quad (1)$$

Here the superscripts ( $l,s$ ) are related to coefficients of the Sonine polynomials. The integral collision cross section of  $l^{\text{th}}$  degree, associated with the collisional dynamics between “ $i$ - $j$ ” pair of species and dependent on the relative speed of collision  $g$ , is expressed as

$$Q_{ij}^{(l)}(g) = 2\pi \int_0^\infty \sigma(g, \chi) (1 - \cos^l \chi) \sin \chi d\chi \\ = 2\pi \int_0^\infty (1 - \cos^l \chi) b db, \quad (2)$$

where  $\sigma(g, \chi)$  is the differential collision cross section,  $b$  is the impact parameter, and  $\chi$  is the angle of deflection given as

$$\chi = \pi - 2b \int_{r_{min}}^\infty \frac{dr}{r^2 \sqrt{\left(1 - \frac{b^2}{r^2} - 2\frac{\Phi_{ij}}{\mu_{ij}g^2}\right)}}. \quad (3)$$

The most important parameter in equation (3) representing the collision dynamics is the interaction potential  $\Phi_{ij}$  of the collision, which depends on the interaction partners  $i$  and  $j$ . In this work, while the elastic neutral-neutral and ion-neutral interactions have been characterized by the phenomenological Lennard-Jones potential [9], the shielded-Coulomb potential has been utilized for charge-charge collisions. Additionally, the contribution from inelastic charge-exchange interactions has been included for ion-parent neutral collisions using the approach suggested by Devoto. Finally, electron-impact momentum transfer cross sections

data are obtained from relevant databases for the electron-neutral interactions. The reduced mass  $\mu_{ij}$ , reduced temperature  $T_{ij}^*$  and dimensionless kinetic energy  $\gamma_{ij}$  mentioned in equations (1)-(3) are given by

$$\begin{aligned} \mu_{ij} &= \frac{m_i m_j}{m_i + m_j} \\ T_{ij}^* &= \left[ \frac{1}{m_i + m_j} \left( \frac{m_i}{T_j} + \frac{m_j}{T_i} \right) \right]^{-1} \\ \gamma_{ij} &= \left( \frac{\mu_{ij} g^2}{2kT_{ij}^*} \right)^{\frac{1}{2}}. \end{aligned} \quad (4)$$

In this section, we provide the transport properties results for air-copper and air-tungsten mixtures at atmospheric pressure, for different proportions of copper and tungsten vapors. The results for air-copper mixtures have already been validated in a previous work [10], while published data does not exist for air-tungsten mixtures to the best of the authors' knowledge.

Fig. 2 depicts the variation of the electrical conductivity  $\sigma$  with temperature for different mole fractions of copper and tungsten in air at 1 bar pressure. The following observations can be made:

- i. The addition of Cu or W results in a significant increase in  $\sigma$  at temperatures lower than 15 kK compared to pure air (the red 0% Cu curve).
- ii. Above 15000 K increasing content of copper and tungsten decrease  $\sigma$  compared to air.
- iii. Tungsten content intensifies the behavior in both temperature ranges resulting in lower conductivity than copper for high temperatures and higher  $\sigma$  for temperatures below approximately 15000 K.

The observation (i) is of concern, since the increase in  $\sigma$  at lower temperatures due to metal vapor increases the joule heating effect and thereby can contribute to a thermal breakdown close to current zero in a circuit breaker.

The variation of dynamic viscosity with temperature for different copper and tungsten content is shown in fig. 3. The viscosity peaks for metal vapor mixtures are lower than that for pure air, while those for 50% and 100% Cu

are lower than those for 50% and 100% W respectively.

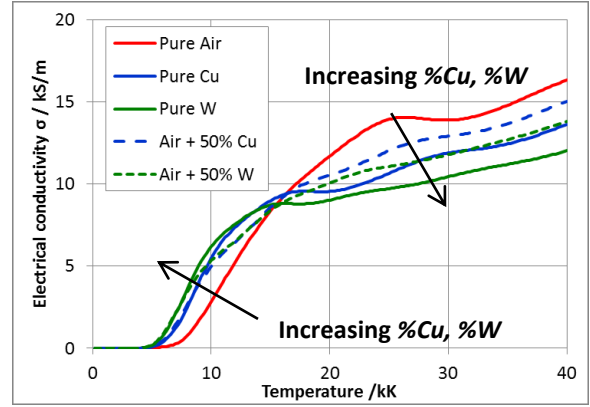


Fig. 2: Plot of electrical conductivity vs. temperature for different mole fractions of either Cu or W in air atmosphere

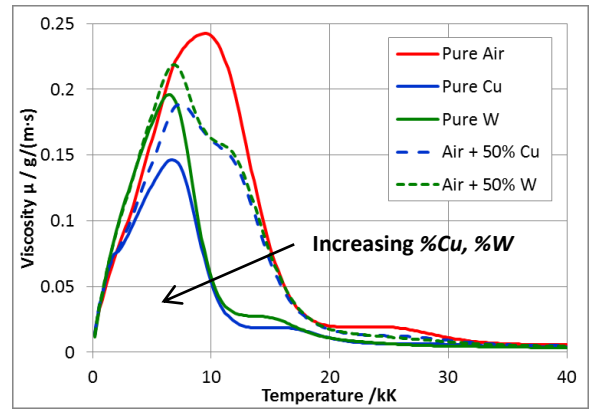


Fig. 3: Plot of viscosity vs. temperature for different mole fractions of Cu and W in air

The viscosity peaks are associated with the onset of ionization and subsequent creation of electrons and ions, thereby increasing the charge-charge cross section and reducing the mean free path. The importance of dynamic viscosity in arc simulations appears through Reynolds number ( $Re$ ), which is the ratio of inertial and viscous forces. For a given geometry, a critical Reynolds number ( $Re_{crit}$ ) can be determined based on simplifying assumptions. If the Reynolds number exceeds the critical limit ( $Re > Re_{crit}$ ), a transition from laminar to turbulent flow occurs. Turbulent flows are well-known to drastically increase heat and mass transfer, and hence can efficiently cool and extinguish the arc.

Finally, the variation of total thermal conductivity with temperature for different copper and tungsten fractions is presented in fig. 4.

The total thermal conductivity is the sum of four different contributions: (i) heavy-species, (ii) electron, (iii) reactive, and (iv) internal thermal conductivities. The contribution from internal thermal conductivity is usually negligible in the entire temperature range, while at temperatures above 20 kK, the contribution from electron thermal conductivity dominates. The three peaks observed for air at 3.5 kK, 7.0 kK and 15 kK correspond to those for diatomic oxygen ( $O_2$ ) dissociation, diatomic nitrogen ( $N_2$ ) dissociation and combined first ionizations of atomic nitrogen (N) and oxygen (O), respectively. Increasing the fraction of metal vapor results in the decrease of all peak magnitudes; with all the peaks vanishing for pure Cu and W. The thermal conductivity of 50% Cu has been observed to be higher than that of 50% W at temperatures above 15 kK, while the thermal conductivity of pure Cu is observed to be higher than that of pure W at temperatures above 20 kK. Physically, thermal conductivity is important since it improves the conduction cooling within a circuit breaker and greater thermal conductivity results in a better gas cooling.

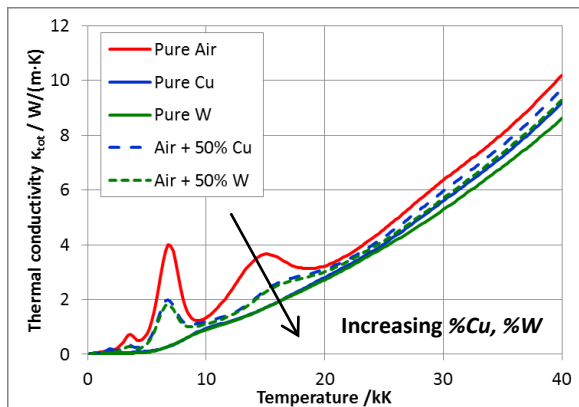


Fig. 4: Plot of thermal conductivity vs. temperature for different mole fractions of Cu and W in air

#### 4 MCCB MOVING CONTACT ARM

For low-voltage molded case circuit breakers (MCCB's), the interruption of high short-circuit currents cause large thermal and mechanical stresses. Due to device miniaturization and increasing demands for higher performance, a prediction of the interruption process is needed to enable design optimization.

One challenge connected to the modeling of MCCB's is the representation of the contact arm motion. In fig. 5 a sketch of a double break contact system of a 630 A rated MCCB is shown, with two different contact arm positions, current path, indication of the arc positions, and two stacks of ferromagnetic splitter plates. In comparison to other contact designs, like in IEC type miniature circuit breakers, the arc burns relatively stable between the fixed and movable contact during contact opening. After a certain contact gap is achieved the arc is pushed by magnetic forces into the stack of splitter plates in order to quench and cool the arc.

For high short-circuit currents the design of these breakers depends on limiting the current to levels well below the prospective short-circuit current in order to reduce the stress on the installation. This is achieved by quickly raising the voltage of the arc above the line voltage through intensive arc cooling and lengthening of the arc by a combination of magnetic forces and fast opening of the movable contact arm. Breakers using this principle are referred to as current-limiting breakers. Because of this current limiting design principle, the contact motion and therefore arc elongation has a large impact on the arc voltage and interruption performance, since a fast arc voltage increase is needed for the limitation of the fault current.

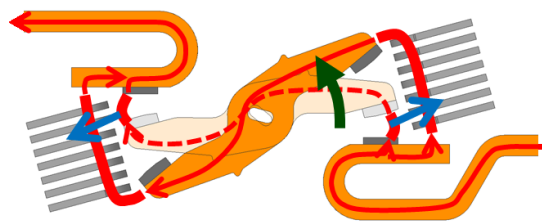


Fig. 5: Arm motion and arc lengthening in a MCCB double-break contact system (sketch)

Therefore the contact arm motion needs to be included in the model; otherwise the whole current limiting process cannot be predicted. For the representation of moving objects in the FEM or CFD model, several different basic opportunities exist, as described in [11]:

- **Mesh deformation:** move contact arm nodes, use mesh morphing algorithm to deform other cells
- **Remeshing:** on the fly agglomeration or splitting of cells based on mesh quality metrics or remeshing of whole domain
- **Layering:** insertion or removal of cell layers
- **Overset grids:** Assembly of several overlapping movable structured grid blocks, interpolation of variables on the boundaries of the blocks
- **Mesh replacement:** Exchange parts or complete mesh with previously prepared mesh, interpolate data from old to new mesh

The selection of the most appropriate method for this application is based on several requirements. First of all the method needs to be easy to use since a complex setup of parameters or procedures is fault prone. Next an emphasis needs to be put on the performance, costly mesh related operations at every time step would limit the overall performance. Furthermore a high mesh quality needs to be assured at any time, since bad mesh quality as result of mesh changes introduces errors and could cause the solution to fail. Finally the method needs to be supported by the applied simulation tools, the CFD solver, FEM solver as well as the coupling tool.

All of these requirements could be met with the mesh replacement approach. Here we create all needed meshes upfront, where each mesh represents a certain contact position. While the simulation is running, meshes are swapped on the fly when needed to represent the motion of the contact. This involves the interpolation of the field values only when meshes are swapped.

Fig. 6 shows the mesh for different contact arm positions and compares morphing with mesh replacement approach. Starting from the mesh that represents the initial contact gap (fig. 6a) several morphing steps while opening the contact arm would lead to a deformed mesh with bad quality metrics. On the other hand, the mesh replacement (fig. 6b) offers high mesh quality any time, depending on the effort spent during mesh generation.

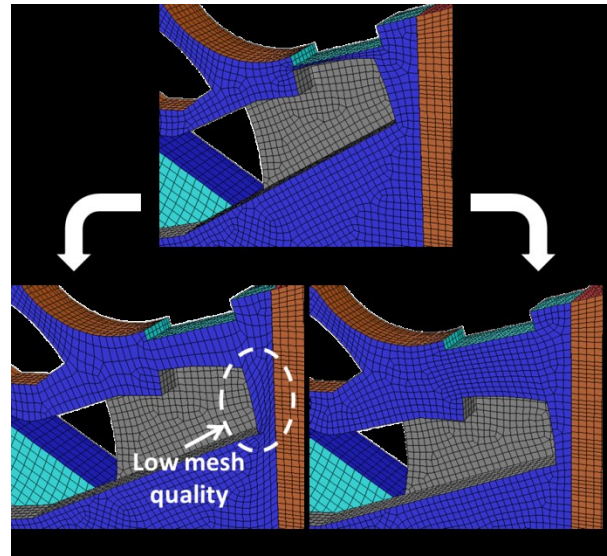


Fig. 6: Mesh at different contact arm position: a) initial contact gap, b) mesh after some morphing steps, c) mesh after several replacement steps

A challenging aspect is the fact that 3 codes have to support this procedure, and the mesh swap needs to be synchronized. When the CFD mesh is changed, the FEM mesh needs to be updated as well; also the neighborhood search that the coupling tool is evaluating to enable the data interpolation needs to be updated. Otherwise invalid data would be transferred between the codes, leading to an invalid solution (or a solver crash). A signal based communication scheme was implemented to handle this appropriately.

Model results highlighting the difference between a stationary mesh model and the mesh replacement approach are shown in fig. 7. For better comparison of measured and calculated voltage, the model result was low-pass filtered since the analog-digital converter used in the test has this characteristic. Therefore one disadvantage of our approach is not visible right away. Due to the small discrete steps that are used to define the contact arm position, the arc voltage also shows a stepwise profile rather than a continuous profile that would be expected by continuous arm motion, as shown in fig. 8. In order to smooth the voltage profile, the arm motion step size could be reduced or additional mesh morphing steps could be introduced.

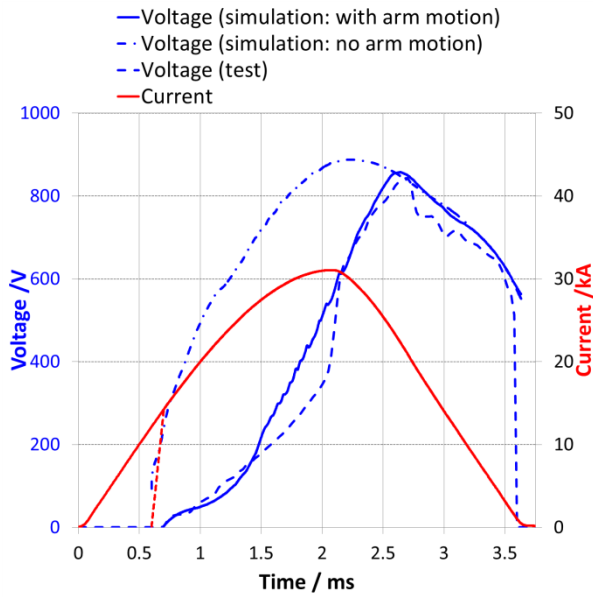


Fig. 7: Comparison of calculated and measured arc voltage, simulation with and without consideration of contact arm motion (440 V, 50 kA, 630 A breaker)

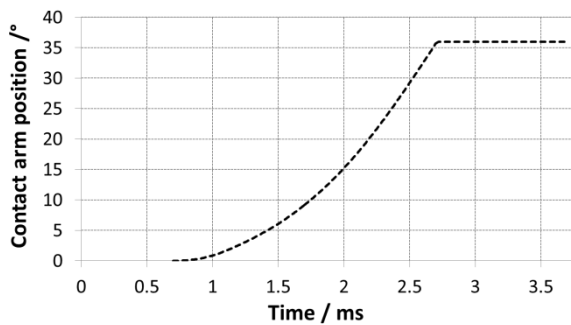


Fig. 8: Contact arm position vs. time curve

In case of no arm motion, the model represents the situation of completely opened contact over the entire duration of simulation. In this case the initial arc is defined as a long conductive channel with a small diameter between fixed and moveable contacts. In this model the current was used as a predefined load rather than as a result of the electric network ODE solver, to allow direct comparison between the two contact arm modelling approaches.

The ignition procedure in case of open contacts is not straightforward, since the long initial arcs lead to a high power input right at the beginning of the simulation, which is started at the time point where Lorentz forces exceed the contact spring forces (pop up current, here about 14 kA at 0.7 ms). In order to get the

model running at all, it is necessary to ramp up the current from zero to the pop up current level in a short time (0.1 ms, see dashed current curve in fig. 7) rather than starting directly at 14 kA. The impact of the open contact position is clearly visible, comparing the voltage trace (simulation: no arm motion) with the measured voltage. Right at the beginning until about 2.5 ms the arc voltage is largely overestimated; therefore the arc energy (46 kJ vs. 24.9 kJ) as well, as shown in fig. 9. The current limiting would be overestimated as well, if this approach would be combined with the electric network ODE model.

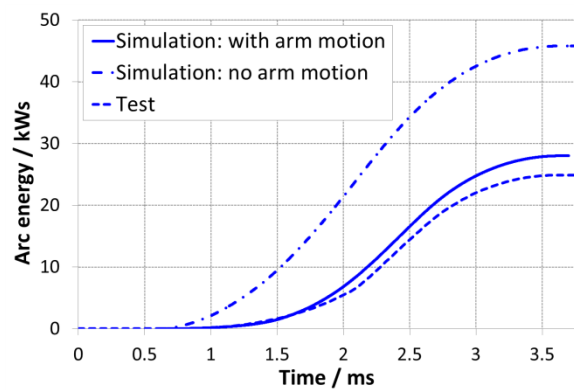


Fig. 9: Arc energy: simulation and test results

The result for the model that includes the contact arm motion is also shown in fig. 7. A much better representation of the arc voltage rise due to arc lengthening and delayed arc splitting in the splitter plates can be seen, in good agreement with the measurement results. With this arc voltage result, the arc energy prediction (28 kJ vs. 24.9 kJ) is much closer to the test results (fig. 9).

A visualization of the model result is given in fig. 10. The arc shape represented by a 12000 K iso-surface is shown for three different time points. In the initial time period (here 0.95 ms) the arc exists in the still small contact gap, which leads to an ejection of a hot plasma jet towards the splitter plates. This hot gas stream heats up the splitter plates, enhancing arc attachment and splitting later on when the arc is moving towards the plates. With increasing contact gap, the arc moves out of the contact gap towards the plates and is finally split into several arcs in the stack of plates, leading to a rapid increase of the arc voltage.

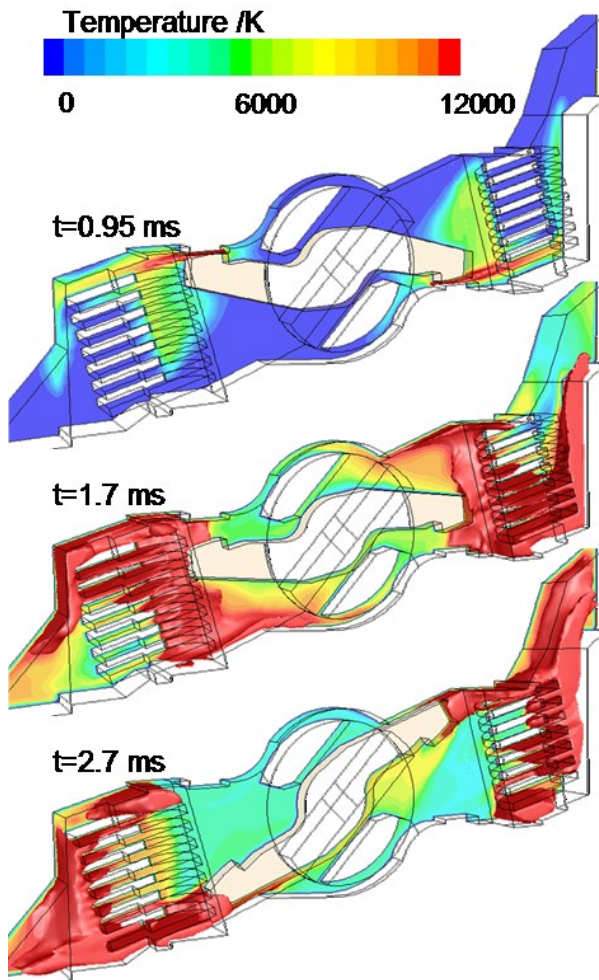


Fig. 10: Model result: temperature inside the MCCB chamber visualized by means of a 12000 K iso-surface (440 V, 50 kA, 630 A breaker)

## 5 MV SWITCHGEAR ARC FLASH

As a third example illustrating modeling challenges, an arc modeling approach for the prediction of arc flash events in medium-voltage (MV) arc flash resistant switchgear is discussed. A typical design of a MV switchgear section is shown in fig. 11.

IEC type arc resistant switchgear is tested according to IEC 62271-200 Annex A, where the switchgear has to withstand up to 1s of internal arcing, causing high mechanical and thermal stresses.

Because these tests are very expensive, various modeling approaches have been developed in the past [12] in order to predict the mechanical loads (pressure rise) due to the arc flash to reduce the number of tests. With a

simplified model that is based on the assumption of uniform distribution of temperature and pressure, prediction of the peak pressure is possible [13]. But in order to perform this calculation, values for the arc energy are needed as input, which are not available without initial testing so far.

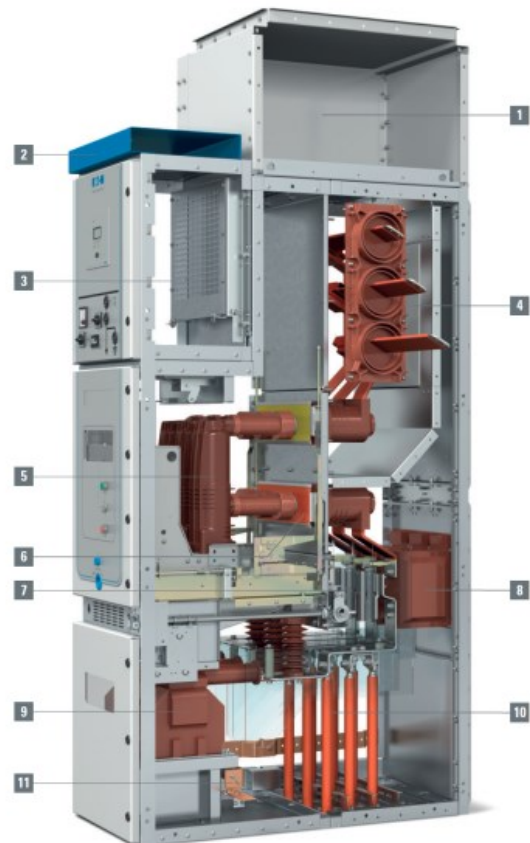


Fig. 11: Eaton MV switchgear: bus bar compartment (4), circuit breaker compartment (5), and cable compartment (10)

In case of a new design, the application of the 3D arc model is attractive, since arc energy as well as pressure rise can be predicted directly. Additionally, when solving beyond the initial arcing period of about 60 ms, thermal loads that could lead to a burn through e.g. of the side panels could also be predicted. But in comparison to a LV circuit breaker, the volume that has to be modeled is significantly larger (e.g. 100x) and the arcing time is much longer (e.g. 1000 ms vs. 10 ms). This leads to high computational cost with calculation time being a major challenge.



Fig. 12: Simplified test setup for arc flash experiments

To investigate the applicability, a simplified switchgear model as described in [14] has been used. The setup as shown in fig. 12 contains a compartment with two sections (1200 mm × 600 mm × 500 mm) with a venting chimney at the top (152 mm × 152 mm). Three electrodes are mounted in the lower section side by side with a gap of 85 mm between each other. In front of the electrodes a metal sheet is mounted where the arc can attach. The model results given in the following text are compared with test results obtained with an 18 kA asymmetrical short circuit current at 24 kV, as can be seen from fig. 13.

A 3D model has been created and calculation was performed for 60 ms of arcing time. In the experiment the arc was ignited with a copper wire across the three electrodes. In the model a conductive channel with 5 mm radius was defined as initial condition.

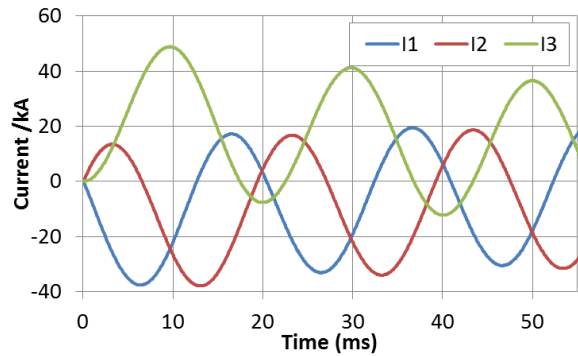


Fig. 13: Three-phase short circuit current

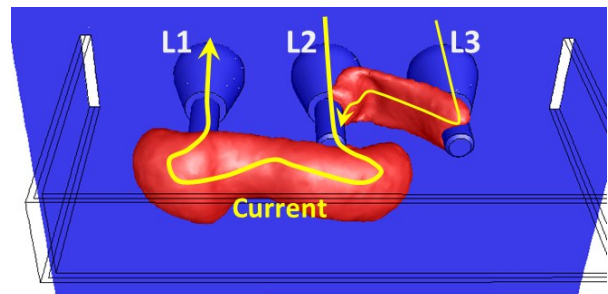


Fig. 14: Arc shape at  $t=2$  ms (1000 K iso surface)

After ignition the arc is moved due to Lorentz forces, as seen in fig. 14. At 2 ms the arc between L1 and L2 bends away from electrodes and the arc between L2 and L3 bends towards the electrodes due to the current loops formed. Further on the arc elongates and attaches to the metal sheet in front of the electrodes, which causes the arc voltage to fluctuate due to the shortening of the arc length. The comparison of the phase-to-phase voltage from simulation and experiment is shown in fig. 15. Considering the complexity of the model, the achievable voltage prediction is sufficient, although the frequency of fluctuations in the simulation result exceeds the measurement results. But more important is the prediction capability with respect to the power and especially of the arc energy, since these values can be used for further investigation using reduced models (CFD or simplified model [12]). These values are given as model and test results in fig. 16. The overall level of arc power is sufficiently predicted and therefore the arc energy as well.

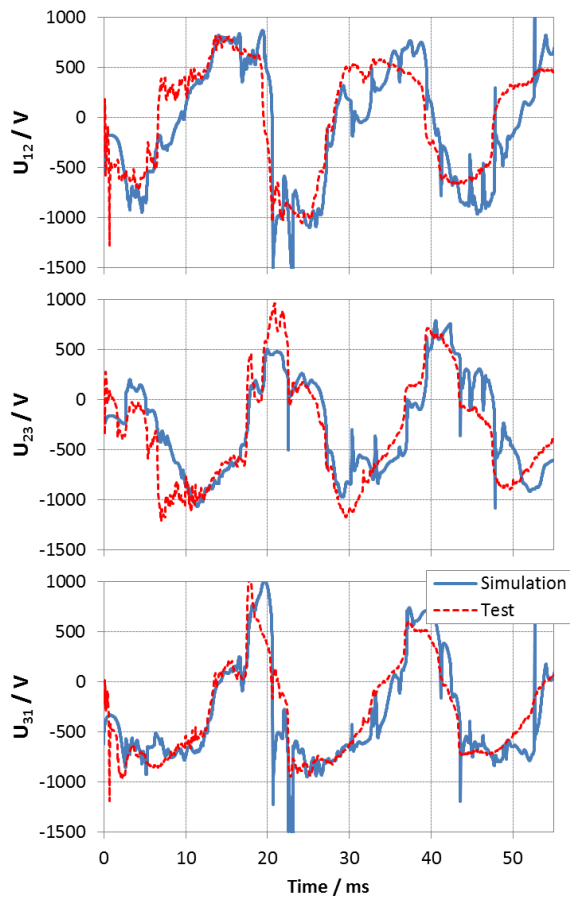


Fig. 15: Phase-to-phase arc voltage, simulation and test results

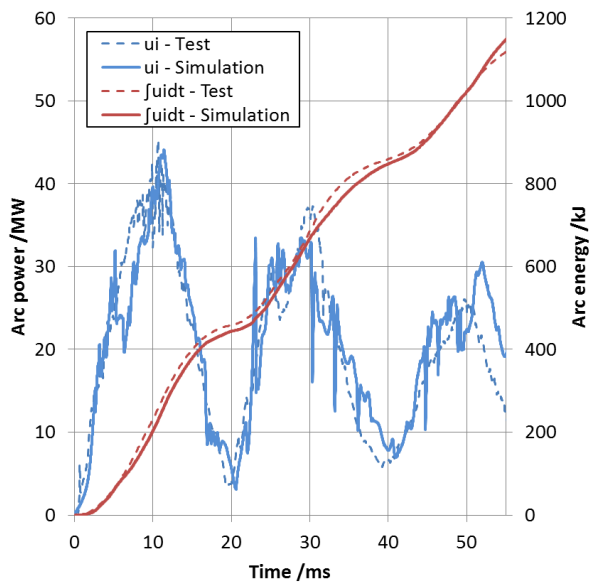


Fig. 16: Arc power and arc energy, comparison of simulation and test results

## 6 CONCLUSION

Numerical methods are used to predict the arc interruption in low-voltage circuit breakers

and the fault arc in medium-voltage switch-gear, where a number of challenges were addressed. Any simulation model needs input parameters which determine the result quality. In case of 3D MHD arc modeling the thermodynamic and transport properties of the plasma, composed of air and metal vapor in our case, are needed. A state of the art calculation approach has been discussed and results for copper and tungsten are presented.

The application of the model is presented for short-circuit interruption of low-voltage circuit breaker (MCCB) and medium voltage switch-gear arc flash. In case of MCCBs, the contact motion needs to be modeled and the chosen mesh replacement method provides the best result quality with high-quality meshes prepared upfront. This avoids a solution dependency of the mesh related procedures which could lead to problems in a long running calculation. The arc flash modeling approach has been presented by means of a simplified compartment, showing the prediction opportunities for arc energy and arc power.

## Acknowledgements

The authors wish to thank Mr. Albert Zacharias for performing calculations and Mr. Wilbert de Vries, Karl-Heinz Mayer and Brian E. Carlson for their continuous support of this effort.

## REFERENCES

- [1] Gleizes A, Freton P, Gonzalez J J, Journal of Physics D: Applied Physics 38 (2005) R153-R183.
- [2] Rümppler Ch, Lichtbogensimulation für Niederspannungsschaltgeräte, Dissertation, Techn. Univ. Ilmenau, Fraunhofer Verlag, 2009.
- [3] ANSYS, Inc., ANSYS, Release 15, Help system, Canonsburg, PA, USA, 2014.
- [4] Rümppler Ch, Stammberg H, Zacharias A, Low-Voltage Arc simulation with Out-Gassing Polymers, In: 57<sup>th</sup> IEEE Holm Conference on Electrical Contacts, Minneapolis, MN, 2011.
- [5] Fraunhofer Institute SCAI, MpCCI 4.4 Documentation, Sankt Augustin, 2015.
- [6] Devoto R S, Physics of Fluids 9 (1966) 1230-1240.
- [7] Devoto R S, Physics of Fluids 10 (1967) 2105-2211.
- [8] Chapman S, Cowling T G, The Mathematical Theory of Non-uniform Gases, Cambridge University Press, 1970.
- [9] Pirani F, Alberti M, Castro A, Moix Teixidor M, Cappelletti D, Chemical Physics Letters 394

(2004) 37-44.

[10] Narayanan V R T, Numerical modeling of post current-zero dielectric breakdown in a low voltage circuit breaker, PhD dissertation, University of Minnesota, 2014.

[11] Rümpler Ch, Zacharias A, Stammberger H, Low-voltage circuit breaker arc simulation including contact arm motion, In: 27<sup>th</sup> International Conference on Electrical Contacts, Dresden, Germany, 2014.

[12] CIGRE, Tools for the simulation of effects of

the internal arc in transmission and distribution, CIGRE WG A3.24, January 26, 2014.

[13] Uzelac N, Dullni E, Kriegel M, Pater R, Application of simplified model for the calculation of the pressure rise in MV switchgear due to internal arc fault, In: 22<sup>nd</sup> International Conference on Electricity Distribution (CIRED 2013), Stockholm, 2013.

[14] IEEE Power & Energy Society Switchgear Committee, C37.20.7 Working Group Report, IEEE, October 11, 2011.

# Future Perspectives on High Voltage Circuit Breaker Research

Seeger M.<sup>1</sup>

<sup>1</sup>ABB Switzerland Ltd, Corporate Research, Segelhofstrasse 1, CH-5405 Baden-Dättwil, Switzerland  
Email: [martin.seeger@ch.abb.com](mailto:martin.seeger@ch.abb.com)

The research on high voltage circuit breakers using SF<sub>6</sub> is addressed. An overview of current state of research in this field will be given and possible future research directions will be discussed on examples. Such directions are, for example, the radiative energy transport, the understanding and description of ablation processes at the nozzle and contact surfaces, the influence of ablated vapors on pressure build up and interruption capability, the electric breakdown processes, departures from equilibrium, turbulence and the importance of magnetic fields and 3D modelling.

**Keywords:** arc, circuit breaker, high voltage, SF<sub>6</sub>

## 1 INTRODUCTION

Circuit breakers are important devices in electrical networks which ensure safe power flow [1],[2]. They have to interrupt normal load and short circuit currents in the range of several kA and several 10...100 kA, respectively. They also have to be able to connect parts of the network, i.e. close on normal and short circuit currents. After current interruption, the network voltage has to be safely withstood. These voltages range from a few 100 V to several 100 kV. In distribution networks at low voltages (<1000 V) mostly air circuit breakers are used. In distribution networks at medium voltage level (<72 kV) gas circuit breakers (SF<sub>6</sub>) and increasingly vacuum circuit breakers are used. In high voltage sub-transmission (<145 kV) and transmission levels (> 145 kV) mainly gas circuit breakers (GCB) using SF<sub>6</sub> are used [1]. All these devices employ an electric arc for interruption of the current at current zero (CZ). In the present contribution the focus will be on HV gas circuit breakers, using SF<sub>6</sub>. Many important aspects of the technological challenges are, however, also applicable to other types of circuit breakers and alternative gases to SF<sub>6</sub>. An overview of research directions in the field of HV circuit breakers was given recently [3]. The present contribution summarizes the main directions and gives examples. Section 2 gives a technology overview, section 3 gives an overview of the different topics of interest, questions, and barriers to future success.

## 2 TECHNOLOGY OVERVIEW

Examples of modern SF<sub>6</sub> high voltage gas

circuit breakers are shown in figure 1. Depending on the application these devices are either encapsulated in grounded metal housings (Gas insulated switchgear) or have insulating housings, so-called live tank circuit breakers. For the highest current ratings, which are needed close to generators with nominal voltages in the range of a few 10...30 kV, generator circuit breakers are used [4].

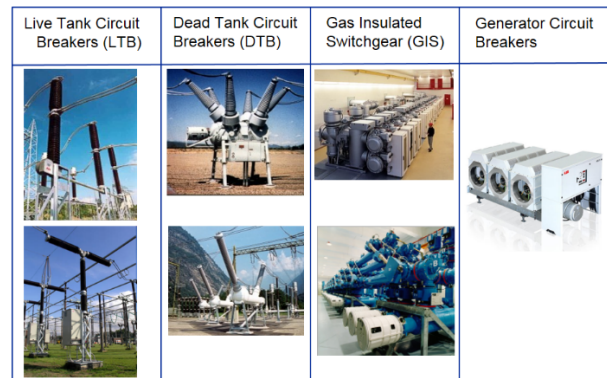


Fig. 1: Example of HV circuit breakers

Beside the differences in external insulation, these devices have common design features, which are shown in figure 2 using the example of a so-called self-blast or auto-expansion CB [1],[5]. The SF<sub>6</sub> fill pressure of such devices is typically in the range of 0.43...0.7 MPa (absolute). In the “closed” contact position, the current flows in the nominal contact system. During an opening operation this current commutes to the arcing contacts. Following the separation of the arcing contacts, an arc is ignited between plug and tulip contacts, surrounded by the nozzles. This is referred to as the arc zone. Usually polytetrafluoroethylene (PTFE) with some

fillers is used for the nozzle material. The arc elongates in length with time due to the contact movement and needs to be extinguished at a CZ crossing of the applied current. This is achieved by a gas flow which cools the arc by convection and turbulence [5]. At low applied currents, e.g. normal load currents, this gas flow is produced by a pressure rise in the compression volume (CV), see figure 2.

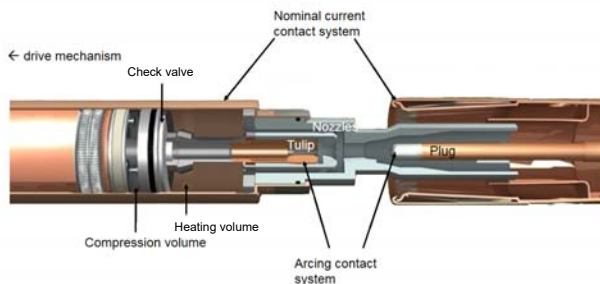


Fig. 2: Arc zone of a typical HV self-blast CB in open contact position

During the opening operation, this volume is shrinking in size, creating an over-pressure. Via a check valve, this pressure is applied to the heating volume, producing a gas flow towards the arc zone. At sufficiently high currents the pressure in the arc zone can be higher than in the heating volume. In this case, ablated polymer vapor can flow to the heating volume, which is referred to as back-heating. A typical example of pressure rise in the heating volume, current and arc voltage during the interruption process is shown in figure 3. In the case of self-blast CBs, the check valve separates the CV from the heating volume during back-heating, which decouples the pressure forces in the heating volume from the drive mechanism. This allows to use drive mechanisms with lower energy requirements. In so-called puffer circuit breakers there is no such separation, i.e. only a compression volume exists, which is then equal to the heating volume [1]. Besides the flow into the heating volume, the arc energy flows into the sufficiently large dimensioned exhaust volumes (not shown in figure 2). When the current reduces during the back-heating process towards CZ, conditions for the reversal of the flow can occur, i.e. gas from the heating volume can flow towards the arc zone, leading to a reduction of the pressure in the heating

volume, see figure 3. This leads to a transition from an ablation controlled arc to a convectively stabilized arc, which is accompanied with a transient change of the pressure and temperature distribution in the arc zone and its surroundings. This phase is referred to as the flow reversal phase.

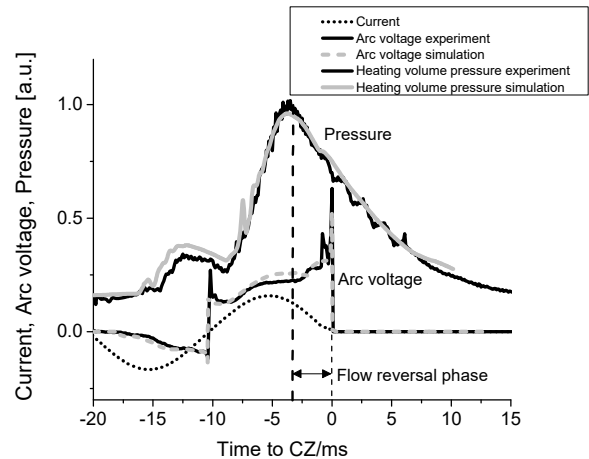


Fig. 3: Typical example of measured and simulated waveforms of current, pressure build up in the heating volume and arc voltage of a self-blast CB (by courtesy of Mahesh Dhotre, ABB Switzerland Ltd). For details of the simulations see [4]

Within the first microseconds after current zero, the current interruption is determined by the competing processes of arc conductance decay and the rise of the applied voltage, which drives a current (“post arc current”) through the still conductive (temperatures around 5000...12000 K) plasma channel [1],[5],[6]. This is referred to as the thermal interruption phase. Once the conductance of the plasma channel drops to a level where no significant heating due to the post arc current can occur, the voltage rise of the network in form of the transient recovery voltage (TRV) has to be withstood. This rise occurs within several ten to several hundred microseconds. Due to the elevated temperature (several thousand Kelvin) of the plasma channel after CZ there is only a limited voltage withstand during this phase. This is referred to as the “dielectric recovery” phase. If the voltage withstand is not sufficiently high, a dielectric failure occurs. This can happen in the former arc channel during the early dielectric recovery within less than 100  $\mu$ s after CZ, typically. During the later

dielectric recovery, it is completely independent of the previous arc channel [7]. For the interruption process the control of the arc conductance decay around CZ is a crucial mechanism for thermal interruption and early dielectric recovery as well. This decay is mainly linked to the pressure in the arc zone at CZ, the convective cooling due to strong pressure gradients and the development of turbulence at the arc boundaries [5]. It can be influenced by the presence of metal vapor. During the dielectric recovery, the control of the electric field, the pressure, the temperature and the gas composition (SF<sub>6</sub>, polymer vapors, metal vapors) in the arc zone is decisive for successful interruption. This needs careful design of the capacitive electric field, the gas flow field in the breaker and control of polymeric and contact material ablation (e.g. [8],[9],[10],[11],[12]).

### 3 IMPORTANT TOPICS IN HV CIRCUIT BREAKER RESEARCH

In the last two decades, progress has been made towards covering higher short circuit current and voltage ratings accompanied by a reduction of size and drive energy. In the circuit breaker development process this needs a sufficiently precise prediction of pressure, temperature, contact and nozzle ablation and their distributions in the CB by simulations based on computational fluid dynamics (CFD). Such simulations for gas CB use compressible gas dynamic equations (e.g. Navier Stokes equations) in a single fluid approximation, where the thermodynamic and transport properties depend on pressure, temperature and composition (e.g. [4]). In this description, local thermodynamic equilibrium (LTE) is usually assumed. In most cases, these simulations are done for axis-symmetric geometries, i.e. in 2D approximation. There are a number of phenomena which are still modelled in a simplified way, for example radiative energy transport (RET), turbulence, electrode and nozzle ablation and departures from the equilibrium. Thus, modelling and validations are important issues in the research of HV circuit breakers. In the following, the main research topics will be shortly discussed on examples.

#### 3.1 RADIATION

Radiation is the most relevant arc cooling mechanism in the high current phase. It leads to ablation, which in turn influences the pressure build up. Around CZ it determines the arc temperature profile, which determines the arc conductance and temperature decay. Significant progress has been obtained in the field of radiative energy transport modelling by use of discrete ordinate method (DOM), the P1 method, and net emission coefficients (NEC) models with suitable band averaging methods (e.g. see [13], [14], [15], [16], [17], [18]). Pressure build up in the heating volume and also in the exhaust volumes can in this way quite reliably be calculated (see e.g. figure 3). Metal and polymer vapors are often taken into account correctly in the thermodynamic and transport properties used for simulation. However, for the radiation properties this is still in an early phase [16] and often only SF<sub>6</sub> radiation data is used for the simulations. The good progress which has been achieved with the DOM in simulations of high voltage CB is accompanied with higher numerical effort since the RET has to be solved for the several directions and the various bands. Much less numerical effort is needed for the P1 model, which approximates the radiation by first-order spherical harmonics. This approximation is suited for optically thick media with large absorption coefficients. In circuit breakers this method alone is not sufficiently accurate. As it has been shown recently it may be used in combination with the DOM to reduce computation time [15]. Net emission coefficient models (NEC) are based on emission only and are of low computational effort. They were used frequently in the past and need to introduce absorption in an empirical way, which generally reduces the accuracy for circuit breaker applications, especially when describing regions far from the arc, e.g. the exhaust or the cooling of the plasma in the heating channel and volume. Thus, the most advanced treatment of radiative energy transport to date is the use of DOM, or a combination of DOM with the P1 approximation. Since these approaches are still consuming a large amount of the computational

time, new, more computationally efficient approaches should be investigated, e.g. as discussed in [17], taking into account higher moments than the P1 model. Such efficient numerical approaches are of high importance, especially when taking into account the need for 3D type simulations. There are still large discrepancies in the radiation spectra used by different groups, which need further clarification. The spectra in the low temperature regions in the arc boundaries, e.g. where molecules are present, need special attention, since it will determine the arc temperature profile in the arc mantle and in the surrounding gas. This will be influenced by admixtures of metal and polymer vapors, e.g. copper and  $C_2F_4$ . The radiation modelling in the field should be, therefore supported by experimental validations under the conditions relevant for circuit breakers, e.g. at high pressures and the relevant temperatures and compositions, as e.g. shown in [19]. In this paper, copper dominated free burning arcs were investigated, which are relevant for low voltage CB. It was found that standard temperature determination methods based on the assumption of thin or thick plasma were limited and simulations of the spectra could give further insight.

### 3.2 CONTACT EROSION AND NOZZLE ABLATION

Polymer ablation (mostly PTFE in  $SF_6$  HV CB) from the nozzle wall is important for the pressure build up due to nozzle clogging or backheating during the high current phase. The influence of the polymer ablation on the transition from the high current phase towards CZ, i.e. the flow reversal phase, is still less well understood than the back-heating phase. The polymer ablation may change in this regime due to absorption of radiation in cold  $SF_6$  [11]. Significant wear of nozzles, as shown in figure 4 might lead to changes in the interruption behavior. The prediction of the shape change of nozzles is, therefore, of high interest for the development and life time predictions. The distribution of polymeric vapor may affect the dielectric withstand after CZ.

Metal vapor affects the radiation and the

electrical conductivity of the arc, which may lower the interruption performance at and after CZ if present in sufficient quantity. Simulations usually contain source terms for polymer ablation (e.g. [4]). The contact erosion can be predicted by relatively simple models, e.g. [10], similarly to the polymer ablation.



Fig. 4: PTFE nozzle after arcing

An important mechanism for the understanding and description of distribution of metal vapor is the formation of droplets and their evaporation, see figure 5 for an example. This image was obtained in a simplified laboratory arrangement, where the arc plasma was extracted from the arc zone through a nozzle hole and injected into a free space. A large number of particles of different size and vapors can be seen. This may be a situation similar to what happens during back-heating in a self-blast circuit breaker. The effect of such particles/vapors on the interruption performance has to be taken into account. Droplet formation and evaporation in the arcing zone under HV CB conditions were studied theoretically by [20]. More investigations of this type in combination with measurements are needed for the various conditions in HV CBs. To validate simulations, experiments should be done where the distribution of metal vapor is determined along with the pressure and temperature fields. For copper-tungsten contacts the ratio between copper and tungsten vapor in the plasma is still not clear, and also needs experimental clarification, e.g. by spectroscopic investigations. Several groups investigated by simulations how copper vapor affects the radiation coefficients and electrical

conductivity. However, for the thermal interruption only little information on the quantitative influence of metal vapor is published, e.g. [21]. For the dielectric recovery there is no experimental data available in SF<sub>6</sub> HV CB describing the relation between metal vapor and dielectric withstand. Quantitative data on such relations are needed, therefore. This could be done by combining theoretical assessment (e.g. [22]) and experimental investigations.

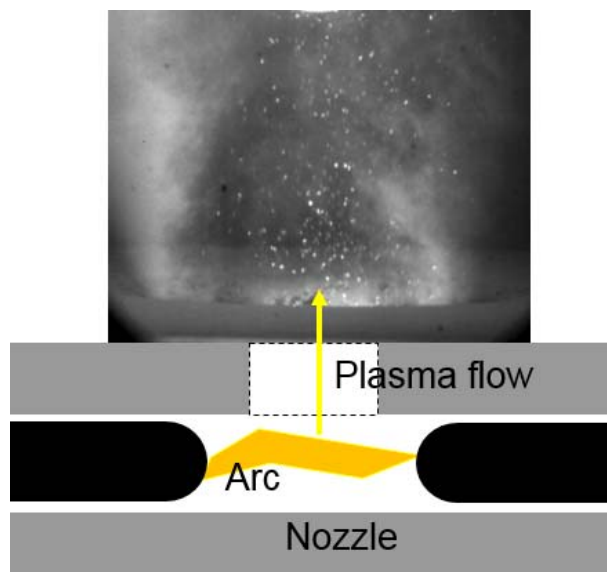


Fig. 5: Example of hot gas cloud produced by a 5 kA arc between Cu/W contacts in a PTFE nozzle. The hot plasma was exhausted upwards through a hole in the nozzle (15 mm in diameter). The set-up was placed in a GIS tank filled with SF<sub>6</sub> at 2bar

### 3.3 TURBULENCE

Turbulence in arcs is generally still not well understood. In simulations of HV CB it is usually treated by Reynolds averaged Navier Stokes methods (RANS) using the k- $\epsilon$  model with various formulations [4],[12],[15] or by the Prandtl mixing length (PMLM) model, e.g. [23],[24]. Different approaches are used and some groups introduce fit parameters to the Prandtl mixing length model tuned to experimental data, as e.g. for reproducing the arc conductance [24]. All these models do not describe satisfactorily the CZ phase and the interruption phase. Turbulence at the CZ arc is produced by the shear flow at the arc boundaries due to the strongly differing

velocities inside and outside the arc. This produces vorticity, which is transferred into the arc by turbulent eddies and efficiently cools the arc. Due to the 3D nature of this process (see figure 6 for an example) 3D large eddy simulation (LES) models might be better suited for simulation. However, the large computational effort makes using such a turbulence model currently still impractical in standard CB simulations. Simpler, more practical but sufficiently precise models have to be identified.

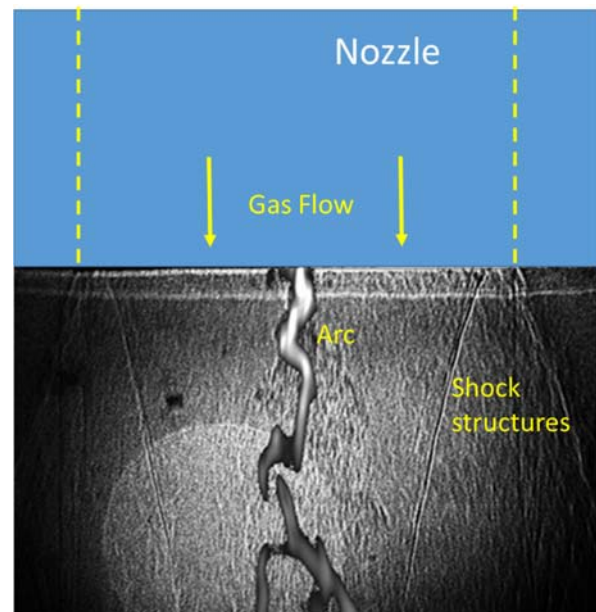


Fig. 6: Superposition of shadowgraph and light emission images of a turbulent 10A (DC) arc in an imposed flow at the exit of a PTFE nozzle (top of the figure). The inner diameter of the flow channel in the nozzle was 17 mm. The stagnation pressure was about 10 bar. The exposure time of the image was 2  $\mu$ s. The flow direction was from top to bottom, indicated by the arrows. Shock structures of the flow can be seen in the shadowgraph image. The image of the light emission (gray scale) shows the 3D structure of the arc outside the nozzle (by courtesy of Emmanouil Panousis, ABB Switzerland Ltd)

The turbulence for low current arcs at CZ cannot be separated from the non-LTE issues which be discussed below, i.e. for the simpler models this has to be taken into account. For validation precise reference experiments are needed, where not only arc voltage and current

is measured precisely close to CZ, but where also the arc temperature and conductivity distribution is addressed.

### 3.4 DEPARTURES FROM EQUILIBRIUM

The validity of the assumption of LTE is discussed widely in the field since decades. It is generally agreed that in the high current plasma this assumption is reasonable and only in the arc fringes some deviations might occur, e.g. [25]. For CB simulations these deviations have only little effect, such that inclusion of non-LTE effects in the high current phase are not of relevance for typical CB simulations. Non-equilibrium effects are probably most relevant for the CZ phase and early dielectric recovery. In [26] the influences of chemical non equilibrium on the arc decay were investigated, showing a significant difference in the species concentrations and higher cooling rate compared to the LTE assumption. The investigation of [25] used a two temperature model for electron and heavy particles. They observed significant deviation from thermal equilibrium when approaching CZ. As a result they showed that the arc conductance was higher in the case of non-thermal equilibrium. The arc conductance decay after CZ was experimentally investigated by [27] showing the large influence of delayed ion recombination on the conductivity decay. These examples show that the inclusion of chemical and thermal non-equilibrium is probably crucial to describe the arc conductance decay around and after CZ. This is probably even more complicated by the fact that the chemical and thermal non-equilibrium is coupled to the radiation and the turbulence, i.e. generally these processes cannot be treated separately. Suited simplifications are needed, therefore. This will need significant effort on simulations and experiments in the future. For validation of models sufficiently precise reference experiments in CB relevant geometries are needed, e.g. in two pressure devices, where stable flow conditions are applied from an external tank. In these experiments, not only the total arc conductance but also the distribution of arc conductance could be determined. This may be done either

directly by electrical methods (e.g. capacitive coupled probes as shown in [28] and resistively coupled probes [29]) or by optical methods [30], e.g. see figure 7.

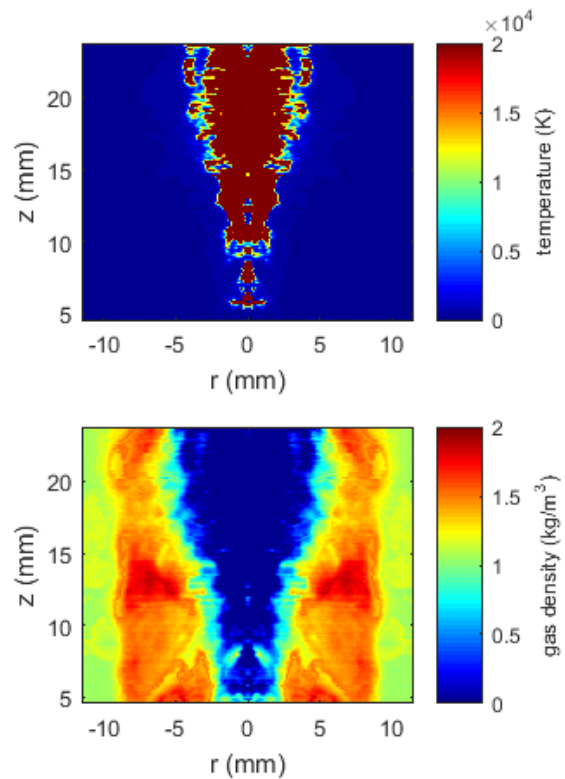


Fig. 7: Measurement of the gas density and temperature of an arc close to CZ. The arcing medium is air at ambient pressure and the arc is axial blown with an overpressure of 2.3 bar. The field of view is behind the stagnation point (in flow direction), where the nozzle system permits optical access to the arcing region and the flow is released into free space; for details of the method see [30]

### 3.5 ELECTRIC BREAKDOWN

For the electric breakdown at CZ, i.e. the thermal interruption phase, the arc energy balance around CZ is decisive. Reliable predictions for this phase are needed to reduce the expensive high power laboratory tests during development. This needs a correct description of the arc conductance taking into account turbulence and departures from equilibrium and composition, as discussed above. For predictions of the thermal interruption the arc conductance has to be coupled to network programs. In this way the arc-circuit interaction, i.e. the current and voltage deformation before and after CZ, respectively, can be calculated and the

development of the arc conductance after CZ can be predicted. Such simulations still show significant deviations from the measurements and the full interruption process cannot be predicted with sufficient accuracy at the moment. Consequently, it is still not possible to replace expensive testing in high power laboratories by simulations of the full process. The dielectric recovery phase that occurs after current zero has been addressed in some publications in the recent years. Streamer and leader models can serve to describe the electric breakdown during the dielectric recovery in a CB, e.g. see figure 8.

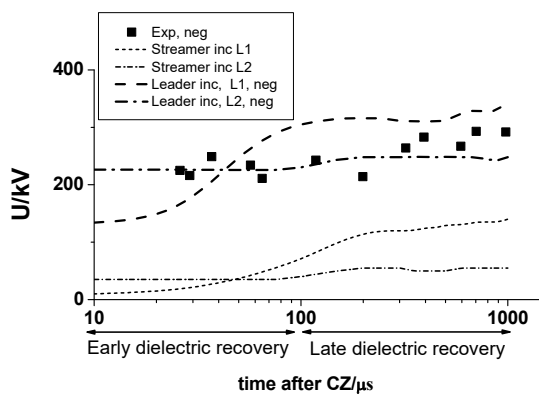


Fig. 8: Measured and simulated dielectric recovery (DR) in SF<sub>6</sub> after interruption of 23 kA<sub>peak</sub>, for details see [7]

The distribution of hot gases in the downstream regions of the flow, e.g. in the exhausts can be calculated and breakdown predictions agree relatively well with the measurements [31],[32]. Crucial is the knowledge of the temperature and pressure dependence of the critical electric field, which was calculated by several groups for SF<sub>6</sub> (e.g. [31]), but also taking into account the effect of PTFE admixtures [33],[34] and also Cu vapor [22]. Experimental validations of these calculations under the conditions found during the dielectric recovery, with gas temperatures typically below 4000 K, are challenging and only slowly progressing. Due to the complex conditions in HV CB (large spatial and temporal variations of pressure, temperatures and compositions) validations of models under the real conditions in circuit breakers are difficult and show large uncertainties. The dielectric breakdown under the conditions of high ion concentrations, i.e.

space charges, elevated temperatures in combination with spatially largely varying particle number densities is not sufficiently understood and needs further experimental and theoretical investigations.

### 3.6 SF<sub>6</sub> ALTERNATIVES

As is well known SF<sub>6</sub> is a unique medium for arc quenching in HV CB [1]. These unique properties are the stability of the molecule, i.e. it recombines after decomposition in an arc; it is not toxic; it has a high heat capacity in the temperature range of interest for interruption (below 5000 K where electrical conductivity is low) and has a quite high critical electric field, resulting in a high dielectric withstand. Due to some of these unique properties it has, however, a large global warming potential of about 23900 (based on 100 year time horizon) [35] and is, therefore, under discussion for regulation of use. Suitable alternatives are investigated since more than a decade but no comparable alternative, i.e. an alternative which combines similar properties as SF<sub>6</sub>, has been found. In some studies CO<sub>2</sub>, e.g. [36] or CO<sub>2</sub> with some admixtures (e.g. [37]) is identified as a promising alternative. It must be noted, however, that its performance is inferior to SF<sub>6</sub>. With improved understanding the CO<sub>2</sub> technology might be further optimized and the performance gap between SF<sub>6</sub> and CO<sub>2</sub> might become smaller. More research is needed for this and all the above discussed topics apply also for CB using CO<sub>2</sub>. Recently wider research activities have been started, scanning the best gases for suitable properties, allowing mixtures of gases, e.g. [38]. All these investigations not only aim at finding a replacement gas for arc quenching, but also for pure insulation applications, e.g. in gas insulated switchgear and substations. Such investigations are important and should be continued. It has to be taken into account that complex mixtures of gases will in most cases not recombine to the original composition but produce other substances with possibly unwanted properties regarding toxicity, GWP and interruption/insulation performance for example. The properties of complex mixtures for use in HV CB may, therefore, change

significantly over the lifetime. This needs further investigations.

## 5 CONCLUSIONS

The present contribution describes important issues in HV CB research. Progress has been achieved in the description of radiative energy transport, which enables a reasonable prediction of pressure build up by using CFD simulations. Still work is needed for more precise radiation spectra including the presence of admixtures from contacts and nozzle material. The admixtures of such polymer and metal vapors regarding distribution, composition and its influence on radiation and interruption capability need further research. For predictions of the interruption performance a better understanding of the phenomena around current zero and the post current zero phase is needed. This needs research on thermal and chemical non-equilibrium and arc induced turbulence, taking into account the coupling of these processes. For the dielectric recovery sufficiently precise breakdown models and validations are needed. Due to the 3D nature of many processes 3D modelling will be increasingly used in the future. The work for identification of alternatives to SF<sub>6</sub> is ongoing and needs to be continued with sufficient effort.

### Acknowledgement

The author would like to thank M. Bujotzek, J. Carstensen, T. Christen, C. Doiron, A. Iordanidis, E. Panousis, M. Schwinne, V. Teppati and T. Votteler from ABB Switzerland Ltd, Corporate Research, for valuable discussions and inputs.

### REFERENCES

- [1] Ryan H M, Jones G R, SF<sub>6</sub> switchgear, Peter Pelegrinus Ltd, London, UK, 1989.
- [2] IEC 62271-100, High-voltage switchgear and controlgear –Part 100: Alternating-current circuit-breakers, Ed. 2.0 2008-04.
- [3] Seeger M, Plasma Chem Plasma Process 35 (2015) 527-541.
- [4] Ostrowski J et al, Int. J. Computational Science and Engineering 9 (2014) 433–444.
- [5] Franck C M et al, Contrib Plasm Phys 46 (2006) 787 – 797.
- [6] Smeets R P P et al, Performance evaluation of high-voltage circuit breakers by means of current zero analysis. In: Transmission and Distribution Conference and Exhibition 2002: Asia Pacific. IEEE/PES 1: 424-429.
- [7] Seeger M et al, J Phys D: Appl Phys 45 (2012) 395204.
- [8] Ruchti C B et al, IEEE Trans. Plasma. Science., PS-14 (1986) 423-434.
- [9] Christen T, Radiation and Nozzle-Ablation Models for CFD simulations of Gas Circuit Breakers, In: Proc. 1st Int Conf Electr Pow Equip – Sw Techn, Xi'an, China, 2011, 471-474.
- [10] Tepper J et al, IEEE Trans Comp Pack Techn 29 (2006) 658-665.
- [11] Seeger M et al, J Phys D: Appl Phys 39 (2005) 5016–5024.
- [12] Bini R et al, J Phys D: Appl Phys 44 (2011) 25203–12.
- [13] Nordborg H et al, J Phys D: Appl Phys 41 (2008) 135205.
- [14] Iordanidis A et al, J Phys D: Appl Phys 41 (2008) 135206.
- [15] Reichert F et al, J Phys D: Appl Phys, 45 (2012) 375201.
- [16] Jan C et al, J Phys D: Appl Phys 47 (2014) 015204.
- [17] Christen T et al, Radiative Heat Transfer and effective Transport Coefficients, In: Heat Transfer, (Ed. Belmiloudi A), InTech, 2011, 101-126 (free online on intechweb.org).
- [18] Zhang J L et al, IEEE Trans. on Plasma Science 30 (2002) 706-719.
- [19] Franke St et al, J Phys D: Appl Phys 47 (2014) 015202.
- [20] Nielsen T et al, J Phys D: Appl Phys 34 (2001) 2022-2031.
- [21] Dommerque R et al, Influence of the electrode vapour contamination on the interrupting limit of SF<sub>6</sub> self-blast-circuit breakers, Part I: Experimental investigations, In: XVIth Symp on Phys of Switching Arc, Brno, Czech Republic, 2005, 55-58.
- [22] Wang X et al, J Phys D: Appl Phys 48 (2015) 155205.
- [23] Yan J D et al, J Phys D: Appl Phys 32 (1999) 1401–6.
- [24] Yan J D et al, The influence of product design parameters on the performance of high voltage circuit breakers, In: XX Symp Phys of Sw Arc, Brno, Czech Republic, 2013, 58-66.
- [25] Wang W et al, J Phys D: Appl Phys 46 (2013) 065203.
- [27] Tanaka Y, IEEE Trans Power Delivery 28 (2013) 2623.
- [28] Rutgers, Ion density and dielectric breakdown in the afterglow of a high-current arc discharge, Kema Sci & Techn Rep 2, 1984, 9, 79-90.

- [29] Hoffacker M et al, A New Method to Measure the Spatial Arc Resistance Distribution of an Axial Blown Switching Arc, In: 17th Int Symp High Volt Eng, Hannover, Germany, 2011.
- [30] Dousset V et al, Simulations and measurements of decaying arcs in high voltage circuit breakers, In: XIX Int. Conf. Gas Discharges and their Appl, Beijing, PRC, 2012, 178-181.
- [31] Stoller P et al, J Phys D: Appl Phys 48 (2015) 015501.
- [32] Yousfi M et al, IEEE Trans Diel and El Ins 12 (2005) 1192-1199.
- [33] Uchii T et al, IEEE Trans Pow Deliv 19 (2004) 124-130.
- [34] Xingwen Li et al, J Appl Phys 114 (2013) 053302.
- [35] Seeger M et al, Investigation on the temperature dependence of the critical electric field in SF<sub>6</sub>/C<sub>2</sub>F<sub>4</sub> mixtures, In: XVIIth Symp on Phys of Switching Arc, Brno, Czech Republic, 2007.
- [36] [https://unfccc.int/ghg\\_data/items/3825.php](https://unfccc.int/ghg_data/items/3825.php)
- [37] Stoller P et al, IEEE Trans Plasma Science 41 (2013) 2359.
- [38] Mantilla M et al, Investigation of the insulation performance of a new gas mixture with extremely low GWP, In: Electrical Insulation Conference (EIC), 2014, 469.
- [39] Franck C M et al, Contr to Plas Phys CPP 54 (2014) 3-13.

# Extended Methods of Emission Spectroscopy for the Analysis of Arc Dynamics and Arc Interaction with Walls

Uhrlandt D., Methling R., Franke St., Gorchakov S., Baeva M., Khakpour A., Brüser V.

Leibniz Institute for Plasma Science and Technology (INP Greifswald), Felix-Hausdorff-Str. 2, 17489 Greifswald, Germany, [uhrlandt@inp-greifswald.de](mailto:uhrlandt@inp-greifswald.de)

Recently, a number of improved methods of optical emission spectroscopy have been proposed for the study of high-current arcs with special emphasis on the treatment of optical thick arc radiation and analysis of the arc dynamics. The paper gives a short review on these methods focusing on the determination of plasma properties by means of comparison of measured and simulated emission spectra and the use of high-speed video spectroscopy. The application of these methods is demonstrated for a specific example; the study of the interaction of arcs with side walls and the impact of ceramic coatings on the wall's protection. For that purpose, a free burning arc experiment with CuW electrodes is used. The strong electrode erosion causes the arc operation in copper vapour with high stability and reproducibility. The arc temperature profile is obtained from measurements of copper line radiation complemented with radiation transport simulations. The impact of the arc radiation on the evaporation of different ceramic coatings of side walls is studied by video spectroscopy. The resulting impact on the heat load of the walls is derived from thermographic measurements.

**Keywords:** optical emission spectroscopy, plasma temperature, arc wall interaction

## 1 INTRODUCTION

Optical emission spectroscopy (OES) has been established as a main diagnostic method for the study of thermal plasmas and the determination of plasma properties like plasma temperature and densities of emitting species as long as the plasma is optically accessible. These measurements are preferentially used for the validation of plasma models. The intense radiation of arcs in the visible range allows measurements with low acquisition time and in small spectral ranges. This would make possible, in general, the study of arcs with high temporal dynamics and high accuracy. However, most of the established methods are limited by a number of required assumptions and other boundary conditions for the radiation analysis.

On the one hand, recording techniques with high temporal resolution (use of photomultiplier or fibre spectrometer) have typically no or low spatial resolution (see e.g. [1]) whereas spatial imaging spectroscopy with intensified charge coupled device (ICCD) cameras are very limited in the repetition time (see e.g. [2]). Imaging spectroscopy coupled with a high speed camera (HSC) (here and later called video spectroscopy) offers an answer to this problem but is not well proven up to now.

One the other hand, most of the established

methods are based on the analysis of line radiation and require an adequate knowledge of specific properties of the radiating species and their atomic transitions in the considered plasma. Methods like single-line or multiple-line analysis and analysis of the line profile width (see e.g. [3]) are limited to line radiation of low optical thickness and plasma temperatures below the normal maximum of the lines. The latter describes the point of maximum intensity before the intensity decreases with increasing temperature due to a significant decrease of the radiator density according to the change of the plasma composition.

The most methods are based on the assumption of local thermodynamic equilibrium (LTE) of the plasma. Furthermore, rotational symmetry of the arc is assumed for the required spatial reconstruction of the local emission coefficient from side-on measurements from only one viewing angle. An exception is the Bartel's method for the evaluation of line radiation showing self-reversal [4]. Here, the plasma temperature can be obtained from the intensity of the side-on measured radiance in the maximum of the line profile with self-reversal. However, the method can fail in the temperature range above the normal maximum.

An alternative to the methods mentioned

above is to start with an assumption of spatial profiles of plasma temperature and radiator densities and applying simulations of side-on spectra by radiation transport calculations (see e.g. [5]). The comparison with calibrated measurements allows the successive improvement of the initial assumptions. This method will be discussed in more detail in section 2.

In view of the recently increased interest on studies of arc interaction with surfaces (electrodes and side walls), in sections 3 to 5 both methods, the temperature determination by radiation transport calculations and side-on measured spectra and the video spectroscopy, will be demonstrated on the example of a free burning arc experiment considering the evaporation of protective layers of side walls. A specific setup with WCu and W electrodes, as described in section 3, provides arcs dominated by the copper evaporation at the cathode which show high stability and reproducibility. Studies of the electrode erosion in arc applications have a long history because this process is a key issue for lifetime and reliability. The same holds for the study of nozzle ablation in high-voltage circuit-breakers focussing mainly on polytetrafluoroethylene (PTFE) [6]. More recently, the replacement of PTFE by other gas-producing polymeric materials has been studied [7-11]. Some of these studies concern also the unintentional and often crucial evaporation of side walls, e.g. in low-voltage circuit-breakers. The possible protection of side walls against heat load and erosion by means of appropriate coatings represents an additional aspect. For example, ceramic coatings offer additional advantages because there are cheap, easy coating techniques are available, and the coating can be partially regenerated from the evaporation products. First studies of the arc interaction with ceramic coatings have been presented in a preceding paper [12]. In this paper, more robust coatings as well as improved diagnostic methods for the analysis of the arc and the evaporation of the coatings are considered.

## 2 OES AND RADIATION TRANSPORT

OES of line radiation from metal vapours (Fe,

Cu, Mg) can be well used for temperature determination in arcs in different gases. The large variety of metal lines in the visible spectrum makes it easy to find lines of atoms and ions or lines corresponding to optical transitions from quite different energy levels in small wavelength ranges which can be recorded simultaneously with high resolution. Boltzmann-plot of line intensities or the ratio of atomic and ionic lines is well applicable as long as the vapour concentration and consequently the optical thickness of the lines are sufficiently low. In contrast to that, lines of broad profiles with large overlapping and often self-reversal can be found in arcs which are dominated by metal vapour [13]. The line emission is accompanied by a significant absorption of the emitted radiation in the near and far surrounding of every emission point. The radiation transport affects the radiation intensity observed from outside as well as the power balance of the arc considerably.

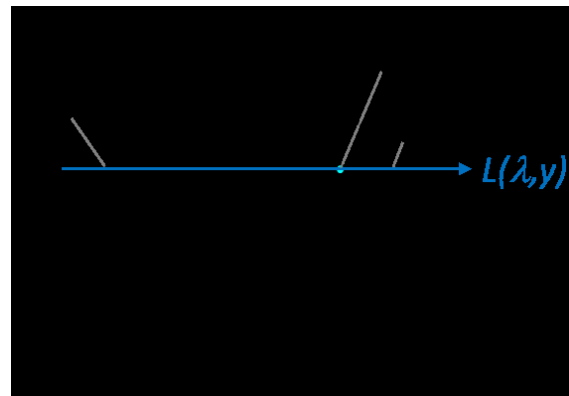


Fig. 1: Scheme of the line of sight (blue) through a plasma cross section (black circle) at the side-on position  $y$

The solution of the radiation transport equation along a line of sight through the arc plasma enables a strict treatment of emission and absorption (see e.g. [5,14]). Let us consider a line of sight along direction  $x$  through the plasma at a side-on position  $y$ . This situation is illustrated in Fig. 1 for the case of cylindrical plasma which is observed from the side perpendicular to the cylinder axis. The position  $x$  varies between  $-x_0$  and  $x_0$  at the borders of the plasma. The spectral radiance  $L$  resulting from this line at the wavelength  $\lambda$  is determined by

$$L(\lambda, y) = \int_{-x_0}^{x_0} \varepsilon(\lambda, x, y) \exp\left[-\int_{x'}^{x_0} \kappa(\lambda, x', y) dx'\right] dx \quad (1)$$

$\varepsilon(\lambda, x, y)$  and  $\kappa(\lambda, x, y)$  are the local spectral emission and absorption coefficients, respectively. In what follows the  $x$ - and  $y$ -dependence in  $\varepsilon$ - and  $\kappa$ -notations is dropped for the sake of simplicity. In both coefficients contributions from spectral lines (bound-bound transitions) and from continuum radiation have to be included. The emission coefficient of a line corresponding to the transition between atomic (ionic) levels  $k$  and  $i$  reads

$$\varepsilon_{ki}^0(T) = \frac{hc}{4\pi\lambda_{ki}} A_{ki} n_k(T) \quad (2)$$

with the central wavelength  $\lambda_{ki}$ , the transition probability  $A_{ki}$ , the speed of light  $c$ , the Planck constant  $h$ , and the density  $n_k$  of the upper excited level. Assuming LTE this density can be expressed by the Boltzmann distribution

$$n_k(T) = n_0(T) \frac{g_k}{Z(T)} \exp\left(-\frac{E_k}{kT}\right) \quad (3)$$

where  $n_0$  is the total species density (atom or ion density for example),  $g_k$  is the statistical weight and  $E_k$  the excitation energy of the level,  $k$  - the Boltzmann constant,  $T$  - the temperature and  $Z(T)$  - the partition function. The corresponding contribution to the spectral emission coefficient is calculated assuming, e.g., a Lorentz line profile with a half half-width  $\lambda_w^{ki}$  and line shift  $\Delta\lambda_{ki}$  according to

$$\varepsilon_{ki}(\lambda, x) = \varepsilon_{ki}^0 \frac{\lambda_w^{ki}}{\pi} \frac{1}{(\lambda - \lambda_{ki} - \Delta\lambda_{ki})^2 + (\lambda_w^{ki})^2} \quad (4)$$

where the values of  $T$ ,  $Z(T)$  and  $n_0(T)$  are taken at the position  $x$ . The species densities result from plasma composition calculations for the respective local temperature and gas pressure applying the Gibbs-free energy minimization method. The corresponding absorption coefficient is calculated applying the Kirchoff's law

$$\kappa_{ki}(\lambda, x) = \varepsilon_{ki}(\lambda, x) B_{\lambda_{ki}} \quad (5)$$

with the Planck function  $B_{\lambda_{ki}}$ .

In the example which will be presented in section 4, the radiation of the arc plasma in a copper-air mixture is considered in a spectral range from 490 to 530 nm for temperatures from 1 up to 20 kK. Here, 13 lines of Cu I (copper atoms), 108 lines of Cu II (singly ion-

ized copper) and in addition a number of lines of oxygen and nitrogen (atoms and ions) are included with atomic data from the Kurucz and NIST Atomic Spectra Database each characterized with a Lorentz line profile. Each line width comprises a base part  $\lambda_w^{min}$  and a part from Stark broadening  $\lambda_w^S$  estimated according to [14-16]. The bremsstrahlung continuum (free-free transitions) and the recombination continuum (free-bound transitions) have been calculated as given in [14] using photoionization cross sections from [17, 18] and momentum transfer cross sections from [19].

As a first assumption for the considered example, a rotational symmetric temperature profile is constructed on the base of radial profiles of measured line intensities. Because the line intensities show mainly a box like profile with a quite flat central region, a temperature profile with a flat centre and a larger slope at outer positions is assumed. Then, the maximum temperature is adjusted by comparing with the measured intensities of Cu I lines at the central side-on position.

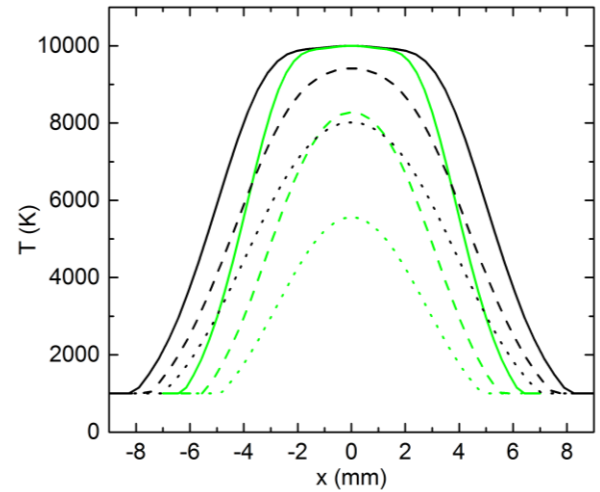


Fig. 2: Examples of considered radial arc temperature profiles (in green and black): temperature along the line of sight for the central side-on position (solid lines) and for side-on positions  $y=3$  mm (dashed lines) and  $y=4$  mm (dotted lines) from the arc axis

Examples of considered temperature profiles are shown in Fig. 1 considering a maximum temperature of 10 kK. Results of simulations of the side-on radiance  $L$  at the central side-on

position ( $\nu=0$ ) for different maximum temperatures (12 and 15 kK) considering a copper vapour pressure of 1 bar (without contributions of air) and a radial temperature profile corresponding to the black profile in Fig. 2 are shown in Fig. 3. The spectral radiance is dominated by Cu I lines at  $\lambda_0=507.6$ , 510.6 and 515.3 nm where the last two show strong self-reversal. Cu II lines at  $\lambda_0=506.5$  and 508.8 nm become visible at 15 kK maximum temperature.

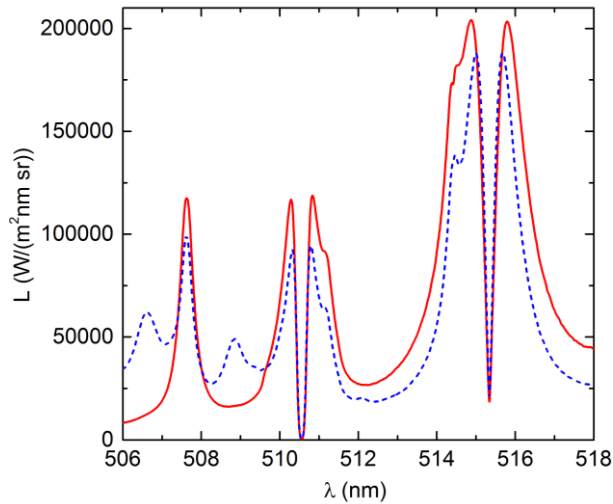


Fig. 3: Examples of radiance simulations for the radial temperature profile similar to the black curve in Fig. 1 but maximum temperatures 12 kK (red solid line) and 15 kK (blue dashed line) for the central side-on position

In the next step, the copper vapour pressure is adjusted mainly by comparing the line profile width of leading lines. Finally, the width of the temperature profile and in addition a radial profile of the copper vapour density is adjusted to find best agreement between simulation and measurements including several side-on positions. The results are presented in section 4.

### 3 EXPERIMENTAL STUDY OF ARC INTERACTION WITH PROTECTIVE COATINGS

An experimental setup in open air with road electrodes of 10 mm diameter, placed in a distance of 70 mm as shown in Fig. 4, is used for the operation of the arc. The lateral surface of the road electrodes is insulated by means of ceramic nozzles in order to fix the arc attachment area, and therefore, the current density at

the electrode surfaces. A tungsten-copper electrode is used on the one side (the cathode in the first pulse), and a tungsten electrode on the other side (different from the setup in preceding studies [12]).

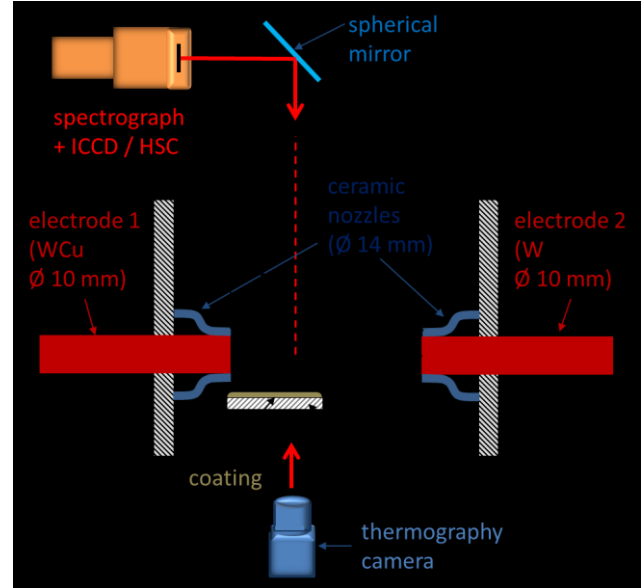


Fig. 4: Setup of the arc experiment

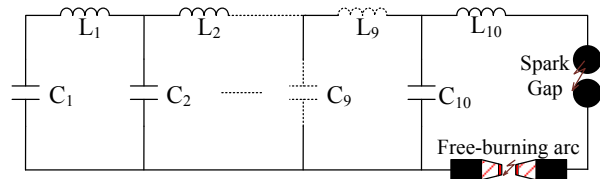


Fig. 5: Electrical circuit arrangement

Nearly rectangular current pulses are produced by means of a circuit shown in Fig. 5. LC elements with constant capacity of about 260  $\mu\text{F}$  and stepwise decreasing inductances from  $L_1=610 \mu\text{H}$  to  $L_{10}=180 \mu\text{H}$  are coupled in series to produce pulses of about 5 ms duration and a peak current of 5.2 kA (first pulse). A spark gap is used for triggering. The arc in the setup shown in Fig. 3 is ignited using a thin copper wire between the electrodes.

Ceramic substrates of 1 mm thickness are arranged sideward to the arc in a distance of about 10 mm to the arc axis. The substrates are coated with ceramic materials  $\text{CaCO}_3$  or  $\text{MgCO}_3$  mixed either with plaster or with an organic binder. A sample of a coated plate is shown in Fig. 6. The arc causes typically a strong evaporation of the coating already during the first pulse.



Fig. 6: Example of a ceramic substrate coated with  $\text{CaCO}_3$  and plaster

Examples of the measured courses of arc current, voltage and power are shown in Fig. 7. Only the first pulse with the maximum power is considered in the arc analysis. The impacts of the later pulses on the substrates are expected to be much lower. The voltage is slightly higher in the case with  $\text{MgCO}_3$  coating because of the vapour impact on the arc conductivity. However, the variation is comparable with the deviations between experiments with the same substrate and coating. Hence, a systematic change of the voltage could not be determined from the experiments.

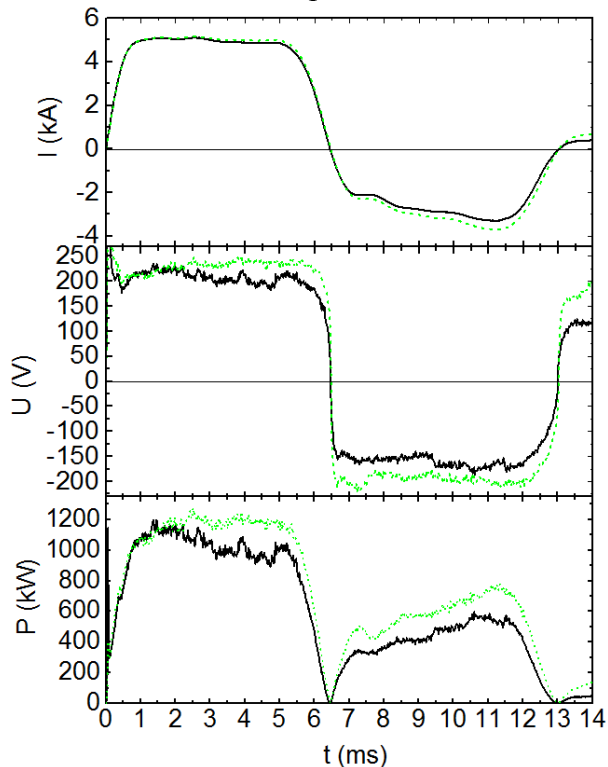


Fig. 7: Examples of arc current  $I$ , voltage  $U$  and power  $P$  for experiments with a ceramic substrate without coating (green dotted lines) and with  $\text{MgCO}_3$  + plaster coating (black solid lines)

The arc radiation is recorded by a spectroscopic system consisting of a 0.5 m spectrograph either coupled with an ICCD (for one 2D image in one experiment) or a HSC (for video spectroscopy). A spherical mirror is used to image the cross section of the arc at a distance of 15 mm far from the electrode (cathode in the first pulse) on the slit of the spectrograph (see Fig. 3). A  $1800 \text{ mm}^{-1}$  grating is applied to record spectral ranges of 12 nm width around different wavelength positions (425, 512, 656 and 744 nm). The ICCD is typically triggered at 4 ms after arc ignition with exposure times between 1 and 5  $\mu\text{s}$ . The HSC at the spectrograph is operated typically with a repetition rate of 4000 frames/s.

An additional colour HSC (not shown in Fig. 4) is used to observe the arc experiment with a repetition rate of 5000 frames/s. Example images recorded 4 ms after arc ignition during the first pulse are shown in Fig. 8. The electrodes are indicated by red lines. The cathode is on the left-hand side. The stable arc, at least near the cathode, caused by the cathode evaporation is illustrated in the case without coating (part (a) of Fig. 8). The impact of the coating evaporation becomes clearly visible in part (b) of Fig. 8.

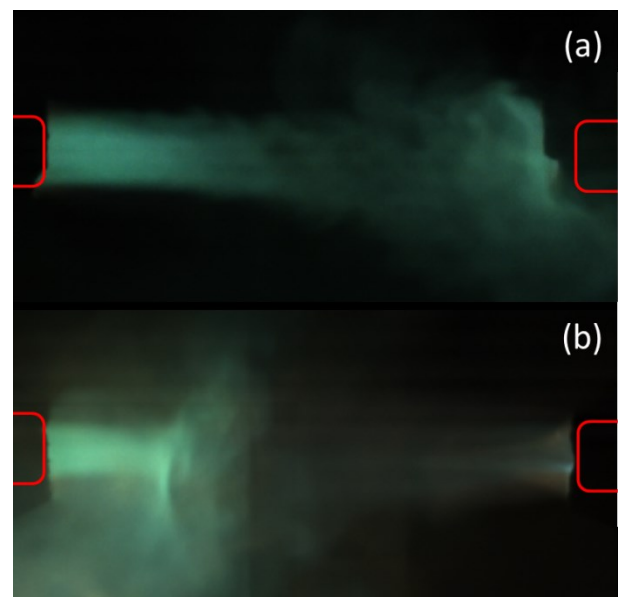


Fig. 8: Arc images at the instant 4 ms after ignition for the case without coating (a) and with  $\text{MgCO}_3$  + plaster coating (b)

Fig. 9 shows an example of a 2D spectral radiance recorded by the ICCD in the wavelength range from 506 to 518 nm (abscissa) after intensity and wavelength calibration. The side-on position over the arc cross section is the ordinate.

The setup is completed by a thermography camera (see Fig. 4) with a spectral sensitivity

range from 7.5 to 12  $\mu\text{m}$ . The camera is used to observe the backside of the coated substrates with a repetition rate of 50 frames/s. An image is shown in Fig. 10. Again, the electrodes (covered by other parts) are indicated by red lines. The yellow region shows the backside of the ceramic substrate, partly covered by the sample holder. The image range marked by the black frame is used to determine an averaged surface temperature of the substrate back side and its temporal evolution after the arc impact.

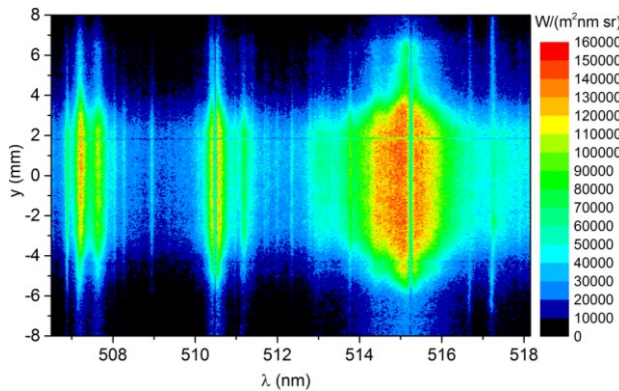


Fig. 9: 2D image of the arc spectral radiance for an axial position 15 mm away from the cathode recorded 4 ms after arc ignition in the case with  $\text{MgCO}_3$  + plaster coating

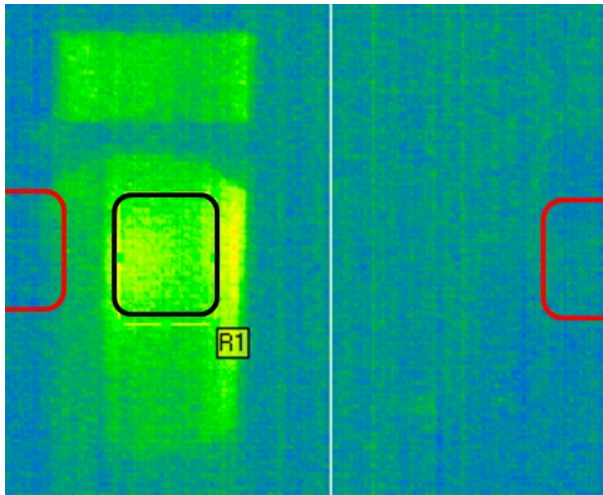


Fig. 10: Image of the thermography camera after arc impact in the case of a substrate with  $\text{MgCO}_3$  + plaster coating

#### 4 RESULTS FOR THE ARC PROPERTIES

The temperature profile of the copper vapour dominated arc is determined based on the spectral radiance measurements recorded at the instant 4 ms after arc ignition (see the example in Fig. 9). Results of the measurements for the central side-on position ( $y=0$ ) are shown in Fig. 11 for three cases. In spite of the different substrate coatings, the spectral radiances are very similar in the considered spectral range. There are dominated by Cu I lines at 510.6 and 515.3 nm (central wavelength each) which show significant self-reversal as expected from the simulations shown in Fig. 3. In addition, a number of other lines without self-reversal in the range from 507 to 508 nm and at 511.3 nm are significant. Notice, that not all lines in the recorded spectrum could be successfully identified because of lack of data. Mg I lines become visible in case of the  $\text{MgCO}_3$  + plaster coating in the range above 516 nm. This is an indication for the pronounced evaporation of the coating in this case.

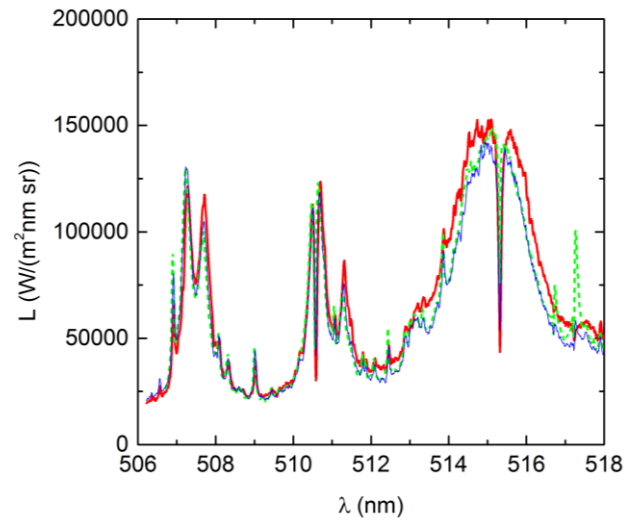


Fig. 11: Measured and calibrated spectral radiance  $L$  for  $y=0$  for the cases of the substrate without coating (solid red line), with  $\text{MgCO}_3$  + organic binder coating (thin solid blue line), and with  $\text{MgCO}_3$  + plaster coating (dashed green line)

Only small deviations in the arc temperature profiles in the three cases are expected because of the similarities of the measured radiances. Therefore, radiation transport calculations as explained in section 2 are used to determine a typical arc temperature profile and a typical profile of the Cu density of the established arc during the first current pulse. Rotational symmetry is assumed. Fig. 12 shows simulation results for the spectral radiance based on the broader temperature profile in Fig. 2 but with peak temperatures of 9 and 10 kK in comparison with one of the measurements. A partial pressure of the copper vapour of 1 bar is assumed in the arc centre with a gradual radial decrease as explained below.

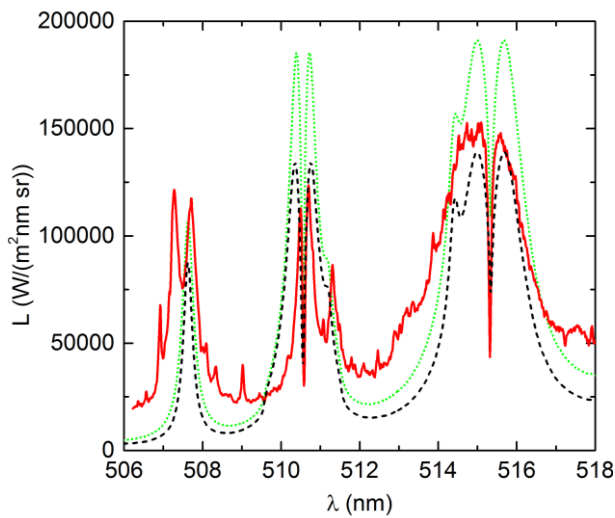


Fig. 12: Spectral radiance  $L$  for  $y=0$  simulated for temperature profiles with the peak temperature 10 kK (dotted green line) and 9 kK (dashed black line) and measured in case of a substrate without coating (red solid line)

The absolute intensity of the Cu I lines can be well simulated when choosing a maximum temperature of 9 kK. The self-reversal and the width of the Cu I line at 515.3 nm is sufficiently reproduced by the choice of the broader radial profile. Remaining discrepancies result from additional lines which are not included in the simulation because of lack of data and from an insufficient description of the line broadening in case of the line at 510.6 nm. Finally, the temperature profile and the profile of the partial pressure of copper given in Fig. 13 have been considered as the best choice after variation and comparison with measured radiances at different side-on positions. Fig. 14 gives an example for the comparison at the side-on position  $y=3$  mm. Again, intensities and widths of the leading lines are reproduced sufficiently well by

the simulation. The spectral radiance corresponding to the maximum of the left-hand wing of the dominant self-reversed Cu I line (around 515 nm) over the arc cross section is shown in Fig. 15 for the three cases considered above. Such values have been obtained from averaging the 2D images (see Fig. 9) over a small spectral range. The comparison with simulation results for few side-on positions shows a quite good agreement. Notice, that the relatively narrow pressure profile of copper have been chosen in order to simulate successfully the spatial profile (see Fig. 15 for example) as well as the inner shape of the self-reversed lines.

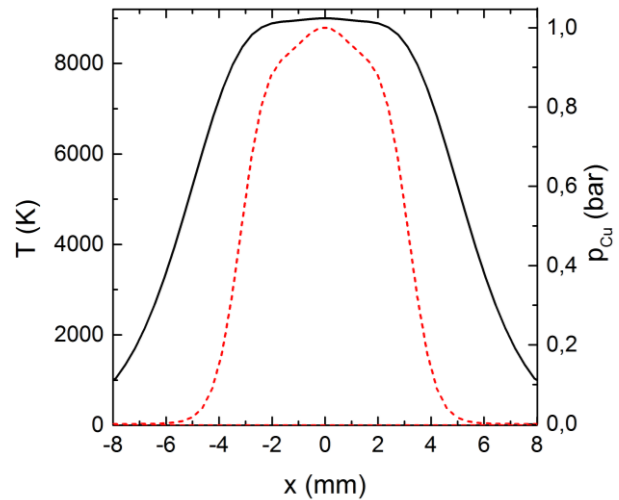


Fig. 13: Typical profiles of the plasma temperature (solid black line) and the copper partial pressure (dashed red line) of the considered arc

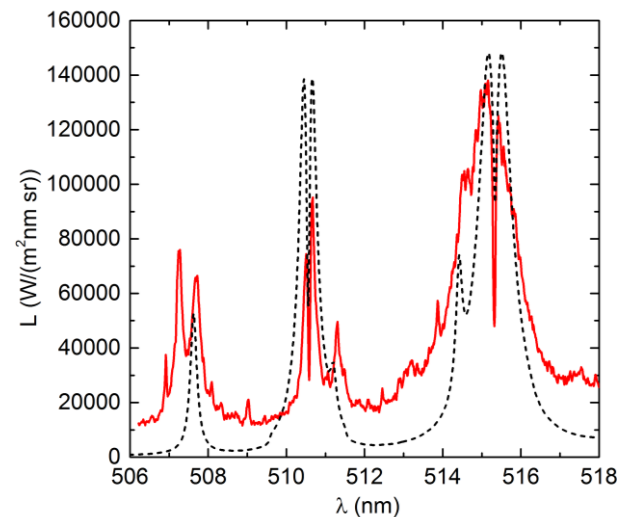


Fig. 14: Spectral radiance  $L$  for  $y=3$  mm simulated for the temperature and pressure profiles in Fig. 13 (dashed black line) and measured in case of a substrate without coating (red solid line)

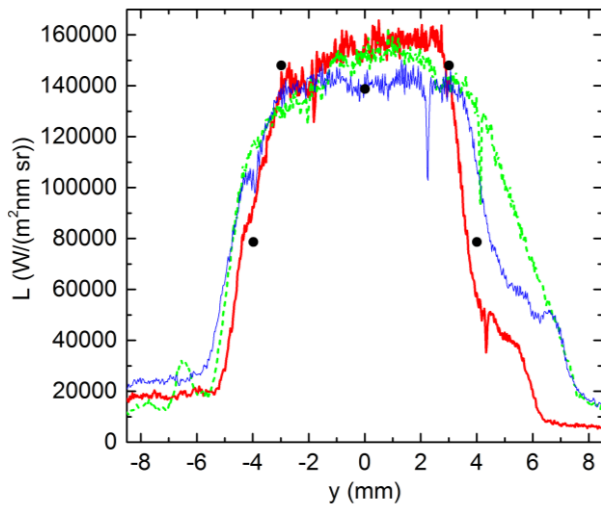


Fig. 15: Spectral radiance  $L$  for about 515 nm (maximum of the left-hand wing of the Cu I line at 515,3 nm) measured in the three cases given in Fig. 11 as a function of the side-on position  $y$  (lines) and from simulations for few side-on positions (solid circles)

Additional estimations become possible based on the rough determination of the arc temperature profile and the copper vapour pressure (see Fig. 13). For simplicity, a homogeneous cylindrical arc in poor copper with a radius of 5 mm and a temperature of 9 kK can be assumed. A net emission coefficient of  $1,29 \times 10^9 \text{ Wm}^{-3}\text{sr}^{-1}$  for such plasma has been calculated in [20]. A total emitted radiation of about 44 kW is obtained considering the arc length of 70 mm which is about 4 % of the typical power during the first pulse (see Fig. 7). Assuming homogeneous distribution of the emitted radiation in radial direction and full absorption at the substrates in a distance of 10 mm from the arc axis, an energy density of  $10 \text{ MWm}^{-2}$  is achieved characterizing the thermal load of the coatings during the first current pulse.

## 5 IMPACT OF PROTECTIVE COATINGS

The thermal load of the samples (substrates with coating) results in a more or less pronounced evaporation of the coating accompanied by a heating of the substrates. The evaporation can be qualitatively estimated by HSC images as shown for example in Fig. 8. A pronounced evaporation has been found in the case of both coatings  $\text{CaCO}_3$  and  $\text{MgCO}_3$  with plaster. The vapour flows into hot regions of

the arc and causes quite visible emission of Ca and Mg, respectively.

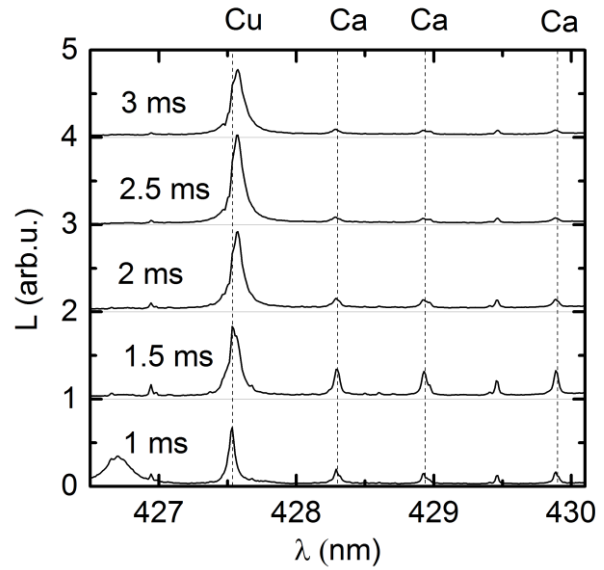


Fig. 16: Temporal evolution of the spectral radiance  $L$  for  $y=0$  in the range of Ca I lines in case of the coating  $\text{CaCO}_3$  + organic binder. The curves are presented with an offset increased by 1 with each time step of 0.5 ms

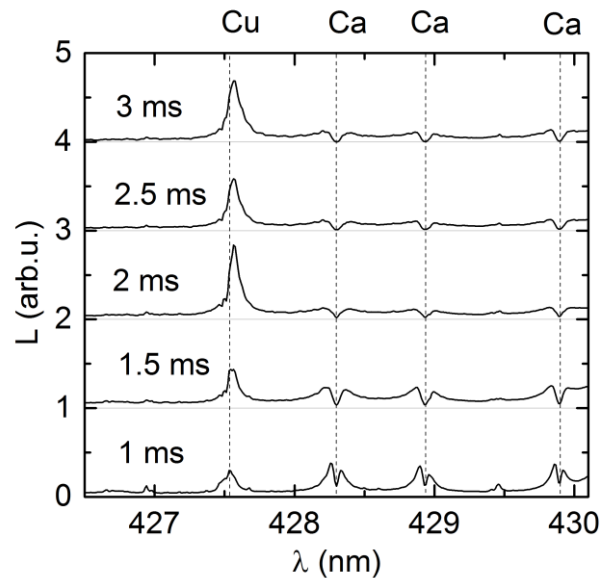


Fig. 17: Temporal evolution of the spectral radiance  $L$  for  $y=0$  as in Fig. 16 but for a in the range of Ca I lines in case of the coating  $\text{CaCO}_3$  + plaster

A quantitative analysis of the evaporation processes becomes possible with the video spectroscopy. Examples of the temporal evolution of the spectral radiance (without intensity cal-

ibration) in the range of Ca I lines are given in Figs. 16 and 17 for two kinds of coatings. Notice, that the evolution can be followed with a time step of 0.25 ms, and only few time instants are presented in the Figures. The evolution of the Cu I line at 42.5 nm can be used to roughly estimate the intensity of the copper dominated arc – a small increase during first microseconds is followed by an almost constant intensity of the Cu I line.

A considerable emission of the Ca I lines is observed in both cases starting already in the first microsecond. The decrease of the lines during next microseconds can be explained with effects of the gas flow; a further establishment of the copper vapour flow from the cathode which displaces the Ca vapour but also other effects in the Ca vapour flow itself. Ca lines of increased profile width and sometimes with self-reversal can be seen in the example in Fig. 17. This promotes the conclusion that the Ca vapour pressure is much larger in the case of the coating with plaster.

The analysis of the Ca line radiation even in the case of higher optical thickness can lead to a quantitative determination of the Ca vapour and, hence, an estimation of the vapour flow. Here, the arc temperature profile estimated by spectrum simulations in the copper-air mixture can be used as a first step. However, composition calculations for the full gas mixture resulting from electrode and ceramic coating evaporation are required for more accurate determination. The final step would be radiation transport calculations for the Ca lines and a comparison with the video spectroscopy results following the approach given above. The application of such a procedure is scheduled for further research.

The thermographic studies have been used to pre-estimate the protection effect of the different coatings. Results for the temporal evolution of the surface temperature of the substrates backside are given in Fig. 18. A number of experiments have been evaluated for the same kind of coating. An appropriate selection of the temporal courses in Fig. 18, two courses in each case, illustrates also the shot-to-shot variation. Despite the variation for the same coating, a systematic difference between the

coatings with organic binder and with plaster is observed. In the latter cases, only slow and low temperature increase at the backside is obtained. In contrast, a heating-up within 1 or 2 seconds up to temperatures which are 16 to 22 degree above the room temperature followed by a slow decrease is observed in the case of organic binders. Such behavior is expected because of the higher stability and lower thickness of the coatings with organic binders. The higher heating-up of the samples with  $MgCO_3$  in comparison with  $CaCO_3$  agrees with earlier findings [12].

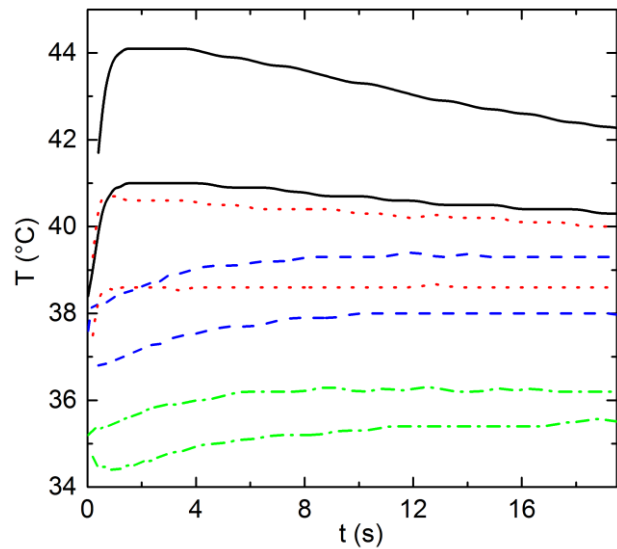


Fig. 18: Temporal evolution of the back-side surface temperature of the substrates for coatings with  $MgCO_3$  + organic binder (black solid line),  $MgCO_3$  + plaster (blue dashed line),  $CaCO_3$  + organic binder (red dotted line),  $CaCO_3$  + plaster (green dash-dotted line)

In conclusion,  $CaCO_3$  coatings with plaster as a binder material provide the best protection because of a pronounced evaporation in comparison with the other cases. However, the low stability and larger inhomogeneity of simple plaster coatings represents a significant drawback. Further studies are required to find optimal coatings with a comparable protection effect and concurrently an appropriate stability.

## 6 SUMMARY AND OUTLOOK

A free-burning arc experiment has been used to demonstrate the application of extended methods of emission spectroscopy for the

study of arc-wall interactions. Radiation transport and plasma composition calculations are used to simulate the spectral radiance of the arc. The comparison with imaging OES represents an interesting way to estimate spatial profiles of the arc temperature and species densities including vapour densities of eroded material.

Exemplary results have been presented for the radial arc temperature profile and the profile of the copper vapour pressure caused by significant electrode erosion. The power loss by the emitted radiation and finally the expected heat load of sidewalls have been estimated from these results. The additional analysis of vapour pressures of eroded wall material, resulting from ceramic layers for example, need more complex composition and radiation transport calculations. This will be subject of future work. The complementary use of video spectroscopy has been illustrated in the paper. This enables an interesting way to study the dynamics of arc temperature and vapour distributions which allows conclusions on the evaporation processes.

Simple ceramic coatings represent a specific option for the heat protection of sidewalls in switch gear because of the strong evaporation under impact of arc radiation. A future use requires additional improvement of coating techniques and the use of binders.

#### REFERENCES

- [1] Tanaka Y, Yokomizu Y, Ishikawa M, Matsumura T, Kito Y, *Phys. D: Appl. Phys.* 30 (1997) 407-416.
- [2] Kozakov R, Kettlitz K, Weltmann KD, Stefens A, Franck CM, *J. Phys. D: Appl. Phys.* 40 (2007) 2499-2506.
- [3] Wiese W L, *Spectrochimica Acta* 46B (1991) 831-841.
- [4] Schneidenbach H, Franke St, *J. Phys. D: Appl. Phys.* 41 (2008) 144016.
- [5] Wendt M, Franke St, *J. Phys. D: Appl. Phys.* 41 (2008) 144018.
- [6] Seeger M, Tepper J, Christen T, Abrahamson J, *J. Phys. D: Appl. Phys.* 39 (2006) 5016-5024.
- [7] Lee A, Heberlein J V R, Meyer T N, *IEEE Trans. Components, Hybrids, and Manufacturing Technol.* 8 (1985) 129-134.
- [8] Rodriguez P, Didier J, Bernard G, Rowe S, *IEEE Trans. Power Delivery* 13 (1998) 480-488.
- [9] Tanaka Y, Shinsei N, Amitani K, Uesugi Y, Wada J, Okabe Sh, *IEEE Trans. Plasma Sci.* 39 (2011) 2776-2777.
- [10] Jonsson E, Runde M, Dominguez G, Friberg A, Johansson E, *IEEE Trans. Power Delivery* 28 (2013) 2065-2070.
- [11] Onchi T, Yanase H, Yamazaki M, Kuroda M, Isozaka M, Sugiyama Sh, Hata J, Yonemitsu K, *IEEJ Trans. PE* 127 (2007) 692-698.
- [12] Uhrlandt D, Gorchakov S, Brüser V, Franke St, Khakpour A, Lisnyak M, Methling R, Schoenemann Th, *J. Phys.: Conf. Series* 550 (2014) 012010.
- [13] Franke St, Methling R, Uhrlandt D, Bianchetti R, Gati R, Schwinne M, *J. Phys. D: Appl. Phys.* 47 (2013) 015202.
- [14] Lochte-Holtgreven W, *Plasma Diagnostics*, North-Holland Publishing Company, Amsterdam, 1968.
- [15] Peytremann E, *A&A* 17 (1972) 76.
- [16] Sahal-Brechot S, Segre ERA, *A&A* 13 (1971) 161.
- [17] Verner D A, Yakovlev D G, *A&AS* 109 (1995) 125.
- [18] Verner D A, Ferland G J, Korista K T, Yakovlev D G, *Astrophys. J.* 465 (1996) 487.
- [19] Kasyanow W, Starosting A, *Sov. Phys. - JETP* 21 (1965) 193.
- [20] Cressault Y, Gleizes A, *J. Phys. D: Appl. Phys.* 46 (2013) 415206.

## Modelling of Turbulent SF<sub>6</sub> Switching Arcs

Zhang Q.<sup>1</sup>, Yan J. D.<sup>1</sup>, Yan G.<sup>2</sup>

<sup>1</sup>Department of Electrical Engineering and Electronics, the University of Liverpool,  
Brownlow Hill, Liverpool, L69 3GJ, UK, [yaneee@liverpool.ac.uk](mailto:yaneee@liverpool.ac.uk)

<sup>2</sup>Henan Pinggao Group Co., Ltd. Nanhuandong Road, Pingdingshan City, 467001, China

The present work aims at a comparative study of the performance of relevant turbulence models in predicting the behaviour of SF<sub>6</sub> switching arcs during the current zero period. Turbulence models studied include the Prandtl mixing length model, the standard k- $\epsilon$  model and its two variants, i.e. the Chen-Kim model and the RNG model. In order to demonstrate the effects of turbulence, a laminar flow case is also modelled. Based on the computational results, a detailed analysis of the physical mechanisms encompassed in each flow model is given to show the adequacy of each model in describing the rapidly varying arcing process during the current zero period. The computed values of the critical rate of rise of recovery voltage (RRRV) are subject to verification by experimental results covering a wide range of discharge conditions. The relative merits of the flow models are discussed.

**Keywords:** SF<sub>6</sub> switching arcs, turbulence models, current zero period

### 1 INTRODUCTION

There is overwhelming experimental and theoretical evidences indicating that an SF<sub>6</sub> arc burning in a converging-diverging nozzle (known as the switching arc) is turbulent and its state close to local thermodynamic equilibrium (LTE) [1]. Such an arcing arrangement is commonly used for the arc interrupter of high voltage circuit breakers (HVCBs). In order to reduce the development cost of HVCBs, it is highly desirable to computationally predict and study the arc behaviour under operational conditions similar to those encountered in a power system. One of the major tasks in achieving full computer aided design of HVCBs is the satisfactory prediction of their thermal interruption capability under turbulent conditions. There is, however, no versatile turbulence model for this purpose with its applicability rigorously verified under different arcing conditions and with different breaker designs. The present work aims at a comparative study of the performance of existing turbulence models in predicting the behaviour of SF<sub>6</sub> switching arcs during the current zero period of an interruption process for which trustworthy RRRV measurement is available.

Based on the LTE assumption, arc flows in turbulent state are usually described by the time averaged Navier-Stokes equations [2] modified to take into account Ohmic heating and radiation loss in the energy conservation equation. The Boussinesq assumption is used

to close the above mentioned conservation equations by relating the Reynolds stress to the gradients of the mean velocity through the concept of eddy viscosity [2]. A turbulence model is therefore required to calculate the eddy viscosity. There are numerous turbulence models reported in the literature [2, 3, 4] but none of them are devised specifically for electric arcs. Modelling of turbulent arcs is still in its infancy, and the mechanisms responsible for the generation of arc instability and the development of arc turbulence are still poorly understood.

There is a direct resemblance between a switching arc and a round free jet, both of which are dominated by shear flow. The most apparent approach for turbulent arc modelling is to start with the examination of the applicability of existing turbulence models, which are devised for shear flows. Of these turbulence models, the Prandtl mixing length model has achieved considerable success in predicting the behaviour of SF<sub>6</sub> switching arcs, notwithstanding the finding that the only turbulence parameter needs to be adjusted, based on test results, for different nozzle geometries [5]. There have been sporadic investigations on turbulent SF<sub>6</sub> arcs using the standard k- $\epsilon$  model [6, 7] and a few of its variants (e.g. using the RNG model [8]), with contradictory claims on the applicability of these models. This is partially caused by a lack of direct verification using reliable measurement of arc

parameters (such as arc voltage, temperature and RRRV) over a sufficiently wide experimental or test conditions.

The present work constitutes a part of our effort towards a versatile turbulence model for switching arcs. The arcing behaviour in a simple two-pressure system is modelled using five flow models, and the test results of Frind et al. [9], Benneson et al. [10] and Frind and Rich [11] are used to judge the relative merits of the models.

## 2 THE GOVERNING EQUATIONS AND TURBULENCE MODELS

The turbulent switching arc and its surrounding flow are described by the time averaged Navier-Stokes equations modified to take into account Ohmic heating and radiation loss. The arc model has been well reported in [12]. At the electric current level used in the present work, it is sufficiently accurate to calculate the electric field using a simplified Ohm's law [12].

The standard k-ε model [2] and its two variants (the Chen-Kim model [3] and the RNG model [4]) have been chosen for the modelling of turbulent SF<sub>6</sub> switching arcs. Since the application of the Prandtl mixing length model has had considerable success, this turbulence model is included in our investigation for comparison. All these turbulence models belong to the category using the concept of effective eddy viscosity,  $\mu_t$ . The Reynolds stresses are linearly linked to the main strain via eddy viscosity by means of Boussinesq assumption [2]. The turbulent Prandtl number ( $Pr_t$ ) provides the link between  $\mu_t$  (for the momentum equations) and turbulent thermal conductivity,  $k_t$  (for the energy equation), which is assumed to be 1 in the present investigation.

In order to demonstrate the effects of turbulence, a laminar case is also included, which is obtained by simply setting  $\mu_t$  and  $k_t$  to zero. For simplicity, the arc models based on laminar flow and turbulent flow will be collectively referred to as the flow models for future reference. Therefore, altogether five flow models are used to study the behaviour of SF<sub>6</sub> switching arcs. The details of the four turbulence models are given below.

### 2.1 PRANDTL MIXING LENGTH MODEL

This is the simplest and also the oldest turbulence model according to which the eddy viscosity is defined as

$$\mu_t = \rho \ell_m^2 \left( \left| \frac{\partial w}{\partial r} \right| + \left| \frac{\partial v}{\partial z} \right| \right) \quad (1)$$

where the length scale is related to the arc's thermal radius through a turbulence parameter,  $c$ , which is given by

$$\ell_m = c \sqrt{\int_0^\infty (1 - T_\infty/T) \cdot 2r dr} \quad (2)$$

where  $T_\infty$  is the temperature near the nozzle wall where the radial temperature gradient is small.

### 2.2 STANDARD K-EPSILON MODEL

This model is the most widely used turbulence model for engineering applications. The equations of this model are those for the turbulence kinetic energy per unit mass,  $k$ , and its dissipation rate,  $\varepsilon$ , which are given below:

$$\frac{\partial(\rho k)}{\partial t} + \nabla \cdot \left( \rho \vec{V} k - \frac{\rho v_t}{\sigma_k} \nabla k \right) = \rho (P_k - \varepsilon) \quad (3)$$

$$\frac{\partial(\rho \varepsilon)}{\partial t} + \nabla \cdot \left( \rho \vec{V} \varepsilon - \frac{\rho v_t}{\sigma_\varepsilon} \nabla \varepsilon \right) = \rho \frac{\varepsilon}{k} (C_{1e} P_k - C_{2e} \varepsilon) \quad (4)$$

where  $P_k$  represents the generation of turbulence kinetic energy due to the mean velocity gradients, which is given by

$$P_k = v_t \left[ 2 \left( \frac{\partial w}{\partial z} \right)^2 + 2 \left( \frac{\partial v}{\partial r} \right)^2 + 2 \left( \frac{v}{r} \right)^2 + \left( \frac{\partial w}{\partial r} + \frac{\partial v}{\partial z} \right)^2 \right] \quad (5)$$

and the eddy viscosity is given by

$$\mu_t = \rho C_\mu k^2 / \varepsilon \quad (6)$$

The recommended values of the model constants are [2]:  $\sigma_k = 1.0$  ,  $\sigma_\varepsilon = 1.3$  ,  $C_{1e} = 1.44$  ,  $C_{2e} = 1.92$  and  $C_\mu = 0.09$  .

### 2.3 CHEN-KIM K-EPSILON MODEL

It has been recognized that the poor prediction of the spread rate of a turbulent round jet by the standard k-ε model is due to the inadequacy of the equation for dissipation rate [3]. For the standard k-ε model a single time scale,  $k/\varepsilon$ , is used which is an over simplification of the multiple time scales associated with energy transfer between eddies of different sizes [3].

A second time scale related to the production of turbulence kinetic energy is thus introduced to reflect the energy transfer rate from large eddies to small eddies, which is controlled by the production range time scale ( $k/P_k$ ) and the dissipation rate time scale ( $k/\varepsilon$ ) [3]. The additional source term

$$S_\varepsilon = \frac{\rho C_{3e} P_k^2}{k} \quad (7)$$

is thus added to the right hand side of equation (4), which allows the dissipation rate equation to respond to the mean strain rate more efficiently, especially in the region where the main strain rate changes rapidly. The recommended values for the model constants are [3]:  $\sigma_k = 0.75$ ,  $\sigma_\varepsilon = 1.15$ ,  $C_{1e} = 1.15$ ,  $C_{2e} = 1.90$ ,  $C_{3e} = 0.25$ , and  $C_\mu = 0.09$ .

## 2.4 RNG K-EPSILON MODEL

The RNG k- $\varepsilon$  model is derived from the instantaneous Navier–Stokes equation using a mathematical approach called the renormalization group [4]. The effects of the small eddies are represented by means of a random forcing function in the Navier–Stokes equation. The RNG procedure systematically removes the small scale eddies from the governing equations by expressing their effects in terms of large scale eddies through the modified viscosity (i.e.  $\nu_t$  in equations (3) and (4) is replaced by the effective viscosity  $\nu_{eff} = \nu_t + \nu_t$  where  $\nu_t$  is the molecular viscosity). In addition, equation (4) contains a strain-dependent correction term which is given by

$$S_\varepsilon = -\frac{\rho C_\mu \eta^3 (1 - \eta/\eta_0) \varepsilon^2}{1 + \beta \eta^3} \quad (8)$$

where  $\eta = (k/\varepsilon) \cdot \sqrt{(\rho P_k / \mu_t)}$ ,  $\eta_0 = 4.38$  and  $\beta = 0.012$ . The other model constants are [4]:  $\sigma_k = \sigma_\varepsilon = 0.7194$ ,  $C_{1e} = 1.42$ ,  $C_{2e} = 1.68$  and  $C_\mu = 0.0845$ .

## 3 RESULTS AND DISCUSSION

Computations have been carried out for the experimental conditions of Frind et al. [9], Benneson et al. [10] and Frind and Rich [11]. Altogether 3 nozzles with different shapes and dimensions as well as electrode configurations have been studied, which are shown in Fig.1.

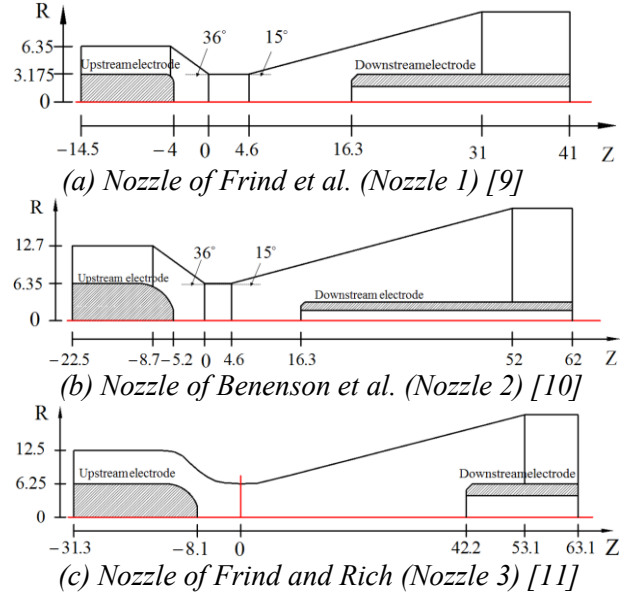


Fig.1: Three nozzle configurations used in the GE experiments. Unit of dimensions: mm

Version 3.6.1 of PHOENICS [13] has been used to solve the governing equations. The boundary conditions for the arc conservation equations and the k- $\varepsilon$  model equations are detailed in [12]. The flow conditions at the inlet and outlet of the nozzles in Fig.1 are set according to the test conditions reported in [9, 10, 11]. At the nozzle inlet, stagnation pressures ( $P_0$ ) ranging from 7.8 atm to 37.5 atm are used. At the nozzle exit, a sufficiently low static pressure ( $P_e$ ) is set for Nozzles 1 and 2, to ensure shock free for the supersonic flow inside the nozzle. For Nozzle 3,  $P_e = P_0/4$ .

The arcing current is linearly ramped down to zero with a fixed rate of decay,  $di/dt$ , from a plateau of 1 kA DC. Two values of  $di/dt$  are used for each nozzle, i.e. 13 and 25  $A\mu s^{-1}$  for Nozzles 1 and 2, and, 13.5 and 27  $A\mu s^{-1}$  for Nozzle 3.

For the Prandtl mixing length model, the turbulence parameter,  $c$ , was adjusted to give the closest agreement between the computed and measured RRRV for a given nozzle geometry. The values of  $c$  for the three nozzles are respectively 0.054 for Nozzle 1, 0.057 for Nozzle 2 and 0.045 for Nozzle 3.

The qualitative features of computational results for different nozzle configurations, and different values of  $P_0$  and  $di/dt$  are similar. Unless otherwise specified, results obtained by the five flow models are given for Nozzle 2 at  $P_0 = 21.4$  atm and  $di/dt = 13$   $A\mu s^{-1}$ . Based on

these results, an analysis of the physical mechanisms encompassed in each flow model is given to show the adequacy of a particular model in describing the rapidly varying arc during current zero period.

### 3.1 ARC BEHAVIOUR BEFORE CURRENT ZERO

The variations of axis temperature and arc radius (defined as the 4000 K isotherm) with axial position at different current levels on the ramp before current zero are, respectively, given in Figs.2 and 3 for those predicted by the standard k-ε model and the Chen-Kim model. Results obtained by the Prandtl mixing length model, the RNG model and the laminar flow model are not given, since the qualitative features of results obtained by the Prandtl mixing length model are the same as those for the standard k-ε model, and results for the RNG model and the laminar flow model are similar to those for the Chen-Kim model.

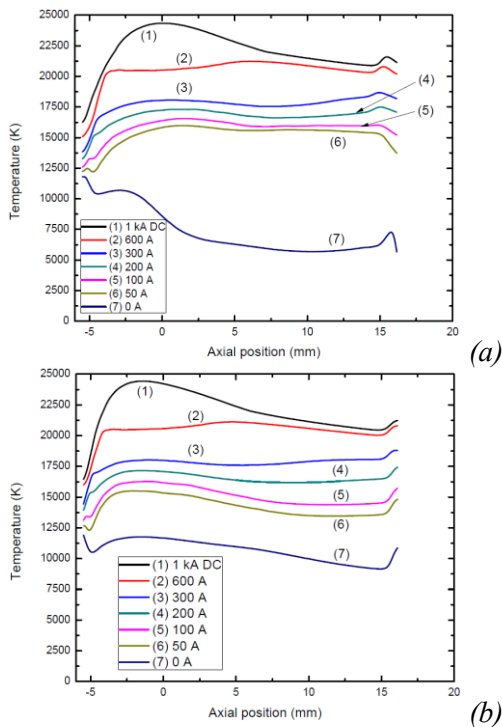


Fig.2: Variation of axis temperature with current decay computed by two flow models. (a) Standard k-ε model and (b) Chen-Kim model

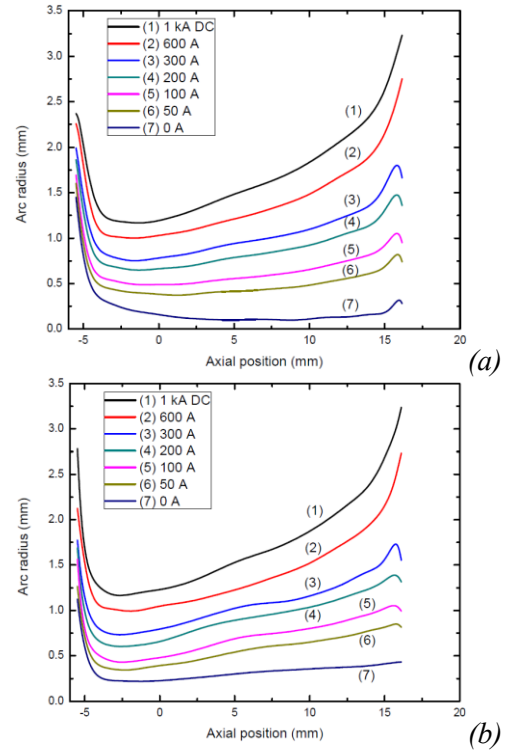


Fig.3: Variation of arc radius with current decay computed by two flow models. (a) Standard k-ε model and (b) Chen-Kim model

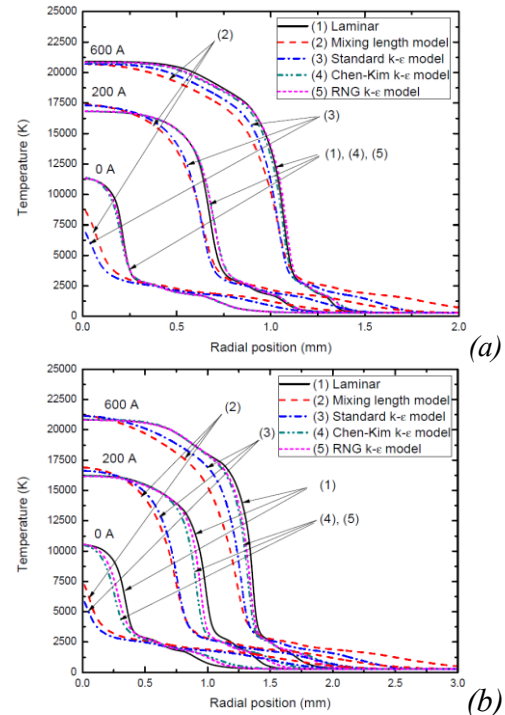


Fig.4: Radial temperature profiles at two axial positions computed by five flow models at three currents before current zero (600 A, 200 A and current zero). (a) Z=2.3 mm and (b) Z=7.9 mm

When the current is large (600 A and above), the axis temperature (Fig.2) and arc radius (Fig.3) predicted by the different flow models show little difference. The axial electric field not only depends on the axis temperature and arc radius but also on the radial temperature profile. Typical radial temperature profiles predicted by the five flow models (e.g. profiles for 600 A in Fig.4) all show a significant high temperature arc core (with the core boundary defined by 83% of the axis temperature), the radius of which is more than 70% of the arc radius for a given axial position, e.g. for  $Z=7.9$  mm and at 600 A, the arc core boundary (predicted by all the five flow models) is around 1 mm and the arc radius is around 1.35 mm (Fig.4(b)). Within this arc core, the temperature is uniform and is not sensitive to flow models. Such temperature profile indicates that within the arc core radiation transport is dominant. Examination of the energy balance reveals that, for all the flow models, radiation is the most important energy transport mechanism inside the arc core. In the thin layer surrounding the arc core (commonly known as the thermal layer, defined as the region between the arc core boundary and the electrical boundary where the temperature is 4000 K), the energy transport processes predicted by different flow models show significant difference. For laminar flow, Chen-Kim and RNG models, Ohmic heating is balanced collectively by radiation, axial and radial convections, while thermal conduction has the least influence. For the Prandtl mixing length model and the standard k- $\epsilon$  model, turbulent thermal conduction and axial convection are the most important energy loss processes. Thus, the radial temperature profile within this thermal layer (profiles for 600 A in Fig.4) is sensitive to flow models. It is also noted that the turbulence effect predicted by the Prandtl mixing length model is stronger than that of the standard k- $\epsilon$  model, which gives slightly lower temperature (Fig.4). Nevertheless, the thermal layer is very thin in comparison with the high temperature arc core. Therefore, it is found that 80% of the current is conducted within the arc core where radiation is dominant, and thus turbulence has little

influence on the arc voltage: the spread in arc voltages computed by the five flow models for the current of 600 A and above is less than 15% of the mean voltage of those predicted by the five flow models (Fig.5). In addition, for all the flow models, the axis temperature is not sensitive to the current (Fig.2), and the arc radius is roughly proportional to the square root of current (Fig.3). The arc voltage is, thus, almost independent of the current (Fig.5) down to approximately 600 A.

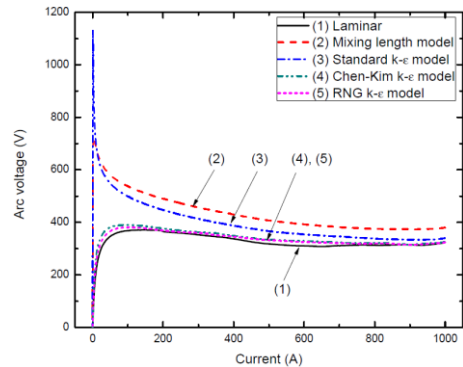


Fig.5: The voltage-current ( $V$ - $I$ ) characteristics for the nozzle arcs computed by five flow models in the current ramp

It is also found that, for all the flow models applied, up to the core boundary, the rate of change of energy storage accounts for less than 7% of the Ohmic heating for the current of 600 A and above. Since the high temperature core is mainly responsible for conducting the current, the arc at high current can be considered in quasi-steady state, although up to the electrical boundary the rate of energy storage accounts for more than 10% of the Ohmic heating.

When the current is further ramped down towards current zero (below 600 A), the axis temperature is reduced due to weakened Ohmic heating (Fig.2). The dependence of the arc radius on current is found to be stronger than that for currents above 600 A (Fig.3). The arc voltage, therefore, starts to rise with decreasing current (Fig.5). The energy balance based on all the flow models indicate that, from the instant of 200 A, the rate of change of energy storage cannot be neglected in comparison with Ohmic heating and the other energy transport mechanisms, which means the arc deviates from quasi-steady state. We therefore

consider that, from the instant of 200 A, the arc starts to be in its current zero period. During this period, the aerodynamic and electrical behaviour of the arc is significantly affected by the current decay, and the state of arc at current zero is determined by the accumulated effects of arcing heating and cooling from the start of the current zero period to current zero. It should however be noted that the definition of the current zero period is not precise. In high voltage gas blast circuit breakers, the threshold value is around 15 kA for a nozzle radius of 12 – 16 mm [14]. The instant from which the arc transits into the current zero period varies for different discharge conditions, especially the rate of change of current.

During the current zero period, the overall features of the transient arc predicted by different flow models become quite different. It has been found that the axis temperature and arc radius predicted by the standard k- $\epsilon$  model and the Prandtl mixing length model decrease rapidly in the last 4  $\mu$ s before the current zero (i.e. when the current level is below 50 A, as shown in Figs.2(a) and 3(a)). This is responsible for the formation of an extinction voltage peak shortly before current zero (Fig.5). For laminar flow, Chen-Kim and RNG models, the axis temperature and arc radius show a monotonic decrease when the current is ramped down towards zero (Fig.2(b) and 3(b)), and the rates of decrease of the axis temperature and arc radius are much lower than those predicted by the Prandtl mixing length model and the standard k- $\epsilon$  model. This gives a much longer characteristic time for the variation of arc conductance ( $\tau_G = G/|dG/dt|$ , where  $G$  is the arc conductance) shortly before current zero predicted by these three models, e.g. immediately before current zero, for the Chen-Kim model  $\tau_G=0.6 \mu$ s, which is much longer than that computed by the standard k- $\epsilon$  model,  $\tau_G=0.04 \mu$ s. As a result, the arc voltages predicted by the Chen-Kim, the RNG and the laminar flow models show no extinction peak before current zero (Fig.5).

The large difference in the overall features of the transient arc predicted by different flow models (Figs.2 and 3) during the current zero period, and the resulting difference in the V-I

characteristics (Fig.5), indicate that the energy transport processes predicted by these models are very different. Examination of the energy balance reveals that, for the Prandtl mixing length model and the standard k- $\epsilon$  model, turbulence thermal conduction gradually becomes important within both the arc core and at the electrical boundary when the current is further reduced towards zero. Thus, the radial temperature profiles (e.g. profiles for 200 A in Fig.4) computed by these two models have considerable radial temperature gradient inside the arc core. Such strong turbulence cooling is responsible to the rapidly reducing arc temperature shortly before current zero as shown in Figs 2(a) and 4.

For the other three models, inside the arc core radiation loss is still the dominant energy loss mechanism, for which the corresponding radial temperature profile still show an apparent arc core (profiles for 200 A in Fig.4). Up to the electrical boundary, axial convection and radiation loss are important, while turbulent thermal conduction (for Chen-Kim and RNG models only) has the least importance.

At current zero, the very low axis temperature renders radiation loss negligible, and the arc behaviour is determined by energy balance up to the electrical boundary. For laminar flow, the Chen-Kim and RNG models, turbulent thermal conduction (for Chen-Kim and RNG models only), radial and axial convective cooling collectively control the thermal state of the arc. For the Prandtl mixing length model and the standard k- $\epsilon$  model, turbulent thermal conduction and radial convective cooling associated with radial mass inflow are dominant cooling mechanisms. As previously mentioned, during the current ramp, the turbulence effect predicted by the Prandtl mixing length model is stronger than that of the standard k- $\epsilon$  model, and thus the arc voltage predicted by the Prandtl mixing length model is always higher (Fig.5). However, such trend is reversed shortly before current zero, during which the temperature and arc radius reduce very rapidly resulting in lower temperature and smaller arc radius at current zero for the standard k- $\epsilon$  model. This corresponds to the highest voltage extinction peak predicted by

the standard k-ε model (Fig.5), and subsequently over-estimations of the thermal interruption of the nozzle by this model (to be discussed below).

### 3.2 ARC BEHAVIOUR AFTER CURRENT ZERO

A linearly increasing voltage at a given rate of rise (dV/dt) is used after current zero to investigate the thermal interruption capability of the nozzle configuration. The value of the rate of rise of recovery voltage (dV/dt), at which the arc will just be extinguished, is commonly known as the critical rate of rise of recovery voltage (RRRV). RRRV indicates the thermal interruption capability of the nozzle. This will be found computationally using the five flow models for comparison with the test results.

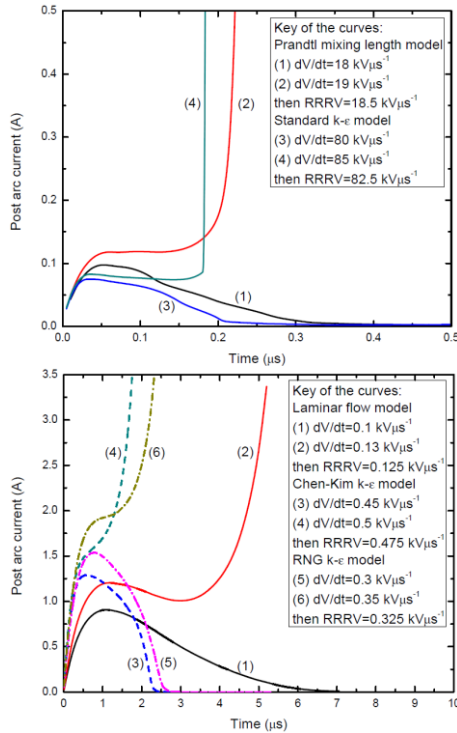


Fig.6: Post-arc current computed by the five flow model

Typical results of post-arc current computed by the five flow models are given in Fig.6. Typical axis temperature and electrical field distributions at different instants after current zero are given in Figs.7 and 8 for the Prandtl mixing length model and the laminar flow model, respectively. Results predicted by the other turbulence models are not given as they are qualitatively similar to those computed by the Prandtl mixing length model.

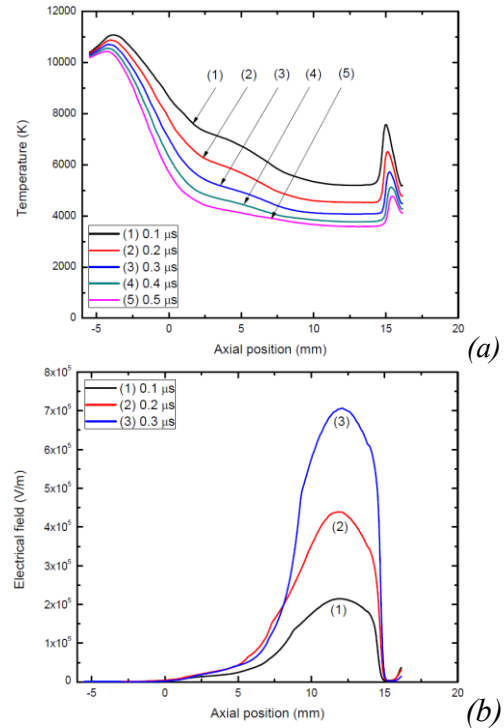


Fig.7: (a) Axis temperature and (b) electrical field distribution at various instants after current zero obtained by the Prandtl mixing length model for dV/dt=18 kVμs<sup>-1</sup>

For the Prandtl mixing length model, when the arc is thermally extinguished, the arc temperature decays rapidly in 0.5 μs after current zero (Fig.7(a)), corresponding to rapid increase of electrical field (Fig.7(b)), in the region of approximately 9 mm downstream of the exit of the flat nozzle throat (i.e. from Z=5 to 14 mm). It is this critical section of the arc that takes up most of the recovery voltage where turbulent thermal conduction and radial inflow cooling are mainly responsible for the rapid cooling of the arc. The standard k-ε model predicts similar arc behaviour after current zero. However, this model predicts a longer critical section than that given by the Prandtl mixing length model, and a more rapid temperature decay rate. This is due to stronger turbulence cooling effects predicted by this model from the instants shortly before current zero as previously discussed. The RRRV computed by the standard k-ε model is therefore significantly higher than that of the Prandtl mixing length model as shown in Fig.6.

The Chen-Kim and RNG models both predict a shorter critical section of the arc and a much slower cooling rate than those predicted by the

Prandtl mixing length model and the standard k-ε model. This is due to much weaker turbulence effects predicted by these two models. The RRRV computed by Chen-Kim and RNG models are therefore of two orders of magnitude lower than that predicted by the other two turbulence models as indicated in Fig.6.

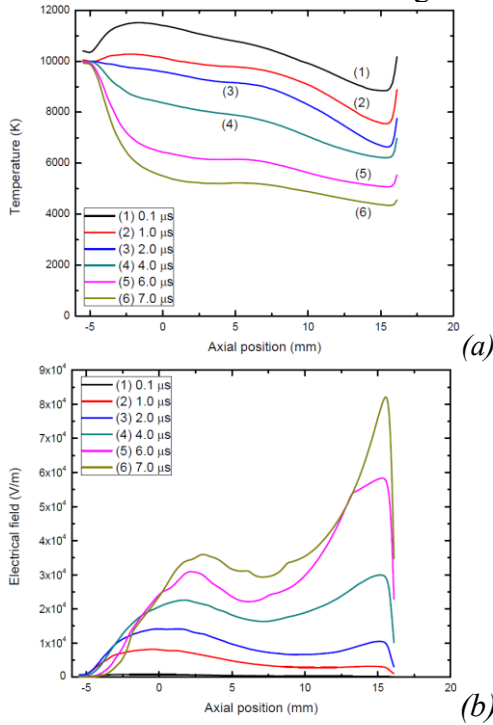


Fig.8: (a) Axis temperature and (b) electrical field distributions at various instants after current zero obtained by the laminar flow model for  $dV/dt=0.1$   $kV\mu s^{-1}$

The laminar flow model predicts a decaying temperature in the whole arc column during the thermal recovery (Fig.8(a)) but the rate of temperature decay is the slowest in comparison with those predicted by the four turbulence models. The electrical field (Fig.8(b)) increases with time due to temperature decay and as a result of axial and radial convective cooling. The peak of the electrical field moves from upstream region to downstream region of the nozzle throat (Fig.8(b)), corresponding to a more rapid rate of temperature decay downstream of the nozzle throat (Fig.8(a)), where axial convection is mainly responsible for arc cooling. RRRV predicted by this model is thus the lowest (Fig.6(b)).

#### 4 COMPARISON WITH EXPERIMENTS

The computed values of RRRV are plotted in

Fig.9 together with experimental results given in [10] for comparison. Such a comparison shows that the RRRV predicted by the laminar flow model is a few orders of magnitude lower than that measured, which indicates that turbulence plays a decisive role in the determination of the thermal interruption capability of the nozzle. Of the four turbulence models, the Prandtl mixing length model can generally give satisfactory predictions of the RRRV with optimised turbulence parameter. This is based on the understanding that the turbulence parameter is fixed for each nozzle. The standard k-ε model grossly over-estimates the RRRV for all discharge conditions investigated. The Chen-Kim and RNG models both predict RRRV of the same order of magnitude of that predicted by the laminar flow model. This means these two models significantly underestimate the turbulence effects, and thus they are not capable of predicting the thermal interruption capability of the nozzle.

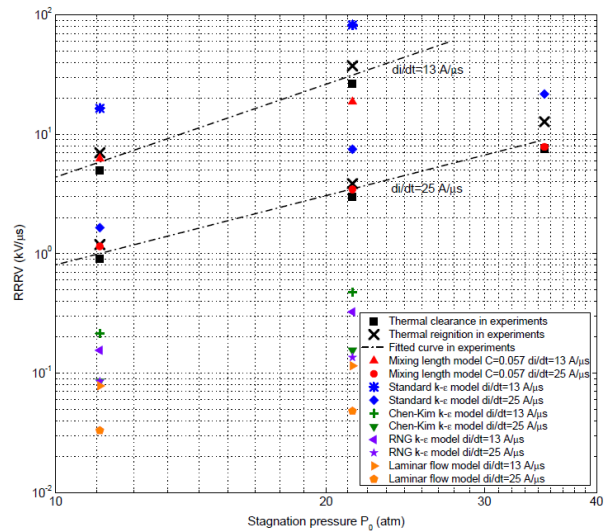


Fig.9: For Nozzle 2: comparison between measured RRRV [10] and predicted RRRV obtained by the five flow models (this work)

It is, however, not sufficient to draw conclusions with regard to the relative merits of turbulence models by comparison of the predicted and measured RRRV based on only one nozzle. We have therefore extended our investigation by considering other nozzle geometries (i.e. Nozzles 1 and 3). Because of the large discrepancy between experimentally measured RRRV and those obtained by laminar flow model and the two variants of the

standard k-ε model, we only test the Prandtl mixing length model and the standard k-ε model. Although the standard k-ε model has grossly over-estimated the RRRV for Nozzle 2, such a conclusion cannot be extended to different nozzles, as it does give good prediction for certain nozzle configuration and discharge conditions (e.g. for Nozzle 1 at P<sub>0</sub>=21.4 atm and di/dt=13 Aμs<sup>-1</sup>) [15]. Comparisons between the predicted and measured RRRV are shown in Fig.10 for Nozzle 1 and Fig.11 for Nozzle 3. Such comparisons show that the standard k-ε model under-estimates the RRRV for Nozzle 1 under most discharge conditions, although it does give satisfactory predictions under certain discharge conditions (e.g. P<sub>0</sub>=18 and 21.4 atm and di/dt=13 Aμs<sup>-1</sup>, Fig.10). Similar to Nozzle 2, the standard k-ε model grossly over-predicts the RRRV in Nozzle 3. The computed RRRV based on the Prandtl mixing length model agrees well with the measured RRRV for Nozzle 3. For Nozzle 1, it gives reasonable predictions for most discharge conditions except for di/dt=13 Aμs<sup>-1</sup>. Actually, for all three nozzles, this model gives similar dependence of RRRV on P<sub>0</sub> for different values of di/dt, while the experimental results for Nozzle 1 indicate much stronger pressure dependence at lower di/dt. In theory, the dependence of RRRV on P<sub>0</sub> should not be sensitive to di/dt. If the dependence of RRRV on stagnation pressure is related to di/dt, this will result in the intersection of lines in Fig.10. Such an intersection would imply that at certain range of P<sub>0</sub>, the RRRV for a lower di/dt would be smaller than that for a higher di/dt. This is not physical. The experimental results for Nozzle 1 at di/dt=13 μs<sup>-1</sup> are therefore not very reliable. It is well known that the value of RRRV has a large shot to shot variation. Error bars of the experimental results of [9, 10, 11] are not given. Taking into account the experimental uncertainties, we argue that the predicted RRRV by the Prandtl mixing length model at di/dt=13 Aμs<sup>-1</sup> for Nozzle 1 is acceptable.

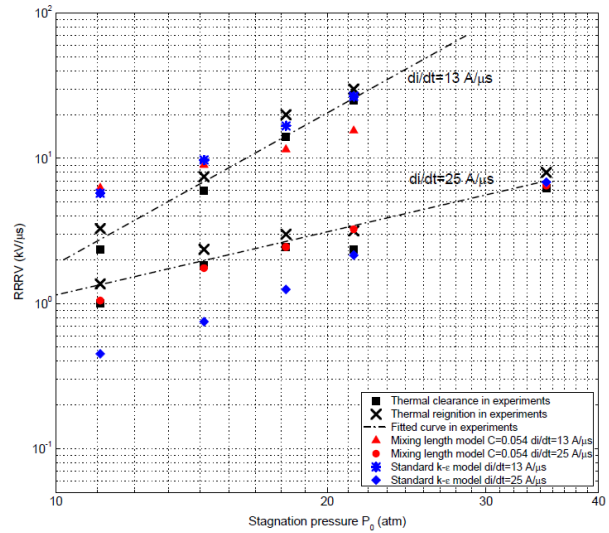


Fig.10: For Nozzle 1: comparison between measured RRRV [9] and predicted RRRV obtained by two flow models (this work)

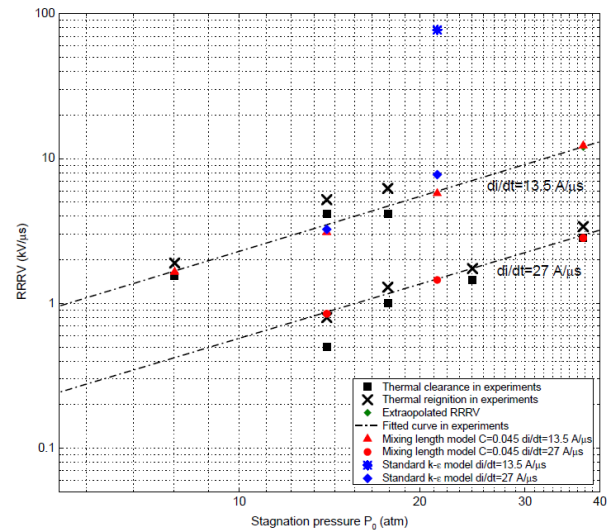


Fig.11: For Nozzle 3: comparison between measured RRRV [11] and predicted RRRV obtained by two flow models (this work)

## 5 RELATIVE MERITS OF TURBULENCE MODELS

Of the four turbulence models, the standard k-ε model and its two variants, with recommended values of turbulence parameters, cannot give satisfactory predictions on the thermal interruption capability of nozzle arcs under the range of discharge conditions studied, unless further optimizations are made on either turbulence parameters or model equations.

The Prandtl mixing length model can generally give reasonable predictions of RRRV for the range of discharge conditions investigated, although the only turbulence parameter needs to be tuned based on one measured RRRV value. This model is therefore preferred if a known RRRV is available. It is also much easier to implement and the computational cost is the lowest.

## 6 CONCLUSIONS

The current zero behaviour of SF<sub>6</sub> switching arcs has been numerically investigated using five flow models: the laminar flow model, the Prandtl mixing length model, the standard k- $\epsilon$  model, the Chen-Kim and the RNG models. These models are assessed by test results produced by GE experiments covering a wide range of discharge conditions [9, 10, 11], and arcs in three nozzle geometries are studied.

Detailed computational results obtained by the five flow models are given for Nozzle 2 at  $P_0=21.4$  atm and  $di/dt=13$  Aus<sup>-1</sup>. The V-I characteristics of the transient arc are predicted by the five flow models. On the flat part of the V-I characteristics (corresponding to higher currents), 80% of the current is conducted by the high temperature arc core where radiation is the dominant energy loss mechanism. Turbulence therefore has little influence on the arc behaviour at high currents, meaning the arc voltage at high current is not an effective means to verify turbulence models. It is also found that, at high currents, the arc is in quasi-steady state, which means the arc behaviour is not sensitive to the rate of current decay, but only to the instantaneous current.

When the arc is further ramped down towards its zero point, the arc cannot maintain quasi-steady state. Hence, it is known to be in current zero period, when the arc behaviour depends on the rate of current decay. Within this period, thermal conduction due to turbulence effects becomes more and more important due to reduced arc size. The V-I characteristics thus become sensitive to flow models. The Prandtl mixing length model and the standard k- $\epsilon$  model both predict a high voltage extinction peak shortly before current zero, and high RRRV after current zero, due to strong turbulence effects and strong cooling associated

with inward cold gas predicted by these two models. The Chen-Kim and RNG models predict much weaker turbulence effects, and thus the computed arc voltages and RRRV are only slightly higher than those predicted by the laminar flow model. Of the four turbulence models, the Prandtl mixing length model gives the best prediction of RRRV when compared with experimental results.

## REFERENCES

- [1] Zhang Q, Modelling of Turbulence SF<sub>6</sub> Switching arcs, PhD thesis, the University of Liverpool, Liverpool 2014.
- [2] Wilcox D C, Turbulence Modeling for CFD, DCW Industries, La Cañada, CA 2006.
- [3] Chen Y S, Kim S W, Computation of turbulent flows using an extended k- $\epsilon$  turbulence closure model, Interim report, NASA, CR-179204, 1987.
- [4] Yakhot V, Orszag S A, Thangam S, Gatski T B, Speziale C G, Phys Fluids A 4 (1992) 1510-1520.
- [5] Fang M T C, Zhuang Q, Guo X J, J Phys D: Appl Phys 27 (1994) 74-83.
- [6] Yan J D, Nuttall K I, Fang M T C, J Phys D: Appl Phys 32 (1999) 1401-1406.
- [7] Song K D, Lee B Y, Park K, J Korean Phys Soc 45 (2004) 1537-1543.
- [8] Bini R, Basse N T, Seeger M, J Phys D: Appl Phys 44 (2011) 025203.
- [9] Frind G, Kinsinger R E, Miller R D, Nagamatsu H T, Noeske H O, Fundamental investigation of arc interruption in gas flows EPRI EL-284 (Project 246-1), 1977.
- [10] Benenson D M, Frind G, Kinsinger R E, Nagamatsu H T, Noeske H O, Sheer, Jr R E, Fundamental Investigation of Arc Interruption in Gas Flows EPRI EL-1455 (Project 246-2), 1980.
- [11] Frind G, Rich J A, IEEE Trans Power Appar Syst 93 (1974) 1675-1684.
- [12] Zhang Q, Yan J D, Fang M T C, J Phys D: Appl Phys 47 (2014) 215201.
- [13] PHOENICS is the name of a commercial CFD package supplied by CHAM which is based at Bakery House, 40 High Street, Wimbledon Village, London, SW19 5AU, UK.
- [14] Yan J D, Han S M, Zhan Y Y, Zhao H F, Fang M T C, Computer simulation of the arcing process in high voltage puffer circuit breakers with hollow contacts, In: Proceedings of FSO2009, Brno, Czech Republic, 2009.
- [15] Zhang Q, Liu J, Yan J D, IEEE Trans Plasma Sci 42 (2014) 2726-2727.

# Modelling Radiative Properties of SF<sub>6</sub> Arc Plasma

Bartlova M.<sup>1</sup>, Bogatyreva N.<sup>1</sup>, Aubrecht V.<sup>1</sup>

<sup>1</sup>Faculty of Electrical Engineering and Communication, Brno University of Technology, Technicka 10, 616 00 Brno, Czech Republic, bartlova@feec.vutbr.cz

The objective of this work is to compare the accuracy of several approximate radiative properties models for the prediction of radiative transfer in SF<sub>6</sub> arc plasma at the temperatures in the range of 300–25000 K and pressure of 1 MPa. Calculated absorption coefficients are used to generate the parameters of different approximate models. In order to compare the accuracy of various approximate models, the radiative transfer inside the cylindrically symmetrical SF<sub>6</sub> plasma with prescribed temperature profile was calculated using the P1-approximation.

**Keywords:** plasma radiation, SF<sub>6</sub> arc plasma, radiative property modelling

## 1 INTRODUCTION

Total energy balance in thermal plasmas is strongly influenced, or even dominated by radiative transport of energy. The radiative fluxes or the balance between emission and absorption of radiative power are very important for an understanding of the physical behavior of the arc plasmas.

Predicting the radiative transfer from an exact resolution of the spectral radiative transfer equation remains a formidable task because of the need to treat continuum radiation and hundreds of spectral lines spanning wavelengths from the far infrared to the short ultraviolet spectral regions. Among various approximate methods [1 - 4] the P1-approximation has extensively been used in association with different simplifications of radiative properties.

The aim of this work is to compare the accuracy of several approximate radiative properties models for the prediction of radiative transfer in SF<sub>6</sub> arc plasma at the temperatures in the range of 300 – 25000 K and pressure of 1 MPa. Calculated absorption coefficients are used to generate the parameters of different approximate models: (1) Planck MAC (Mean Absorption Coefficient), Rosseland MAC and their combination for two different splitting of frequency interval; (2) Planck MAC and Rosseland MAC calculated for frequencies grouped based on frequency and also on magnitude of absorption coefficients; (3) SLW (Spectral Line Weighted Sum of Gray Gases) model, combined with Planck MAC and Rosseland MAC. In order to compare the accuracy of various approximate models, the

radiative transfer inside the cylindrically symmetrical SF<sub>6</sub> plasma with prescribed temperature profile was calculated using the P1-approximation. It is shown that good accuracy with exact spectral integration gives the combination of Planck and Rosseland MAC calculated for frequency and magnitude grouping.

## 2 ABSORPTION COEFFICIENTS AND APPROXIMATE MODELS

Absorptivity  $\kappa_\nu$  is proportional to the concentrations of the chemical species occurring in the plasma. In SF<sub>6</sub> plasma, we assume following species: SF<sub>6</sub> molecules, S and F neutral atoms, S<sup>+</sup>, S<sup>+2</sup>, S<sup>+3</sup>, F<sup>+</sup>, F<sup>+2</sup> ions and free electrons. Equilibrium composition of the plasma was computed using Tmdgas computer code [5].

Spectral absorption coefficients  $\kappa_\nu$  were calculated using semi-empirical formulas to represent both continuum and line radiation. Continuum spectrum is formed by bound-free transitions (photoionization) and free-free transitions (bremsstrahlung). Photoionization cross sections for neutral atoms were calculated by the quantum defect method of Burgess and Seaton [6], the cross sections of photoionization of ions and free-free transitions were treated using Coulomb approximation for hydrogen-like species [7]. In the discrete radiation calculation spectral lines broadening and their complex shapes were considered. The lines are broadened due to numerous phenomena; the most important are Doppler broadening, Stark broadening, and resonance broadening. Calculated total spectral absorption coef-

ficients for SF<sub>6</sub> plasma at the pressure of 1 MPa and the temperatures of 5 000 K and 15 000 K are presented in Fig. 1.

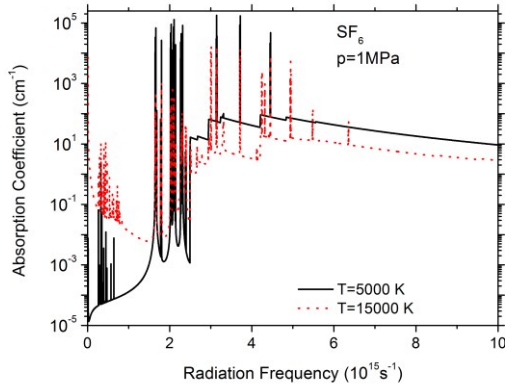


Fig. 1: Absorption coefficients of radiation for SF<sub>6</sub> plasma

## 2.1 PLANCK AND ROSSELAND MAC MODEL

Mean absorption coefficient (MAC) models use a splitting of the spectral range into several frequency groups across which the absorption coefficient is assumed to be constant and equal to a mean value  $\bar{\kappa}_v$ . The more frequency groups, the more accurate results we get. However, the number of groups should be minimized to decrease the computation time. In this work, the frequency interval ( $10^{12}$  -  $10^{16}$ ) s<sup>-1</sup> was split into

- (a) five frequency groups with splitting (0.001, 1, 2, 3.3, 8, 10) $\times 10^{15}$  s<sup>-1</sup>
- (b) ten frequency groups with splitting (0.001, 0.151, 0.89, 1.585, 2.172, 2.488, 3.143, 4.117, 4.839, 8.441, 10) $\times 10^{15}$  s<sup>-1</sup>

The mean values of absorption coefficients were taken as either Planck ( $\kappa_P$ ) or Rosseland ( $\kappa_R$ ) means:

$$\kappa_P = \int_{\nu_k}^{\nu_{k+1}} \kappa_\nu B_\nu d\nu / \int_{\nu_k}^{\nu_{k+1}} B_\nu d\nu, \quad (1)$$

$$\kappa_R^{-1} = \int_{\nu_k}^{\nu_{k+1}} \kappa_\nu^{-1} \frac{dB_\nu}{dT} d\nu / \int_{\nu_k}^{\nu_{k+1}} \frac{dB_\nu}{dT} d\nu, \quad (2)$$

where  $B_\nu$  denotes the Planck function. The five spectral bands and the mean absorption coefficients for temperature of 15 000 K are shown in Fig. 2 with the high resolution spectra. The temperature dependence of mean absorption coefficients for five groups splitting is shown in Fig. 3.

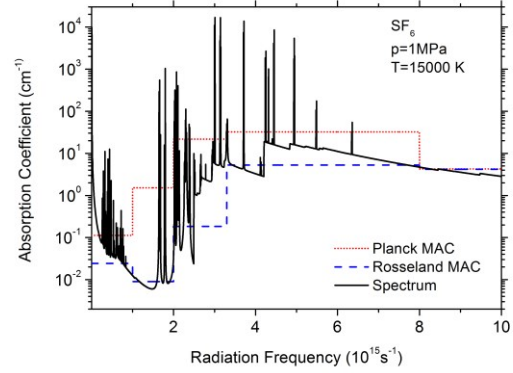


Fig. 2: The high resolution spectrum of SF<sub>6</sub> plasma compared with Planck and Roseland MAC

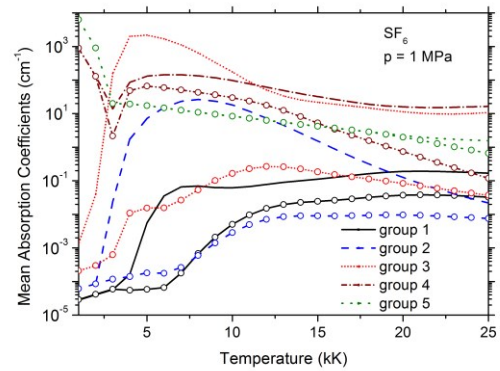


Fig. 3: MAC as a function of temperature for five groups splitting: lines – Planck MAC, lines + symbols – Rosseland MAC

It can be seen that Planck MACs overestimate the influence of spectral lines, on the other hand Rosseland MACs underestimate it. Great difference between Planck and Rosseland MAC occurs especially for groups 2 and 3 (i.e. for frequencies from ( $1 \times 10^{15}$  -  $3.3 \times 10^{15}$ ) s<sup>-1</sup>).

## 2.2 $\kappa$ -BASED GROUP AVERAGING

To improve the accuracy of the group averaging method 2.1, further splitting of particular frequency groups to subgroups based on the magnitude of  $\kappa$  was proposed in [8]. The frequency interval was split into 8 frequency groups

(0.001, 1, 1.4, 1.77, 2, 2.2, 2.5, 3, 10) $\times 10^{15}$  s<sup>-1</sup>.

Every frequency group was divided to 4 subgroups based on the magnitude of  $\kappa_\nu$  (in cm<sup>-1</sup>)

$$\kappa_\nu \in \{0, 0.1\}, \{0.1, 1\}, \{1, 10\}, \{10, \infty\}.$$

Planck and Rosseland MACs were calculated for each subgroup.

### 2.3 SLW MODEL

The Spectral Line Weighted Sum of Gray Gases (SLW) model has been developed by Denison and Webb [9]. In this model the absorption coefficient domain is divided into several ranges  $m$  (in our case  $m = 10$ ), bounded by  $k_{j+1}$  and  $k_j$ ,  $k_{j+1} > k_j$ . The lower ( $k_1$ ) and upper ( $k_m$ ) bounds of the domain partition are chosen such that  $k_1$  is smaller than minimum  $\kappa_\nu$ , and  $k_m$  is greater than maximum  $\kappa_\nu$ . The absorption coefficient boundaries  $k_j$  are obtained by equally partitioning the absorption coefficient domain in a logarithmic scale. For each absorption coefficient range  $j$ , associated frequency ranges  $\Delta\nu_{j,i}$  are defined such that for each  $\nu$  in  $\Delta\nu_{j,i}$  the actual absorption coefficient  $\kappa_\nu$  lies in the range  $\{k_j, k_{j+1}\}$  (Fig. 4).

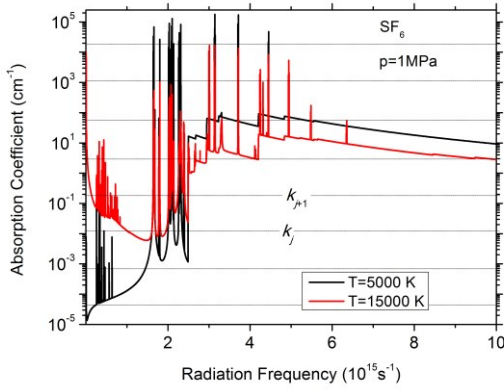


Fig. 4: SLW absorption coefficients domain partition

Representative constant absorption coefficient values within each range are chosen as:

- $\bar{\kappa}_j^* = \sqrt{k_j k_{j+1}}$
- Planck mean, i.e.  $\bar{\kappa}_j = \kappa_{Pj}$
- Rosseland mean, i.e.  $\bar{\kappa}_j = \kappa_{Rj}$

The radiation transfer equation for each coefficient range can be written as

$$\vec{\Omega} \cdot \nabla I_j = -\bar{\kappa}_j (I_j - B_j), \quad (3)$$

where  $\vec{\Omega}$  is the unit direction vector and the weights  $B_j$

$$B_j = \sum_i \int_{\Delta\nu_{j,i}} B_\nu d\nu. \quad (4)$$

### 3 P1-APPROXIMATION

In order to compare the accuracy of various

approximate models, the radiative transfer inside the cylindrically symmetrical SF<sub>6</sub> plasma with prescribed temperature profile was calculated using the P1-approximation. The P1-approximation consists of expanding radiative intensity in spherical harmonics and including only the first order terms. Under this assumption the equation of radiative transfer leads to simple elliptic equation for the group density of radiation  $U_j$

$$\nabla \cdot \left[ -\frac{c}{3\bar{\kappa}_j} \nabla U_j \right] + \bar{\kappa}_j c U_j = 4\pi B_j \bar{\kappa}_j. \quad (5)$$

The group radiative flux  $\vec{F}_j$  is given by

$$\vec{F}_j = -\frac{c}{3\bar{\kappa}_j} \nabla U_j. \quad (6)$$

The net emission of radiation is then

$$\nabla \cdot \vec{F}_R = \sum_j \nabla \cdot \vec{F}_j. \quad (7)$$

Figures 5 – 8 compare the net emission calculated with various average absorption coefficients with results of the exact spectral integration [8]. In Fig. 5, MACs for 5-groups frequency splitting were used; Fig. 6 shows results of MACs for 10 frequency groups. Results of  $\kappa$ -based group averaging are shown in Fig. 7. In Fig. 8, the spectral averaging based on SLW model is presented.

It can be seen that Planck MAC overestimate the net emission in all cases. The combination of Planck and Rosseland MACs was carried out such that Planck MAC were considered in frequency groups with low values of  $\kappa_\nu$ , in groups with high values of  $\kappa_\nu$  Rosseland MAC were used. The best fit with exact spectral integration was achieved using combination of Planck and Rosseland MACs calculated for  $\kappa$ -based averaging.

### 4 CONCLUSIONS

Comparison of the net emission in SF<sub>6</sub> plasma predicted using P1-approximation with various approximate radiative models and exact spectral integration have been performed. Planck MAC overestimate both emission and absorption of radiation for all used radiative models. Good accuracy with exact spectral integration gives the combination of Planck and Rosseland MAC calculated for frequency and magnitude grouping.

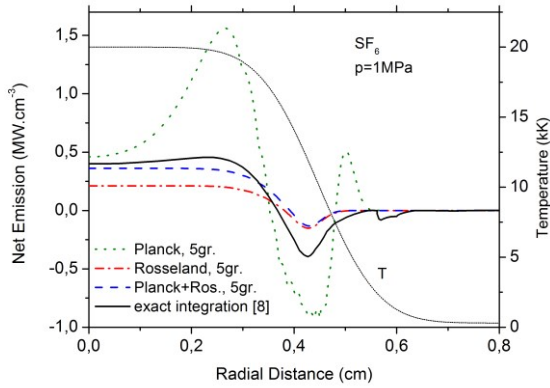


Fig. 5: Comparison between net emission obtained from exact spectral integration [8], and from Planck or Rosseland MAC for 5-groups frequency splitting

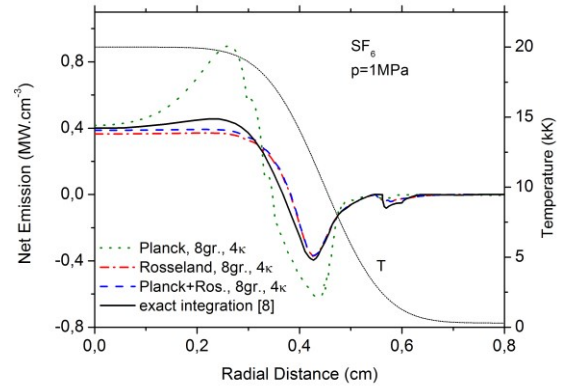


Fig. 7: Comparison between net emission obtained from exact spectral integration [8], and from Planck or Rosseland MACs for  $\kappa$ -based spectral averaging

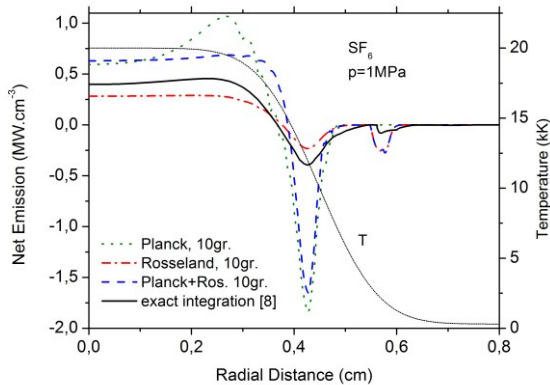


Fig. 6: Comparison between net emission obtained from exact spectral integration [8], and from Planck or Rosseland MAC for 10-groups frequency splitting

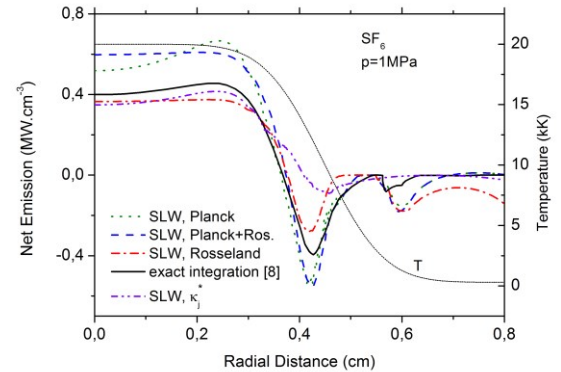


Fig. 8: Comparison between net emission obtained from exact spectral integration [8], and from SLW model

### Acknowledgements

The authors gratefully acknowledge financial support from the Ministry of Education, Youth and Sports under project No. LO1210 solved in the Centre for Research and Utilization of Renewable Energy and from the Czech Science Foundation under project No. 15-14829S.

### REFERENCES

[1] Raynal G, Gleizes A, Plasma Sources Sci Technol 4 (1995) 152-160.  
 [2] Aubrecht V, Bartlova M, Coufal O, J Phys D: Appl Phys 43 (2010) 434007.  
 [3] Peyrou B, Chemartin L, Lalande Ph, Cheron B

G, Riviere Ph, Perrin M Y, Soufiani A, J Phys D: Appl Phys 45 (2012) 455203.  
 [4] Modest M F, Radiative Heat Transfer, McGraw-Hill, New York 1993.  
 [5] Coufal O, Sezemsky P, Zivny O, J Phys D: Appl Phys 38 (2005) 1265-1274.  
 [6] Burges A, Seaton M, Rev Mod Phys 30 (1958) 992.  
 [7] Liebermann R, Lowke J J, JQSRT 16 (1976) 253-264.  
 [8] Nordborg H, Iordanidis A A, J Phys D: Appl Phys 41 (2008) 135205.  
 [9] Denison M K, Webb B W, J Heat Transfer 115 (1993) 1004-1012.

# Diffuse Coplanar Surface Barrier Discharge: Influence of Gas Humidity on Plasma Parameters

Čech J., Šťáhel P., Dvořáková H., Černák M.

CEPLANT - R&D Center for Low-Cost Plasma and Nanotechnology Surface Modification,  
Masaryk University, Kotlářská 2, 611 37 Brno, Czech Republic, cech@physics.muni.cz

It was found that the working gas humidity influences substantially the parameters of diffuse coplanar surface barrier discharge. The absolute humidity of air or N<sub>2</sub> has a strong influence on the discharge pattern and its macroscopic homogeneity. The amount of H<sub>2</sub>O in working gas influences also generated radicals and the plasma chemistry. We suggest that the humidity of working gas should be a controlled parameter of in-line atmospheric pressure plasma treatment under real industrial conditions.

**Keywords:** DCSBD, barrier discharge, atmospheric pressure, humidity, pattern, OES

## 1 INTRODUCTION

The surface energy of commonly used materials, such as polymers (foils, nonwovens), exhibits low values of surface energy not sufficient for industrial processing (printing, adhesion, etc.) [1]. The atmospheric pressure plasma technologies gained an irreplaceable position in industrial surface modifications of such low-added value materials increasing their surface energy using environmentally friendly plasma treatment in safe gasses (air, N<sub>2</sub>, O<sub>2</sub>, Ar, ...) [2–5]. The dielectric barrier discharges and jets [6–8] are the most significant plasma sources developed and tested for atmospheric pressure plasma modifications.

The presented study investigates the parameters of diffuse coplanar surface barrier discharge (DCSBD) [9]. This type of dielectric barrier discharge offers several industrially important attributes needed for high-speed in-line plasma processing: generation of highly non-equilibrium macroscopically homogeneous plasma with high power density (100 W/cm<sup>3</sup>), easy scalability, long lifetime and capability of plasma processing in a wide range of working gases.

In present study the influence of working gas humidity on the plasma properties of DCSBD was investigated for two most common processing gases in industry – air and nitrogen. The influence of the absolute humidity on the discharge pattern and also on the plasma characteristics was studied using digital photography and optical emission spectroscopy.

## 2 EXPERIMENTAL

The experimental setup with DCSBD source is given in Fig. 1. The power input into plasma layer of 8×20 cm<sup>2</sup> (thickness of 0.3 mm) was 350 W at 15 kHz. Synthetic air/N<sub>2</sub> (0.1 MPa) was used with total mass flow of 5 slpm. The humidity of working gas was controlled from 2 to 80 g<sub>H<sub>2</sub>O</sub>/ m<sup>3</sup><sub>GAS</sub> by mixing of dry gas with gas flowing through thermostatic heated bubbler filled with distilled water. The relative humidity and temperature of gas were recorded using Extech Instruments RH520 and absolute humidity of the gas was then calculated. For N<sub>2</sub> the absolute humidity was recalibrated using the data for synthetic air.

Discharge spectra were recorded using Jobin-Yvon Triax 550 spectrometer equipped by liquid nitrogen cooled CCD detector. Discharge patterns were taken by digital camera.

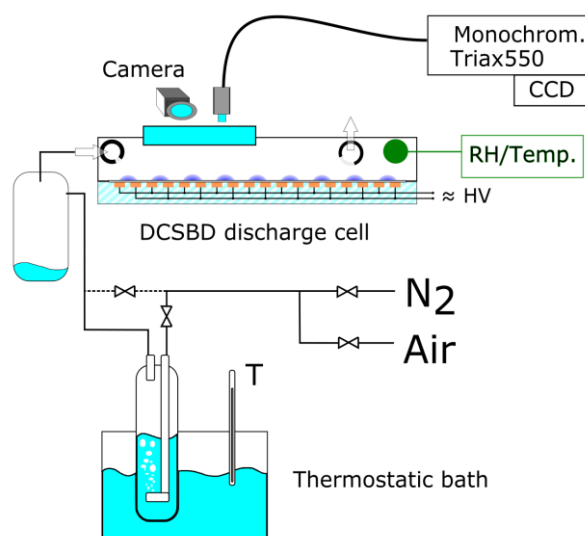


Fig.1: Setup of experiment and diagnostics

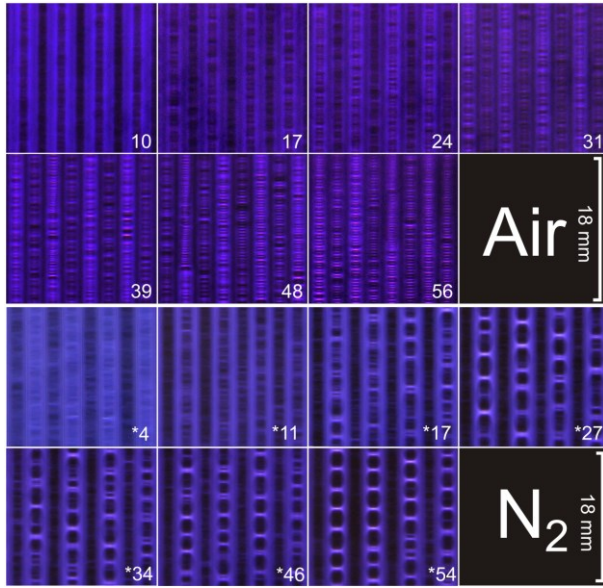


Fig.2: The discharge pattern evolution with increase of absolute humidity of gas ( $g_{H_2O}/m^3_{GAS}$ )

### 3 RESULTS AND DISCUSSION

In Fig. 2 the DCSBD discharge pattern evolution is given with respect to the absolute humidity of working gas with exposure time 1/40 s. For DCSBD generated in artificial air the discharge remains diffuse even for relatively high absolute humidity of 20-30  $g_{H_2O}/m^3_{GAS}$ . For comparison, under standard pressure of 101 kPa, temperature of 25°C and 80% rel. humidity the absolute humidity is approx. 18  $g_{H_2O}/m^3_{GAS}$ . With further increase of air humidity the diffuseness is lost at the expense of densification and spatial stabilization of filamentary part of the discharge. For DCSBD generated in  $N_2$  the loss of discharge diffuseness occurs at absolute humidity numbers lower comparing to synthetic air (Fig. 2). The discharge collapses then in a sparse, honeycomb-like filamentary structure.

The difference in the behavior of DCSBD in humid gas (synthetic air/ $N_2$ ) is observable also in optical emission spectra (OES). The OES of DCSBD consists of  $N_2$  molecular bands (2<sup>nd</sup> positive, 1<sup>st</sup> negative and 1<sup>st</sup> positive systems). Emission bands of NO- $\gamma$  system and atomic oxygen lines were also present in synthetic air. In  $N_2$  the emission bands of NO- $\gamma$  system were also present (oxygen impurities and/or  $H_2O$  as possible sources of oxygen). The emission of OH radical was present under the presence of water vapors in processing gas, i.e., air or  $N_2$ .

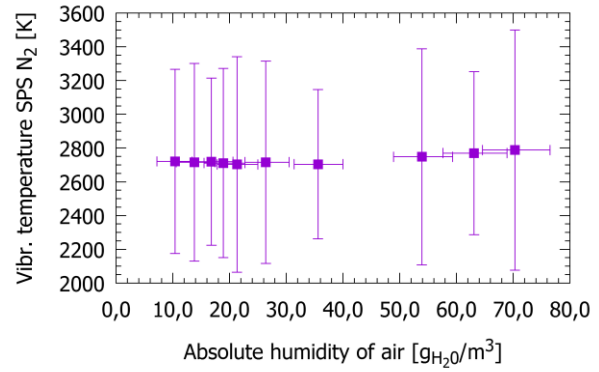


Fig.3: Vibration temperature of SPS with respect to the absolute humidity of air ( $g_{H_2O}/m^3_{AIR}$ )

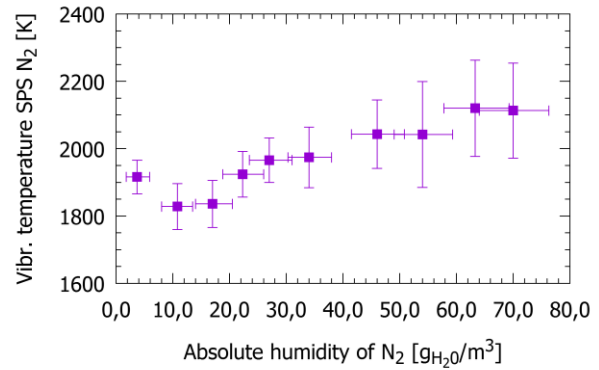


Fig.4: Vibration temperature of SPS with respect to the absolute humidity of  $N_2$  ( $g_{H_2O}/m^3_{AIR}$ )

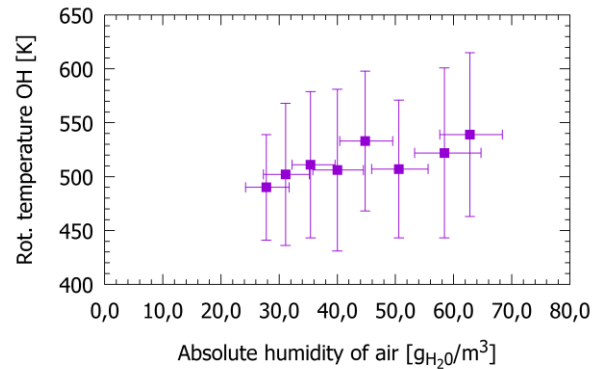


Fig.5: Rotational temperature of OH with respect to the absolute humidity of air ( $g_{H_2O}/m^3_{AIR}$ )

The spatially unresolved vibration ( $T_{vibr}$ ) and rotation ( $T_{rot}$ ) temperatures of DCSBD represents mainly the behavior of filaments between electrodes [10, 11]. In air the  $T_{vibr}$  is higher than in  $N_2$  (compare Figs. 3 and 4). In air the  $T_{vibr}$  does not depend on the gas humidity, while in  $N_2$  the increase of humidity leads to increase of  $T_{vibr}$ . This correlates with the behavior of micro-discharges in Fig. 2. Whereas the filaments in  $N_2$  become pronounced and enlarged with increase of gas

humidity, in air the filaments remains practically the same - just closer to each other. This discharge densification in humid air is accompanied by the slight increase in rotational temperature of OH, see Fig. 5. The  $T_{\text{vibr}}$  was estimated from the intensities of 2<sup>nd</sup> positive system of N<sub>2</sub> (SPS), band 0-2 at 380 nm. The  $T_{\text{rot}}$  of OH was estimated from the OH band Q1 at 308 nm.

When the Figs. 3, resp. 4 and 5 are compared the non-equilibrium character of DCSBD in dry or humid gas is clearly visible. The vibration temperature is considerably higher than rotational temperature, i.e.  $T_{\text{vibr}}$  being 2700 K, resp. 2000 K (air, resp. nitrogen), while  $T_{\text{rot}}$  remaining between 500 K and 550 K.

The influence of humidity of working gas on the plasma properties of DCSBD can be seen also in the OES characteristics. The values of intensity of SPS (N<sub>2</sub>) remained practically uninfluenced, so the relative intensities with respect to SPS were introduced for OH, O and NO- $\gamma$ . Namely following lines/bands intensities were compared: SPS – band 2-0 at 298 nm, OH radical – integrated bands R1 and R2 at 306 nm, NO- $\gamma$  system – band 0-3 at 259 nm and O atomic lines intensity – integrated triplet lines at 777 nm.

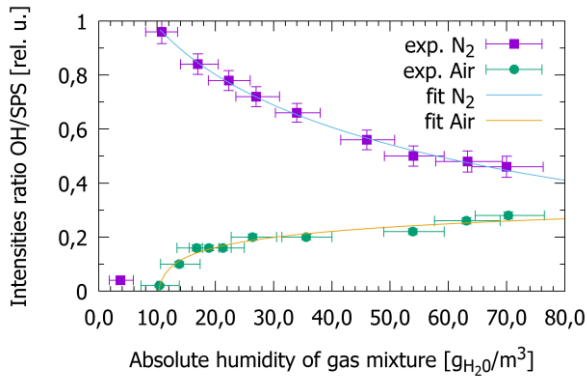


Fig.6: OH intensity dependence on  $g_{\text{H}_2\text{O}}/m^3_{\text{GAS}}$

In Figs. 6, 7 and 8 the courses of relative intensities of OH, NO- $\gamma$ , resp. O are given with respect to absolute humidity of working gas. In air the relative emission intensity of OH radical increases with increase of water content (saturation above 40  $g_{\text{H}_2\text{O}}/m^3_{\text{GAS}}$ ). In N<sub>2</sub> the relative emission intensity of OH decreases with water content increase (barring nearly no OH emission in dry N<sub>2</sub>). The relative intensities of O, resp. NO- $\gamma$  in air DCSBD also

decreases with increase of water content. In Figs. 6 to 8 the rel. intensities were rescaled to the common maximum value of approx. 1 for better readability of graphs. The actual maxima of rel. intensities (instrumental function un-corrected) were as follows: 0.02 for NO- $\gamma$ /SPS ratio, 0.04 for O/SPS ratio and 0.5, resp. 0.14 for OH/SPS ratio in N<sub>2</sub>, resp. in air.

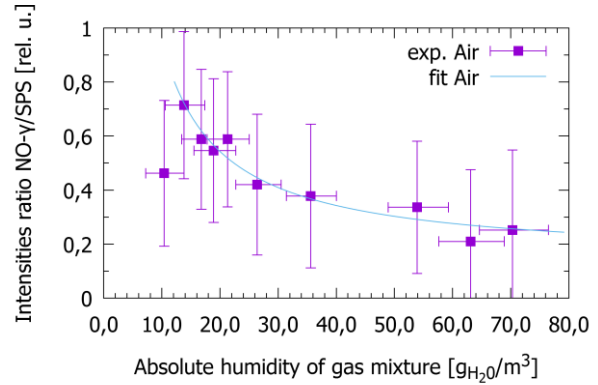


Fig.7: NO- $\gamma$  intensity dependence on  $g_{\text{H}_2\text{O}}/m^3_{\text{AIR}}$

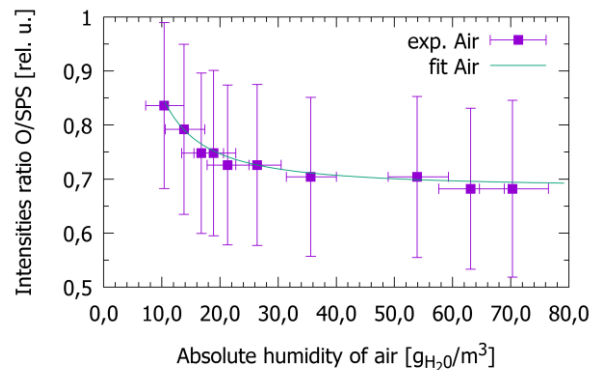


Fig.8: O intensity dependence on  $g_{\text{H}_2\text{O}}/m^3_{\text{AIR}}$

The results obtained using discharge imaging and optical emission spectroscopy show substantial influence of water vapors presence in the working gas on the plasma chemistry and the overall behavior of DCSBD discharge. For further clarification of this influence the plasma-chemistry model and the data on the absolute density of generated plasma species are necessary, e.g., adoption of techniques like laser induced fluorescence [12, 13] and laser diode optical absorption spectroscopy [14] could be of a great interest for further research on this topic.

#### 4 CONCLUSION

The absolute humidity of working gas has significant influence on the behavior of DCSBD.

The micro-discharges patterns in humid air densify in thin channels, while in N<sub>2</sub> the sparse honeycomb-like structures appear. The micro-discharges' patterns correlate with vibrational temperatures that were higher in air, while lower in N<sub>2</sub>. The vibrational temperatures increases with increasing concentration of water vapors in N<sub>2</sub>, while remains constant in air. These differences are also clearly observable in the trends of relative intensities of OH radical.

The influence of water vapors concentration on the parameters of DCSBD was measured through extended range of water vapor concentration – from 2 to 80 g<sub>H<sub>2</sub>O</sub>/ m<sup>3</sup><sub>GAS</sub>. Even though the detailed mechanisms of plasma-chemical processes in DCSBD in humid air or nitrogen are not known at the moment, the results can be of great interest for plasma applications of DCSBD plasma source in industry, see e.g. [15].

The results presented in this work make demands on the extension of monitored parameters of DCSBD in plasma applications, i.e., to follow and/or influence the working gas humidity. Presented results could be also of importance for applications using other types of dielectric barrier discharges, however for better understanding of plasma processes in humid gasses further research using e.g. laser induced fluorescence spectroscopy and/or laser diode absorption spectroscopy is necessary.

#### Acknowledgements

This research has been supported by the project CZ.1.05/2.1.00/03.0086 funded by European

Regional Development Fund and project LO1411 (NPU I) funded by Ministry of Education Youth and Sports of Czech Republic.

#### REFERENCES

- [1] Kogelschatz U, Eliasson B, Egli W, Le J. Phys. IV 07 (1997) C4–47–C4–66.
- [2] Wagner H-E, Brandenburg R, Kozlov K V, Sonnenfeld A, Michel P, Behnke J F, Vacuum 71 (2003) 417–436.
- [3] Kogelschatz U, Plasma Phys. Control. Fusion 46 (2004) B63–B75.
- [4] Pappas D, J. Vac. Sci. Technol. A Vacuum, Surfaces, Film. 29 (2011) 020801.
- [5] Černák M, Černáková L, Hudec I, Kováčik D, Zahoranová A, Eur. Phys. J. Appl. Phys. 47 (2009) 22806.
- [6] Bruggeman P, Brandenburg R, J. Phys. D. Appl. Phys. 46 (2013) 464001.
- [7] Foest R, Kindel E, Ohl A, Stieber M, Weltmann K-D, Plasma Phys. Control. Fusion 47 (2005) B525–B536.
- [8] Černák M, Ráhel' J, Kováčik D, Šimor M, Brablec A, Slaviček P, Contrib. to Plasma Phys. 44 (2004) 492–495.
- [9] Šimor M, Ráhel' J, Vojtek P, Černák M, Brablec A, Appl. Phys. Lett. 81 (2002) 2716.
- [10] Čech J, Sťahel P, Navrátil Z, Eur. Phys. J. D 54 (2009) 259–264.
- [11] Čech J, Sťahel P, Navrátil Z, Černák M, Chem. List. 102 (2008) s1348–s1351.
- [12] Dilecce G, Ambrico P F, Simek M, De Benedictis S, Chem. Phys. 398 (2012) 142–147.
- [13] Dilecce G, Ambrico P F, Simek M, De Benedictis S, J. Phys. Conf. Ser. 227 (2010) 012003.
- [14] Röpcke J, Lombardi G, Rousseau A, Davies P B, Plasma Sources Sci. Technol. 15 (2006) S148–S168.
- [15] Prysiaznyi V, Zaporojchenko V, Kersten H, Černák M, Appl. Surf. Sci. 258 (2012) 5467–5471.

## **Microdischarge in the Vortex Gas Flow**

Chernyak V., Solomenko Ok., Solomenko Ol., Lendiel V., Kalustova D.,  
Prsyazhnevych I.

*Taras Shevchenko National University of Kyiv, Glushkova av. 4g, Ukraine, [chernyak\\_v@ukr.net](mailto:chernyak_v@ukr.net)*

Current-voltage characteristics of the DC microdischarge were investigated in the work. The plasma jet parameters were evaluated by emission spectroscopy method. The component composition and the temperatures of excited electronic, vibrational and rotational levels of plasma component of microplasma were determined by using emission spectra. It was found that nitrogen was the main component of microdischarge plasma. Also NO and OH molecular bands were presented in the spectrum.

**Keywords:** atmospheric pressure plasma, microdischarge, plasma jet

### **1 INTRODUCTION**

Today, the development of atmospheric pressure microplasma jet is highly promising and perspective, because such plasma system is a source of low temperature atmospheric pressure non-equilibrium plasmas. Numerous plasma components such as activated components of oxygen or nitrogen, charged particles, electric fields and even UV radiation leads to different reactions in the treated tissues, allowing to use of microdischarge systems for various applications. The main advantages of these systems are their compactness, and the fact that the plasma is not limited by the sizes of electrodes. The ability to adjust the size of the plasma jet allows to locate the area of microplasma jet influence. It is important in the case of working with living tissues, in blood coagulation, in dentistry, in treating patients with diabetes, the plasma sterilization of living tissues etc. Conversely, it is also possible to increase the area of plasma in cases where it is necessary.

Commonly used discharges for the generation of atmospheric pressure plasmas are barrier discharge, corona discharge and microdischarge. The last one is similar to the glow discharge at low pressure. The microdischarge is the least studied among those discharges.

This research studies the properties of atmospheric pressure DC microdischarges in the air vortex flow. The electrical parameters of the discharge and optical characteristics of the microdischarge plasma jet have been studied.

### **2 EXPERIMENTAL SETUP**

The Fig.1 shows a schematic representation of atmospheric pressure microdischarge plasma generator, which has axially symmetric design with geometry similar to the known HF systems [1]. The internal high-voltage electrode (rod) has a rounded end. Its diameter is 1 mm. The role of the second external grounded electrode is performed the body of this design. The outlet aperture diameter ( $d$ ) was  $0.5 \div 2.0$  mm. The space between the electrodes was blown over by the vortex flow of working gas. Air was used as working gas.

The working gas is introduced tangentially to the side wall of the cylinder, thus forming a reverse vortex flow. Plasma jet rotates under the influence of the gas flow, gliding over the surface of the upper electrode. The design provided an additional channel of gas supply to the reaction chamber. The system can work both horizontally and vertically.

The main advantage of the method of emission spectroscopy is the ability to investigate plasma parameters without interfering in plasma itself. Plasma emission spectroscopy usage allows to determine the composition of the plasma, the temperatures population of excited electronic levels and determining the vibrational and rotational temperatures of atomic and molecular plasma components. This is why this method is used for the research of plasma microplasma jet system described above.

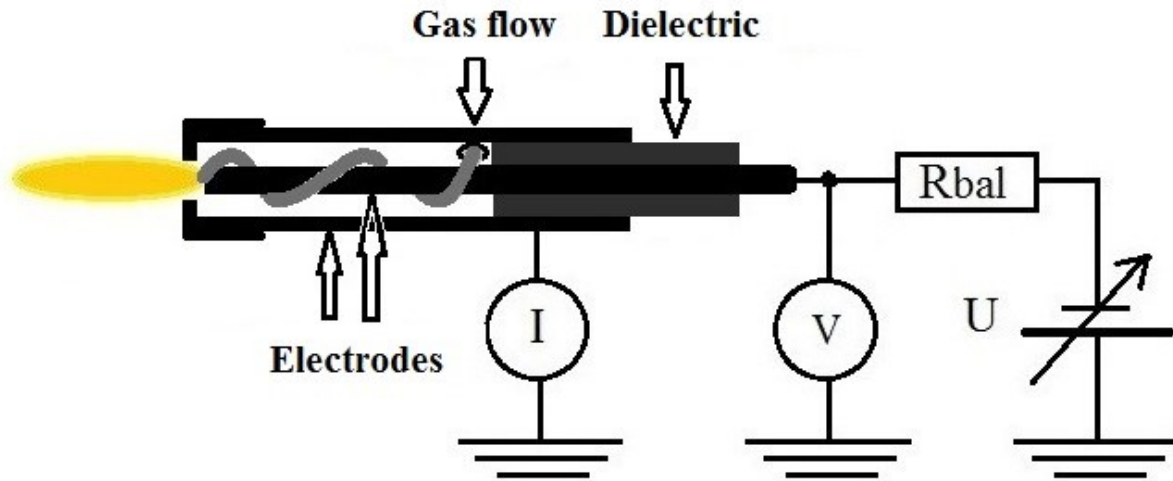


Fig.1: Electrical scheme for generation of atmospheric pressure microplasma jet

### 3 RESULTS

The current-voltage characteristics (CVC) measurements of microdischarge were performed for different air flows ( $G = 1 \div 4$  L/min). Also different output diameters (from which microdischarge jet was blown out) were used by using different caps: from  $d = 0.5$  mm to  $d = 2.0$  mm with step of 0.5 mm. The measurement results of CVC with the positive potential of the high voltage electrode are presented in Fig.2. As in previous work [2], the extreme points on the ordinates axis correspond to the breakdown voltage.

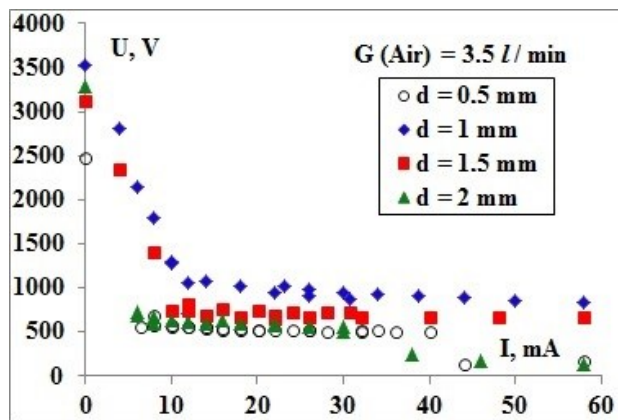


Fig.2: Current-voltage characteristic of the microdischarge which were blowing thru the hollow  $d$  (0.5-2 mm) with gas flow  $G = 3.5$  l/min. Working gas – air

As it can be seen from the Fig. 2, the CVC has monotone character and the voltage decreases with outlet diameter  $d$  increasing, except in the case of output diameter  $d = 0.5$  mm. The same characteristic was observed for another gas

flows.

Optical emission spectroscopy of plasma-generated microplasma jet was made by CCD-based spectrometer Solar TII (S-150-2-3648 USB) in the wavelength range of 200 – 1100 nm with spectral resolution of approximately 0.2 nm.

Typical emission spectra of microjet plasma in the wavelength range of 200 – 650 nm and in the wavelength range of 650 – 1100 nm are shown on Fig.3 and Fig.4 respectively. Both spectra are normalized at maximum. Molecular  $N_2$  band in wavelength range of 335 – 339 nm and atomic oxygen multiplet on wavelength 777 nm are distorted by too large intensity. It should be noticed that intensity of UV part of emission spectra is by 3-4 orders more intense than its IR part.

Emission spectra of the microplasma are multicomponent. The presence of atomic oxygen multiplets (777, 844 and 926 nm) and molecular bands of NO, OH,  $N_2$  (B-A) and  $N_2$  (C-B) and also  $N_2^+$  is shown.

The  $N_2$  molecular bands are the most intensive in comparison to others molecular spectra. For that reason  $N_2$  molecular bands were used for the determination of vibrational ( $T_v^*$ ) and rotational ( $T_r^*$ ) temperatures of plasma components. The temperatures of  $N_2$  molecules were determinate by comparing the experimental spectra with spectra simulated in Specair code. The Fig.5 shows comparison of experimentally measured spectra with  $N_2$  (C-B) spectra simulated with program code "Specair".

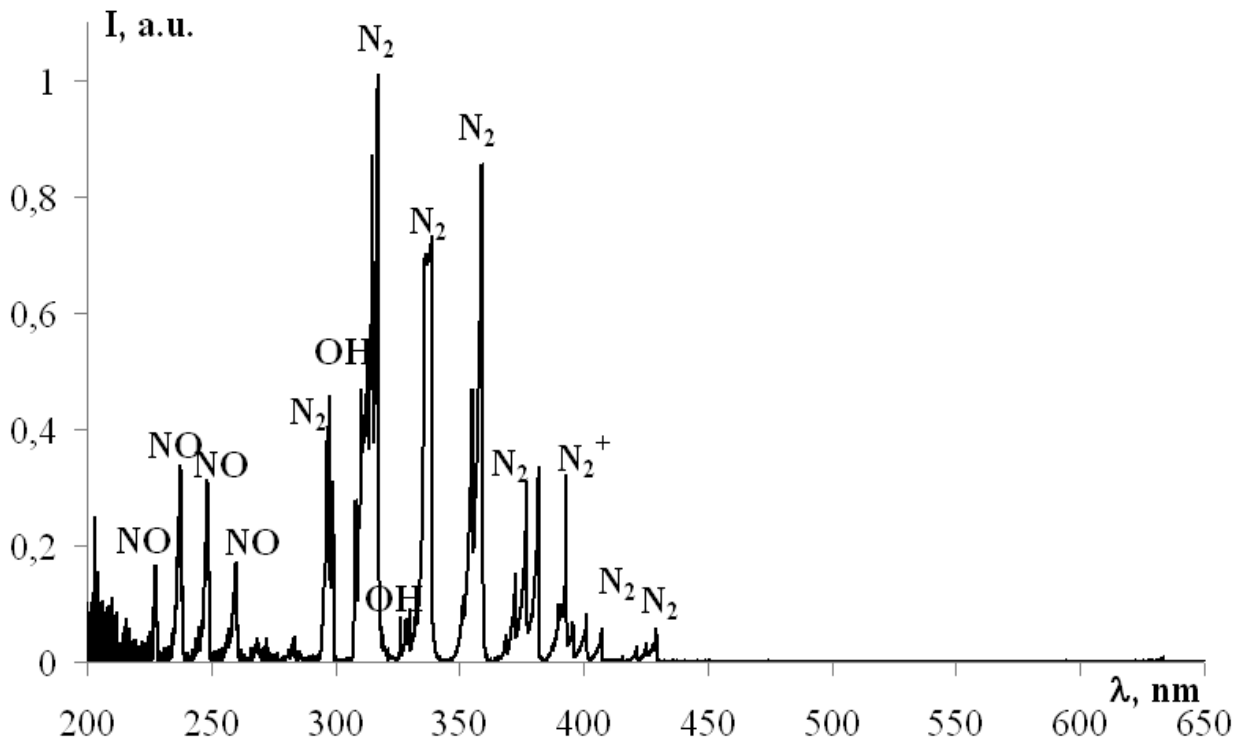


Fig.3: Typical emission spectra of microjet plasma in the wavelength range of 200 – 650 nm

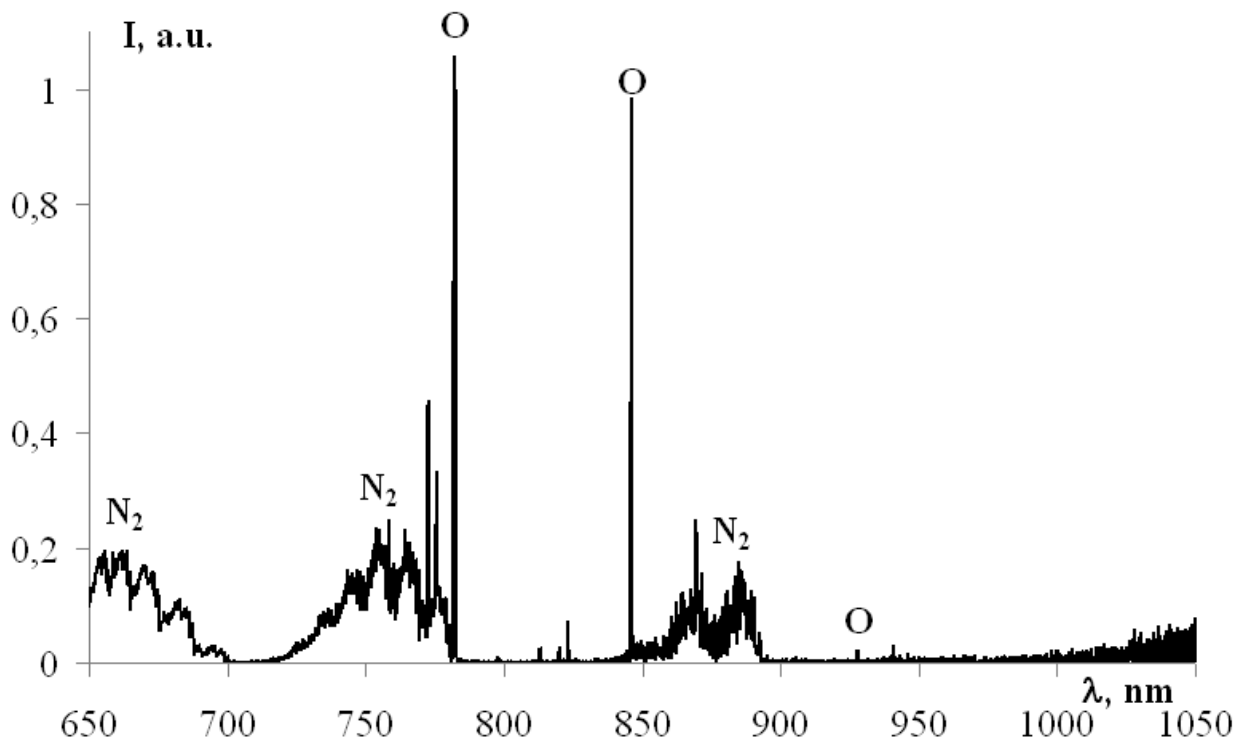


Fig.4: Typical emission spectra of microplasma jet in the wavelength range of 650 – 1100 nm

The plasma discharge was diagnosed at different discharge currents (20 and 30 mA) and along the plasma jet height ( $z$ ). The air flow was 3.8 L / min.

The oxygen  $T_e^*(O)$  has been defined via the

Boltzmann plots method. The three most intense multiplets (777.2 nm, 844 nm, 926 nm) and data from [3] are used in this method. It was found  $T_e^*(O) = 3000$  K. The error of  $T_e^*$  definition is approximately

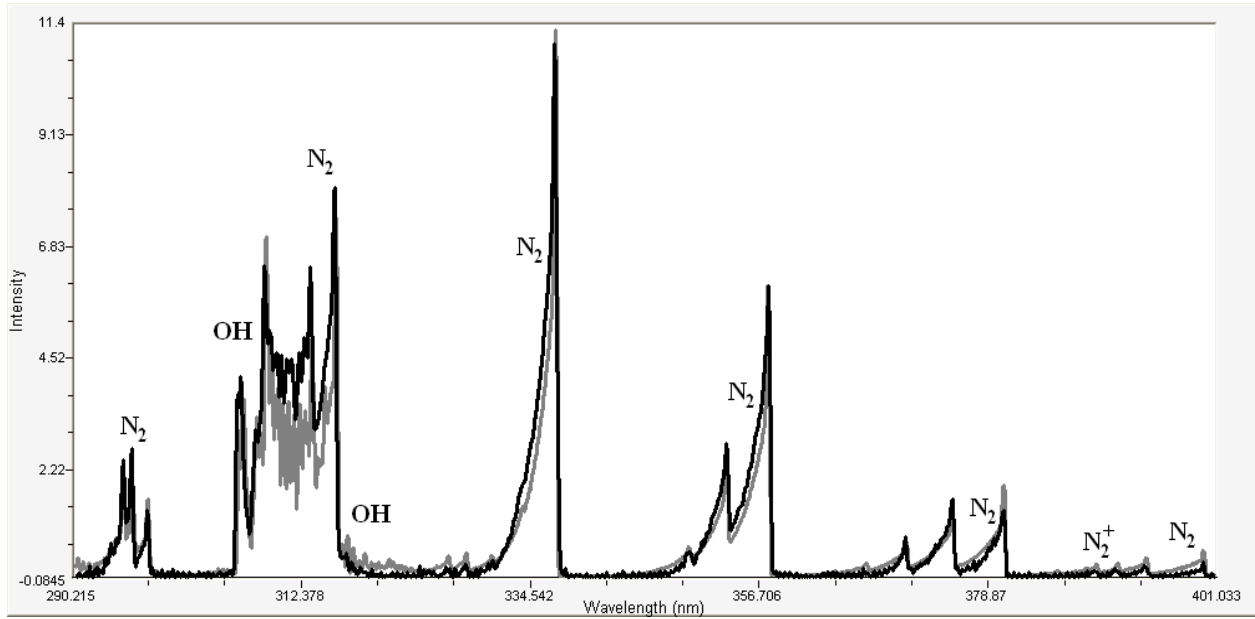


Fig.5: Experimental emission spectrum (black spectrum) of microplasma jet and its comparison with spectra simulation (gray spectrum)

1000 K, so we can say that the components temperature has low dependence on current. Axial temperatures ( $T_v^*$  and  $T_r^*$ ) distribution for N<sub>2</sub> under different current (20 and 30 mA) is presented at Fig.6 in case of output diameter of system –  $d = 1.5$  mm.

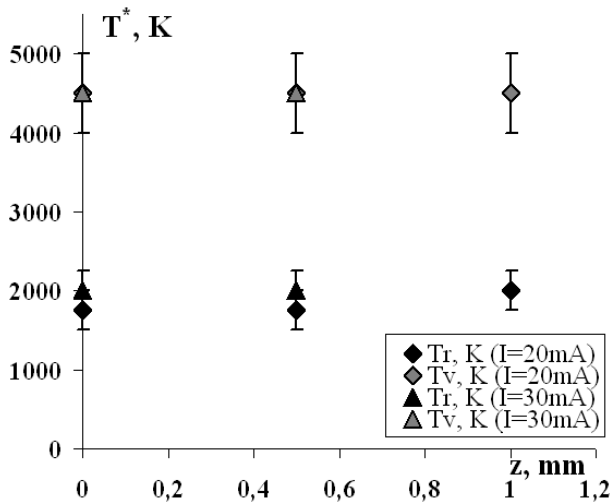


Fig.6: Axial distribution of N<sub>2</sub> (C-B) vibrational and rotational temperatures along the outside part of plasma jet. There  $z = 0$  mm shows the temperatures of microplasma near the output hollow of the grounded electrode.

The temperatures  $T_r^*(N_2)$  increased slowly (within the error margin) with height of the plasma jet while  $T_v^*(N_2)$  remains constant. The temperature  $T_v^*$  of N<sub>2</sub> molecules, within

the error margin, does not change with the changes of current. However,  $T_r^*(N_2)$  increased slowly within the error margin.

#### 4 CONCLUSIONS

- The non-monotonously voltage drop depends on the output diameter of the system.
- The atomic oxygen lines and NO, OH, N<sub>2</sub> and N<sub>2</sub><sup>+</sup> molecules were presented in the emission spectra of the microplasma.
- The temperatures  $T_v^*(N_2)$  and  $T_e^*(O)$  do not change with changes of current. However,  $T_r^*(N_2)$  increased slowly within the error margin.
- The temperature  $T_r^*(N_2)$  is slowly increasing with along the axis of the plasma jet while  $T_v^*(N_2)$  remains constant.

#### Acknowledgements

This work was partially supported by Ministry of Education and Science of Ukraine, National Academy of Sciences of Ukraine, and Taras Shevchenko National University of Kyiv.

#### REFERENCES

- [1] Herrmann H W, Henins I, Park J, Selwyn G S, Phys. Plasmas 6 (1999) 2284-2289.
- [2] Solomenko Ok V, Lendiel V V, Chernyak V Ya, et al. Probl. Of Atom. Sci. and Techn. Series: Plasma Physics 20 (2014) 241 - 244.
- [3] Czernichowski A, In: 19<sup>th</sup> Int. Symp. on Plasma Chem. Bochum, Germany, 2009, 1-4.

# **Change of the Thermal Profile in the Modern MCCB by the Different Electrical Contact Resistance**

Dostal L.<sup>1</sup>, Dohnal P.<sup>1</sup>, Valenta J.<sup>1</sup>

<sup>1</sup>*Centre for Research and Utilization of Renewable Energy (CVVOZE), Technicka 10, 616 00 Brno, Czech Republic,*

The paper deals with the change of temperature rise of the MCCB at the steady state. The critical parts under the study are main contacts and contact lever. The movable contact in focus is modern, rotoactive system which moves contact along a circular path and his material is harder than the fixed one. It causes sequential sag of the movable contact followed by a deformation of the fixed one. Consequently, the contact area between the pair of contacts is increasing, but the contact material is losing during the arc quenching. Rests and dirt layers appear on the contact surfaces and causes increase electric and thermal resistances between contacts. Temperature rise of the device with additive layers after arcing increases against new one at the steady state.

The profiles of the temperature rises are computed using finite volume method (FVM). The first part of the paper focuses on the calculation of the thermal losses of the electrical current path at rated current with the different electrical contact resistance.

The last part of the paper describes laboratory measurements performed for numerical calculations verification. Results of the laboratory measurements proved the accuracy of the finite volume method model.

**Keywords:** MCCB, temperature profile, thermal losses, Computational Flow Simulation

## **1 INTRODUCTION**

From the tripping method point of view, molded case circuit breakers (MCCB) are equipped with the electronic and thermo-magnetic (TMA) trip units. The electronic tripping units contain a microprocessor that monitors and evaluates the overcurrent. The TMA tripping unit includes a bimetal part, which trips a circuit breaker in case of an overcurrent (a low multiple of the rated current) and an electromagnet, which evaluates the short circuit (the higher multiples of the rated current). Basic function of the tripping units consists of the generation of a tripping order when the circuit-breaker current exceeds the allowed overcurrent.

Overload tripping is executed by the thermal tripping unit with calibrated setting. This setting could be influenced by thermal losses, between the contact lever with the movable contacts and the hold contacts, be the layers of dirt's due do proximity of contacts and TMA unit.

## **2 CONTACT RESISTANCE**

Contact resistance refers to a quality of connection of two contacts. Minimization of this resistance is highly required mainly in closed area of MCCB. Any contact surface is not evenly smooth and an electric current passes

from one contact to the other only through certain areas. This so called constriction effect is one of the main causes of the contact resistance between contacts.

Only a small part of the total contact surface presents its own contact area for contact surface ( $S_Z$ ). The current paths, which get narrower in this place, are called constriction surfaces, and current flows just through this small contact surface ( $S_U$ ). Contact surface ( $S_P$ ) is the surface, where the body of the contact is deformed by the contact force. This surface can be covered by non-conductive layers in some parts. Therefore, the surface ( $S_P$ ) is larger than the surface ( $S_U$ ) through which the current flows.

Actually, for the most metals constriction surface is covered by oxide or dirt layers with different properties in comparison with the pure metals. For the thin layers (e.g. molecular layer of an oxide), the electrons can penetrate by tunneling effect and the behavior of the layer corresponds to the pure metal. In fact, this layer of oxide or impurity should be thicker and consequently the resistance rises.

### **2.1 TEMPERATURE RISE OF A CONTACT**

When the current flows through the contact resistances, the contacts are heated and it should lead to oxidation of the contact areas. An excessive

temperature rise can cause softening of the contacts, leading to the melting of the constriction surfaces and finally to the contacts welding. The temperature rise  $\Delta\vartheta_s$  of the constriction surface is approximately proportional to the square of the voltage between contacts [4]

$$\Delta\vartheta_s = \vartheta_s - \vartheta_0 = \frac{\Delta U_s^2}{8\lambda\rho} \quad (1)$$

where  $\vartheta_s$  is the contact surface temperature [°C];  $\vartheta_0$  is the conductor temperature near the contact surface [°C];  $\Delta U_s$  is the voltage drop on the constriction surface;  $\rho$  is electrical resistivity of the material [ $\Omega\text{m}$ ];  $\lambda$  is the coefficient of thermal conductivity [ $\text{Wm}^{-1}\text{K}^{-1}$ ].

The temperature rise of the material of contacts consists of two parts:

- steady-state temperature rise  $\Delta\vartheta_i$  on the conductor dependent on a square of current

$$\Delta\vartheta_i = \frac{I_z^2 R_V}{\alpha S_{chl}} \quad (2)$$

- temperature rise  $\Delta\vartheta_U$  on the terminal dependent on voltage between contacts

$$\Delta\vartheta_U = \frac{U_s \sqrt{\Delta\vartheta_i}}{2\sqrt{\lambda\rho}} \quad (3)$$

The total temperature rise is:

$$\vartheta_s = \Delta\vartheta_i + \Delta\vartheta_U + \Delta\vartheta_s + \vartheta_{\text{ambient temp.}} \quad (4)$$

## 2.2 NUMERICAL MODEL

Numerical model is based on the real MCCB. Figure 1 shows current-carrying path of MCCB model. All parts (include splitter plates, case, mechanism etc.) of MCCB are involved to model for proper heat transfer modeling. Also there were included neighborhood and income and outcome conductors properly rated. The main part of the MCCB is the cassette with contacts and arc-quenching system. The most critical part is the movable contact with measuring points MP5 and MP6. This part is heated from both end contacts, and has a very low cooling surface.

Evaluation is carried on the middle pole of the MCCB, which is influenced from both sides by the other two poles with the same current flowing through.

Real model contains 9 measuring points with thermocouples marked as (MP..) connected directly with current carrying part for measuring of the temperature. This method also enables to measure voltage drop using the DC current between these points. This voltage data was used for the setup of the evaluation configuration heating on the current-carrying part.

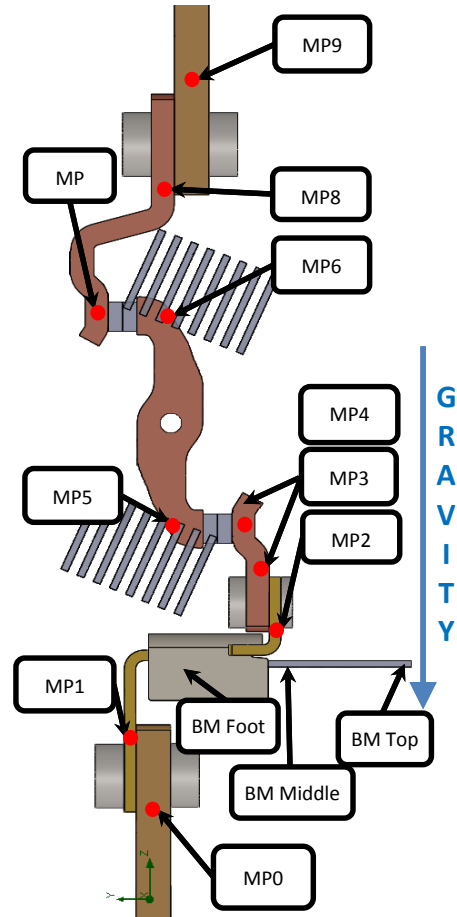


Fig.1: Simulation model with measuring points

## 2.3 INPUT DATA FOR SIMULATION

There are several boundary conditions used in the model, which are very important for appropriate results. The most important are as follows:

- Material prop. - Thermal Dependent (TD)
  - specific heat
  - thermal conductivity
  - electrical conductivity
- Thermal and electrical resistances (TD)
- Emissivity, electric current (DC), gravity, ambient temp., humidity, pressure etc.

Flow simulation is evaluated by the finite volume method (FVM) all using computational code Flow Simulation made by SolidWorks

corporations

### 3 RESULT AND DISCUSSION

In the test are measured data for first sample from the sample set. Data of recorded temperature are displayed in the fig.2. For the same case of voltage drops is created the FVM model

that outputs very close results in the temperature rise. Curves for temperature rise measured (Msg T: Sa01) and voltage drops (Msg U: Sa01) of fig 4 are near the same with value evaluated, see curve (Sim T(U): 0%) in both graphs. Remark: 0% means the same resistivity as the Sample 1.

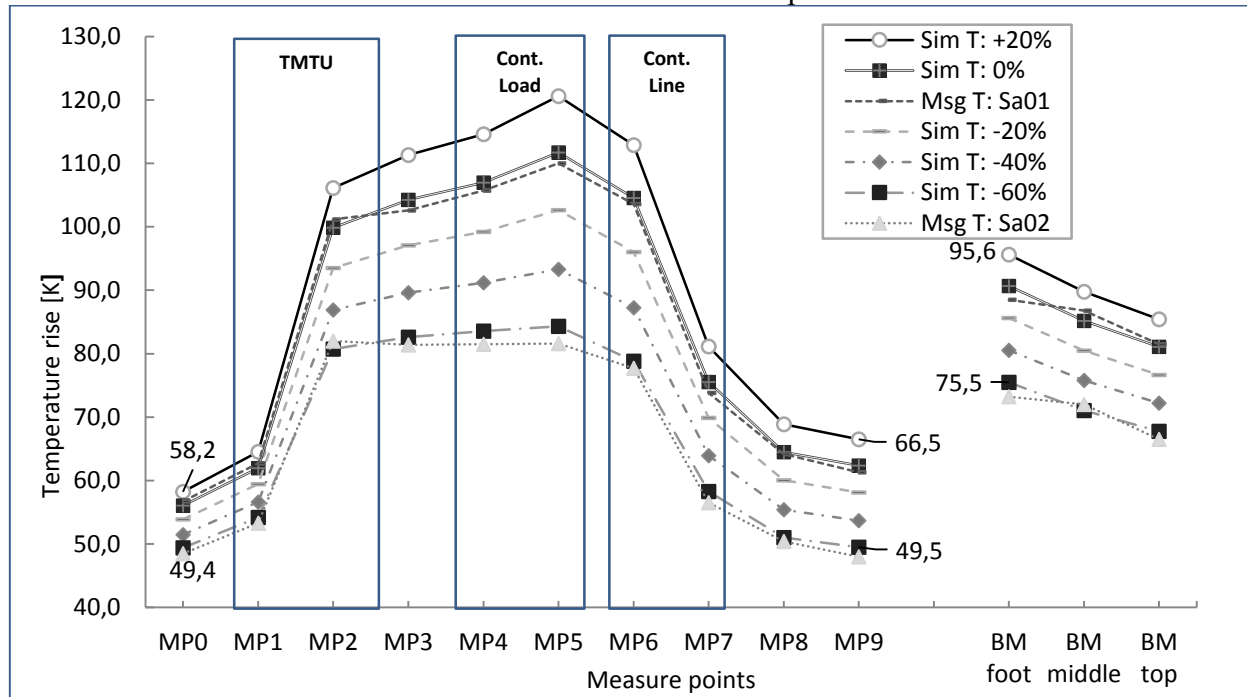


Fig. 2: Numerical model and recorded data with measuring points

Measured overall resistance of sample 1 is higher than mean value of standard samples. The model with no deviation of resistance of contacts from the original sample 1 is set for evaluation. Also there were performed simulations with same model with resistivity of contacts decreased by the 20%, 40% and 60% off and raised up by the 20% of overall resistivity of current path. These changes should decrease or increase temperature on the MCCB terminals which is limited to 70K by the standard. In the fig. 2 are solutions of temperatures and

comparison. The highest temperature is on the contact close to heated bimetal (MP5 and MP6). Temperatures on bimetal itself are marked as BM foot, BM middle and BM top. In cases with increased and decreased resistivity of one contact significant change of temperature of terminal occurs. Also it is possible to predict from overall resistivity of MCCB pole the temperature rise of contact. This should prevent wrong function of contact system after tripping or detect possible problem in manufacture process before the final test.

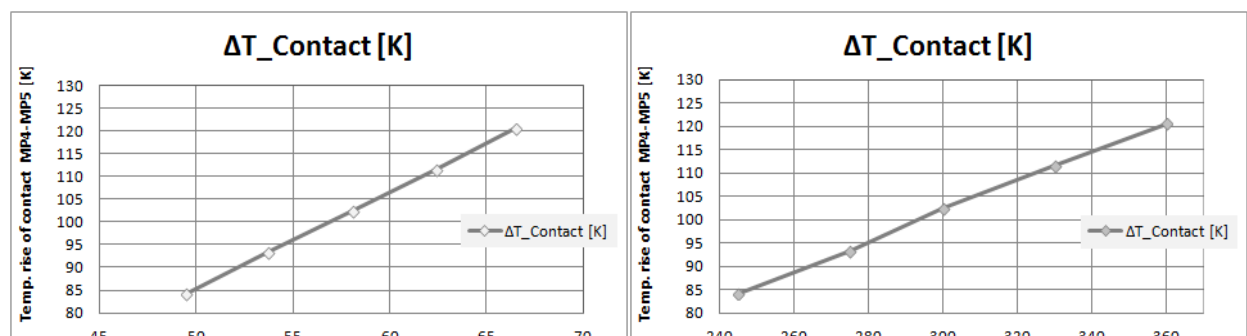


Fig. 3: Numerically modeled prediction curves for temperature rise of contact from temperature rise at terminals and from DC resistivity of MCCB model

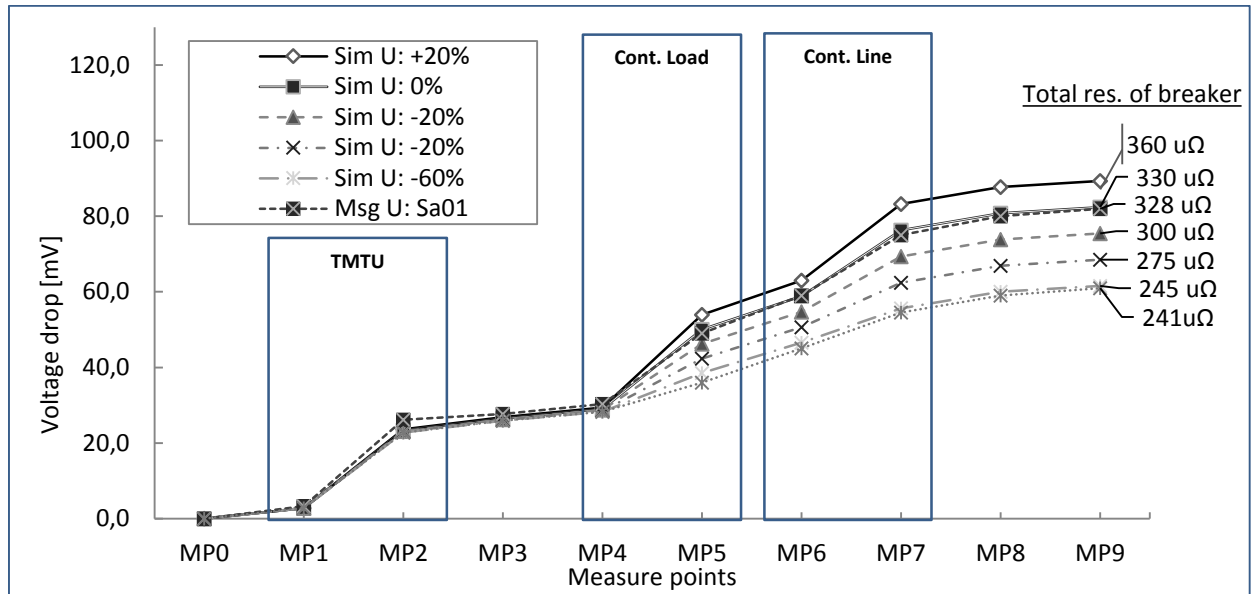


Fig. 4: The resistivity curves – voltage drops against income flag at various contact resistivity and total DC resistivity of the circuit breaker

Prediction curves are shown in fig. 3. The FVM solution was verified on the second sample with voltage drop decreased by the 21mV over whole current-carrying path at rated current related to decreased resistivity at contact area. It is nearly equal to -60% case in the model. In fig. 2 is shown thermal profile of this model, as Msg T: Sa02. It is clear, that the model corresponds with measured data in both cases.

This referred model in 3D system is now “trained” for the evaluation of problems related to this contact from whole contact system. Now are added features for prediction of two parametrical (both contacts independently) due to unpredictable behavior after breaking of highest current (shorts) near to breaking capability of MCCB.

The aim of research through the modeling is also the bimetal which maintains inverse delay switching of overcurrent. There are affect between contact and his temperature and temperature. Bimetal is heated up with contact heating, so if there is wrong contact with higher resistivity it could involve higher temperature at bimetal and change of inverse time curve to short of its time or decreasing set limiting current.

#### 4 CONCLUSION

The article deals with innovative system of design and diagnostics of modern MCCB. For design of newest circuit breakers are used

minimal amount of materials and heating of contacts and current-carrying path rises up to temperature rises over 100K are necessary to optimize current-carrying parts for temperature rise at terminal according to given standards. Described method is one of more outputs of accurate model used for easy design and diagnostics of MCCB in the switchboard, mainly after the heavy network faults braked up by MCCB. This method should be used also for purposes in examination of new MCCB or re-check of MCCB in service.

#### Acknowledgements

The authors gratefully acknowledge financial support from the Ministry of Education, Youth and Sports under project No. LO1210.

#### REFERENCES

- [1] Bergheau J M, Fortunier R, Finite Element Simulation of Heat Transfer, Wiley, Hoboken NJ 2008, ISBN 9781848210530.
- [2] Balaji C, Essentials of Radiation Heat Transfer, 2014, ISBN 978-1-118-90831-0.
- [3] Moran M J, Principles of Engineering Thermodynamics, 8th ed., Wiley, Hoboken NJ 2015, ISBN 978-1-118-96088-2.
- [4] Szandtner K, Contact resistance, temperature rise and losses of the electrical terminals, Hungarian Copper Promotion Centre 2007. Available at: [http://www.medportal.sk/system/files/publikacie/prechodovy\\_odpor.pdf](http://www.medportal.sk/system/files/publikacie/prechodovy_odpor.pdf).

## Preliminary Study of Mixing of Plasma Species in a Hybrid-Stabilized Argon-Water Electric Arc

Jeništa J.<sup>1</sup>, Takana H.<sup>2</sup>, Uehara S.<sup>2</sup>, Nishiyama H.<sup>2</sup>, Murphy A. B.<sup>3</sup>, Bartlová M.<sup>4</sup>, Aubrecht V.<sup>4</sup>

<sup>1</sup>*Institute of Plasma Physics AS CR, v.v.i., Za Slovankou 3, 182 00 Praha 8, Czech Republic, jenista@ipp.cas.cz*

<sup>2</sup>*Institute of Fluid Science, Tohoku University, 2-1-1 Katahira, Aoba-ku, Sendai, Miyagi, 980-8577, Japan, nishiyama@ifs.tohoku.ac.jp*

<sup>3</sup>*CSIRO Materials Science and Engineering, PO Box 218, Lindfield NSW 2070, Australia, Tony.Murphy@csiro.au*

<sup>4</sup>*Brno University of Technology, Technická 8, 616 00 Brno, Czech Republic, bartlova@feec.vutbr.cz*

This paper focuses on numerical simulation of mixing of plasma chemical species in the discharge and near-outlet regions of the worldwide unique type of thermal plasma generator with hybrid stabilization of electric arc by axial argon flow and tangential water vortex. Results of simulation for 300-500 A indicate inhomogeneous mixing of argon and oxygen-hydrogen species for all currents. The argon diffusion mass flux is driven mainly by the concentration and temperature space gradients.

**Keywords:** arc discharge, combined diffusion coefficients, inhomogeneous mixing, mass fraction

### 1 INTRODUCTION

The so-called hybrid stabilized electric arc, developed at IPP AS CR, v.v.i. in Prague, utilizes a combination of gas and vortex stabilization. In the hybrid argon–water plasma torch, the arc chamber is divided into the short cathode part, where the arc is stabilized by tangential argon flow, and the longer part, which is stabilized by water vortex. The arc is attached to the external water-cooled rotating disk anode at a few millimetres downstream of the torch orifice. At present, this arc has been used for plasma spraying, pyrolysis and gasification of waste and production of syngas from biomass [1].

In our experimental configuration water species are created by evaporation from a water column in the tangential direction, while argon is flowing axially into the discharge chamber where argon species are mixed with the water ones (Fig. 1). Recently it was proved from spectroscopic experiments made in IPP AS CR, v.v.i., [2] that argon and water plasma components are mixed only partially within the discharge chamber and, in addition, that mixing of individual components depends also on arc current. Since the studied plasma in the hybrid stabilized electric arc is quasi-laminar with steep radial temperature and velocity gradients [3] it can be expected that mixing and demixing processes will be important. Here we present a novel numerical model of

the hybrid-stabilized argon-water electric arc including the plasma species mixing model using the so called "combined diffusion coefficients method" [4, 5]. It has already been successfully applied by some authors to describe mixing of species in different arc discharges [6, 7]. Diffusion processes due to gradients of mass density, temperature, pressure, and an electric field are considered in the present model.

### 2 ASSUMPTIONS AND PHYSICAL MODEL

The following assumptions for the model are applied:

- 1) argon-water plasma itself is in local thermodynamic equilibrium,
- 2) the model is axisymmetric (2-dimensional),
- 3) the plasma flow is turbulent and compressible,
- 4) gravity effects are negligible,
- 5) the magnetic field is generated only by the arc itself,
- 6) the partial characteristics method for radiation losses is employed,
- 7) transport and thermodynamic properties for argon-water plasma mixture are calculated rigorously from the kinetic theory [8, 9] and they depend on temperature, pressure and argon mass fraction,
- 8) the combined diffusion coefficients are also functions of temperature, pressure and argon mass fraction.

Radiation losses from the argon-water arc are calculated by the partial characteristics method [10]. Continuous radiation, discrete

radiation consisting of thousands of spectral lines, molecular bands of O<sub>2</sub>, H<sub>2</sub>, OH and H<sub>2</sub>O have been included in the calculation of partial characteristics [11]. Broadening mechanisms of atomic and ionic spectral lines due to Doppler, resonance and Stark effects have been considered. The partial characteristics are function of temperature, pressure and an average argon mass fraction, determined from the ratio of mass flow rates of argon to water plasmas.

Turbulence is modelled by Large eddy simulation (LES) with the Smagorinsky subgrid-scale model with the constant values of the Smagorinsky coefficient ( $C_s = 0.1$ ) and the turbulent Prandtl number ( $Pr_t = 0.9$ ). The Van Driest damping function near the walls is employed to suppress turbulence [12].

The resulting set of conservative governing equations for density, velocity, energy and argon mass fraction (continuity, momentum, energy and species equations) was solved numerically by the LU-SGS method [13] coupled with Newtonian iterative method. The same method was successfully applied for calculation under the assumption of homogeneous plasma mixing. To resolve compressible phenomena accurately, the Roe flux differential method [14] coupled with the third-order MUSCL-type TVD scheme [15] is used for convective term. The electric potential is calculated using the Tridiagonal Matrix Algorithm (TDMA) enforced with the block correction method.

The computer program is being elaborated in the Fortran language. The task has been solved on an oblique structured grid with nonequidistant spacing. The total number of grid points was 38 553, with 543 and 71 points in the axial and radial directions respectively. Calculation domain is shown in Fig. 1.

### 3 DETAILS OF THE SPECIES MIXING MODEL

Only one species equation is required in the combined diffusion coefficients method, say for the species of gas A (argon), with the equation for argon species flux [16]:

$$\frac{\partial}{\partial t}(\rho f_A) + \nabla \cdot (\rho \vec{u} f_A) = -v \cdot \vec{J}_A \quad ,$$

$$\vec{J}_A = -\Gamma_f \nabla f_A + \Gamma_f \frac{f_A}{M_A} \nabla M_A - \Gamma_f \frac{f_A}{M} \nabla M + \Gamma_P \nabla (\ln P) - \bar{D}_{AB}^T \nabla (\ln T) - \Gamma_E \nabla \Phi - \frac{\mu_t}{Sc_t} \nabla f_A \quad ,$$

where  $\rho$  is the mass density,  $f_A$  is the mass fraction of species A (gas A = argon),  $\vec{J}_A$  is the argon diffusion mass flux,  $\Gamma_f, \Gamma_P, \Gamma_E$  are the transport coefficients for the ordinary, pressure and electric field diffusions respectively,  $M_A$  is the average molecular weight of argon,  $M$  is the average molecular weight of all particles of gas mixture,  $\bar{D}_{AB}^T$  is the combined temperature diffusion coefficient,  $\mu_t$  is the eddy viscosity,  $Sc_t$  is the turbulent Schmidt number ( $Sc_t=1$ ). The last term accounts for the diffusion of the argon species due to turbulence. The water species mass fraction  $f_B$  can be easily calculated from the closure condition  $f_A + f_B = 1$ .

### 4 RESULTS

Mixing of plasma species has been studied so far for 300–500 A and for 22.5 and 40 slm (standard liter per minute) of argon. The very first results of the model are illustrated in Figs. 2-4, showing the contours of the argon mass fraction, temperature and the combined ordinary diffusion coefficient for 300 and 500 A. We can conclude that:

- Mixing of argon and water plasma species is inhomogeneous under the studied conditions.

- Temperature and ordinary (concentration) diffusions are the most dominant contributions in the argon mass diffusion flux. Diffusion due to pressure gradients is lower and due to the electric field is practically negligible.

- Argon species are dominant in the central regions of the arc, water ones in arc fringes. Argon mass fraction in the central arc region also increases with current and argon mass flow rate. One of the reasons for this dependence is obvious from the plots: the combined ordinary diffusion coefficient decreases with temperature in the arc core (500 A), preventing thus higher mixing of argon and water

plasma species. The combined temperature diffusion coefficient (not shown) exhibit the same temperature dependence.

- These first results agree with our former experiments carried out 2 mm downstream of the nozzle orifice: calculated radial temperature profiles exhibit very good qualitative and quantitative agreements with the measurements. Qualitative agreement was also obtained for the radial argon mole fraction profiles.

## 5 CONCLUSIONS

The results confirmed inhomogeneous mixing of argon and water plasma species in the discharge region calculated by the combined diffusion coefficients method. Argon mass fraction in the axial region of the discharge increases with current and argon mass flow rate. Diffusion of species is influenced by highly nonlinear dependence of the combined diffusion coefficients on temperature, pressure and argon mass fraction.

### Acknowledgements

The authors are grateful for the financial support under the Collaborative Research Project (J15059) of the Institute of Fluid Science, Tohoku University, Sendai, Japan, and for their computer facilities. Our appreciation goes also to the projects GA15-19444S and GA15-14829S. The access to the CERIT-SC computing and storage facilities at Masaryk University in Brno provided under the programme Center CERIT Scientific Cloud, part of the Operational Program Research and Development for Innovations, reg. no. CZ. 1.05/3.2.00/08.0144 is highly appreciated.

## REFERENCES

- [1] Oost Van G, Hrabovsky M, Kopecky V, Konrad M, Hlina M, Kavka T, Chumak O, Beckman E, Verstraeten E J, Vacuum, 80 (2006) 1132-1137.
- [2] Hrabovský M, Kopecký V, Sember V, Kavka T, Chumak O, Konrád M, IEEE Trans. Plasma Sci. 34 (2006) 1566-75.
- [3] Jeništa J, Takana H, Nishiyama H, Bartlová M, Aubrecht V, Křenek P, IEEE Trans. Plasma Sci. 42 (2014) 2632–2633.
- [4] Murphy A B, Physical Review E 48 (1993) 3594-3603.
- [5] Murphy A B, J. Phys. D: Appl. Phys 34 (2001) R151-R173.
- [6] Chen X, Cheng K, Int. J. Heat and Mass Transfer 47 (2004) 5139-5148.
- [7] Murphy A B, Pure Appl. Chem. 68 (1996) 1137-42.
- [8] Murphy A B, Arundell C J, Plasma Chem. Plasma Process. 14 (1994) 451-490.
- [9] Murphy A B, Plasma Chem. Plasma Process. 20 (2000) 279-297.
- [10] Aubrecht V, Lowke J J, J. Phys. D: Appl. Phys. 27 (1994) 2066-2073.
- [11] Bartlova M, Aubrecht V, Czech. J. Phys. 56 (2006) B632-B637.
- [12] Pope S B, Turbulent Flows, Cambridge University Press, Cambridge 2000.
- [13] Jameson A, Yoon S, AIAA Journal 25 (1987) 929-935.
- [14] Roe P L, J. Comput. Phys. 43 (1981) 357–372.
- [15] Leer Van B, J. Comp. Phys. 32 (1979) 101-136.
- [16] Murphy A B, Nature.com 4 (2014), paper No. 4304.

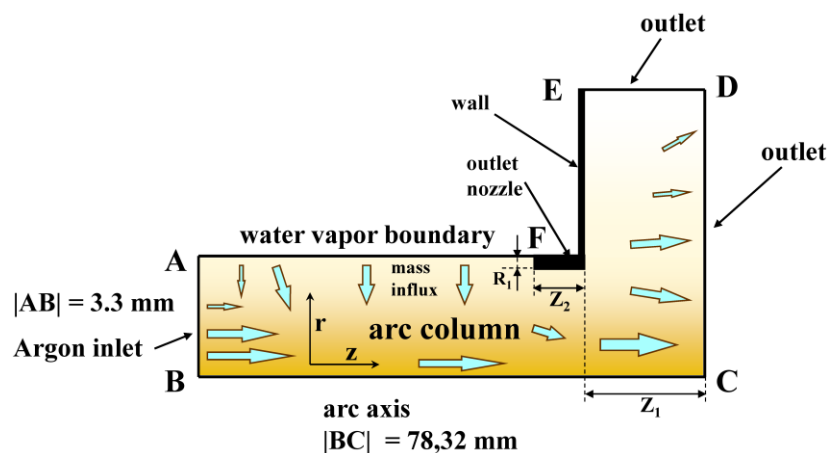


Fig. 1: Calculation domain for our problem. Argon flows axially through the AB line (+z direction) while water evaporates along the water vapor boundary AF (-r direction)

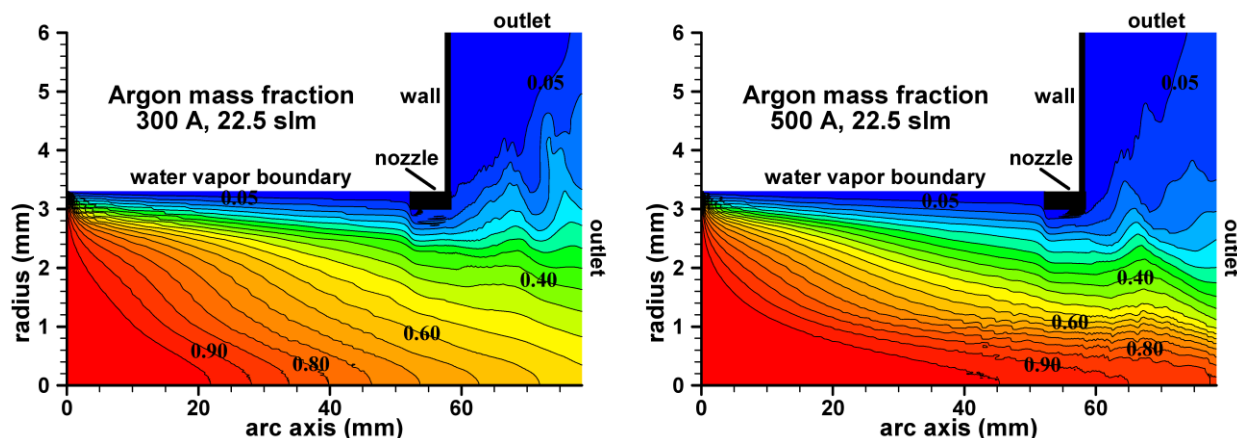


Fig. 2: Isoleths of argon mass fraction for 300 A (left) and 500 A (right) discharges. Water mass flow rates are  $0.228 \text{ g} \cdot \text{s}^{-1}$  (300 A) and  $0.329 \text{ g} \cdot \text{s}^{-1}$  (500 A); argon mass flow rate is 22.5 slm for both currents. The increase of argon mass fraction in the centre of the arc for higher current is clearly visible. Contour increments are 0.05

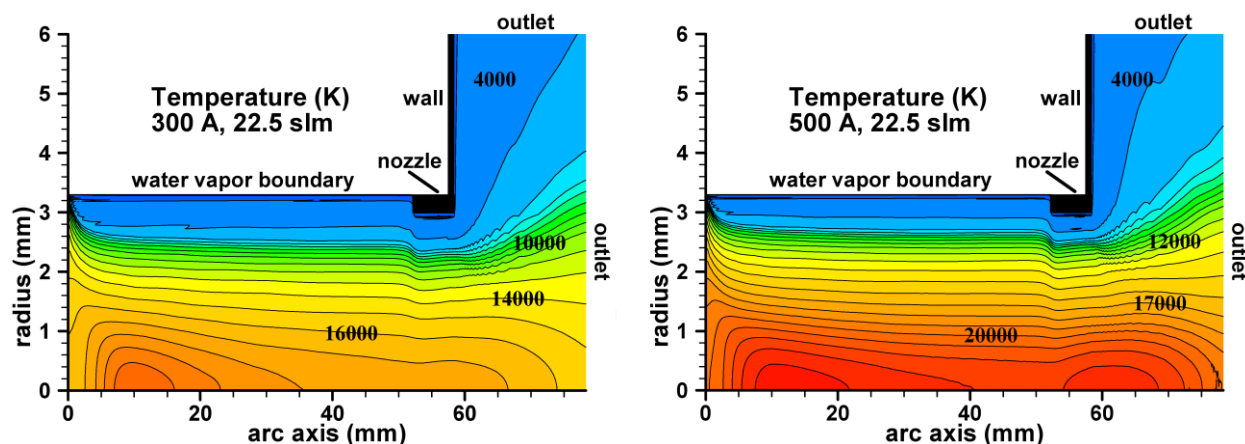


Fig. 3: Isotherms for the same conditions as in Fig. 2. Temperature in the arc core and the temperature gradients in arc fringes are higher for higher current

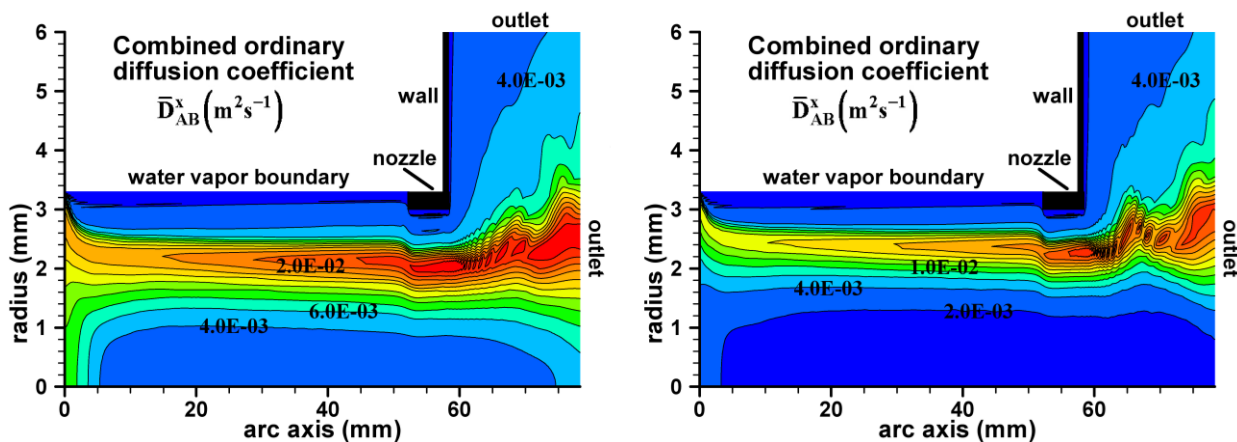


Fig. 4: Combined ordinary diffusion coefficient for the same conditions as in Figs. 2, 3 (left—300A, right—500A). The arc core for 500 A shows the lower values of the coefficient compared to 300 A

## Nisin Immobilization on Plasma Treated Polyvinyl Alcohol Films

Kolarova Raskova Z.<sup>1</sup>, Stahel P.<sup>2</sup>, Hrabalickova M.<sup>1</sup>, Sedlarik V.<sup>1</sup>

<sup>1</sup> Centre of Polymer Systems, Tomas Bata University in Zlin, tr. Tomase Bati 5678, 76001 Zlin, Czech Republic, zraskova@cps.utb.cz

<sup>2</sup>Department of Physical Electronics, Faculty of Science, Masaryk University, Kotlarska 267/2, Brno Czech Republic, pstahel@physics.muni.cz

Nisin protein attachment on chemically crosslinked polyvinyl alcohol surface activated in atmospheric Dielectric Coplanar Surface Barrier Discharge was carried out in this work. Plasma activated PVA surfaces show improved level of nisin attachment in comparison with untreated films. In addition, the extent of the nisin surface immobilization and its release strongly depends on crosslinking degree of PVA substrate.

**Keywords:** nisin, polyvinyl alcohol, surface modification, antimicrobial activity, crosslinking

### 1 INTRODUCTION

Antimicrobial peptides such as bacteriocin, Nisin (approx. 3.4 kDa), have been studied as a preserving agent since fifties of the last century [1-3]. Nisin is an effective inhibitor of Gram positive bacterial strains and promising antimicrobial agent for polymer materials and coatings [3-6]. Novel strategies for the antimicrobial properties of the polymer materials include bacteriocin binding to create active surface. Controlling protein and peptide adhesion is an important issue in many fields especially in medicine [6-8].

Polyvinyl alcohol (PVA) is commonly used biocompatible water soluble polymer material which offers functional groups for possible protein binding and crosslinking for hydrogel preparation.

Surface immobilization of the nisin of various surfaces has been already reported [8, 9]. However, its immobilization of plasma activated xerogel system (i.e. solvent free cross-linked PVA) is unique.

Atmospheric plasma is used in this study because of sufficient uniformity and easy applicability for continuous low-cost surface plasma treatment [9-13]. In this study, we used the Dielectric Coplanar Surface Barrier Discharge (DCSBD).

This work deals with description of (i) the nisin surface immobilization on the cross-linked PVA films activated by DCSBD technique, (ii) nisin surface antibacterial activity and (iii) release kinetics in a physiological environment.

### 2 EXPERIMENTAL

PVA (PVA Mowiol 8-88, Sigma Aldrich) films were prepared by solvent cast technique (10 wt. %, 85 °C) from aqueous solution. Glutaric acid (GA, Sigma Aldrich) was used as crosslinking agent. The several crosslinking degrees were chosen: 0, 5, 10, 20 and 40% [14]. The surface of the foils was activated by Dielectric Coplanar Surface Barrier Discharge (DCSBD), RPS 40 systems (Roplass s.r.o., Czech Republic) [15, 16], in ambient air under the following conditions: power density 7 W/cm<sup>2</sup>, frequency 25 kHz, with the treatment time of 10 s. The distance of the sample surface from the discharge plate was 0.3 mm. The samples were moved through plasma layer to obtain homogeneous treatment. Then, on the surface of treated PVA films, 40 µl of commercial nisin (Sigma-Aldrich) solution were applied (nisin was dissolved in phosphate saline solution, the pH value was set at 4.5 and the nisin concentration was 525 µg/ml). The samples were incubated for 20 minutes at room temperature. Then, the surface was dried, shortly rinsed off by demineralized sterilized water and dried again. The plasma treatment was applied again as a final processing.

The nisin release from the PVA surface into the physiological solution and nisin stability were studied by using Tricine SDS-PAGE (at 16 % and 4 % separating and stacking acrylamide gel containing 3 % bis-acrylamide, proteins and peptides were visualized by staining solution methanol/acetic acid/ water/

Coomassie Blue G250 and also by silver staining. After electrophoresis, the bands from the electrophoregrams were cut out and after spot detaining the peptide was extracted by 5% formic acid/acetonitrile (1:2) solution, the nisin concentrations were analysed by means of UV-VIS with Sunrise microplate ELISA reader (Tecan, Switzerland) at the wavelength of 595 nm). Water contact angle (WCA) of the treated/untreated films was measured by means of optical method, at room temperature; three 10  $\mu$ l drops were leaved on the surface for 20 s. Measurements were taken from 3 different locations by using Surface Energy Evaluation system (See System, Advex instruments s.r.o., Czech Republic). Atomic force microscopy (AFM) was proceed on ICON, Bruker, USA. The antimicrobial assay was carried out by using the agar (Mueller-Hinton) diffusion testing against the sensitive bacterial strains: *Staphylococcus aureus* CCM 885 to analyse possible antimicrobial activity loss [8, 17]. The activity was expressed as diameter of zones of microbial inhibition (IZ) growth occurring around the sample. Reduction of antibacterial activity was calculated as IZ ratio of samples after given time from their preparation and freshly prepared samples.

The results presented further represents average values from at least 5 measurements. Standard deviation value was always up to 10 % of average value.

### 3 RESULTS AND DISCUSSION

Figure 1 shows effect of plasma treatment on nisin immobilization and thus on the surface topology of the PVA substrates. The changes in roughness indicate the nisin absorption.

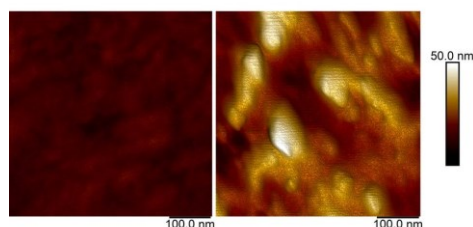


Fig. 1: AFM image taken 14 days after treatment; PVA/GA, crosslinking degree: 20%, RF power 7W/cm<sup>2</sup>, treatment time 10s, without (left) and with nisin (right)

A hydrophilic character (wettability) of PVA films significantly increased after the plasma treatment, see Figure 2. The significant decrease of WCA was observed because characteristic polar functional groups were introduced onto the PVA surface, after plasma treatment [12]. According to the measured contact angle, the total surface free energies  $\gamma^{\text{total}}$  and its components: Lifschitz-van der Waals and electron acceptor/electron donor ( $\gamma^{\text{LW}}$ ,  $\gamma^{\text{AB}}$ ) were calculated by Owens-Wendt fit, using water/diiodomethan, see Table 1[1]. The  $\gamma^{\text{AB}}$  component of the surface free energy increases with the plasma treatment, what indicates polar groups (attachment via covalent bonds). Also the total surface energy increases, what enables nisin adhesion. With nisin immobilization on the surface, the  $\gamma^{\text{LW}}$  increase, thus, the van der Waals interactions predominate. The total surface free energy increased too. The different trend (WCA increase) with nisin adhesion demonstrates decreased wettability, suggesting the hydrophobic nisin groups attendance. It was found out that water contact angle drop of plasma treated PVA films was sufficient for PVA wettability sustainment (WCA decrease is higher than 50 % of the initial value). Moreover, the treated films reveal homogeneity of their surfaces in comparison to the untreated films that showed different wettability at different places. While non-crosslinked PVA films and films with low crosslinking degree up to 5 % show only slightly decreased wettability in comparison with untreated PVA films, samples with higher crosslinking degree (10 and 20 %) show significant increase in WCA (Figure 2). Maximal WCA of 84° was obtained for PVA with at 20 % of crosslinking. This can be attributed to protein surface adhesion when nisin was bond on PVA substrate. It also reveals optimal PVA crosslinking degree for the protein efficient surface immobilization.

Effect of crosslinking degree on amount of nisin adsorbed on PVA substrate can be clearly recognized in the release study presented Figure 3. Initial concentration of nisin is in agreement with WCA measurements (Figure 2). It is also evident that crosslinking degree of PVA influences extent

of nisin adsorption as well as its release profile. Pure PVA (without crosslinking) show no affinity towards nisin. Nisin was washed off from the PVA surface after 1-24 hours in salt solution. However, PVA films cross-linked with di-carboxylic acid (GA) and plasma treated show enhanced surface affinity to the bacteriocin-nisin. The highest nisin surface

adsorption was found for the samples with 10 % crosslinking degree. More intensive initial introducing of crosslinking connections leads to apparent change of material properties and formations of inhomogeneity on the surface.

Table 1. The influence of plasma treatment and nisin adsorption on  $\gamma^{AB}$  and  $\gamma^{LW}$  components of the surface free energy of PVA films with different crosslinking degree

crosslinking %GA/mJm <sup>-2</sup>	Untreated		Treated		Treated+nisin	
	$\gamma^{LW}$	$\gamma^{AB}$	$\gamma^{LW}$	$\gamma^{AB}$	$\gamma^{LW}$	$\gamma^{AB}$
0	24.5	11.25	4.06	40.27	39.1	19.8
5	32.7	11.79	5.63	47.44	40.26	21.59
10	33.1	12.05	9.21	45.82	42.05	28.34
20	31.06	13.67	11.35	52.21	37.95	34.19
40	32.44	14.64	0.72	64.83	36.68	19.08

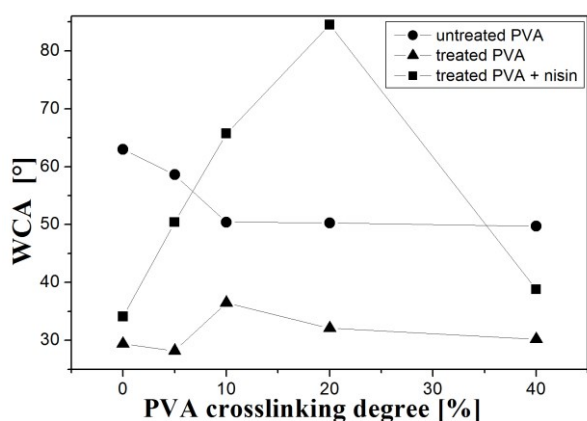


Fig. 2: The contact angle dependence as a function of PVA crosslinking degree; RF power 7W/cm<sup>2</sup>, treatment time was 10 s

The microbial assay showed that nisin can be stable and active against Gram positive *Staphylococcus aureus* even after 90 days (Figure 4). Reduction of antibacterial activity of the cross-linked PVA films with attached nisin can be seen in Figure 4. Only 35 % reduction of antimicrobial activity was observed in the case of nisin containing PVA samples with 20 % crosslinking degree. It should be mentioned that synergy effect of the crosslinking agent, GA, cannot be omitted. Modest antibacterial activity of GA in the cross-linked PVA systems has been found. However, this factor does not represent significant contribution to antibacterial activity of the PVA/GA/nisin samples [18]. Therefore nisin

can be supposed to the principal antibacterial agent in the studied systems.

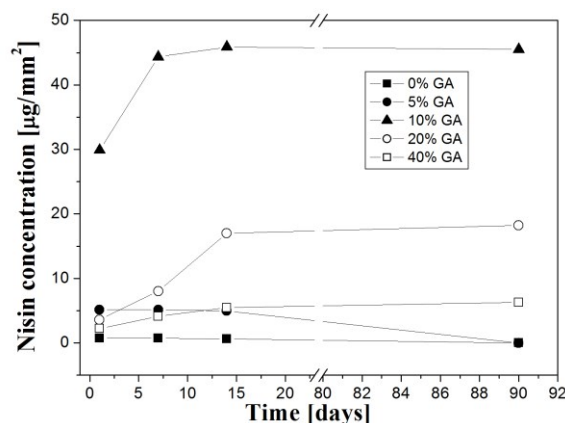


Fig. 3: Nisin release from the treated PVA films, after immersion in physiological solution

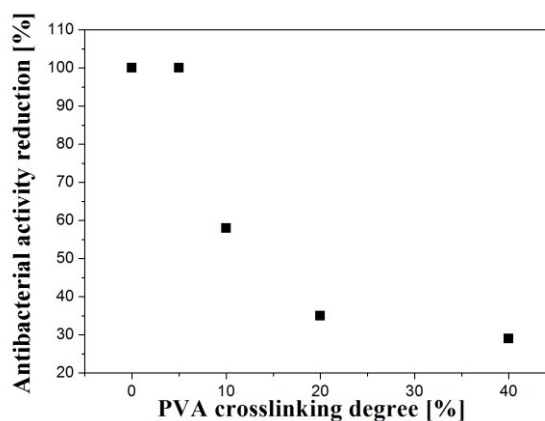


Fig. 4: Antibacterial activity change of PVA films with attached nisin after 90 days against *Staphylococcus aureus* (CCM 888)

#### 4 CONCLUSIONS

Improved adhesion of nisin on biocompatible glutaric acid cross-linked polyvinyl alcohol surface due to plasma treatment by Dielectric Coplanar Surface Barrier Discharge activation was studied in this work. It was found that not only plasma treatment but also PVA crosslinking degree has the crucial effect on both extent of nisin surface attachment as well its antibacterial activity and release kinetics. Crosslinking degree in range 10 – 20 % was evaluated as optimal for preparation of relatively water-stable peptide coatings that can sustain also the antibacterial properties with potential applicability in medical field. The achievement of improved control by plasma treatment techniques have been attractive. The optimal PVA surface modification can be enhanced by combination of conventional techniques and solvent-free techniques, especially by using DCSBD plasma. The latter one can represent novel and promising method for biomaterials design.

#### Acknowledgements

This work was supported by the Ministry of Agriculture of the Czech Republic (grant No. QJ1310254) and the Ministry of Education, Youth and Sports of the Czech Republic – Program NPU I (LO1504), co-funded by European Regional Development Fund.

#### REFERENCES

[1] Ryder M, Schilke K F, Auxier J A, McGuire J, Neff J A, *Jour. Colloid and Interface Sci.* 350 (2010) 194-199.  
[2] Yin H, Mix R., Friedrich J F, *J. Adhesion Sci. Techn.* 25 (2011) 799.

[3] Naik R, Stringer S J, Agarwal G, Jones S E, Stone M O, *Nat. Mater* 1 (2002) 169.  
[11] Resa C P, Jagus R J, Gerschenson L N, *Mater Sci and Engineering C* 40 (2014) 281-287.  
[4] Nechifor C D, Ciobanu C L, Dorohoi D O, Ciobanu C, *U.P.B. Sci. Bull. A* 71 (2009) 101-106.  
[5] Cho D, Lee S, Frey M W, *Journal of Colloid and Interface Sci.* 372 (2012) 252-260.  
[6] Karam L, Jama Ch, Dhulster P, Chibib N, *J. Mater. Environ Sci.* 4 (2013) 798-821.  
[7] Kafi A, Magniez K, Fox B L, *Composites Science and Technology* 71 (2011) 1692-1698.  
[8] Donegan M, Dowling D P, *Surface and Coatings Technology* 234 (2013) 53-59.  
[9] Kim K, Lee S M, Mishra A, Yeom G, *Thin Solid Films* (2015) in press.  
[10] Conyers L B, In: *Radiation in Art and Archeometry*, (Ed. Creagh D C and Bradley D A). Amsterdam: Elsevier, 2000, 1-14.  
[11] Gubskaya A V, Khan L J, Valenzuela L M, Lysniak J K, *Polymer* 54 (2013) 3806-3820.  
[12] Siow K S, Brichter L, Kumar S, Griesser H J, *Plasma Process. Polym* 3 (2006) 392-418.  
[13] Friedrich F J, *The Plasma Chemistry of Polymer Surfaces: Advanced Techniques for Surface Design*, Wiley-VCH, Weinheim 2012.  
[14] Saraf A, Johnson K, Lind M L, *Desalination*, 333 (2014) 1-9.  
[15] Cernak M, Kovácik D, Rahel J, Stahel P, Zahoranova A, Kubincova J, Toth A, Cernakova L, *Plasma Phys. Control. Fusion* 53 (2011) 124031.  
[16] <http://www.roplass.cz>  
[17] Bhatia S, Barti A, *J Food Sci Technol.* 52 (2015) 3504-12.  
[18] Hrabalíková M, *Immobilization of Biologically Active Compounds in the Water-soluble Polymer Matrix*, PhD Thesis, TBU, Zlín, 2015.

# Investigation of Plasma Properties in a Narrow Gap for Short Time Current

Runge T.<sup>1</sup>, Kopp T.<sup>1</sup>, Kurrat M.<sup>1</sup>

<sup>1</sup> Technische Universität Braunschweig, Institute for High Voltage Technology and Electrical Power Systems, Schleinitzstraße 23, 38106 Braunschweig, Germany, t.runge@tu-braunschweig.de

In the current study an experimental model was established, in which the plasma is quenched in a defined narrow gap and tested with an 8/20  $\mu$ s impulse current with an amplitude of 23 kA. The experimental model is equipped with an outlet duct of different cross sectional areas. The measured data such as arc voltage and current are used in order to estimate the plasma properties electrical conductivity and pressure.

**Keywords:** surge current, plasma properties, lightning protection, spark gap

## 1 INTRODUCTION

The use of surge protective devices (SPD) is necessary to prevent destruction of electrical components. The SPD based on spark gap technology ensure a galvanic separation between the system and the neutral conductor before the surge occurs. During surge event the spark gap ignites. Due to the arc, the surge is bypassed to the neutral conductor. The arc represents a failure which allows the flow of a failure current which is feed by the energy grid. Suppression of this current can be achieved by extinguishing the arc, which is necessary to prevent tripping of the main fuse. It is common use to quench the arc in a narrow gap which leads to a lower cross section of the arc and to an ablation of the chamber walls. Thus the current will be limited. If the limitation suffices to reach zero current, than the arc extinguishes, this ensures a galvanic separation again.

For a better understanding of the arc extinction process, it is necessary to know how the arc in the narrow gap behaves during a surge. To suppress the failure current it is necessary to increase the arc voltage. In [1] and [2] it has been shown that a chamber wall ablation increases the arc voltage due to a cooling effect of the gas [3]. Furthermore, the ablation leads to an increase of the pressure in the narrow gap. To reduce the pressure the narrow gap can be equipped with small outlet ducts. The influence of different cross sections of the outlet ducts on the pressure and electrical conductivity of the arc is investigated through measurements and simplified mathematical relations in this research.

## 2 METHODOLOGY

In order to investigate the plasma properties in a narrow gap an experimental model was established in the laboratory. The measured arc voltages for impressed impulse currents are then implemented in a simple mathematical model in order to evaluate the plasma properties. Subsection 2.1 presents the experimental setup and 2.2 introduces the mathematical modelling.

### 2.1 EXPERIMENTAL SET-UP

The selected test objects are rotational symmetrical spark gaps (Figure 1). Each cylindrical arc chamber consists of two tungsten copper electrodes (75 % / 25 %) with an outlet duct in the left electrode and a cylindrical shell made of polyoxymethylen (POM).

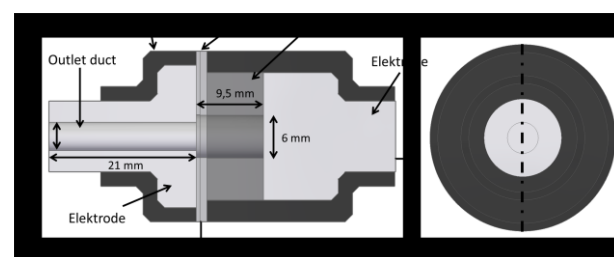


Fig.1: Top view (right) with section line for the side view (left) of the spark gap

The arc chamber has a gap length of 9.5 mm and a diameter of 6 mm. The test objects have different outlet ducts with diameters of 1 mm, 2 mm and 4 mm and a length of 21 mm. An insulating housing prevents external flashovers. Before surge the chamber is filled with air, due to wall and electrode ablation during surge the gas in the chamber is assumed to be a mixture of air, POM and copper.

Surge impulse currents (8/20 microseconds) according to IEC 62475 applied to the spark gaps ignite the arc plasma. The current amplitude is limited to 23 kA. The arc starts at the ignition aid on the left side and spreads out towards the opposite electrode. The arc plasma becomes hot and the pressurized plasma streams out through the outlet duct in the left electrode.

All test objects are subjected to several surge currents. Each impulse current and arc voltage are recorded. A typical surge current and arc voltage are shown in Figure 2. The impulse current is reasonably divided in three different phases: ignition, high current phase and undershoot due to oscillating circuit in the test setup [2].

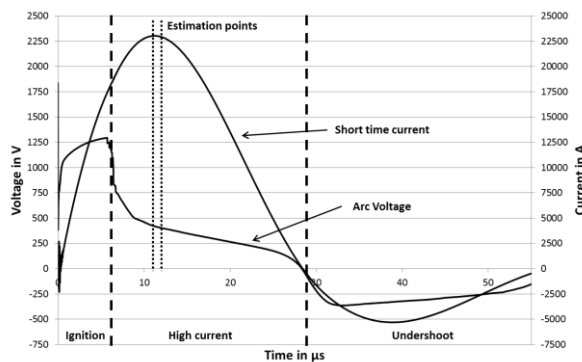


Fig.2: Typical surge current and arc voltage of a spark gap with 4 mm outlet duct diameter

The arc voltage of the hot plasma after current peak yields a decreasing plasma conductance within the high current phase. The electrical conductance depends on the geometrical current flow and plasma conductivity, which is assumed as a state variable. The gradient of the decreasing plasma conductivity is important for the current interruption capability of a spark gap. Plasma temperature and pressure determine the electrical conductivity. The tested various outlet duct diameters cause different pressure values. Therefore different arc voltages are measured.

## 2.2 MATHEMATICAL MODEL

The measured parameters are used in simplified relations to calculate the plasma properties. These properties are investigated for two different time points, at maximum current at 11 μs and 1 μs after maximum current (Figure 2).

For the electrical conductivity it is assumed, that the spark gap between the electrodes is completely filled with homogeneous plasma [4], while the outlet duct is neglected.

The voltage drop over the arc root is assumed to be constant with 16.5 V [5]. Based on these assumptions the el. conductivity can be calculated using Equation (1) with the current  $i$  and the arc voltage  $u_{arc}$ :

$$\sigma = \frac{i * length}{(u_{arc} - 16.5 V) * \pi * (diameter/2)^2} \quad (1)$$

In order to estimate the temperature and pressure the calculation of the electrical conductivity of air in [6] can be used (Figure 3). In this experimental model the nature of the gas is not pure air but a mixture of air, POM and copper. The deviations of pure air and a POM-air mixture in the electrical conductivity can be neglected [7]. Also the influence of copper vapour can be neglected at high temperatures [8]. Using these results the needed pressure at different temperatures can be calculated to get the estimated electrical conductivity.

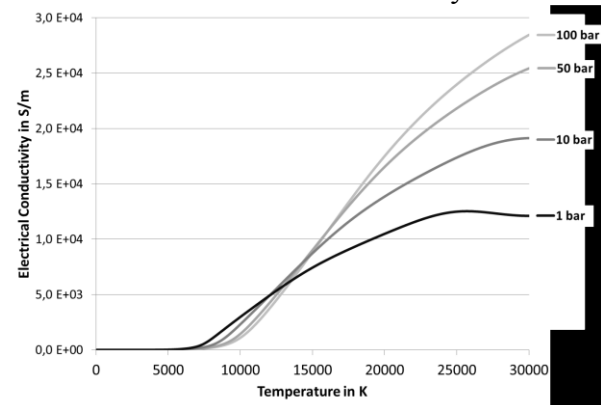


Fig.3: Electrical conductivity of air as a function of the temperature and pressure up to 100 bar and 30000 K [6]

Another method to estimate the temperature and pressure is to use the radiation of the plasma. Therefore the radiated power has to be known. An assumption is that the radiated power is a constant proportion of the input energy. With a radiation model like the net emission coefficient (NEC) the needed pressure at different temperatures can be calculated to get the estimated radiation power. The published results in [9] of the NEC of air for optical thin mediums in Figure 4 could be used. The deviations caused by the POM in the gas can be

neglected again whereas the influence of copper vapour cannot be neglected [10].

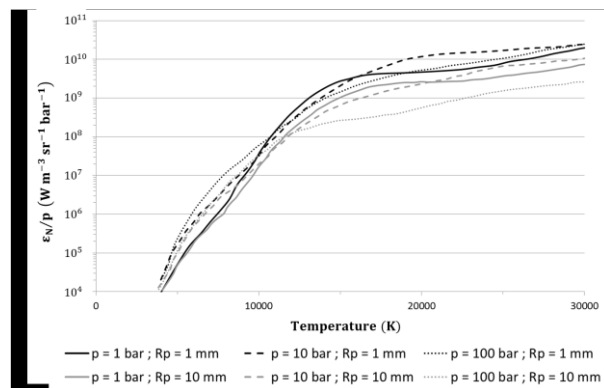


Fig.4: Reduced NEC of air plasma for different values of the radius and pressure [9]

A targeted comparison between both methods to get a more precise estimation of the pressure and temperature cannot be done due to the unknown radiated power and exact mixture of gas in the chamber.

However, in order to get a first assumption of the pressure in the chamber a pressure range can be estimated. Therefore the calculated electrical conductivity of the plasma and the results of [6] are used. The temperature is assumed to be in a range from 25000 K up to 30000 K. From these extreme values two values of the pressure can be deduced and a pressure range can be given.

### 3 RESULTS AND DISCUSSION

The applied surge impulse current is predefined by the generator according to IEC 62475 and varies only negligible with the device under test. At 11  $\mu$ s the current reaches its maximum with 23000 A in the next microsecond the current is decreasing about 200 A to 22800 A. Like the current the voltage drop is decreasing over the investigated time (Figure 5). In contrast to the current the voltage varies with different outlet duct diameter and is increasing with increasing diameter. The differences between an outlet duct diameter of 1 mm and 2 mm are only small at both time points, whereas the voltage is about 40 V to 50 V higher at 4 mm. Because of same current flow through the plasma the different voltages using different outlet duct diameters has to be determined by the electrical conductivity, which is also decreasing with increasing diameter of the outlet duct (Figure 6).

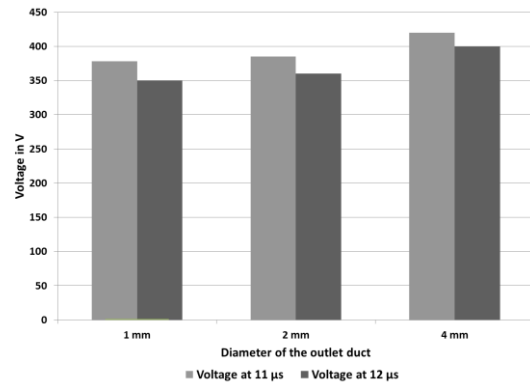


Fig.5: Voltage of the investigated spark gap with different outlet duct diameters at different time points

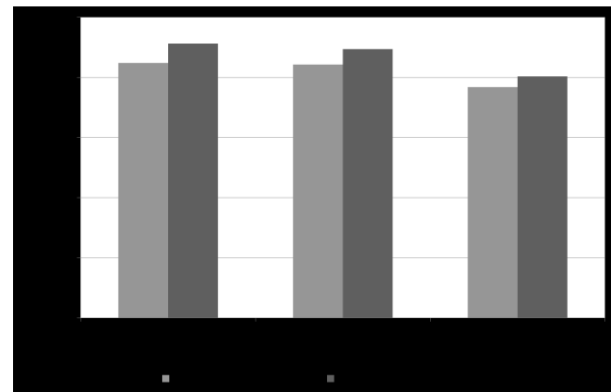


Fig.6: Electrical conductivity of the plasma in the investigated spark gap with different outlet duct diameters at different time points

Due to decreasing current over time a first assumption is that the electrical conductivity decreases as well. In this case, caused by faster decreasing arc voltage compared to a slower declining current, it can be ascertained that the electrical conductivity has to be increasing.

An increasing electrical conductivity is caused by an increasing temperature, pressure or a combination of both. Due to unknown exact temperature the pressure cannot be calculated. Instead, a temperature and pressure range can be given. The estimated pressure ranges of the plasma at different outlet duct diameters over the time are shown in Figure 7.

A consideration of the time dependence of the plasma pressure shows an overlapping of the pressure ranges. Due to this the time depended behaviour cannot be ascertained, but with the assumption that temperature is not fast increasing, but rather slightly decreasing, it can be predicted that plasma pressure increases further after current maximum. Considering the ideal gas law at constant volume, pressure

is proportional to the product of mass and temperature. Thus, in order to get an increasing pressure the mass has to increase. An increasing mass of the plasma in the spark gap should be caused by the ablation of the chamber wall, which is investigated in other publications as [1] and [2]. This ablation has to be greater than the mass loss due to mass flow through the outlet duct to increase the mass of the plasma.

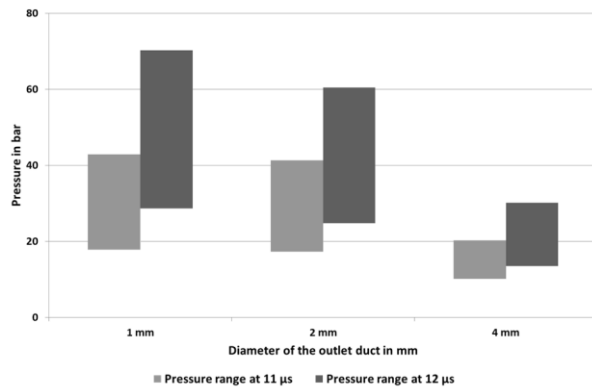


Fig. 7: Plasma pressure range in the investigated spark gap with different outlet duct diameters at different time points

Considering the influence of the outlet duct diameter on the pressure a clear tendency cannot be ascertained due to overlapping ranges. But with the assumption that temperature is nearly constant over the investigated outlet duct diameter range, it can be predicted that pressure decreases with increasing outlet duct diameter. Again considering the ideal gas law the mass has to decrease as well. This should be caused by a greater mass flow through the outlet duct due to a greater cross sectional area with increasing diameter.

#### 4 CONCLUSION

A first estimation of plasma properties in a spark model with different outlet ducts at 23 kA surge impulse currents was achieved. The results give a first overview about the possible pressure ranges. Due to overlapping ranges no tendency of pressure can be ascertained. But with the assumptions that temperature is rather slightly decreasing than increasing over the investigated time and nearly con-

stant over the investigated outlet duct diameter range a prediction of the pressure behaviour is given.

The plasma pressure seems to be still increasing shortly after current maximum. This leads to a higher electrical conductivity. As a consequence of the combination of increasing electrical conductivity and decreasing current the voltage is decreasing. The investigation of the influences of enlarged outlet duct diameters predicts a decreasing pressure. Consequentially the electrical conductivity declines and the voltage rises.

In order to suppress the failure current it is necessary to raise the arc voltage, which is determined by the electrical conductivity. To obtain a declining electrical conductivity the temperature and pressure has to be controlled. One method to control the plasma pressure is the modification of the outlet duct like it is shown in this investigation.

#### REFERENCES

- [1] Schottel B, Kurrat M, In: International Conference on Phenomena in Ionized Gases, Granada 2013, PS2-013.
- [2] Schottel B, Kurrat M, In: International Conference of Gas Discharges and Their Application, Beijing, 2012, p. 226-229.
- [3] Pospiech J, Ein neues Prinzip für Blitzstromableiter im Niederspannungsnetz, Books on Demand, 2001.
- [4] Schottel B et al, In: International Conference on Lightning Protection, Shanghai, 2014, p. 1400-1404.
- [5] Yokomizu Y et al, J. Phys. D: Appl. Phys. 29 (1996) 1260-1267.
- [6] Murphy A B, Plasma Chemistry and Plasma Processing 15 (1995) 279-307.
- [7] Ma Q et al, IEEE Transactions on Plasma Science 37 (2009) 261-269.
- [8] Cressault Y et al, In: International Conference on Gas Discharges and Their Applications, Xi'an, 2006, p. 133-136.
- [9] Peyrou B et al, J. Phys. D: Appl. Phys. 45 (2012) 455203.
- [10] Kloc P et al, J. Phys. D: Appl. Phys. 48 (2015) 055208.

# Diagnostics of Extinguishing Process in Low Voltage Devices by Pressure Field Measurement

Valenta J.<sup>1</sup>, Dohnal P.<sup>1</sup>, Dostál L.<sup>1</sup>

<sup>1</sup>Centre for Research and Utilization of Renewable Energy, FEEC, Brno University of Technology, Technická 10, Brno, Czech Republic, valentaj@feec.vutbr.cz

The article deals with the diagnostics of extinguishing process in low voltage devices by the means of pressure measurement in several points. The first part explains the technique of pressure measurement in switching devices and focuses on proper sensor properties and the problems of natural frequencies of the whole setup. The second part contains an example of pressure measurement analysis of the real device under real conditions, i.e. with the values of short-circuit currents in the range of tens of kA of prospective current with full voltage performed in the Laboratory of switching devices, Brno University of Technology. The last part compares the diagnostics method based on pressure measurement with other diagnostics techniques suitable for arc burning study under real conditions.

**Keywords:** pressure measurement, extinguishing process

## 1 INTRODUCTION

During opening of the mechanical switch under load or fault conditions, an electric arc is ignited between contacts. The whole process is finished after arc extinction, which may be, mainly for short-circuit conditions, very demanding.

The arc behavior can be mathematically described by the well-known magnetohydrodynamic equations, consisting from equations describing fluid flow (1-3) and equations describing electromagnetic field, which are Maxwell's equations.

$$\frac{\partial \rho}{\partial t} + \operatorname{div}(\rho \mathbf{v}) = 0 \quad (1)$$

$$\frac{\partial(\rho \mathbf{v})}{\partial t} + \operatorname{div}(\rho \mathbf{v} \mathbf{v}) = \rho \mathbf{f}_e + \nabla p + \operatorname{div} \bar{\tau} \quad (2)$$

$$\frac{\partial(\rho H)}{\partial t} + \operatorname{div}(\rho H \mathbf{v}) = \quad (3)$$

$$\operatorname{div}(k \nabla T) + \rho \mathbf{f}_e \cdot \mathbf{v} + q_H + \operatorname{div}(\bar{\tau} \cdot \mathbf{v}) + \frac{\partial p}{\partial t}$$

As follows from equation (2), the arc movement towards quenching chamber is mainly influenced by pressure field distribution (which in turn is connected with Joule heating) and by magnetic field creating electrodynamic forces acting on arc. Thus, the knowledge of pressure field distribution in real devices helps to understand arc behavior.

## 2 PRESSURE MEASUREMENT

To measure pressure during extinguishing process, one needs to be familiar with several phenomena and their proper treatment so that the measured values and pressure curves depict the correct situation.

In the following paragraphs, some of the important phenomena are explained with the help of experiments. The results of these experiments showed relative importance of these phenomena for proper curves reading.

### 2.1 REDUCTION OF SENSOR ACCELERATION

During extinguishing process, the electrodynamic forces may create acceleration of the whole tested device, which could be detected by piezoelectric pressure sensors. This could be partially avoided by proper device and sensor fixation, which is, however, sometimes difficult to fully fulfil – e.g. for somewhat flexible plastic parts of the device. The other thing is that some sensors are more vulnerable to detect device acceleration than others. The whole phenomenon mainly arises when relatively small pressures are to be measured.

This can be seen in Fig. 1. The pressure curve on the left side represents the pressure in the chamber, while on the right, when the arc is clearly extinguished, there is a “false” pressure coming from device and sensor vibrations. To avoid this, the device has to be fixed properly and other sensor more resistant

against acceleration has to be used.

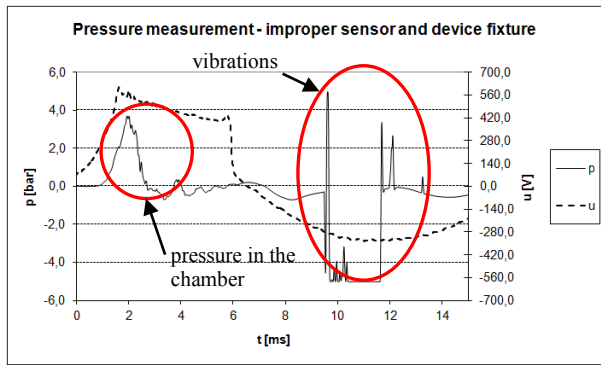


Fig.1: Acceleration captured by pressure sensor

## 2.2 RESONANT FREQUENCIES OF ADAPTER

To connect sensor to the point where the pressure is to be measured, it is necessary to use an adapter requiring only small diameter (typically M3-M5) so that there is only little influence on the aerodynamic conditions in the device under test. Typical configuration is presented in Fig. 2.

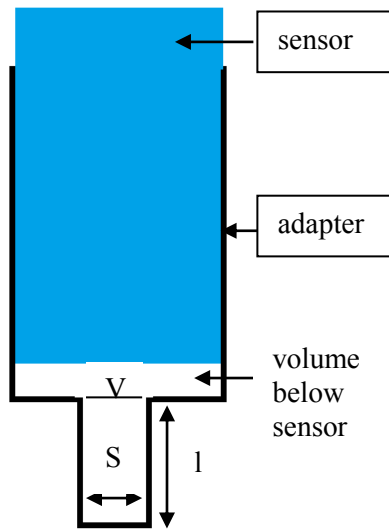


Fig.2: Sensor and adapter creating Helmholtz resonator

The sensor and adapter create so call Helmholtz resonator with natural resonant frequency of pressure oscillations. The resonant frequency is given by the following formula:

$$f_n = \frac{a}{2\pi} \sqrt{\frac{S}{V \cdot l}}, \quad (4)$$

Where  $a$  stands for the speed of sound in the given area,  $V$  is the volume of the cavity,  $S$  is

the cross-section of the channel and  $l$  is the length of the channel. The volume  $V$  acts like a spring and the volume of the channel acts like a mass.

For practical measurement of the pressure during arc burning, it is necessary to distinguish between pressure change due to arc or air movement and “false” pressure change due to resonance in the adapter. The latter one has to be filtered-out by some means. The problems may occur when the oscillation frequency is near to the pressure changes in the chamber.

This can be seen in Fig. 3-5. Fig 3 shows the pressure curve without any filtering. The pressure oscillations are not caused by arc movement, but arise from resonance behavior of the adapter. Fig. 4 shows the same measurement, but the pressure curve is filtered-out. There are many suitable filters to do so. The most commonly used are low-pass filter (sometimes possible to be hardware implemented) and moving average. The latter one was used in Fig. 4 with 15 samples to be averaged every time. This phenomenon can't be simply avoided by lower sampling frequency.

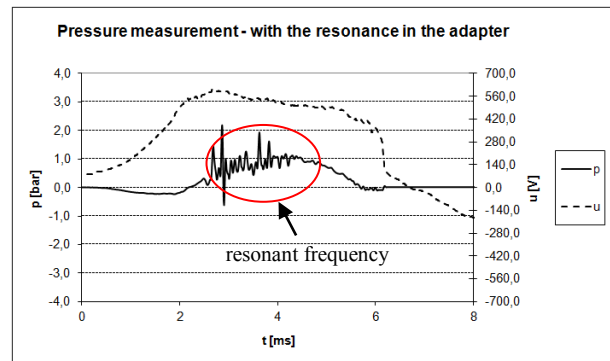


Fig.3: Pressure measurement with adapter resonant frequency

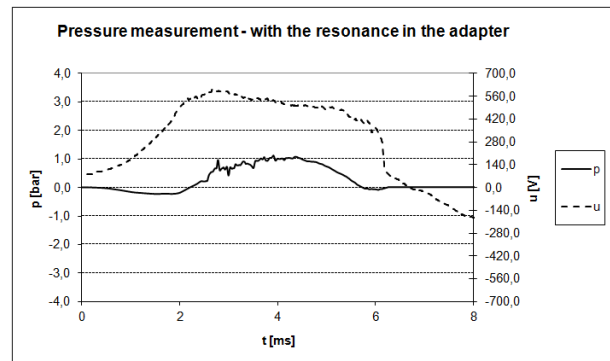


Fig.4: Pressure measurement with filtered-out adapter resonant frequency

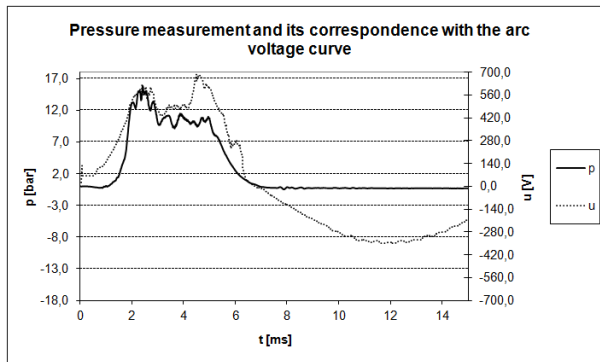


Fig.5: Pressure measurement with filtered-out adapter resonant frequency

However, when the filters are being used, it is necessary to be conscious about pressure changes in the chamber due to arc (air) movement. These have not to be filtered out! An example is shown in Fig. 5. There is an evidence that the pressure changes somewhat correspond to the arc voltage changes and are not given by adapter resonant frequency.

### 2.3 THERMAL SHOCKS TO THE PRESSURE SENSOR

Since the arc plasma has very high temperature, the thermal shock to pressure sensors occurs when they are not properly protected. This phenomenon usually leads to pressure decrease to unphysical negative values. Fig. 6 compares the pressure measurements with and without protection against thermal shock.

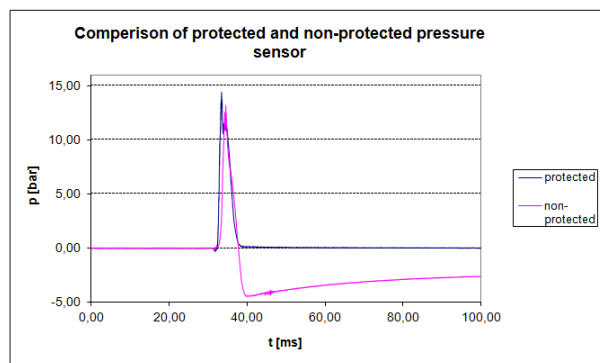


Fig.6: Pressure measurement with and without protection of the pressure sensor

To protect the pressure sensor, two important things have to be taken into account - the protective “grease” composition and the thickness of the protective layer. Most suitable materials are based on silicon grease. Also the more viscous greases can be used, but here, the thickness is of high importance.

### 3 EVALUATION OF PRESSURE CONDITIONS UNDER REAL CONDITIONS

The following examples (Fig. 7 and 8) show the pressure evaluation taken under real conditions – prospective currents in the range of tens of kA and test voltage 440 V.

Fig. 7 shows the example of device failure (low-voltage circuit breaker) which was simulated by change in quenching chamber. It is visible how the pressure corresponds with the current value. The peaks of the pressure are lacking for about 0,5-0,8 ms, because the pressure was measured outside the chamber. The aim was to verify the maximum pressures on plastics parts.

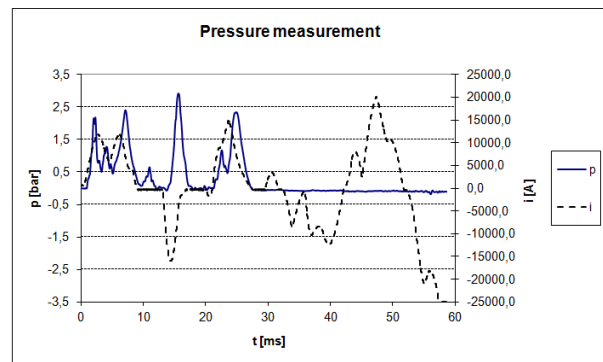


Fig.7: Pressure measurement with simulated failure

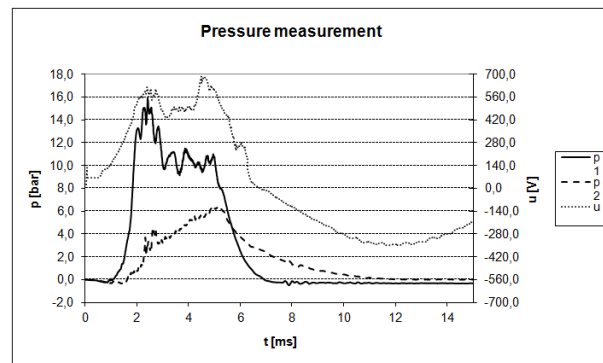


Fig.8: Pressure measurement for arc behaviour estimation

Fig. 8 shows two different points where the pressure was measured – in front of the chamber (p1) and behind the chamber (p2) of low-voltage circuit breaker. The peak values influence the required strength of the construction parts. The simultaneous oscillations after 2ms show the movement of the arc in the chamber – from the derivative of the pressure curves, it is clear that the arc travels in the chamber

forward and backward, however, the voltage shows no arc reflection from the chamber at the beginning.

#### **4 SUMMARY**

There are many methods for arc diagnostics in low-voltage devices. The advantage of pressure measurement is that it requires no opening of the device under test (the small holes are filled with sensor adapters) provided that the required strength of the parts is not adversely affected, or usage of transparent covers (optical diagnostics), which may affect gas dynamics.

However, it is necessary to treat several phenomena mentioned above to get reliable results.

From the pressure curves, it is possible to get not only maximal values necessary for strength of plastics parts, but it is possible to estimate gas movement and potential problems in quenching chamber aerodynamic conditions. The pressure measurement may also serve as a method for validation of CFD models of electric arc.

#### **Acknowledgements**

The authors gratefully acknowledge financial support from the Ministry of Education, Youth and Sports under project No. LO1210 and from Czech Science Foundation under project No. 15-14829S.

#### **REFERENCES**

- [1] Valenta J, Vávra Z, Pressure Conditions in LV Circuit Breakers, In: Proceedings of the XVIIth Symposium on Physics of Switching Arc, Volume I: Contributed Papers, ÚVEE FEKT VUT Brno, Brno, 2007, 213-216, ISBN: 978-80-214-3359-5.
- [2] [https://en.wikipedia.org/wiki/Helmholtz\\_resonance](https://en.wikipedia.org/wiki/Helmholtz_resonance) (on-line on 10.7.2015).
- [3] Blažek J, Měření a analýza spalovacích tlaků (Katedra vozidel a motorů), Technická univerzita Liberec, Liberec, 2012.
- [4] Boulos M I, Fauchais P, Pfender E, Thermal Plasmas – Fundamentals and Application, Volume I, Plenum Press, New York 1994, ISBN 0-306-44607-3.
- [5] Blazek J, Computational Fluid Dynamics: Principles and Applications, Elsevier Science Ltd, Oxford, 2004, ISBN 0 08 043009 0.
- [6] Ferziger J H, Peric M, Computational Methods for Fluid Dynamics, Springer-Verlag, Berlin, 2002, ISBN 3-540-42074-6.

# PLASMA PHYSICS AND TECHNOLOGY

## EDITORS:

I. ALI-BLÁHOVÁ, Czech Technical University in Prague, Faculty of Electrical Engineering  
Technická 2, 166 27 Praha 6, Czech Republic

V. AUBRECHT, Brno University of Technology, Faculty of Electrical Engineering and Communication  
Technická 3058/10, 616 00, Brno, Czech Republic

V. FANTOVÁ, Czech Technical University in Prague, Faculty of Electrical Engineering  
Technická 2, 166 27 Praha 6, Czech Republic

## EDITORIAL BOARD:

J. PÍCHAL (chairman), Czech Technical University in Prague, Faculty of Electrical Engineering  
Technická 2, 166 27 Praha 6, Czech Republic

P. BAROCH, University of West Bohemia, Faculty of Applied Sciences  
Univerzitní 8, 306 14 Plzeň, Czech Republic

M. BARTLOVÁ, Brno University of Technology, Faculty of Electrical Engineering and Communication  
Technická 2848/8, 616 00, Brno, Czech Republic

P. BARTOŠ, University of South Bohemia in České Budějovice, Faculty of Agriculture  
Studentská 13, 370 05 České Budějovice, Czech Republic

O. KLIMO, Czech Technical University in Prague, Faculty of Nuclear Sciences and Physical Engineering  
V Holešovičkách 2, 180 00 Praha 8, Czech Republic

V. KRÁHA, Czech Technical University in Prague, Faculty of Electrical Engineering  
Technická 2, 166 27 Praha 6, Czech Republic

J. MLYNÁŘ, Institute of Plasma Physics AS CR  
Za Slovankou 1782/3, 182 00 Praha 8, Czech Republic

J. PAVLŮ, Charles University in Prague, Faculty of Mathematics and Physics  
V Holešovičkách 2, 180 00 Praha 8, Czech Republic

J. ROSENKRANZ, Czech Technical University in Prague, Faculty of Electrical Engineering  
Technická 2, 166 27 Praha 6, Czech Republic

D. TRUNEC, Masaryk University, Faculty of Science  
Kotlářská 267/2, 61137 Brno, Czech Republic

## PUBLISHER:

CZECH TECHNICAL UNIVERSITY IN PRAGUE, Faculty of Electrical Engineering, Department of Physics  
Žitkova 1903, 166 36 Praha 6, Czech Republic

## EDITORIAL OFFICE:

CZECH TECHNICAL UNIVERSITY IN PRAGUE, Faculty of Electrical Engineering, Department of Physics  
Technická 2, 166 27 Praha 6, Czech Republic

PLASMA PHYSICS AND TECHNOLOGY publishes original experimental and theoretical papers of both a fundamental and applied nature that contribute to the understanding of phenomena related to plasma. The range of contributions encompasses: tokamaks and other magnetic confinement devices; short lived plasmas (plasma focus, z-pinch, particle beam-plasma interaction, X-ray sources); laser plasma; non-equilibrium low temperature plasma; thermal plasmas; plasma in technology, biology and medicine; fundamental plasma physics; plasma theory and simulation.

PLASMA PHYSICS AND TECHNOLOGY is published three times a year.

MINISTRY OF CULTURE  
OF THE CZECH REPUBLIC  
REGISTRATION NUMBER  
**MK ČR E 21495**

ISSN: 2336-2626 PRINT  
ISSN: 2336-2634 ONLINE

COVER DESIGN: ALŽBĚTA SLÁMOVÁ